Simulating Radiation Damage in Austenitic Stainless Steel and Ni-based alloys

Zainab Al Tooq

A Doctoral Thesis
Submitted in partial fulfilment of the requirements for the award of Doctor of Philosophy of Loughborough University

June 2013

Abstract

The evolution of materials at an atomistic level may have vital consequences for the properties of materials. Therefore, modelling long time scale behaviour of defects in a material is very important, particularly for those used in nuclear power plants. The materials used in nuclear power plants should have good mechanical properties to overcome the corrosive environment and high temperature. Examples of these materials are the austenitic stainless steel and the Ni-based alloys due to their high temperature properties. Molecular Dynamics (MD) and on the fly Kinetic Monte Carlo (otf-KMC) techniques have been used to model the radiation damage in austenitic stainless steel and the Ni-based alloys. This thesis represents the main findings obtained.

Three potentials were implemented and used to study radiation damage in austenitic stainless steel. Structural properties such as the elastic constants for the point defects in the pure metals were first calculated. This was followed by calculating the formation energies and migration energies of vacancy and self interstitial defects in the pure metals. Different calculations were performed using each potential on the ternary alloy (Fe with 10 at.% Ni and 20 at.% Cr) and the binary alloy (Ni with 20 at.% Cr) . For example, the segregation in these alloys was investigated using Monte Carlo simulations and results obtained for both alloys at high temperature MD. Furthermore, the vacancy formation energies were calculated for both alloys using all the potentials.

Radiation damage at Grain Boundaries (GBs) in fcc Ni and a Ni-Cr binary alloy has been studied using MD and otf-KMC techniques. From the results obtained, the mobility of interstitials were found to be higher than that of vacancies and tend to move quickly to the GB. Vacancies are found to migrate to the GB if they are near otherwise they tend to form clusters in the bulk. During the simulations, interesting mechanisms were observed for the point defects migration and recombinations. Large roughening at the GB was observed, especially in the alloy system and overall the total number of defects accumulated on the GB after multiple collision cascades were relatively small.

The radiation in fcc Ni resulting from low energy collision cascades was also modelled using MD and otf-KMC techniques. This part of work aimed replicating the observations seen in experiment and trying to understand them. Recombinations between vacancies and interstitials were found to happen from large distances with low barriers. Most defects produced from low energy collision cascades were found to recombine or interstitials were found to form clusters. Modelling the evolution of the vacancies shows the possibility of producing Stacking Fault Tetrahedra (SFT) which were found to dissociate at 200°C.

Acknowledgements

I am very grateful for my supervisor, Dr. Steven D. Kenny for giving me this opportunity to do this PhD and for providing unlimited support and excellent guidance during the work in this project. I am very thankful to Prof. Roger Smith for his unlimited support, useful discussions and giving me lots of codes that have been very useful in this research.

I owe great thanks to Marc Robinson for his help getting started with the project and all of his useful codes including the visualisation software which has been used throughout this project. I must also thank Louis Vernon for developing the otf-KMC which has been used during this project. I owe special thanks for my colleagues Chris Scott, Tomas Lazauskas and Miao Yue for developing the otf-KMC code which have been used during this research. I must also thank Chris Scott for the visualisation software that has been used to produce pictures and videos during the project. Similarly I am grateful to all material modelling group whom I shared an office, especially, Chris Scott, Sabrina Blackwell, Tomas Lazauskas, Miao Yue and Xiao Gai for all useful and productive discussions. I must also thank Dr. Carlos F. Sanz-Navarro for his part in the development of the LBOMD molecular dynamics package.

I would like to acknowledge PERFORM60 for funding this project and Loughborough University High Performance Computing (HPC) and HPC Midlands for the computing time which has been used throughout this project. I must thank the management of Bahrain Training Institute for giving me a leave to complete my study.

I am grateful to all of my family for their support, unlimited patience and encouragement during the course of the project especially my loving parents, my husband Ebrahim Al Tooq, my children Fatema, Noor and Hussain Al Tooq.

Contents

List of Figures

List of Tables

Chapter 1

Introduction

Nuclear energy represents a very promising source for electricity at low costs. Therefore, there has been a large body of work aimed improving the future of the nuclear energy through improving the safety of nuclear reactors and increasing their efficiency. There is a need to introduce a reliable material that can be used in construction of the nuclear reactors that will operate at higher temperatures and will operate for longer timescale in the corrosive environment.

The main types of materials used in construction of nuclear reactors include: nuclear fuels, cladding in which the fuel is contained and vessels and pipes in which the coolant is circulated. All of these materials are subject to corrosion due to the interaction between them and the reactor environment. The reactor environment is considered to be a very corrosive environment due to exposing to the coolant, high temperature, high pressure and the radiation.

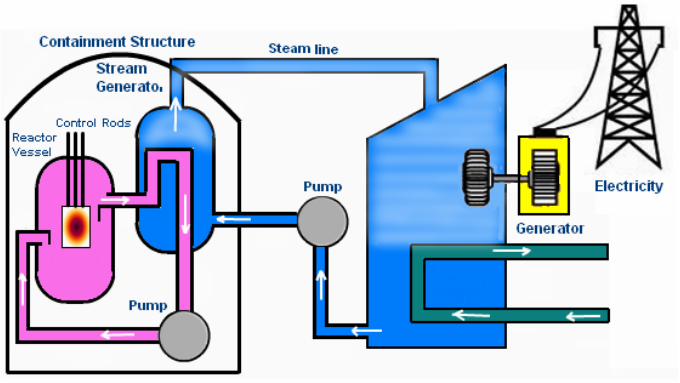

Figure 1.1: Illustration of nuclear vessel reactor and how the nuclear energy used to generate electricity. This picture is taken from [1].

Many atomistic modelling studies have been conducted for this purpose, most of them share the feature of transferring kinetic energy to an atom usually called Primary Knock on Atom (PKA) and studying the displacement per atom (dpa) introduced in the material. In addition, the evolution of damage over long time scale is studied to look at the ability of the material to heal through recombinations between point defects.

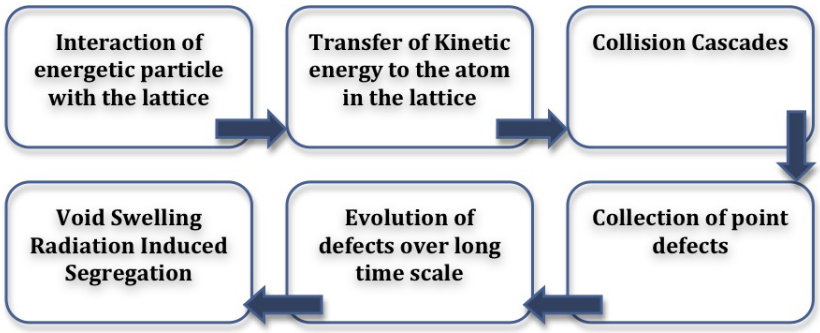

Figure 1.2: Effect of radiation on materials, important radiation effects are radiation induced segregation and the formation of voids, these tend to degrade the materials' properties.

There have been numerous materials that stand as interesting candidates for use in construction of the tubes and vessels in nuclear power plants, such as stainless steel which represents one of the main construction materials of nuclear reactor. In addition, lots of researches were conducted in Ni-based alloys because of their high temperature properties. Furthermore, studies on oxide-dispersion-strengthened alloy with nano particles oxides of yttria are promising, because of their stability under irradiation. Knowledge of the radiation damage in these materials plays an important role in predicting their lifetime.

Knowledge in radiation damage can be obtained through two main approaches. Experiments form an important approach to studying radiation damage in materials. Experimental studies of these processes are, however, often expensive and time consuming. Furthermore due to a lack of available experimental reactors other sources for replicating radiation damage must often be employed. On the other hand, computer simulation has been widely used to study the radiation damage in recent years. The simulation allows easier control of the irradiation conditions such as the temperature and the composition of the materials studied. Linking simulation to experimental knowledge helps understanding the effect of radiation on material and the mechanism by which this happens.

1.1 Computer Simulation

Computer simulation at atomistic level provides an important tool to study radiation damage. Traditionally this has been done at the atomistic level by imparting energy to an atom, the Primary Knock on Atom (PKA), and evolving the damage using Molecular Dynamics (MD) ([16] & [17]). Work over longer timescales has generally involved rate theory methods [18].

MD has been an extremely powerful tool to address many problems related to radiation damage and has given insight into numerous aspects regarding radiation damage. The limitation of the simulation time attainable, however, means that the evolution of radiation damage cannot be simulated over realistic timescales. For example it will be impossible to model multiple collision cascades to the system using MD over a realistic timescale which has driven the need for other techniques that allow modelling for longer time. One of these techniques is the on-the-fly kinetic Monte Carlo (otf-KMC) ([19], [20] & [21]) that allows modelling of complex systems, as it calculates the barriers at each step, and allows much longer timescales to be modelled, as it only follows diffusion events. Therefore using MD to model the initial phase of a collision cascade followed by otf-KMC to model the subsequent diffusion of defects is an extremely powerful tool for modelling the long time evolution of cascades.

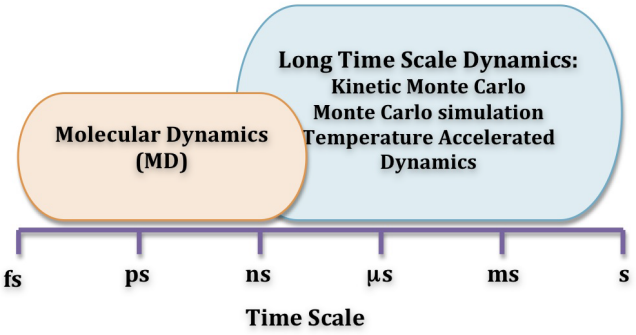

Figure 1.3: Illustration of the limitation of the time attainable using MD and how the other techniques allows modelling for longer times.

1.2 Materials of Interest

As explained earlier, the material that will be used in nuclear power plants should have special properties in order to overcome the aggressive corrosion environment and the high

temperature. Examples of materials that represent an interesting class for the next generation of nuclear power plants are austenitic stainless steel and Ni-based alloys. In this work we focus on the ternary alloy (Fe-Ni-Cr) and the binary alloy (Ni-Cr).

1.2.1 Austenitic Stainless Steel

Austenitic stainless steel is an iron based alloy with chromium (5-25%) and nickel (8-30%). The presence of chromium causes it to have a good corrosion resistance. Moreover, the presence of nickel reduces its brittleness at low temperatures. Furthermore, austenitic stainless steel has very good mechanical properties and can be used at temperatures above 550°C. The properties of austenitic stainless steel also can be enhanced by adding other elements such as molybdenum. Due to these properties, austenitic stainless steel has many applications and it represents one of the major construction materials in the nuclear industry.

The compositions for the ternary alloy studied in this work is (70 at.% Fe, 20 at.% Cr and 10 at.% Ni). From the phase diagram for the FeCrNi at 650°C, the ternary alloy, around the concentration of interest, can be a face-centred cubic (fcc) solid structure or a combination of body-centred cubic (bcc) and fcc structures as shown in figure (1.4). The ternary alloy of interest is paramagnetic at the operating temperature of a nuclear reactor as can be seen in the magnetic phase diagram for $Fe_{80-x}Ni_xCr_{20}$ [3] shown in figure (1.5).

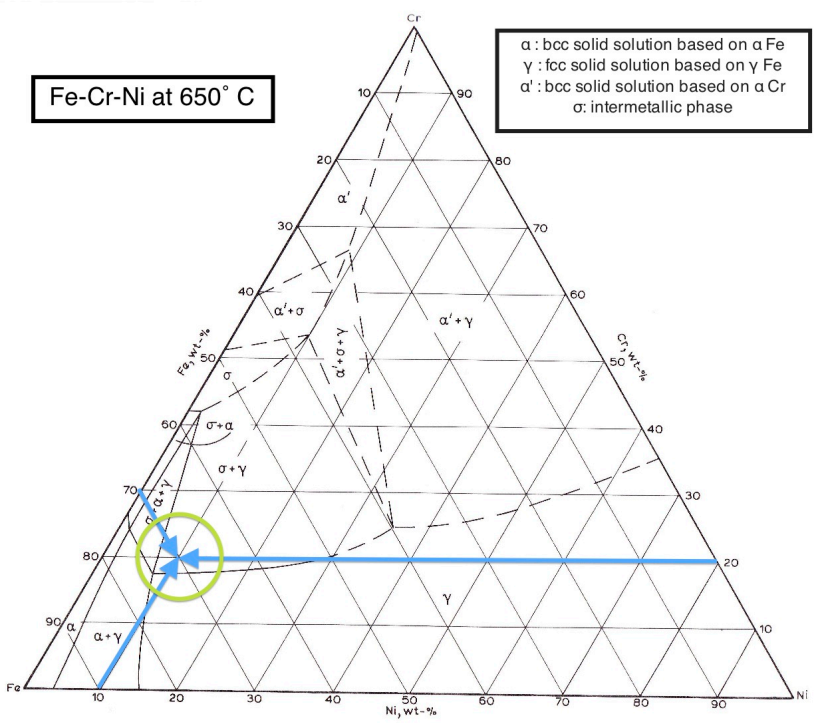

Figure 1.4: The phase diagram of the ternary alloy at 650°C, the green circle allocates the ternary alloy near concentration of interest. This picture is taken from [2].

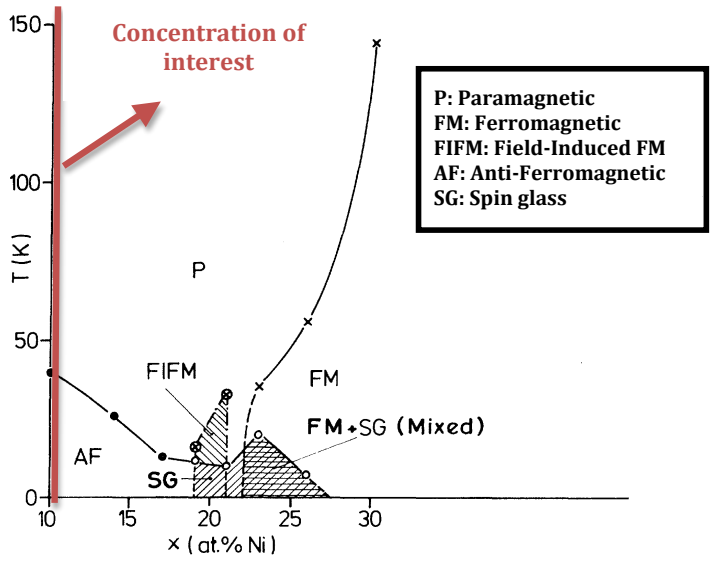

Figure 1.5: Magnetic phase diagram of the ternary alloy as a function of Ni concentration and temperature. The figure shows that the alloy of interest (shown by the red line) is paramagnetic at the temperature of a nuclear reactor. This picture is taken from [3].

1.2.2 Ni-based Alloys

Ni-based alloys represent a very interesting class of materials that have many application such as gas turbines that operates at high temperatures. This is due the presence of the γ' phase, which causes the Ni-based alloys to have a high temperature creep resistance. This is in addition to the oxidation and corrosion resistance, which result in Ni-based alloys being a strong candidate to replace the stainless steel as it can be used at 700°C operating temperature or higher.
In this work we concentrate on the binary alloy (80 at.% Ni and 20 at.% Cr). The binary alloy has an fcc structure at the operating temperature of the nuclear power plant as shown in figure (1.6).

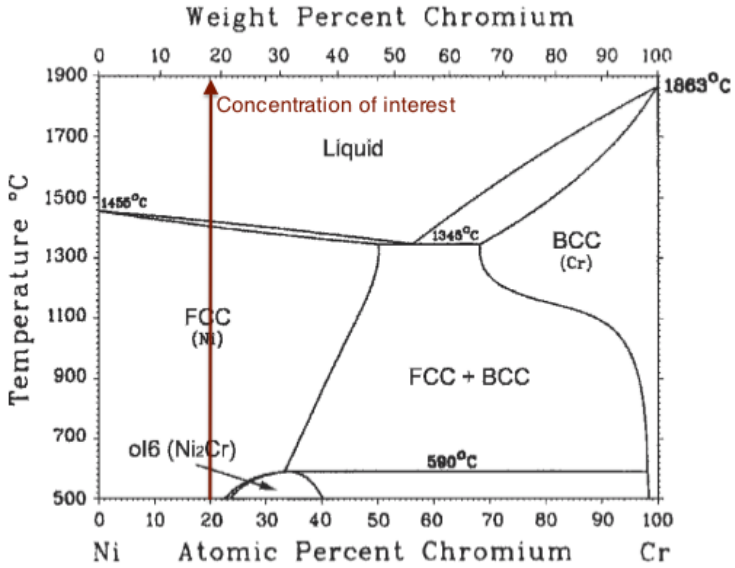

Figure 1.6: The phase diagram of the binary alloy as a function of the Cr composition and the temperature. This picture is taken from [4].

1.3 Research Goals

PERFORM60 is a European project that combines experiments and simulation in order to investigate and to understand the radiation damage on materials of interest. The main goal for the project is to extend the lifetime of the material used in nuclear power plant to over 60 years from around 30 to 40 years now. Therefore, within the project lots of experiments were performed and lots of models were introduced in order to gain deeper understanding of these materials and hence predict their lifetime. The project also involves studying variety

of materials with large range of compositions which helps in choosing the right compositions for longer lifetime.

Overall, the aim of studying radiation damage is to look at the defects produced in a material and studying their evolution over time. Our role in the project was to find the transition paths and transition rates of point defects in the ternary alloy. Since modelling the material requires a good potential that is capable of representing the interactions in the system correctly, the first goal of this research was to study the ternary potentials provided by G. Bonny (member of the project) in order to make sure the potential is good enough to perform the calculations. During the last three years, three potentials were provided for this purpose and our aim was to implement and test these potentials.

The second goal of this research was to model the radiation damage in the pure Ni and the binary alloy at the Grain Boundaries (GBs). Different kinds of GBs were studied and the evolution of defects resulted from 1 keV collision cascades were studied. Also the vacancy and Cr segregation to the GBs and the damage resulted from multiple collision cascades were studied.

The last goal for this research was to study the radiation damage in bulk fcc Ni for low energy collision cascades. The motivation behind that work was trying to replicate the results obtained in experiments and trying to explain the observations seen in these experiments.

1.4 Thesis Layout

The rest of this chapter discusses previous work done on studying the radiation damage in these materials. It includes both experimental and the modelling work. Chapter 2 introduces the methodology used in this research. The chapter consists of four main sections. The first section starts by introducing the Molecular Dynamics (MD) along with its important aspects such as the interatomic potentials, the algorithm used to evolve the system, boundary conditions, system thermalisation, system minimisation and visualisation. In the second section we explain the Long Time Scale Dynamics techniques (LTSD) used in this work. This includes the saddle finding methods and the barrier calculating techniques. It also explains the otf-KMC algorithm used. Parallalisation is explained in the third section and an overview of the analysis techniques used is shown in the last section.

Chapter 3 explains the ternary potentials and it consists of three main sections. Three

potentials were provided for the ternary system, therefore, each potential is discussed in one section. For each potential, the energy formalism is explained along with the implementation of the potential. This is followed by the formation and migration energies obtained for the point defects in the pure materials and the alloys which compared with the available results from Density Functional Theory (DFT). Also the results obtained for the segregation in the ternary and the binary alloys are discussed along with results obtained from high temperature MD for both alloys. For each potential the difficulties involved in its implementation are discussed.

Chapter 4 discusses the main results obtained from modelling radiation damage in fcc Ni and Ni-Cr binary alloy at the GBs using MD and otf-KMC technique. The chapter includes an explanation of the construction process of the GBs studied and the main results obtained. The chapter illustrates the interesting transitions mechanisms and the GB roughening seen during the simulation.

Chapter 5 highlights the main findings from modelling the radiation damage in fcc Ni with low energy collision cascades. The chapter starts by explaining the experimental observations and explains the main findings at room temperature and at 200°C. Furthermore, the chapter presents the mechanism for the recombinations between the vacancies and the interstitials that seen during the simulation.

Chapter 6 summaries all results obtained and gives general conclusions. It also highlights the possible future extensions.

1.5 Previous Work

Material swelling represents one of the main effects of radiation on materials as it will change the dimension of the material. Radiation Induced Segregation (RIS) is also a very important radiation effect on materials, which is simply the redistribution of an alloy's species that occurs due to the radiation damage, often as a result of defects diffusion. RIS is very important as it will result in depletion or enrichment of species in one region which in its turn changes the properties of the alloy. The main factor behind the RIS is the diffusion of the defects in the alloy, therefore, there have been lots of researches aimed to understand the general trend of segregation in the stainless steel and Ni-based alloys by looking to the defects diffusion under different irradiation conditions such as temperature and dose rate. In addition, the change in segregation was investigated as a function of the solute composition.

1.5.1 Radiation Induced Segregation

RIS plays an important role in degradation of material near sinks especially at the GBs. The different diffusion rates of the elements in the alloy result in some of them being attracted to the GBs which causes other elements moving away from the GBs. This results in changing the composition at the GB, which could have vital consequences on the lifetime of the material. RIS can be different from equilibrium segregation where the disorder at the interface is due to the energy difference between the different sites, which allow atoms to deposit themself in particular sites.

Experiments on RIS

RIS was first observed by Hanneman and Anthony in 1968 [22] in Al binary alloys where they proved that point defect fluxes were produced in the Al binary alloys when exposed to irradiation. Since then, lots of experiments were conducted to stand behind the mechanism by which this happens. The mechanism by which these experiments performed can be divided into two main steps:

1. Irradiation of the material with fast particles such as protons or neutrons. This should create defects in the material.

2. Measuring the local composition of each element at the sink. This can be done using Auger electron spectroscopy [23] or scanning transmission electron microscope.

Many experimental studies were carried to study the swelling and RIS in the austenitic stainless steel. For instance, the swelling in austenitic alloys was studied by T. R. Allen, J. I. Cole, J. Gan, G. S. Was, R. Dropek and E. A.Kenik [24]. In their experiment they studied the effect of changing the percentages of Ni, Mo, P and Zr on the swelling. Eight alloys were used in the experiment with different compositions, where every alloy was irradiated with 3.2 MeV protons at 400 °C. In their results, they showed that increasing the percentage of Ni in an alloy of (Fe - 18%Cr - x%Ni) will reduce swelling, however, it will increase segregation. Increasing Mo and P in an alloy of (Fe - 16%Cr - 13%Ni) and Zr in an alloy of (Fe - 18%Cr - 9.5%Ni) will reduce both segregation and swelling. They also studied the correlation between swelling and RIS in these alloys and found that if the RIS results in decreasing the lattice parameter of the material then this will result in reduced swelling.

In addition, the swelling has been studied in annealed 304 and cold-worked stainless steels at 300 °C [25]. The research focussed on studying the effect of helium along with temperature and dose on void swelling. The main observation was that He is a necessity for the void

formation at the experiment conditions for both alloys with the void formation sooner in the 304 stainless steel than in the 316 stainless steel at 300°C and 330°C.

Microstructure evolution of a proton irradiated austenitic Fe-Cr-Ni alloy were also studied ([26], [27] & [28]). The researches focussed on the effect of dose and temperature on the voids and dislocation loops. In the later research, three alloys were used for the experiment, 304 stainless steel, 304 stainless steel with Si and 304 stainless steel with Cr and Ni. Results showed that the Si will stop the void swelling as no void was noticed in the alloy with Si. Furthermore, the study of RIS showed enrichment of Ni and depletion of Cr at grain boundaries in the alloy with Cr and Ni.

More research has been conducted to understand RIS in austenitic alloys. Specimens of 304 and 316 stainless steel were used in experiments at 350 °C to study the effect of displacement rate on RIS [29]. The results showed more segregation in alloys with higher Ni concentration and that the RIS increases as the dose rate decreases. Furthermore, the effect of adding an oversized solute on RIS has been studied [30]. The main observation from this experiment was the reduction of RIS by adding the oversized solute. The mechanism by which this happens was the solute-vacancy trapping where this decreases the Cr depletion at the GBs with the Zr solute being more effective than Hf due to the large binding energy between Zr and the vacancy.

One of the serious problems in a material that could result from exposing to radiation is Irradiation Assisted Stress Corrosion Cracking (IASCC). J. T. Busby, G. S. Was and E. A. Kenik [31] studied the IASCC to identify if RIS plays an important role in IASCC. Experiments and modelling were performed by removing the dislocation loops from irradiated stainless steel and keeping the RIS. Results obtained showed that RIS of Cr, Ni, Si or P is not the main elements of IASCC.

RIS in Ni-based alloys has been also studied [32]. In the later experiment, RIS was measured for three alloys, (Ni - 18% Cr), (Ni - 18% Cr - 9%Fe) and (Ni - 18% Cr - 0.08% P). Cr depletion and Ni enrichment were found in the binary alloy with RIS increasing as the temperature increases. Adding the Fe in the alloy results in less Cr depletion and Ni enrichment due to Fe diffusing faster than Ni. However adding the P in the alloys implies strong P enrichment and more Cr depletion at the GB. Furthermore, the researcher introduced the possibility of thermal non-equilibrium segregation (TNES) when material thermalised to 1100°C or 750°C and cooled using different techniques such as water quench and furnace

cool. For the first binary alloy (Ni - 18% Cr), enrichment of Ni and depletion of Cr was observed when cooling using water quench and the opposite observed when using furnace cool. Enrichment of phosphorous, depletion of chromium and Ni depletion were observed for all cases in (Ni - 18% Cr - 0.08% P). For (Ni - 18% Cr - 9%Fe), Cr enrichment was observed for experiments at 1100°C and Cr depletion occurred when the alloy first thermalised to 750°C.

Modelling RIS

RIS in the ternary alloy has been also studied by Piochaud [5]. He developed a Pair Interaction Model (PIM) based on DFT data where he used it to find the RIS profile using Atomic Kinetic Monte Carlo (AKMC) simulation. PIM was built assuming the interstitial formation energies strongly depend on the local environment in the ternary alloy. This model was found to reproduce the DFT formation energies, however, the values obtained using it restricted the segregation of Ni and the RIS profile obtained was not in good agreement with the experimental results. Another model not dependent on the DFT data, developed by Piochaud was capable of reproducing a RIS profile that shows Ni enrichment and Cr depletion in good agreement with the experimental results as can be seen in figure (1.7).

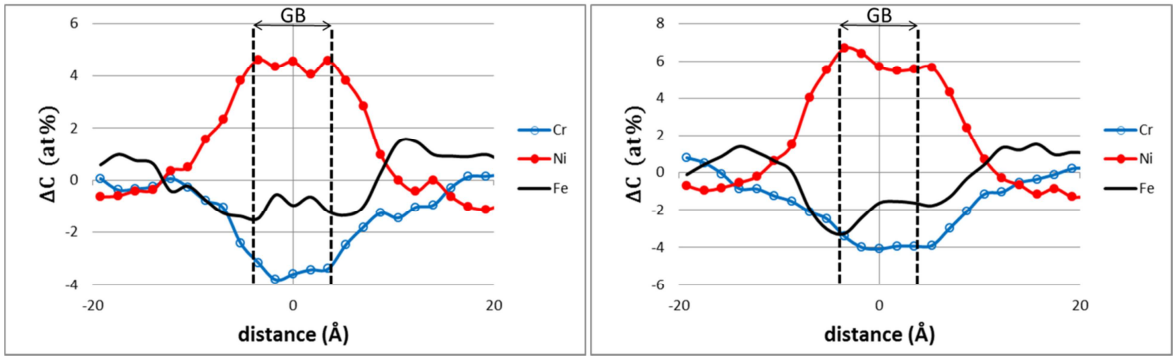

Figure 1.7: RIS profile in the ternary alloy obtained from AKMC simulation done by Piochaud. The left figure shows the profile at 500 K and the right figure at 723 K. The profile shows Cr depletion and Ni enrichment at the GB. This picture is taken from [5].

Another model has been developed to study the RIS at GBs in austenitic steel by Nastar [33]. The model is based on the segregation produced by vacancies and interstitials. The results obtained emphasises the role of thermodynamic properties on the 'W-shaped' profile. The results succeeded to identify two types of parameters that are responsible for the 'W-shaped profile', local equilibrium between the GB plane and the adjacent plane and the transport

coefficient.

1.5.2 Defects Formation and migration energies

Experimental

Due to impurities that exist in materials, it is not easy to calculate the formation and migration energies of point defects in experiment especially in the ternary alloy. Experimental vacancy formation energies in pure elements, however, exist. For instance, H. Matter, J. Winter and W. Triftshäuser [13] used positron annihilation spectroscopy to find the vacancy formation energies in pure Ni and Fe as shown in table (1.1).

Metal	fcc Ni	fcc Fe	bcc Fe
Vacancy formation energy (eV)	1.55 ± 0.05	1.40 ± 0.15	1.60 ± 0.10

Table 1.1: Vacancy formation energies in pure metals obtained from experiment. These values are taken from [13].

C. Dimitrov and O. Dimitrov studied the formation and the migration energies of point defects in high Ni fcc ternary alloy [34] and high Fe fcc ternary alloy [35]. They used electrical resistivity recovery measurement to obtain their results. The main findings from their experiments were:

- Increasing the composition of Ni in the alloy increases the mobility of the self interstitial defects.
- The vacancy mobility does not change while Ni in range (20 - 45%), however, the migration energy for a vacancy is higher when the composition of Ni is 75%.
- In high purity Fe alloy, the self interstitial was found to diffuse over longer distances as temperature increases.

Simulation

Since it is very hard to find a ternary potential to describe the interactions in the ternary system, there are lack in models for the ternary alloy. However, Piochaud [5] succeeded to determine the point defect formation energies in the ternary alloy. His calculations were done using DFT calculations using VASP code. Piochaud used the values of the formation energies obtained for the vacancies and $\langle 100 \rangle$ dumbbell to develop a model to calculate the formation energies as a function of the number of Ni and Cr in the first nearest neighbours

to the defect. The models obtained were found to reproduce well the DFT values.

Also, there have been lots of models to describe binary alloys. For example, lots of models can be found on the binary system Fe-Cr [36], [37], [38] & [39]. Most of this research dealt with the interaction of Cr precipitates and dislocations in bcc Fe-Cr system. Also, MD and Embedded Atomic Method have been used to study Hydrogen embrittlement in Ni-based alloys [40].

Furthermore, the ab initio method was used to study Ni-Fe-Cr alloys by J.D. Tucker 2008 [41]. Tucker studied two binary systems, Ni-Cr and Ni-Fe systems. She focused in her work on the diffusion mechanism of vacancy and interstitial defects in the two systems. Tucker succeeded to calculate diffusion coefficients for the defects. She calculated the migration barriers of the defects and studied the effect of local environment on changing them. Tucker showed that Ni is the slowest and Cr is the fastest among the three species in term of the speed of diffusion. Furthermore, she found that Cr shows a tendency to bind with interstitials comparable to Fe in Ni based binary alloy. However, both species will not bind with vacancy defect. In addition, Tucker studied the Radiation-Induced Segregation (RIS) in the fcc Ni-Cr-Fe system.

Chapter 2

Methodology

2.1 Molecular Dynamics

2.1.1 Introduction

Along with the rise in the interest of studying and understanding different phenomena in many subjects, the need for tools to perform such research has grown. Computer simulation has been an important tool to study many different kinds of research. Molecular Dynamics (MD) simulation for instance has proven to be an extremely powerful tool to study lots of aspects in different subjects such as biology and radiation damage since it was introduced in 1950s [42].

MD simulation at atomistic level has been used widely in materials modelling. The aim of the MD simulation is to model the movement of atoms in the simulation system. This is done by calculating the positions, velocities and accelerations of atoms using the interaction forces acting on them which is done by solving Newton's equations of motion:

$$\mathbf{F} = m\mathbf{a}, \tag{2.1}$$

$$\mathbf{F} = -\frac{\partial U}{\partial \mathbf{r}}, \tag{2.2}$$

$$\mathbf{a} = -\frac{\partial U}{\partial \mathbf{r}}/m, \tag{2.3}$$

where force acting on atoms $\mathbf{F}$ is the derivative of the potential energy $U(\mathbf{r})$ and $\mathbf{a}$ is the acceleration.

A key factor of getting the most from the MD simulation is using a good interatomic poten-

tial to describe the interaction of atoms in a lattice. Interatomic potentials can be divided into two main types, the first type is to describe the long range interactions such as the Embedded Atomic Method (EAM) potential and the second the short range interactions such as Ziegler-Biersack-Littmark (ZBL) universal potential.

An MD simulation may sometimes requires the atoms in the lattice studied to be in their minimum energy positions. There are different minimisation techniques available to be used within MD simulation such as Conjugate Gradient method. Furthermore, different kinds of constraints can be implemented to the simulation box during an MD simulation such as fixing few layers, using periodic boundary conditions or having thermal layers. This helps to maintain the simulation conditions close as much as possible to the reality conditions, which enhance getting more realistic output from the simulation.

Throughout this project, MD package developed by Loughborough University (LBOMD) [43] has been used. LBOMD package was written to run the MD simulation to an input lattice along with set of user input files to choose simulation conditions. The main input file allows the user to set the main parameters of the simulation such as type of simulation, boundary conditions, time of simulation and the required amount of output. A picture of the input file is shown in figure (2.1). Other input files for example will control the constraints of the boundary conditions, thermalisation time, interatomic potential and the parameters required for the collision cascades.

BEGIN	/* BGORCT => BEGIN or CNTIN (RESUME)
EQUIL	/* SIMUSTAGE => EQUIL(EQUILIBRATION) or PRODU (PRODUCTION)
COLLI	/* SIMUTYPE : COLLI, INDEN
PURNi	/* IDENT=> SIX CHARACTER IDENTIFIER OF THIS RUN
1 1 1	/* PBCX,PBCY,PBCZ
5.00000	/* PCSKIN => SKIN OF NEB-LIST AS % OF CUTOFF
1.000000	/* DT => INTEGTATION TIMESTEP (fS)
20000	/* RUNTIM => TOTAL RUN TIME (fS) DURING PRODUCTION STAGE
0	/* FE_FLAG (SET 1 FOR EMBEDDING CONTINUUM)
0.8302	/* YOUNGS eV/A^3 (REQUIRED FOR MULTISCALE MODEL)
0.278	/* POISSONS (REQUIRED FOR MULTISCALE MODEL)
1.438	/* ROE (ATOMIC MASS)/A^3 (REQUIRED FOR MULTISCALE MODEL)
NOSE-HOOVER	/* THERMTYPE => THERMOSTAT TYPE (NO_THERMOSTAT,NOSE-HOOVER,..)
298.0000	/* TTEMP => LATTICE TEMPERATURE (K)
00.0000	/* PTEMP => PROJECTILE/INDENTER TEMPERATURE (K)
1000.00	/* SAFEVR => FAILSAFE FILE EVERY (fs)
50.00	/* PICEVR => PICTURE FILE OUTPUT EVERY (fS)
.T.	/* Include atom Kinetic Energy in PIC file
.T.	/* Include atom Potential Energy in PIC file
.T.	/* Animation flag
1000000.0	/* Update animation input every (fs)
0	/* Ionic systems only: DPMTA = 0; FMMP = 1
.T.	/* Output for NEB
.F.	/* Output charges in xyz's
.F.	/* Output velocities in xyz's
.T.	/* Zip flag
.F.	/* fix atoms when outside certain range
100	/* fix atoms when more than this distance away (Ang) (when above is true)
.F.	/* charge recovery simulation
100	/* half life to use in charge recovery simulation (fs)
1.0	/* time step for updating charge recovery sim (fs)
.F.	/* create backup of FAILSAFE.DAT whenever a new one is written
.T.	/* Pipe positions in, return energy and forces (single point evaluation only!)
.T.	/* Minimal file output (only writes animation-reference.xyz)

Figure 2.1: The main input file of LBOMD which allows the user to set the main parameters for MD simulation such as the type of simulation, simulation time and how much output is required.

The main aim from this section is to discuss the main aspects of the MD simulation used in this work. These are shown in figure (2.2).

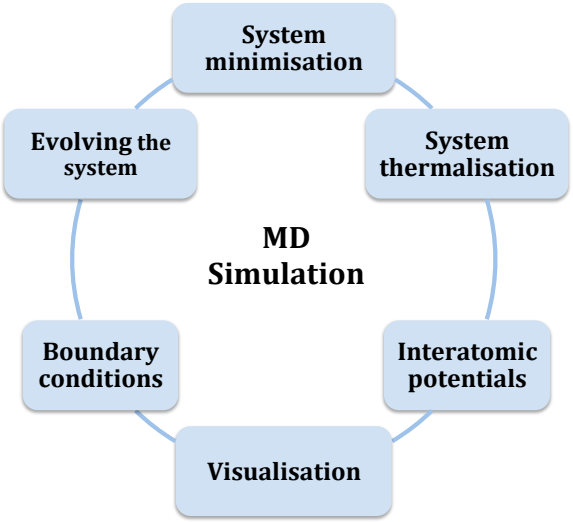

Figure 2.2: Main aspects of the MD simulation used in this work. Some of these are essential to run the MD simulation such as evolving the system and the interatomic potentials and some should aim to make the simulation conditions closer to realistic conditions, such as the system thermalisation.

2.1.2 Interatomic Potentials

Choosing the right potential to represent the atomic interaction is crucial in MD simulation. Many potentials have been developed to be used to describe the atomic interaction depending on the species studied such as Pair, Embedded Atomic Method (EAM) and Ziegler-Biersack-Littmark (ZBL) potentials.

Pair Potentials

The pair potential is an easy potential to implement in which the total energy of an atom is a function of the interatomic separations of the neighbouring atoms and can be represented by:

$$U = \frac{1}{2} \sum_{i,j(j \neq i)} V_{ij}(R_{ij}), \tag{2.4}$$

where R_{ij} is the separation of a pair atoms i and j.

Pair potentials are the earliest form of potentials, which form the basis of lots of later potentials. It is proven to represent the interaction of noble gases very well, however, it has drawbacks when used for metals. The main drawback of the pair potential is that it is found to be not enough to represent the bulk modulus of all materials and cannot reproduce the

elastic constants unless it satisfies the Cauchy relation ($C_{12} = C_{44}$). Furthermore, the pair potential is found to represent the energies of point defects and surfaces very poorly [44], which introduces the need for modification in the pair potential in order to use it with point defects.

Embedded Atomic Method

An important potential is the Embedded Atomic Method (EAM) developed by Daw and Baskes [45], which has proven to represent interatomic interactions very well for different materials. EAM considers each atom as an impurity embedded in a sea of electrons of all remaining atoms. In other words this means that the total potential is the summation of the impurity potential and the host potential. The host potential here can be represented by the pair potential:

$$U_1 = \frac{1}{2} \sum_{i,j(j \neq i)} V_{ij}(R_{ij}). \tag{2.5}$$

The other term of the EAM is the embedding term which can be written as:

$$U_2 = \sum_i F(\bar{\rho}), \tag{2.6}$$

which represents the energy of embedding an atom into a local density $\bar{\rho}$. The electron density of an atom here is assumed to be the summation of all densities of surrounded atoms.

$$\bar{\rho} = \sum_{j \neq i} \rho_j^a(R_{ij}), \tag{2.7}$$

combining the two terms we get:

$$U = \sum_i F(\sum_{j \neq i} \rho_j^a(R_{ij})) + \frac{1}{2} \sum_{i,j(j \neq i)} V_{ij}(R_{ij}). \tag{2.8}$$

The form of F and V_{ij} can be established from the physical properties of the solid such as lattice constants and formation energies of the point defects. Since the $F(\rho)$ does not depend on background density, one can use the same function obtained for a pure system in an alloy system.

Although EAM has many applications in different fields such as bulk properties and grain boundaries [46], it is unable to estimate the potential energy well for materials with directional bonding. This is due to that density in EAM is represented by linear summation of

the neighbouring atoms densities. This led to the development of the Modified Embedded Atomic Method (MEAM) [47] which takes care of this limitation by including an angular dependent contribution.

Modified Embedded Atomic Method (MEAM)

The main aims of the MEAM [47] are to include interaction of atoms that are more than just the first neighbours and also to include directional bonding forces. The formula for the total energy using MEAM is the same as the one used in EAM, however, an angular dependent term is included when dealing with the electron density:

$$\rho_{h,i} = \sum_{j \neq i} \rho_j^a(R_{ij}) - a \sum_{j \neq i, k \neq i} (1 - 3\cos^2 \theta_{jik}) \rho_j^a(R_{ij}) \rho_k^a(R_{ik}), \tag{2.9}$$

where ρ^a is the atomic electron density at distance R, a is constant depends on the type of atoms and θ_{jik} is the angle between atoms j, i and k.

The first term in the above equation is the same one used in EAM and the second term is the modification to include directional bonding. The MEAM is found to describe the elastic properties and point defects well. Furthermore, it is found to represent the properties of semiconductors and interfaces well [48].

ZBL potential

When the distance between atoms becomes small, most of the potentials fail to correctly represent the interactions between the atoms. Therefore, it is preferable to use another potential to describe the short range interactions. The Ziegler-Biersack-Littmark (ZBL) universal potential for short ranges [49] has been widely used to describe the atomic interaction at close ranges. The ZBL potential is represented as follows:

$$V(r) = \frac{Z_1 Z_2}{R} \phi_{\mathrm{ZBL}}(R), \tag{2.10}$$

where Z_1 and Z_2 are atomic numbers and $\phi_{\mathrm{ZBL}}(R)$ is:

$$\phi_{\mathrm{ZBL}}(R) = \sum_{i=1,4} A_i \exp(-b_i R / a_u), \tag{2.11}$$

where b_i and A_i are constants and a_u is:

$$a_u = \frac{0.8854}{Z_1^{0.23} + Z_2^{0.23}} a_{Bohr}, \tag{2.12}$$

where a_{Bohr} equal 0.539177 Å.

A spline function is normally used to connect between the actual potential and the ZBL potential. Cutoff distances that determine where the pair potential splined or connected to ZBL are determined to give the best smooth functions and derivatives and to reproduce defect threshold energies. The spline function used in this work is of the following form:

$$S(r) = \exp(f_1 + f_2 r + f_3 r^2 + f_4 r^3 + f_5 r^4 + f_6 r^5), \tag{2.13}$$

where f_1, f_2, f_3, f_4, f_5 and f_6 are constants. Figure (2.3) shows an example of splining the potential to ZBL potential.

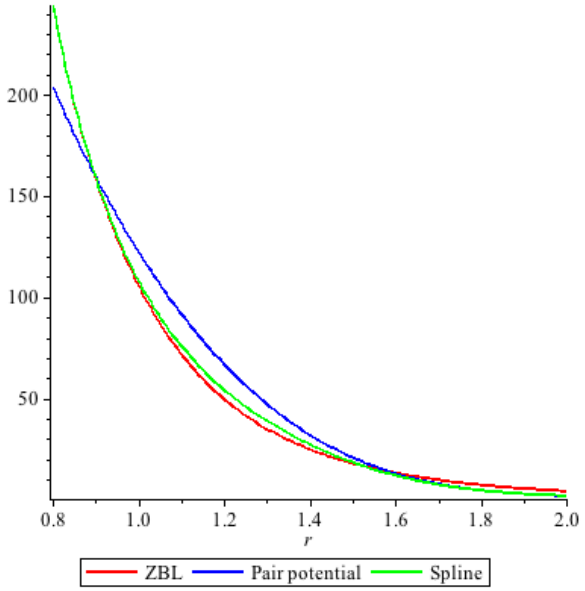

Figure 2.3: An example of splining the pair potential to ZBL potential for short ranges. A cutoff distance of 1.9 Å is chosen to connect the pair potential with the spline function and it is connected to the ZBL potential at a separation of 0.9 Å.

2.1.3 Evolving the system

A numerical algorithm is needed to evolve the system with respect to time. Velocity Verlet algorithm [50] was used to integrate Newton's equations of motion numerically within molecular dynamics. The velocity Verlet algorithm can be obtained by expanding the distance, velocity and acceleration using Taylor expansion as follows:

$$r(t + \delta t) = r(t) + v(t)\delta t + \frac{1}{2}a(t)\delta t^2 + O(\delta t^3), \tag{2.14}$$

$$v(t+\delta t) = v(t) + a(t)\delta t + \frac{1}{2}a'(t)\delta t^2 + O(\delta t^3), \tag{2.15}$$

$$a(t+\delta t) = a(t) + a'(t)\delta t + O(\delta t^2), \tag{2.16}$$

from where we can get,

$$a'(t) = \frac{a(t+\delta t) - a(t)}{\delta t} + O(\delta t). \tag{2.17}$$

The later equation can be then substituted in velocity equation (2.15) which will give:

$$v(t+\delta t) = v(t) + \frac{1}{2}[a(t) + a(t+\delta t)]\delta t + O(\delta t^3), \tag{2.18}$$

where equations (2.18) and (2.14) represent velocity Verlet equations.

2.1.4 Boundary Conditions

To overcome MD limitations related to the size of cell simulated, it is very useful to use boundary conditions to model smaller systems but keep the properties of the larger systems. This also helps in reducing the computational complexity. There are two types of boundary conditions which can be used in computer simulation, periodic and fixed boundary conditions.

Periodic Boundary Conditions

Periodic boundary conditions are mainly used to overcome the problem of a finite cell. In other words, using periodic boundary conditions means that if an image leaves from one side of the simulation box, another image will enter from the opposite face. This helps mimic simulating larger cells. Periodic boundary conditions are often used when dealing with collision cascade at high energies as the system used must be large enough to contain the resulting collisions.

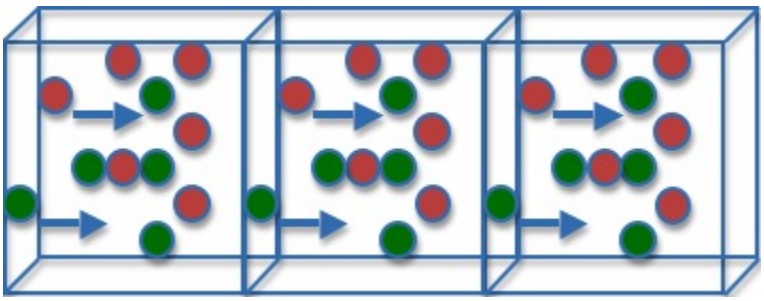

Figure 2.4: Periodic boundary conditions.

For all bulk systems studied in this work, generally periodic boundary conditions are used in all directions.

Fixed Boundary Conditions

Fixing the boundary condition means that the atoms are not allowed to move. Keeping them fixed helps minimising the complexity of the simulation process, however, it is important to make sure that this has no effect on the accuracy of the simulation. For example, we needed to fix few layers in the planes parallel to grain boundaries to make sure atoms will not move during simulation as shown in figure (2.5).

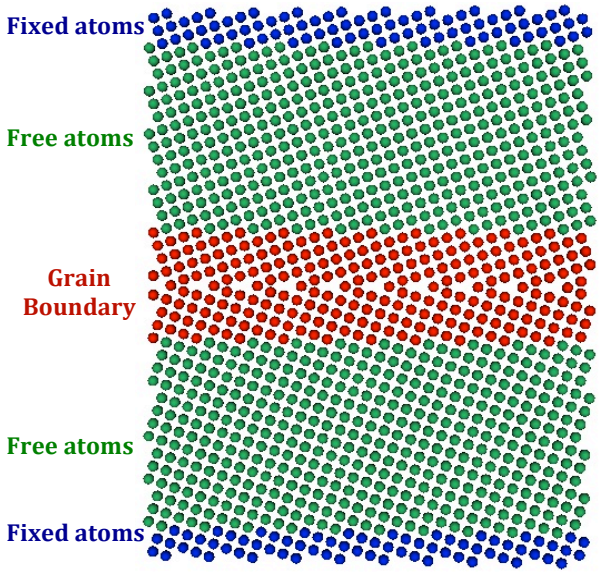

Figure 2.5: The figure shows the boundary conditions used when modelling the GB system. A few layers have been fixed in the direction parallel to the GB and periodic boundary conditions in the remaining two directions. This figure is adapted from [6].

2.1.5 System Thermalisation

In some cases, using thermal layers is required to maintain the temperature of the system at the desired temperature. This will be the case when an excess energy is introduced in the system by collision cascades. This should increase the energy of the system and therefore the temperature should increase. When the system is very big, the excess energy dissipates, however, if the system is small, thermal layers are needed to remove the excess energy and to bring the system to the required temperature. The actual temperature can be calculated

as follows:

$$\text{Actual Temperature} = \frac{2 * \text{Total Kinetic Energy}}{3 * \text{Boltzmann Constant} * \text{Number of moving atoms}}. \tag{2.19}$$

Calculating the actual temperature helps us to decide if thermal layers are needed or not. The thermal layers are implemented using thermostats within MD.

The main goal of using a thermostat within MD is to maintain the temperature of the system at the required one, which includes either heating or cooling the system. There are two main thermostats available to be used within the LBOMD package, Nosé-Hoover and Berendsen thermostats. The Berendsen thermostat [51] works by scaling the velocity at each step in a way that the change in temperature with time is directly proportional to the difference between the actual temperature T and the desired temperature T_0,

$$\frac{dT}{dt} = \frac{1}{\tau}(T_0 - T), \tag{2.20}$$

where τ is the coupling factor. So the scaling factor equal,

$$\lambda = \left[1 + \frac{\Delta T}{\tau_T}\left(\frac{T}{T_0} - 1\right)\right]^{\frac{1}{2}}, \tag{2.21}$$

where τ_T is time constant. Although the velocity rescaling thermostats are fast, they do not generate the correct canonical ensemble. However, in practise all thermostats generate an approximate canonical ensemble.

The other thermostat we have used is the Nosé-Hoover thermostat ([52] & [53]) which works by introducing a friction coefficient. This thermostat compares the kinetic energy of a system with the kinetic energy obtained using the required temperature and will adjust the velocities according to that. Although Nosé-Hoover is known to preserve the canonical ensemble, it needs a longer time to reach the required temperature because of the high oscillations it creates. All thermalistion carried in this work is done by using Berendsen thermostat.

2.1.6 System Minimisation

It is very important to make sure that the system used within MD is in equilibrium to get an accurate output. To minimise a system, two main inputs are required, the method that will be used to minimise the system and the required tolerance. There are different minimisation techniques that can be used such as the conjugate gradient method, damped MD and limited

memory BFGS minimiser.

Conjugate Gradient Method

The Conjugate Gradient method (CG) [54] is an iterative method that can be used to find the minimum of a non linear function ϕ. It represents one of the important minimisers within MD because it has high rate of convergence and does not require large storage. It starts by calculating the initial gradient which is taken to be the initial direction from the initial point R_0:

$$d_0 = g_0 = - \bigtriangledown \phi(R_0). \tag{2.22}$$

After that iterative steps start:

1. Calculate α using a secant line search method to minimise ϕ in the d_k direction.
2. Calculate new position,
$$R_{k+1} = R_k + \alpha_k d_k. \tag{2.23}$$
3. Calculate new gradient,
$$g_{k+1} = - \bigtriangledown \phi(R_{k+1}). \tag{2.24}$$
4. Calculate β,
$$\beta_{k+1} = \frac{g_{k+1} - g_k}{\parallel g_k \parallel^2} * g_{k+1}. \tag{2.25}$$
5. Calculate new direction,
$$d_{k+1} = g_{k+1} + \beta_{k+1} d_k. \tag{2.26}$$
6. Go to 1.

At each step the energy of the system is compared with the previous energy until the energy difference is within the required tolerance.

Damped MD

Damped MD is another method that is used for minimisation within MD. It mainly works by moving atoms using velocities with the need to introduce a damping constant which controls the rate of convergence. The oscillations introduced should bring the system to equilibrium eventually. This method can be used when system is far from equilibrium.

LBFGS Minimiser

Another method used for minimisation is Broyden-Fletcher-Goldfarb-Shanno (BFGS) method which works by using approximation of the Hessian which will need to be corrected at each step. The steps involved in BFGS minimiser is similar to CG method with the involvement of the Hessian to find the direction of minimisation, First the initial direction need to be obtained:

$$A_0 d_0 = g_0 = - \bigtriangledown \phi(R_0), \tag{2.27}$$

where A_0 is the initial approximation of the Hessian and d_0 is the initial direction. After that iterative steps start:

1. Calculate α using secant line search method.

2. Calculate new position,
$$R_{k+1} = R_k + \alpha_k d_k. \tag{2.28}$$

3. Calculate new gradient,
$$g_{k+1} = - \bigtriangledown \phi(R_{k+1}). \tag{2.29}$$

4. Calculate A_{k+1},
$$A_{k+1} = A_k + \frac{(g_{k+1} - g_k)(g_{k+1} - g_k)^T}{(g_{k+1} - g_k)^T \alpha_k d_k} - \frac{A_k(\alpha_k d_k)(\alpha_k d_k)^T A_k}{(\alpha_k d_k)^T A_k (\alpha_k d_k)}. \tag{2.30}$$

Since the history of the Hessian is stored, it will involve the need for very large storage which is the main disadvantage of the BFGS method over CG method. However, the development of the limited memory BFGS (LBFGS) version allows the user to control the storage required by discarding the old correction to the Hessian and keeping the recent ones. This results in LBFGS being a very efficient and flexible minimiser especially for minimising a system that involves large numbers of variables.

2.1.7 Visualisation

After running MD, one is required to analyse the output to understand what really happens during the simulation. One efficient way to analyse output from MD is to visualise the system. Two 3D visualisers have been used to analyse the MD output in this work, the Atomistic Visualisation and Analysis Software AVAS [55] developed in 2010 and visualiser developed by C. Scott in 2012 [7] . Both visualisers use POV-ray to render atoms along with different codes written in C and Python languages. They allow looking through the

atoms in the system with the ability to zoom and rotate the system. The atoms can be either coloured using the type of species or the displacement with the availability to view a coloured bar that maps the colours. They also include different filters that allow different ways of analysing the output. For example, one can look through the displacement of atoms using the displacement filter and through the defects in the system through the point defects filter. Examples of other available filters are Q4 filter that colours the atoms according to the Q4 parameter and a crop filter that allows slicing of the system so one can only look through one part of the system. Figure (2.6) shows an example of using the visualiser to look into defects in a system after a collision cascade.

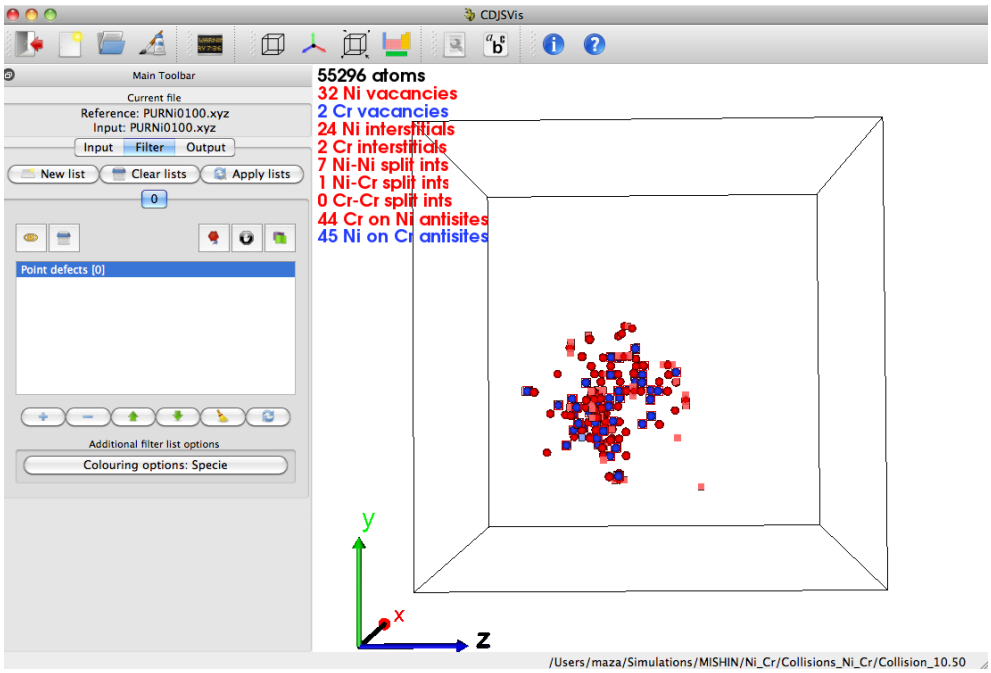

Figure 2.6: 3D Visualiser used throughout this work [7]. The picture shows the defects in a system after a collision cascade.

2.2 Long Time Scale Dynamics (LTSD)

Given that the size of the simulation box and the time attainable are restricted when using MD simulation, different techniques have been introduced to allow modelling for longer time scales and for bigger systems. One type of these important techniques is the accelerated molecular dynamics such as Temperature Accelerated Dynamics (TAD), Hyperdynamics and Parallel Replica dynamics [18].

TAD is based on increasing the speed of the transition by raising the temperature where frequent events simulated by TAD must obey the harmonic transition theory. The MD is run at a temperature higher than the required temperature so the energy barriers can be calculated for events and the time at the high temperature before it can be extrapolated to the time at the required temperature. Furthermore, Parallel Replica Dynamics requires the infrequent events obey the first order kinetics. It includes replication of images, dephasing, detecting transition, continuation and so on. One of the disadvantages of parallel replica dynamics is that it does not advance the time in the dephasing stage. On the other hand, Hyperdynamics works by modifying the potential with a bias potential given that it must be zero at the dividing surface. This will cause the transition on the bias potential surface to be accelerated and the time is enhanced at each step.

In this work to overcome the time limitation in MD, the modelling carried out can be divided into two main stages. The first stage was modelling collision cascades in the system and the second stage was modelling the evolution of defects that resulted from the first stage. The initial collision cascade phase is modelled using MD for 20 ps with a variable time step depending on the kinetic energy and potential energy within the system. On the fly KMC (otf-KMC) has then been used to model the evolution of defects after collision cascades.

The on the fly KMC was initially introduced by Henkelman [19], where he used it to model Al(100) crystal growth. Henkelman used the dimer method to find the relevant transitions. He then calculated the rate of each transition using harmonic transition theory, where the clock was advanced with a chosen transition. The otf-KMC algorithm used in this work was initially developed by Louis Vernon [56]. The original otf-KMC algorithm starts by identifying defects, which is done by comparing the system after a collision cascade to the reference system. Once these are identified, large numbers of searches are initialized to find the unique saddles points using one of the saddle finding methods such as the Activation and Relaxation Technique and Dimer method. These are described in detail in the next section. After finding the approximate saddles heights, one of the barrier finding methods such as the climbing image nudged elastic band method (CI-NEB) [11] is used to calculate the barriers E_b for each transition found. The rate of each transition is calculated using the Arrhenius equation:

$$\text{Rate} = v \exp(-E_b/k_b T), \tag{2.31}$$

where v is the transition prefactor and is taken to be 10^{13} s^{-1}, k_b is Boltzmann constant and T is the temperature.

A random number is generated between 0 and the sum of the rates for all transitions and a transition is chosen by stepping through all transitions cumulatively until the random number is exceeded. The time is accumulated by:

$$\text{Time} = -\frac{\log_e(x)}{\sum_{i=1}^{i=N} Rate_i}, \tag{2.32}$$

where x is a random number between 0 and 1 and N is the total number of transitions found at the step. Finally the system is evolved by the chosen transition and all the processes repeated again.
The otf-KMC algorithm has been modified during this research by C. Scott and T. Lazauskas. The main aim of modifying the otf-KMC algorithm was to increase the efficiency and decrease the computational time and cost. The main modifications added to the algorithm are:

- Atoms included in search and force evaluation:
  The defects in a system are identified by comparing the initial system to the reference system. To increase the efficiency of the algorithm, volumes are constructed around the defects found. The idea behind that is trying to only include the atoms surrounding the defects within certain radius in the search for possible transitions. This should reduce the computational time and also increase the chance for finding all possible transitions. The distances used are set to be in an input file so the user can change the values according to the best values for system used; the parameters that need to be set are:

  1. Search initial radius: this includes the atoms that can be part of the initial search vector, typically second Nearest Neighbour distance (NN). Defects are classified as being part of the same cluster if within double this parameter of each other.
  2. Graph radius: this radius is used when a building graph network and it should include the search initial radius. 3NN distance is used in this work.
  3. Search move radius: this radius should be bigger than the graph radius and it includes the atoms that can move during the search for possible transitions.
  4. Saddle convergence radius: this radius must be at least equal to the move radius and will include the atoms that can move during convergence to the saddle such as when using Lanczos algorithm. The reason behind including more atoms in the atoms used in convergence step is that we need more accuracy at this stage.

5. Inclusion radius: this should include all atoms that are included in force evaluation and it should be far more than all the above radii.

An illustration of these distances are shown in figure (2.7).

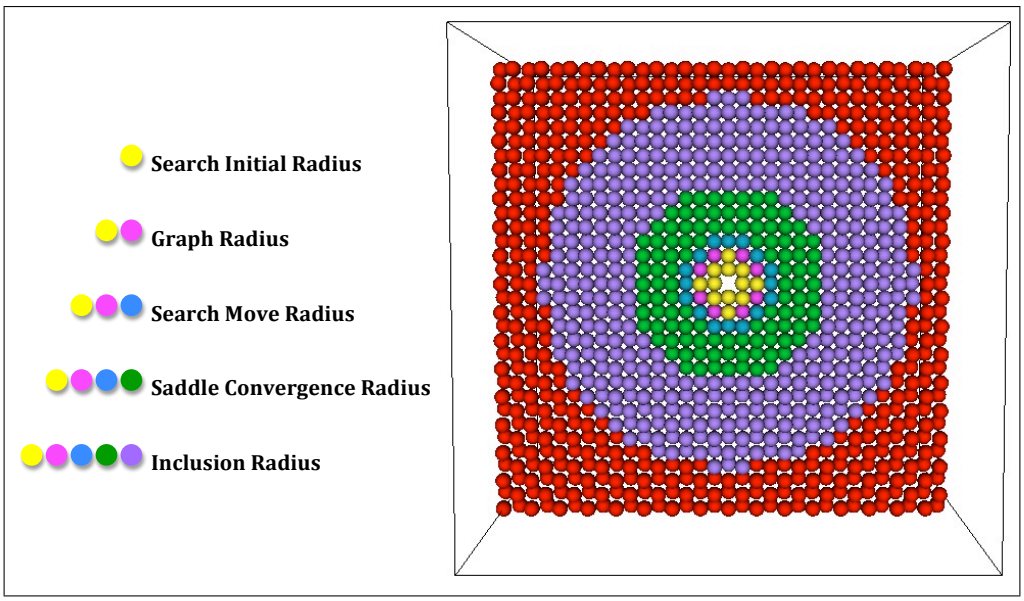

Figure 2.7: Explanation of the parameters used for creating the defect volume, the picture shows a vacancy and the atoms that are included in each part of the otf-KMC algorithm. The red spheres represent the remaining atoms in the system.

- Defect volumes and combined volume:
  As illustrated in the last point, the defect volume will be built to contain the isolated defects or cluster of defects and the atoms surround them. Each of these defect volumes is given a private hash key that will be used to identify if this defect volume has been seen at any stage of the simulation. If two or more defect volumes share atoms within the graph radius, a combined volume will be constructed to include those defect volumes. The main aim from this is to try to find transitions that could include the two defect volumes and also to find any transitions that could be missed when doing searches on the single defect volume.

- Using Lanczos Algorithm for saddle convergence:
  The original otf-KMC algorithm find the possible transitions in two main stages: searching for the saddle using one of the saddle finding techniques then calculating the energy barrier E_b using one of the barrier finding methods such as Climbed-Image Nudged Elastic Band (CI-NEB). The new modification to the algorithm is to use the dimer method to get close to the saddle and then use the Lanczos algorithm [57] to convert

the Hessian into a tridiagonal matrix where minimisation along the lowest eigenvalue should bring us to the saddle. The activation barrier E_b is the energy difference between the initial system and the saddle. This reduces the computational time significantly and the results obtained were in excellent agreement with results obtained using CI-NEB.

- Storing and reusing defect volumes:
  A very important modification to the otf-KMC algorithm is to store the transitions found for the defect volume if the success rate is within the required percentage. All saved defect volumes are kept in one folder where the defect volumes at each step are compared to the stored ones and a transformation matrix is used to reuse all transitions in the stored defect volumes. The reuse part at the moment is only implemented for the defect volumes and not the combined volumes.

The main steps involved in the otf-KMC algorithm are shown in figure (2.8).

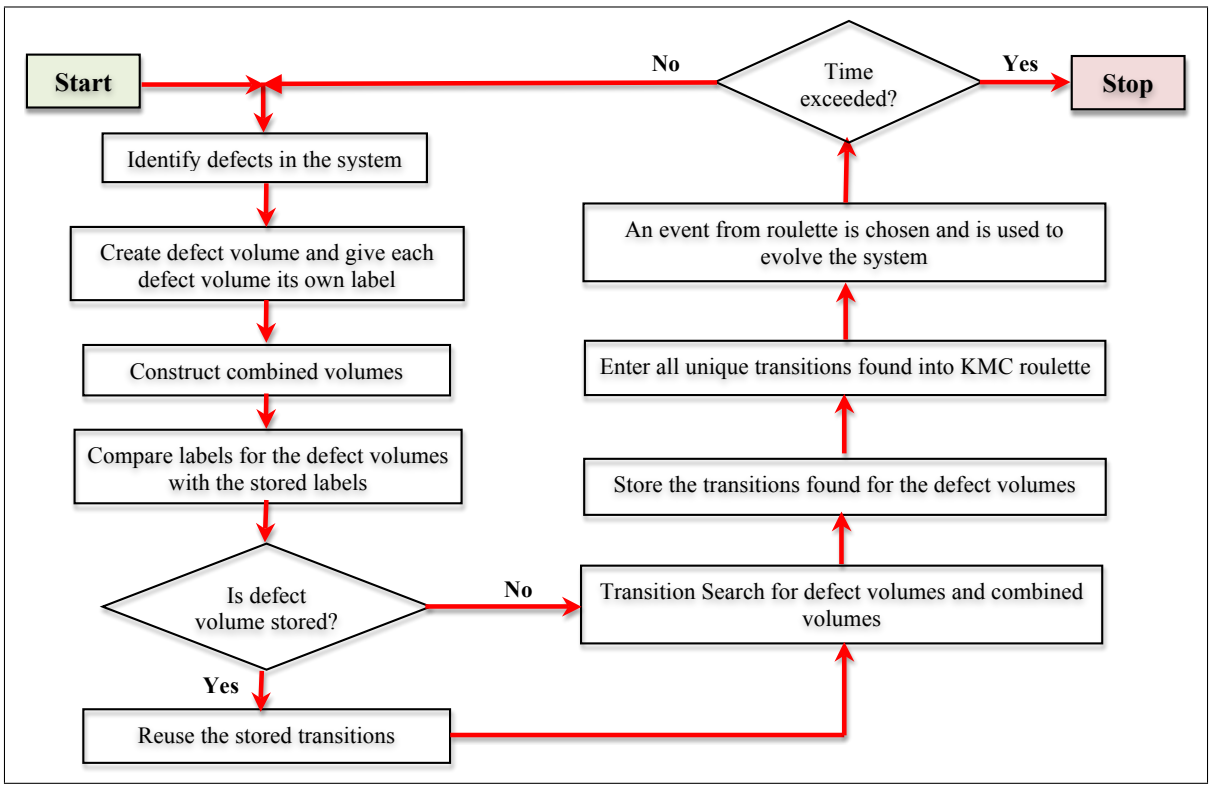

Figure 2.8: Illustration of the otf-KMC technique used to simulate the evolution of the defects resulted from collision cascades by finding all unique transitions at each step.

2.2.1 Saddle Finding Methods

The first step to find the energy barrier of an event is to find the saddle point which represents a maximum on Minimum Energy Pathways (MEPs). The saddle point can be found using

the saddle finding methods which require only the knowledge of an initial state. Examples of saddle finding methods are the Activation and Relaxation technique, Relaxation and Translation and the Dimer method.

Activation and Relaxation (ART)

The Activation and Relaxation technique was developed by Barkema and Mousseau in 1998 [58]. ART algorithm requires only an initial state and consists of three main steps:

- Escaping from a local minimum: this is done by an initial random displacement from the minimum. The displacement could include one or more atoms, however, it will be more efficient when atoms displaced are within the area surrounding the defect. The direction of the displacement is chosen to be along the force resulting from the displacement. The aim from this step is to leave the basin so it is very important to make sure that we left it but one still in the basin of interest. This is done by checking that the increment in force component parallel to the displacement is getting very small or the ratio between the parallel and perpendicular force component is less than a given value. In this work a single point R is considered in 3N space and displaced to R^* using a random displacement vector $\vec{N}$ as shown in figure (2.9).

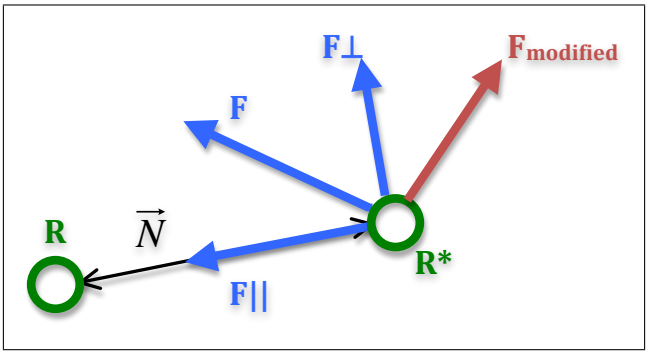

Figure 2.9: This figure shows the components of force resulting from a random displacement from point R to point R^* using a random displacement vector $\vec{N}$ used in the ART method to escape from a basin. The modified force vector is described below.

- Moving to an adjacent saddle: the next step is to introduce a modified force vector:

$$\mathrm{F}_{\mathrm{modified}} = \mathrm{F} - (1+\alpha)\mathrm{F}_{\parallel}, \tag{2.33}$$

where the total force F can be decomposed into parallel and perpendicular forces. α is a control parameter usually set to be 0.15/displacement. After the modified force is

determined the point R^* is moved to R^{**} with a step size δt:

$$R^{**} = R^* + \mathrm{F}_{\mathrm{modified}}\delta t \tag{2.34}$$

The direction of the modified force is then followed until it will find a saddle point. Changing the sign of the component of the force which is parallel to $\vec{N}$ is considered to be an indication of crossing a saddle point.

- Minimising to new minimum: once the saddle point is found, a minimisation technique such as conjugate gradient can be used to bring this saddle to a new minimum. To avoid the convergence to the original minimum it is usual to move slightly post the saddle point before minimisation.

Relaxation and Translation (RAT)

The Relaxation and Translation (RAT) method was developed by Vernon [56] and the main motivation behind it was that the ART method gave Vernon lots of transitions duplicates for the calculations he did and thus he would have needed to do larger number of searches before he can make sure that all possible transitions have been explored. The basic concept of the RAT method is based on the ART method. There are two main steps involved in RAT method:

- Force minimisation: similar to ART method the force acting on the search point is decomposed into perpendicular and horizontal forces and the search point is relaxed along the perpendicular vectors to $\vec{N}$. The size of the relaxation step (Step_i) is altered by looking through the relative change in the perpendicular forces:

$$\mathrm{ratio} = \frac{\mathrm{F}_{\perp \mathrm{i}} - \mathrm{F}_{\perp \mathrm{i\text{-}1}}}{\mathrm{F}_{\perp \mathrm{i}}}, \tag{2.35}$$

where $\mathrm{F}_\perp$ is the perpendicular force to $\vec{N}$ and the step size is changed as follows:

$$\mathrm{Step}_i = \begin{cases} \mathrm{Step}_{i-1} + 20\% \times \mathrm{Step}_{i-1} & \mathrm{ratio} < 1.2 \\ \mathrm{Step}_{i-1} - 50\% \times \mathrm{Step}_{i-1} & \mathrm{ratio} > 1.2 \end{cases}$$

Figure (2.10) shows how the forces are decomposed and how the point search is minimised.

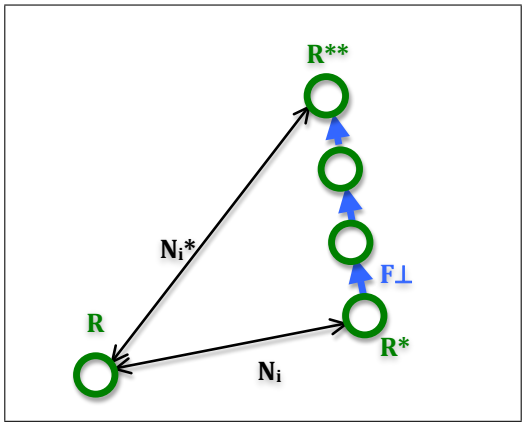

Figure 2.10: This figure shows the components of force resulting from the random displacement of point R to point R^* using a random displacement vector $\mathbf{N}_i$ and then minimising the point search along span of perpendicular vectors to $\mathbf{N}_i$ used in RAT method.

- Translation to new minimum: after the point R^* is relaxed to R^{**}, new translation vector can be constructed:

$$\mathbf{N}_{i+1} = \frac{\mathbf{N}_i + \mathbf{N}_i^*}{|\mathbf{N}_i + \mathbf{N}_i^*|}. \tag{2.36}$$

The saddle point is detected by checking the dot product between the parallel force component to the displacement and N_i. If this value is positive then this indicates a saddle has been crossed.

Dimer Method

The Dimer method developed by Henkelman and Jónsson [59] represents one of the most powerful and fast methods to find the saddle from only an initial configuration. It is represented by two images separated by distance ΔR from a common point R as shown in figure (2.11).

$$R1 = R - \Delta R\vec{N}, \tag{2.37}$$

$$R2 = R + \Delta R\vec{N}, \tag{2.38}$$

where $\vec{N}$ is a unit vector.

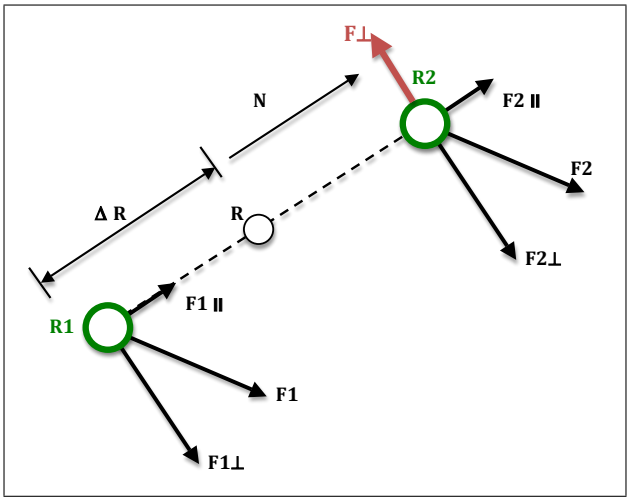

Figure 2.11: Representation of the forces acting on the dimer. The figure shows the two images that represent the dimer and the force decomposition on each image.

At each point the energy and forces can be calculated and these energies and forces can be used to calculate the total energy and force acting on the dimer,

$$\begin{cases} \mathrm{E_{dimer}} = \mathrm{E_1} + \mathrm{E_2}, \\ \mathrm{F_R} = \frac{\mathrm{F_1}+\mathrm{F_2}}{2}, \\ \mathrm{C} = \frac{(\mathrm{F_2}-\mathrm{F_1}).\vec{N}}{2\Delta R}, \\ \mathrm{E_R} = \frac{\mathrm{E_{dimer}}}{2} + \frac{\Delta R}{4}(\mathrm{F_1}-\mathrm{F_2}).\vec{N}, \end{cases}$$

where $\mathrm{E_{dimer}}$ is the energy of the dimer, $\mathrm{F_R}$ is the force at the middle between the two images, C is the curvature and $\mathrm{E_R}$ is the energy at the middle.

The Dimer method consists mainly of two steps. The first step is minimising the dimer energy by rotation. There are several methods to be used for this purpose such as Modified Newton method or CG. This step involves rotating the dimer along the rotational force:

$$\mathrm{F_\perp} = \mathrm{F_{\perp 2}} - \mathrm{F_{\perp 1}}, \tag{2.39}$$

where,

$$\mathrm{F_{\perp i}} = \mathrm{F_i} - (\mathrm{F_i}.\vec{N})\vec{N}. \tag{2.40}$$

Once the dimer is rotated, the dimer is aligned along the lowest curvature mode, therefore the net force acting on dimer should pull it towards the minimum. Therefore, a modified force is created that will bring the dimer towards the saddle in the translation step:

$$\mathrm{F}^{*} = \begin{cases} -\mathrm{F}_{\parallel}, & \text{if } C > 0 \\ \mathrm{F}_{\mathrm{R}} - 2\mathrm{F}_{\parallel}, & \text{if } C < 0 \end{cases}$$

where $\mathrm{F}_{\parallel}$ is the parallel force component acting on dimer and F_{R} is the force acting at the middle of the dimer.
Moving along the modified force should bring the dimer to the saddle.

Minimum Mode Following Algorithm (MMFA)

The basic idea to find the saddle point with only the knowledge of the initial state is to climb up from the initial to the saddle using the vector of the lowest eigenvalue (minimum mode) of the Hessian matrix. The problem with this approach is the massive computational efforts and time needed to construct the Hessian matrix and calculate the lowest eigenvalue especially for large systems.
A Minimum Mode Following Algorithm (MMFA) has been developed by Pedersen, Hafstein and Jónssen [57] in 2011. The MMFA could be used to climb up from initial point to the saddle without the need of constructing the Hessian matrix. This is done by introducing the effective force:

$$\mathrm{F}^{\mathrm{eff}} = \mathrm{F} - 2(\mathrm{F}.v_{min})v_{min}, \tag{2.41}$$

where v_{min} is a normalised eigenvector corresponds to the lowest eigenvalue of the Hessian matrix.

v_{min} can be found by constructing the Hessian which includes the second derivatives of the potential energy, diagonalising the matrix and find the lowest eigenvalue. However, since we do not need the whole element in the Hessian matrix, the construction of the Hessian matrix can be emitted from this process and the lowest eigenvalue can be calculated during the simulation by calculating only needed values. For instance, a similar technique used in the dimer method can be used here as the dimer after rotation is along the minimum mode direction. Another approach which has been used to obtain the lowest eigenvalue is using the Lanczos algorithm [60] which can be used to obtain the lowest eigenvalue without the need of constructing the Hessian matrix.

For this work, the dimer method is used to get close to the saddle and then the Lanczos algorithm is used for saddle convergence. The Lanczos algorithm is used to convert the Hessian into tridiagonal matrix where Linear Algebra Package (LAPACK) is used to find

the lowest eigenvalue of the resulted matrix. This reduces the computational time was spent by minimisation and finding the Minimum Energy pathway (MEP) using NEB technique.

2.2.2 Barrier Calculating

After a saddle has been found, various methods can be used to calculate the barrier and find the Minimum Energy Pathway (MEP) such as the Nudged Elastic Band and the String method. An illustration of the MEP between two minima is shown in figure (2.12).

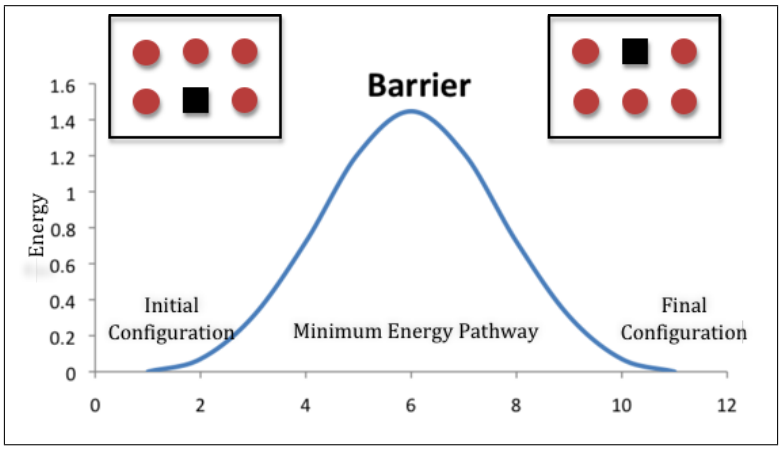

Figure 2.12: This figure shows an example of the MEP between two minima and the required energy to move from the first minimum to the second minimum.

Nudged Elastic Band Method

Nudged Elastic Band (NEB) is a method to find the minimum energy pathway between an initial and final state which introduced by H. Jónsson et al. in 1998 [61]. This is done first by constructing set of images between the two states and adding a spring interaction between them. The resulted band is brought to minimum by optimization. The images will be effected by the true force and the spring force. To prevent both the spring and the true force from effecting the convergence to the MEP, only the perpendicular component of the true force and the horizontal component of the spring force are considered. The steps of implementation of NEB method can be summarised as follows:

1. A band is created with (N + 1) equally spaced images between the initial and the final state by linear interpolation which is used as an initial guess of the MEP. Minimising of these images will result in them being relaxed to either the initial or the final state. Therefore, a spring is introduced between every two images so the total force F_i^{NEB} at

each image i is the summation of the spring force $F_i^{S\parallel}$ which acts horizontally to the band and the true force $F_i^{\perp} = -\Delta_i V$ where V is the potential energy of the image:

$$F_i^{NEB} = F_i^{\perp} + F_i^{S\parallel}, \tag{2.42}$$

where,

$$F_i^{S\parallel} = k(|R_{i+1} - R_i| - |R_i - R_{i-1}|)\hat{\tau}_i, \tag{2.43}$$

where $F_i^{S\parallel}$ is the spring force, $F_i^{\perp}$ is the true force, k is the spring constant and $\hat{\tau}_i$ is unit tangent vector dependent on the potential energy V_i. In the numerical approximation it is defined by:

$$\tau_i = \begin{cases} R_{i+1} - R_i, & V_{i-1} \leq V_i \leq V_{i+1} \\ R_i - R_{i-1}, & V_{i-1} \geq V_i \geq V_{i+1} \\ (R_{i+1} - R_i).V_{max} + (R_i - R_{i-1}).V_{min}, & V_i \leq V_{i-1}, \leq V_{i+1} \\ (R_{i+1} - R_i).V_{min} + (R_i - R_{i-1}).V_{max}, & V_i \leq V_{i+1}, \leq V_{i+1} \end{cases}$$

where V_{max} and V_{min} is the maximum and the minimum energy difference between V_{i+1} and V_{i-1}.

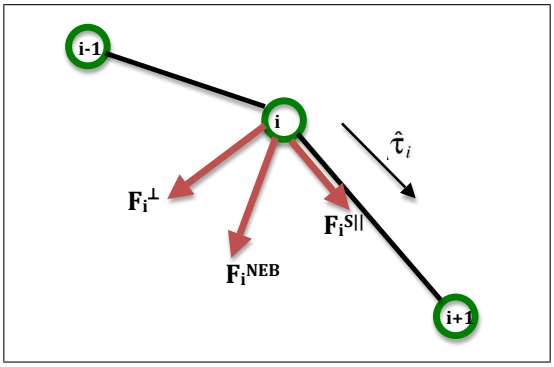

Figure 2.13: Illustration of the forces acting on an image in the NEB method. Two forces acting on each image, the horizontal spring force and the perpendicular true force.

2. Applying a minimisation technique will bring the images closer to the MEP after some iterations. CG technique has been used to minimise each image simultaneously until the initial NEB guess lies on the MEP. Figure (2.14) shows an explanation of the initial guess of the MEP which is brought to the actual MEP by minimisation.

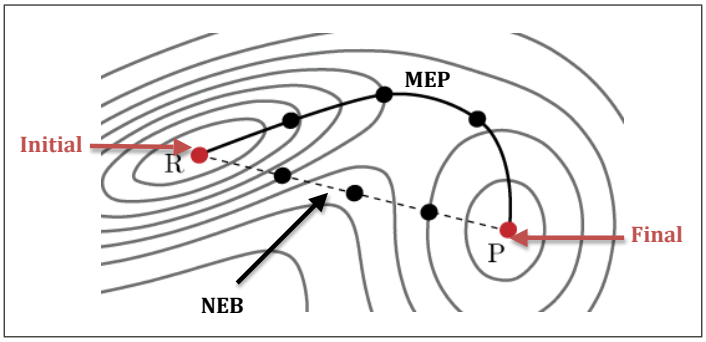

Figure 2.14: Illustration of how the NEB band is constructed between the initial and the final states. Simultaneous minimisation should bring the NEB band to the MEP.

3. The energy of the saddle is obtained by interpolation because the exact saddle may lie between two images. A good improvement of the NEB is using the Climbed image [11] which is implemented by movement of the image with the highest energy which can be identified after some iterations of the original NEB perpendicularly to the band. This will result in images converging to the MEP and the climbing image to the saddle point which will escape the interpolation step by converging directly to the saddle point. An example of the difference obtained using both NEB and CI-NEB is shown in figure (2.15).

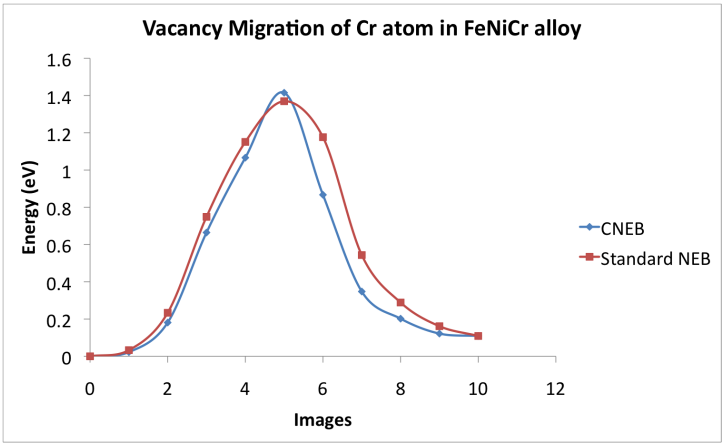

Figure 2.15: Example of using both NEB and CI-NEB to find the migration barrier of a Cr atom to a vacancy in FeNiCr alloy. The figure illustrates that when using CI-NEB, the climbed image converges more exactly to the saddle. A difference of 4.55 % in the barrier is found between both methods.

String Method

Similar to NEB method the String method ([62], [63]) requires an initial and final configuration to draw the minimum energy pathway. String method includes two steps. The first step of String method is the Evolution step which is just the same as the NEB method, however, the spring effect is obtained by constraining the distances between the images. This step will force the string closer to the minimum energy pathway by allowing the images to move using the perpendicular component of the true force. This is followed by a reparameterisation step in which the atoms are redistributed evenly again along the string. These two steps are repeated until a reasonable tolerance is achieved. Climbing image technique can be used to converge to the saddle. An example of the energy barriers for point defects in fcc Fe calculated using both CI-NEB and String method are shown in table (2.1).

Transition	CI-NEB (eV)	String (eV)	Difference(%)
Vacancy Migration	1.4633	1.4914	2.81
Rotation of [100] dumbbell	0.44	(failed)	
Translation of [100] dumbbell	0.6213	0.6528	3.15
Translation and rotation of [100] dumbbell	0.30	0.31	1.0

Table 2.1: Comparison of the energy barriers obtained for point defects in fcc Fe using CI-NEB and the String method. The table shows difference in the values obtained with the String method failing to find the barrier of the rotation of [100] dumbbell.

2.2.3 Reuse the stored transitions

One of the main modification to the otf-KMC code is storing the transitions of a specific defect and then trying to use them when same defect is found during the simulation. This modification has been implemented by T. Lazauskas. Both the saddles and the final points associated with a transition are stored where comparing the hash key of the defect volume with the stored defect volumes will allow us to know if we are having the same defect. If the same defect is recognised, then both the saddles and the finals for all transitions need refining. A transformation matrix is used to refine both saddles and finals. As the resulted states are only approximation, we need to find more accurate states. For the finals, we minimise them to get to the exact finals, however, for the saddle we need to do more work. Since we know that we are very close to the exact saddle, the Lanczos algorithm is used to convert the Hessian matrix to tridiagonal matrix and LAPACK is used to find the lowest eigenvalue. Following the eigenvector associated with the lowest eigenvalue of the Hessian bring us to the saddle. The migration barrier is taken to be the difference between the initial and the saddle.

Using reuse boosts our simulation time especially when we have isolated defects in the system, however, since we don't store defect volumes that are part of combined volume the reuse did not help in reducing the computational time in those cases. We have few cases that combined volume does not change during simulation because the chosen transitions are associated with defects that are not included in the combined volume, reuse would make a difference for these cases but its implementation for combined volumes was not feasible in the time allocated for this study.

2.3 Parallelisation

During the otf-KMC technique, parallelisation has been improved by C. Scott. The main steps that the main server will do are:

- Minimising the initial system.
- Identifying defects in the initial system.
- Building defect volumes and combined defect volumes.
- Comparing hash keys for the present defect volumes with the stored ones and determining how many refinement or searches are required for the defect volumes and the combined ones.

After that, the server set a queue for all work need to be done for multiple processors. The queue order is as follows:

1. Refinement of the stored transitions.
2. Transition searches for the defect volumes.
3. Refinement of the stored transitions that will be available after finishing the transition searches. This will be the case if we have the same defect more than once.
4. Transition searches for the combined volumes. This should be kept to the end to make sure we don't have any duplicates.

This parallelisation was very efficient especially when used with Loughborough University's high performance computer (Hydra).

2.4 Analysis Techniques

The analysis techniques used in this work are explained here. This includes calculating some structural properties such as elastic constant, defects formation energies, defects migration energies, collision cascade technique and Monte Carlo simulation.

2.4.1 Lattice Constant

The lattice parameters were obtained by plotting the total energies versus the lattice parameters. The required lattice parameter gives the minimum total energy as shown in figure (2.16).

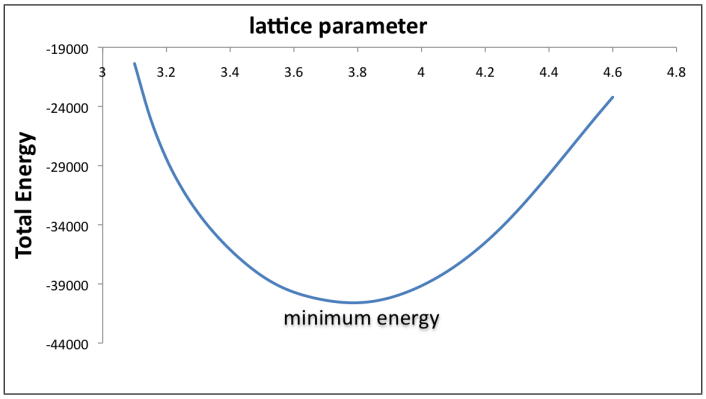

Figure 2.16: Illustration of how the lattice parameter is calculated, the total energy is plotted against the lattice spacing with the lattice parameter giving the minimum energy.

2.4.2 Defects Formation Energies

The formation energies for defects were calculated by comparing the energies of the perfect lattice of N atoms with the one containing the defect. The formation energy of a defect E_f can be calculated as follows:

$$E_f = E_{def}^T - \sum_{i=1}^{K} N_i E_i^{bulk}, \tag{2.44}$$

where E_{def}^T is the total energy of the system with the defect, i represents the species in a system of a total of K species, N_i is the number of atoms of specie i in the defective system and E_i^{bulk} is the energy of an atom of specie i in the perfect lattice. Figure (2.17) shows the types of defects studied.

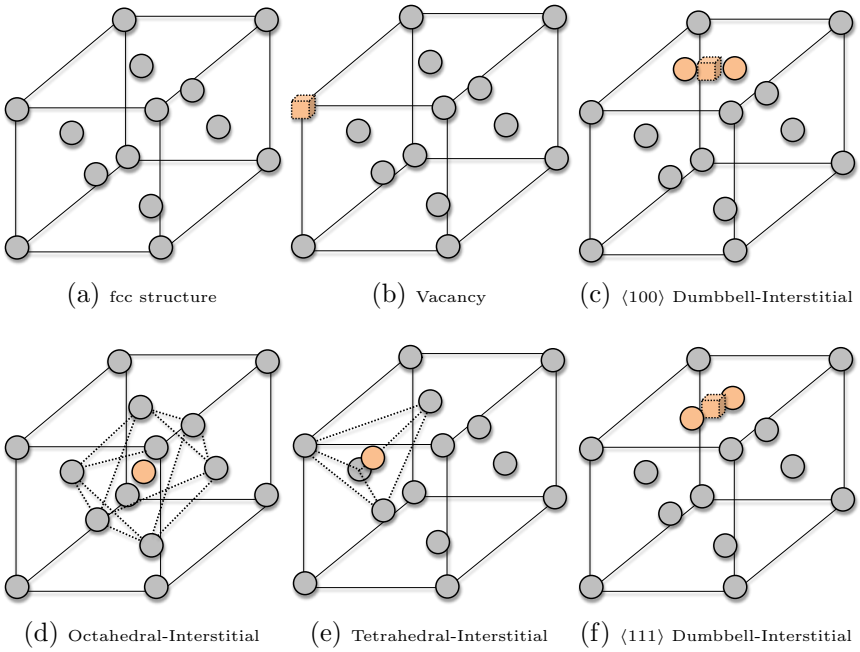

(a) fcc structure (b) Vacancy (c) ⟨100⟩ Dumbbell-Interstitial

(d) Octahedral-Interstitial (e) Tetrahedral-Interstitial (f) ⟨111⟩ Dumbbell-Interstitial

Figure 2.17: Illustration of type of defects studied in this work.

Another type of defect that resulted in some of the simulation is the Stacking Fault Tetrahedron (SFT) which is a common vacancy cluster in fcc structure. It has a shape of four equilateral stacking faults in {111} planes intersecting along ⟨110⟩ edges. Examples are shown in figure (2.18).

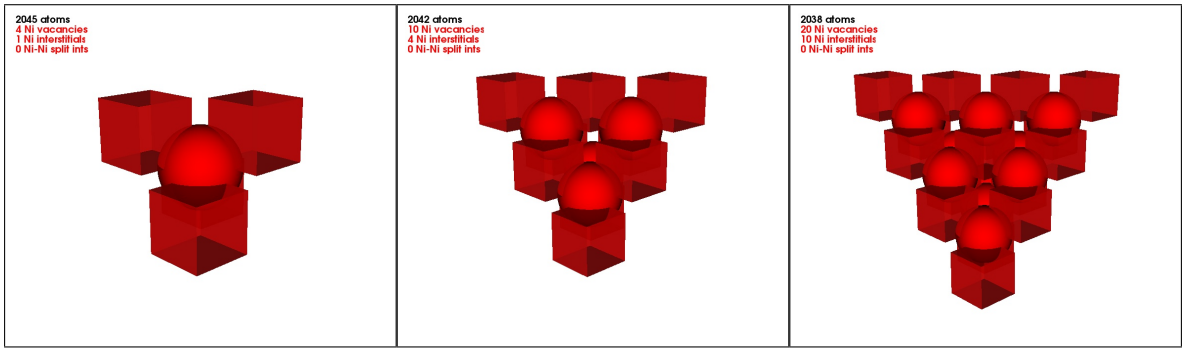

(a) 3 Vacancies SFT. (b) 6 Vacancies SFT. (c) 10 Vacancies SFT.

Figure 2.18: Examples of the SFT vacancy cluster in an fcc structure. The spheres in this figure represent interstitials and the cubes represent vacancies.

2.4.3 Collision Cascade

The collision cascade used to study radiation damage, is initialised by imparting an atom usually called the Primary Knock-on Atom (PKA) with a given kinetic energy in a certain

direction. This is followed by analysing the resulting collisions and the defect formation with respect to time. Different values of energies were studied. The sizes of the simulation cells were chosen taking into consideration that it is enough to contain all the collisions and not too big to reduce simulation complexity. Different directions are used for initialising the collision cascades as shown in figure (2.19).

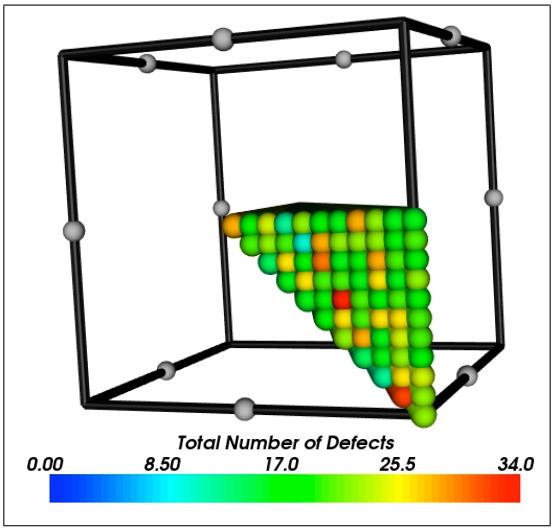

Figure 2.19: Illustration of the directions used to perform collision cascades in this work. In this figure the PKA is chosen to be the atom in the centre of an fcc structure with the collision cascades implemented in 66 directions considering the symmetry of the fcc structure. The figure shows the residual defects as a function of the PKA direction in one of the systems used which is explained in more details in the next chapters.

2.4.4 Model Alloys

Alloy percentages

Two systems are studied. The first system is the ternary system with 10 at.% Ni, 20 at.% Cr and 70 at.% Fe. The second system is the binary system with 80 at.% Ni and 20 at.% Cr. The systems were produced randomly in the fcc structure with the required percentages.

Monte Carlo Simulation

The Metropolis Monte Carlo algorithm [64] is used to find lower energy configurations. First, the algorithm starts by calculating the energy of the initial configuration. Second, it chooses two random atoms from the initial configuration and swaps them if they are different. This is followed by calculating the energy of the system after swapping. If the energy after the

swapping is lower than the initial energy, then the movement is directly accepted. However, if not, then the movement will be accepted with probability of :

$$p = \exp\left(-\frac{\Delta E}{KT}\right), \tag{2.45}$$

where ΔE is the difference between the energies before and after swapping, T is the temperature and K is the Boltzmann constant. Figure (2.20) shows the steps of Monte Carlo simulation.

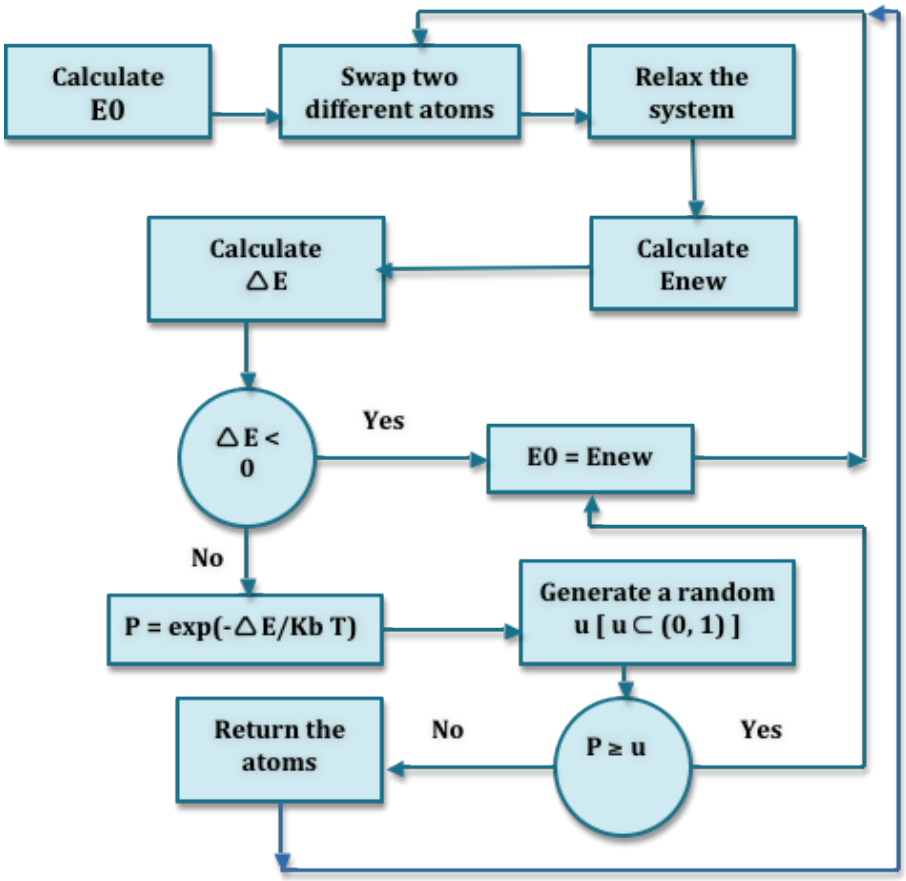

Figure 2.20: Explanation of the main steps involved in Monte Carlo simulation which is used to investigate the structures of both of the ternary and the binary systems. Lattices used in this calculation contain 2048 atoms.

Chapter 3

Ternary Potential

3.1 Introduction

Using the correct potential to describe interatomic interactions between the atoms in the system is a key factor in accurately modelling materials. A reliable potential will be capable of producing the basic properties of a specific material. Experimental data and DFT data represent the data that a good potential must be able to reproduce. The importance of this data varies depending on what the potential will be used for. In our case, since the potential is used to study the defects and their migration, defect formation and migration energies are the main items of interest. Three potentials have been provided for this purpose. In this chapter, what is expected and required from the ternary potentials are explained. Also the implementation of each potential and the difficulties behind employing them will be explained.

3.2 What is expected?

The first test for the ternary potential is the ability to reproduce the properties for pure elements (Fe, Ni and Cr). These properties include the lattice constants, formation energies, migration energies, binding energies of a vacancy and point defects. A list of the expected values from the potential are shown in tables (3.1), (3.2), (3.3) and (3.4). The expected values in these tables are obtained from ([15], [65], [14], [66] & [67]).

Property	**Iron**	**Nickel**	**Chromium**
C_{11}(GPa)	154	247	249
C_{12}(GPa)	122	147	178
C_{44}(GPa)	77	125	143
E_0(fcc)(eV/at.)	-	4.45	-
E_0(bcc)(eV/at.)	-	4.35	-
E_0(hcp)(eV/at.)	-	4.42	-
a_0(fcc)(Å)	3.425 - 3.562	3.519	3.520 - 3.610
a_0(hcp)(Å)	-	-	-
a_0(bcc)(Å)	2.832 - 2.860	2.801	2.878 - 2.885
E_{SF}(mJ/m^2)	4	111 - 128	156 - 341
E_f(Vac)(eV)	1.82 - 1.95	1.37 - 1.45	2.14
E_f($\langle 100 \rangle$ SIA)(eV)	3.20 - 3.62	4.07 - 4.11	-
E_f($\langle 110 \rangle$ SIA)(eV)	4.17 - 4.82	4.91 - 4.99	-
E_f($\langle 111 \rangle$ SIA)(eV)	4.56	4.69 - 4.72	-
E_f(Octa SIA)(eV)	4.35	4.25 - 4.32	-
E_f(Tetra SIA)(eV)	3.66 - 4.32	4.69 - 4.71	-

Table 3.1: Target values for the pure elements (Fe, Ni & Cr) that are a good potential is expected to reproduce, these include the lattice parameters and the formation energies of vacancies and point defects.

Configuration	**fcc Ni matrix**	**fcc Fe matrix**	**fcc Cr matrix**
Vac $\rightarrow$ Fe	0.97*	0.62†	NA
Vac $\rightarrow$ Ni	1.09*	0.89†	NA
Vac $\rightarrow$ Cr	0.83*	0.65†	NA

Table 3.2: DFT vacancy migration barriers ($*$ DFT - Ref. [14], † DFT - Ref. [15]). The table shows the energy barriers (eV) required for an atom (Fe, Ni or Cr) to jump to a vacancy in its first nearest neighbours position in one of the pure elements.

Ni matrix	**1nn**	**2nn**	**Fe matrix**	**1nn**	**2nn**	**Cr matrix**	**1nn**	**2nn**
Vac-Vac	0.01	−0.1	Vac-Vac	0.06/0.08	0.07	Vac-Vac	0.15	−0.09
Fe-Vac	−0.02	−0.01	Ni-Vac	0.09	0.01	Fe-Vac	−0.11	−0.01
Cr-Vac	−0.05/−0.061	0.01	Cr-Vac	0.03	−0.05	Ni-Vac	−0.07	−0.03
Fe-Fe	−0.11	0.01/0.02	Ni-Ni	0.11	0.06	Fe-Fe	−0.07	−0.01
Cr-Cr	0.04/0.11	0.11/0.12	Cr-Cr	−0.06	−0.01	Ni-Ni	−0.14	0.00
Fe-Cr	−0.16	0.01	Ni-Cr	0.05	−0.03	Fe-Ni	−0.11	−0.00

Table 3.3: The table shows the binding energies (eV) of solute-solute and vacancy-solute in fcc Ni, fcc Cr and fcc Fe, obtained from DFT calculations.

fcc Ni matrix	**DFT binding Energy (eV)**	**fcc Fe matrix**	**DFT binding Energy (eV)**
Ni-Fe	−0.05/−0.06	Fe-Ni	−0.33
Ni-Cr	0.45/0.53	Fe-Cr	0.07
Fe-Fe	−0.48	Ni-Ni	−0.21
Cr-Cr	0.93	Cr-Cr	−0.27
Cr-Fe	NA	Ni-Cr	−0.11

Table 3.4: The table shows the ⟨100⟩ dumbbell binding energies in fcc Ni and fcc Fe obtained from DFT calculations.

3.3 First Potential

A ternary potential was provided by Bonny on September 2010 [8] to describe the interactions in the ternary alloy. The potentials for the pure elements were chosen from the available potentials in the literature. Ackland 97 [68] was chosen for pure Fe, Mishin 04 [69] for pure Ni and Olsson 05 [70] for pure Cr. These potentials were chosen as they well reproduce the ⟨112⟩ gamma line as shown in figure (3.1).

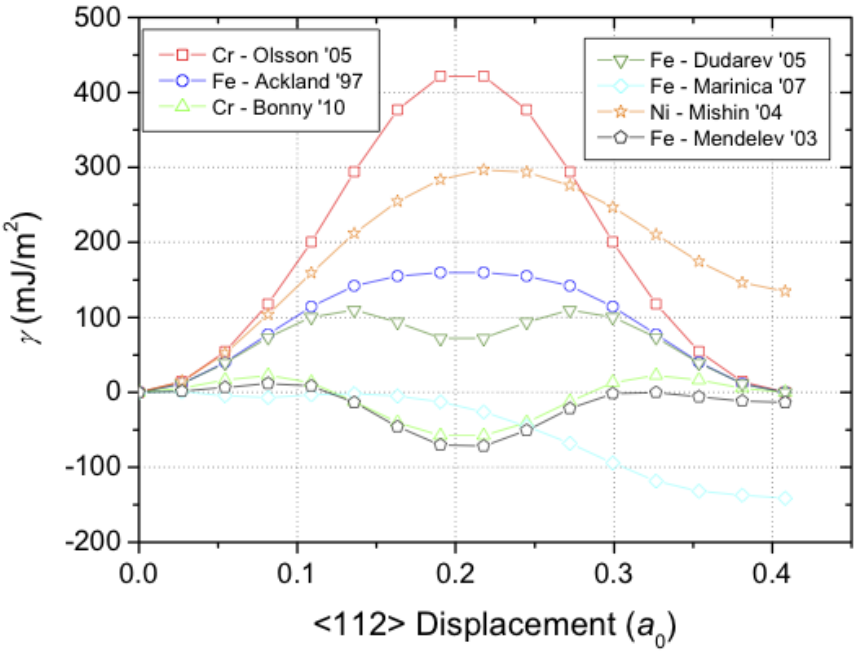

Figure 3.1: ⟨112⟩ gamma cut calculated with different potentials. The gamma cut is connected to the mobility of 1/6 ⟨112⟩ partial dislocations and need to be smooth. Three potentials were found to well reproduce this cut and therefore have been chosen to represent the interactions of the pure elements in the ternary potential. These potentials are Olsson 05 for Cr, Ackland 97 for Fe and Mishin 04 for Ni. This picture is taken from [8].

In this section, the implementation of this potential, results obtained using it and the difficulties are explained. The potential for the pure elements will be discussed first and the cross potentials will follow.

3.3.1 Pure potentials

Pure fcc Fe

Ackland 97 [68] was used to describe the atoms interaction in pure fcc Fe. EAM [45] was used to construct the potential which has the following form:

$$U = \frac{1}{2}\sum_{i\neq j=1}^{N} V_{ij}(R_{ij}) - \sum_{i=1}^{N}\left(\sum_{j=1}^{N}\phi_{ij}(R_{ij})\right)^{\frac{1}{2}}, \tag{3.1}$$

where the first term represents the pair potential and the second term is the embedding term.

Pair potential: The pair potential given by Ackland was expressed by cubic spline as follows:

$$V(R_{ij}) = \sum_{k=1}^{m} a_k (r_k - R_{ij})^3 H(r_k - R_{ij}), \tag{3.2}$$

where a_k, r_k are constants shown in table (3.5) and H is the Heaviside function.

k	1	2	3	4	5	6
a_k (eV/Å^3)	−36.559853	62.416005	−13.155649	−2.721376	8.761986	100.000
r_k (Å)	1.180	1.150	1.080	0.990	0.930	0.866025

Table 3.5: The table shows the parameters to calculate Ackland pair potential in fcc Fe (all values need to be normalised to the bcc Fe lattice constant 2.8665 Å).

Embedding Term: Similar to the pair potential, Ackland used a cubic spline to express the ϕ term,

$$\phi(R_{ij}) = \sum_{k=1}^{2} A_k (R_k - R_{ij})^3 H(R_k - R_{ij}), \tag{3.3}$$

where A_k, R_k are constants shown in table (3.6) and H is the Heaviside function.

k	1	2
A_k (eV^2/Å^3)	72.868366	−100.944815
R_k (Å)	1.30	1.20

Table 3.6: The table shows the parameters to calculate Ackland density in fcc Fe (all values need to be normalised to the bcc Fe lattice constant 2.8665 Å).

The ϕ term goes below zero at some values of R_{ij}, therefore ϕ is set to be equal to the maximum value that it reaches (3.22248041 eV) for all values less than $0.6349939 a_0$.

Spline and ZBL Potential: The Ackland pair potential was calculated as follows:

$$V(R_{ij}) = \begin{cases} \sum_{k=1}^{m} a_k (r_k - R_{ij})^3 H(r_k - R_{ij}), & R_{ij} \leq 1.9 \\ \exp(f_1 + f_2 R_{ij} + f_3 R_{ij}^2 + f_4 R_{ij}^3 + f_5 R_{ij}^4 + f_6 R_{ij}^5), & 0.9 < R_{ij} < 1.9 \\ \frac{Z_{Fe} Z_{Fe} e^2}{R_{ij}} \phi_{ZBL}(\frac{R_{ij}}{a_s}), & R_{ij} \leq 0.9 \end{cases}$$

where f_1, f_2, f_3, f_4, f_5 and f_6 are constants as shown in table (3.7). $Z_{Fe} = 26$ is the atomic number of Fe.

f_1	f_2	f_3
30.247107	−92.533341	142.350341
f_4	f_5	f_6
−110.846669	41.549765	−6.007544

Table 3.7: The table shows the parameters used to fit the spline for Ackland potential that was used to connect the pair potential to the ZBL potential. The f_k's are in units Å^{-k}.

Furthermore, to make sure that the potential works for all ranges, the derivative of the embedding term was set to zero if the summation of the density goes to zero as it is undefined at zero due to the following term in the force calculations:

$$\frac{1}{\sum_{j=1}^{N} (\phi_{ij}(R_{ij}))^{\frac{1}{2}}}.$$

Pure Cr potential

The Olsson 2005 potential [70] was used to describe the Cr-Cr interaction. Olsson used a two band model to describe the total potential of Cr-Cr atoms. His total potential was represented as follows:

$$U = \frac{1}{2} \sum_{i \neq j=1}^{N} V_{ij}(R_{ij}) + F(\rho_b), \tag{3.4}$$

where the first term represents the pair potential and the embedding term is represented by the second term.

Pair potential: Similar to Ackland potential the pair potential given by Olsson was expressed by cubic spline as follows:

$$V(R_{ij}) = \sum_{i=1}^{m} a_i (R_{ij} - r_i)^3 H(r_i - R_{ij}), \tag{3.5}$$

where a_i, r_i are constants shown in table (3.8) and H is the Heaviside function.

i	1	2	3	4
a_i (eV/Å^3)	-165.0	78.49908	-78.15495	1.8679553
r_i (Å)	0.976	1.150	1.216	1.650

Table 3.8: The table shows the parameters used to calculate Olsson pair potential in fcc Cr (all values need to be normalised to the nearest-neighbour distance in Cr (2.4924 Å)).

Embedding Term: Similar to the Ackland, Olsson used a cubic spline to express the ϕ term,

$$\phi(R_{ij}) = \sum_{k=1}^{m} b_k (r_k - R_{ij})^3 H(r_k - R_{ij}), \tag{3.6}$$

where b_k, r_k are constants shown in table (3.9) and H is the Heaviside function.

k	1	2	3
b_k (eV/Å^3)	-11.0828	0.013905	-0.447541
r_k (Å)	0.963	1.284	1.685

Table 3.9: The table shows the parameters used to calculate Olsson potential density in fcc Cr, (r_k values need to be normalised to the nearest-neighbour distance in Cr (2.4924 Å)).

The embedding term was calculated as follows:

$$F(\rho_b) = A_1\sqrt{\rho_b} + A_2{\rho_b}^2 + A_3{\rho_b}^4, \tag{3.7}$$

where A_1, A_2 and A_3 are constants shown in table (3.10).

A_1 (eV$^{\frac{1}{2}}$)	A_2 (eV^{-1})	A_3 (eV^{-3})
-0.56479	-8.8959×10^{-4}	9.0265×10^{-8}

Table 3.10: The table shows the parameters used to calculate Olsson potential embedding term.

Spline and ZBL Potential: The spline function and ZBL potential were implemented so the pair potential was calculated as follows:

$$V(R_{ij}) = \begin{cases} \sum_{i=1}^{m} a_i (R_{ij} - r_i)^3 H(r_i - R_{ij}), & R_{ij} \leq 1.2 \\ \exp(f_1 + f_2 R_{ij} + f_3 R_{ij}^2 + f_4 R_{ij}^3 + f_5 R_{ij}^4 + f_6 R_{ij}^5), & 0.5 < R_{ij} < 1.2 \\ \frac{Z_{Cr} Z_{Cr} e^2}{R_{ij}} \phi_{ZBL}(\frac{R_{ij}}{a_s}), & R_{ij} \leq 0.5 \end{cases}$$

where f_1, f_2, f_3, f_4, f_5 and f_6 are constants as shown in table (3.11). Z_{Cr} is the atomic number of Cr (equal 24).

f_1	f_2	f_3
22.236825	−94.257228	244.573237
f_4	f_5	f_6
−323.384851	203.005073	−48.328778

Table 3.11: The table shows the parameters used to fit the spline for Olsson potential which was used to connect the pair potential to the ZBL potential. The f_k's are in units Å^{-k}.

Pure Ni potential

The Mishin 2004 potential [69] was used to describe Ni-Ni interaction. The total potential for Mishin potential was written as:

$$U = \frac{1}{2}\sum_{i\neq j=1}^{N} V_{ij}(R_{ij}) + \sum_{i=1} F_i(\bar{\rho}_i), \tag{3.8}$$

where the first term represents the pair potential and the embedding term is represented by the second term.

Pair potential: Mishin's pair potential differs from Ackland and Olsson as it was written in a generalized Lennard-Jones form:

$$V(R_{ij}) = \psi\left(\frac{R_{ij}-r_c}{h}\right)\left[\frac{V_0}{b_2-b_1}\left(\frac{b_2}{z^{b_1}}-\frac{b_1}{z^{b_2}}\right)+\delta\right], \tag{3.9}$$

with:

$$z = \frac{R_{ij}}{r_1}, \tag{3.10}$$

$$\psi(x) = \begin{cases} \frac{x^4}{1+x^4}, & x<0 \\ 0, & x\geq 0 \end{cases}$$

where V_0, b_1, b_2, r_c, h, δ and r_1 are constants shown in table (3.12).

V_0 (eV)	b_1	b_2	r_c (Å)	$h(\mathring{A})$	δ (eV)	r_1 (Å)
-3.5126×10^3	4.7067×10^{-3}	0.15106	5.168	3.323	3.6046×10^3	3.8673×10^{-4}

Table 3.12: The table shows the parameters used to calculate Mishin pair potential in fcc Ni.

A transformation was needed for the pair potential before it was considered:

$$V(R_{ij}) = V(R_{ij}) - 2g_{Ni}\rho(R_{ij}), \tag{3.11}$$

where g_{Ni} is constant equal 58.549 eV.

Embedding Term: The ϕ term was calculated as follows,

$$\phi(R_{ij}) = \psi\left(\frac{R_{ij} - r_c}{h}\right)\left[A_0 z^y e^{-\gamma z}\left(1 + B_0 e^{-\gamma z}\right) + C_0\right], \tag{3.12}$$

with:

$$z = R_{ij} - r_0, \tag{3.13}$$

where A_0, B_0, C_0, r_0, y and γ are constants shown in table (3.13). The A_0 is eliminated using the condition of unit host electron density in the fcc lattice.

B_0 (Å)	C_0 (1/Å)	r_0 (Å)	y	γ (1/Å)
1.1914×10^5	0.20329	-3.138	19.251	168.02

Table 3.13: The table shows the parameters used to calculate Mishin potential density in fcc Ni.

The embedding term was calculated by equating the universal equation of state to the total potential where,

$$\bar{\rho}_i = \sum_{i \neq j} \phi_j(R_{ij}), \tag{3.14}$$

$$E(a) = E_0\left[1 + \alpha x + \beta\alpha^3 x^3 \frac{2x+3}{(x+1)^2}\right] e^{-\alpha x}, \tag{3.15}$$

where,

$$x = \frac{a}{a_0} - 1, \tag{3.16}$$

$$\alpha = \left(-\frac{9\Omega_0 B}{E_0}\right)^{\frac{1}{2}}, \tag{3.17}$$

$$\Omega_0 = \frac{a_0^3}{4}. \tag{3.18}$$

Parameters used to calculate the above terms are given in table (3.14).

β	a_0 (Å)	E_0 (eV)	B (GPa)
0.4890×10^{-2}	3.52	-4.45	181.0

Table 3.14: The table shows the parameters used to calculate Mishin potential embedding term.

Final transformation was required to get the values of the embedding term,

$$F(\bar{\rho}) = F(\bar{\rho}) + g_{Ni}\bar{\rho}. \tag{3.19}$$

Spline and ZBL Potential: As the tabulated values used here, the value of the cutoff distance was the first value in the tabulated data. Spline function and ZBL potential were implemented so the pair potential was calculated as follows:

$$V(R_{ij}) = \begin{cases} \psi\left(\frac{R_{ij}-r_c}{h}\right)\left[\frac{V_0}{b_2-b_1}\left(\frac{b_2}{z^{b_1}} - \frac{b_1}{z^{b_2}}\right) + \delta\right], & R_{ij} \leq 1.501 \\ \exp(f_1 + f_2R_{ij} + f_3R_{ij}^2 + f_4R_{ij}^3 + f_5R_{ij}^4 + f_6R_{ij}^5), & 0.6 < R_{ij} < 1.501 \\ \frac{Z_{Ni}Z_{Ni}e^2}{R_{ij}}\phi_{ZBL}(\frac{R_{ij}}{a_s}), & R_{ij} \leq 0.6 \end{cases}$$

where f_1, f_2, f_3, f_4, f_5 and f_6 are constants as shown in table (3.15). Z_{Ni} is the atomic number of Ni (equal 28).

f_1	f_2	f_3
30.834369	-131.470230	290.681792
f_4	f_5	f_6
-317.050323	162.036241	-31.209951

Table 3.15: The table shows the parameters used to fit the spline for Mishin potential which was used to connect the pair potential to the ZBL potential to describe small atomic separations. The f_k's are in units Å^{-k}.

For the values of the density that were out of the range of the tabulated data, the equation of the density was used. However, for the values of the embedding term that were out of tabulated range, the following equation was used:

$$F(\rho) = \begin{cases} \text{Tabulated data by Mishin [71]}, & \rho \geq 0.00836 \\ S = ax^2 + bx, & \rho < 0.00836 \end{cases}$$

where $a = 1137.3851$ eV and $b = -33.7970$ eV.

3.3.2 Cross Potentials

Three versions of the cross potential were provided by Bonny [8] labelled, P-100826, P-100819 and P-100831. Two of these are used in the thesis, P-100819 given below and P-100831 given in chapter 4. In all of the three versions, the cross pair potentials were expressed as cubic spline,

$$V(R_{ij}) = \sum_{k=1}^{m} a_k (R_{ij} - r_k)^3 H(r_k - R_{ij}), \tag{3.20}$$

where a_k, r_k are constants depend on the type of atoms and H is the Heaviside function. These constants are different for each version. Constants used for Fe-Cr, Fe-Ni and Ni-Cr cross potentials (P-100819) are given in table (3.16).

P-100819		Fe-Ni	Fe-Cr	Ni-Cr
k	r_k(Å)	a_k(eV/Å^3)	a_k(eV/Å^3)	a_k(eV/Å^3)
1	2.00000000	−89.9741079	212.248091	−112.540558
2	2.42857143	0.948228599	−18.7472151	−3.89173781
3	2.85714286	−0.767221580	5.05480164	0.827364103
4	3.28571429	−2.88779594	−3.31230927	−3.01075131
5	3.71428571	3.11855586	0.893495199	1.98565278
6	4.14285714	−2.27511405	−0.121033387	−1.03261848
7	4.57142857	1.05387129	0.0336552327	0.372395335
8	5.00000000	−0.197080398	−0.00391441695	−0.0508004843
9	1.90000000	−1000.0000000	−1000.0000000	−1000.0000000

Table 3.16: The table shows the parameters used for cross pair potentials given by the first ternary potential.

Spline and ZBL potential

The cut-off distances used for the cross potentials were 0.8 and 2.1 Å for Fe-Cr and 0.8 and 1.95 Å for both Fe-Ni and Ni-Cr. Constants used for the spline function are shown in table (3.17).

Constant	Ni-Cr	Fe-Ni	Fe-Cr
f_1	6.529676	8.275315	9.724190
f_2	11.514119	3.988480	-4.703002
f_3	-34.950086	-22.231142	-3.464720
f_4	34.892408	24.881719	5.335811
f_5	-15.891523	-12.272112	-2.555838
f_6	2.678043	2.172228	0.381091

Table 3.17: The table shows the parameters used to fit the splines for the cross pair potentials given by the first ternary potential. The f_k's are in units Å^{-k}.

3.3.3 Transformation for the pure potential

According to Bonny [8], transformations were implemented to the pure potentials as follows:

$$\hat{T}: \begin{cases} V^{eff}(R_{ij}) = V(R_{ij}) - 2C\phi(R_{ij}), \\ \phi^{eff}(R_{ij}) = S\phi(R_{ij}), \\ F^{eff}(\rho) = F(\frac{\rho}{S}) + \frac{C}{S}\rho, \end{cases}$$

where C and S are constants given in table (3.18).

Element	C	S
Fe	0.105328897	0.0443767064
Ni	$1.19677485 \times 10^{-5}$	0.999998420
Cr	-0.0308810873	0.0503694498

Table 3.18: Transformation Coefficients for the first ternary potential.

3.3.4 Results obtained using the first potential

Pure fcc Fe

Lattice parameter: Ackland 1997 [68] was used within the molecular dynamics to calculate the value of the lattice constant for fcc Fe. The lattice parameter was found to be 3.68 Å which matches exactly the lattice constant found by Mendelev 2003 [72] also using the Ackland 1997 potential.

Defect formation energies: The formation energies for point defects in pure fcc Fe are shown in table (3.19). The results show that $\langle 100 \rangle$ dumbbell is the most stable interstitial defect and that the empirical potential underestimates the formation energy of $\langle 111 \rangle$ dumbbell

and tetrahedral defect when compared to the ab-initio results.

Configuration	DFT ([15]) (eV)	Ackland97 (eV)
Vacancy	1.95	1.94
⟨100⟩ dumbbell	3.63	3.64
Octahedral	4.353	4.26
⟨111⟩ dumbbell	4.559	3.86
Tetrahedral	4.322	3.91

Table 3.19: The formation energies of point defects in pure Fe using Ackland potential. The table shows that the potential underestimates the formation energies for the ⟨111⟩ dumbbell and tetrahedral point defects.

Defect migration energies

Migration of vacancy: The energy pathway for vacancy migration shows that an atom moves from the first nearest neighbour to the vacancy leaving another vacancy. The potential overestimates the migration energy of the vacancy as it found the vacancy migration barrier equal 1.47 eV compared to 1.05 eV from the DFT results.

Migration of [100] dumbbell: Three interesting energy pathways were found by which a [100] dumbbell can migrate. The first one consisted of translation and rotation which resulted in [001] dumbbell or [010] dumbbell as shown in figure (3.2). The second pathway contained only a rotation which resulted into [001] or [010] dumbbell as shown in figure (3.3). The barriers were 0.30 eV for the shift and rotation pathway and 0.45 eV for the rotation only. In the third pathway the [100] dumbbell was found to shift to another [100] dumbbell with a 0.46 eV energy barrier as shown in figure (3.4). The possible pathways with migration barriers of [100] dumbbell are summarised in table (3.20).

Initial Configuration	Final Configuration	Energy Barriers (eV)
[100] dumbbell	[010] or [001] dumbbell	0.45
[100] dumbbell	Shifted [010] or [001] dumbbell	0.30
[100] dumbbell	Shifted [100] dumbbell	0.46

Table 3.20: The table shows the migration barriers for three transitions for ⟨100⟩ dumbbell in fcc Fe using Ackland potential, rotation, translation and rotation and translation. The last transition is found to have the lowest barrier.

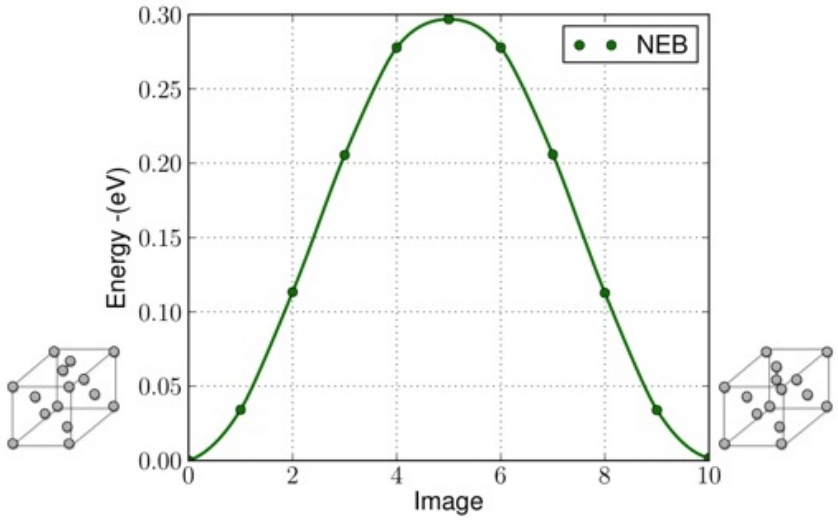

Figure 3.2: The figure shows the migration energy required for [100] dumbbell translation and rotation in fcc Fe using Ackland potential.

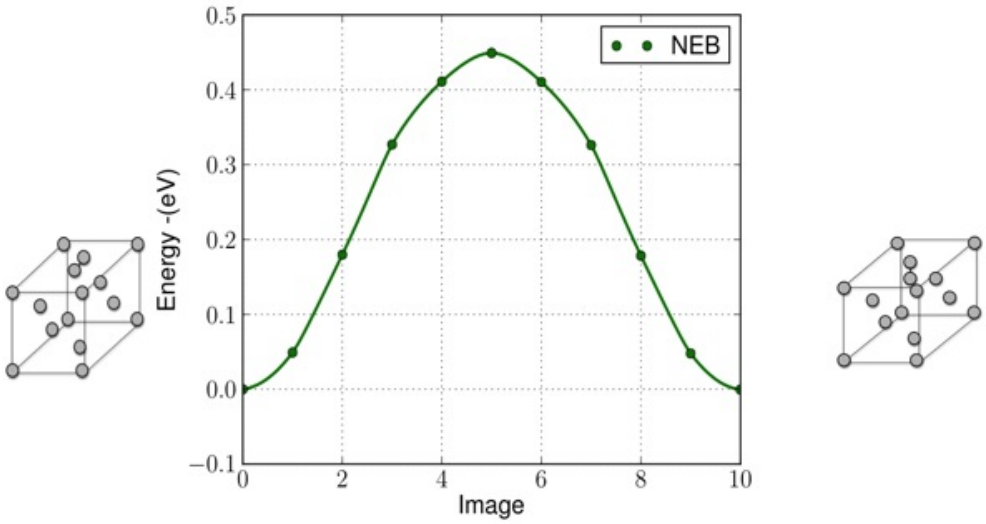

Figure 3.3: The figure shows the migration energy required for [100] dumbbell rotation only in fcc Fe using Ackland potential.

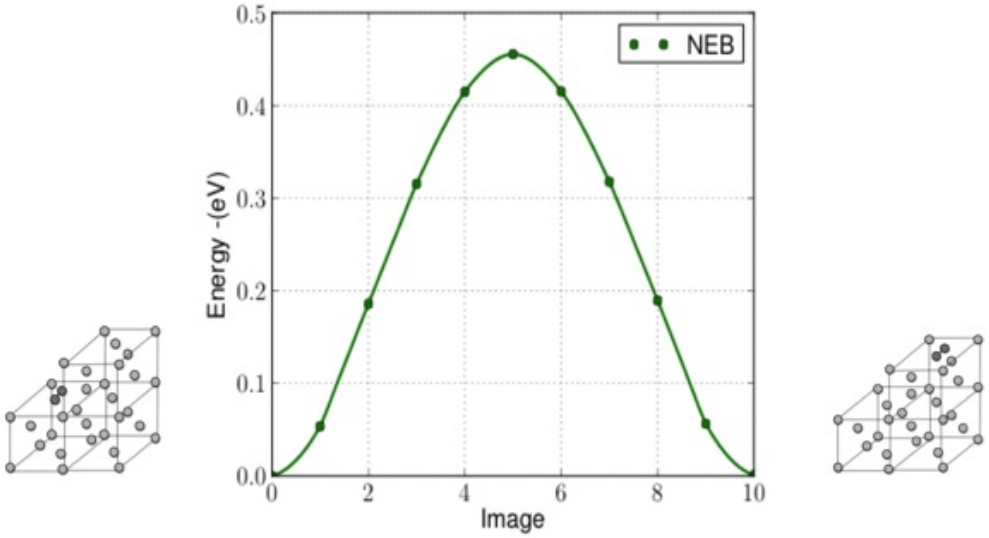

Figure 3.4: The figure shows the energy required for [100] dumbbell translation only in fcc Fe using Ackland potential.

Migration of ⟨111⟩ dumbbell: Three different pathways for the ⟨111⟩ dumbbell were found. The first one was the rotation from ⟨111⟩ dumbbell to [100] , [010] or [001] dumbbell with barrier of 0.19 eV. The second pathway was from ⟨111⟩ dumbbell to tetrahedral interstitial with barrier of 0.11 eV followed by translation to an unidentified metastable defect (close to the tetrahedral interstitial defect) with a barrier of 0.15 eV.
The third pathway was a shift to another ⟨111⟩ dumbbell with a barrier of 0.24 eV as it moves diagonally between two directions before it rotates to the new ⟨111⟩ dumbbell and then from this ⟨111⟩ dumbbell to another unidentified metastable interstitial defect. The possible pathways with migration barriers of the ⟨111⟩ dumbbell are summarised in table (3.21).

Initial Configuration	Final Configuration	Energy Barriers (eV)
⟨111⟩ dumbbell	[100], [010] or [001] dumbbell	0.19
⟨111⟩ dumbbell	Tetrahedral	0.11
⟨111⟩ dumbbell	Metastable defect	0.15
⟨111⟩ dumbbell	Shifted ⟨111⟩ dumbbell	0.24

Table 3.21: The table shows the migration barriers of ⟨111⟩ dumbbell in fcc Fe using Ackland potential.

Migration of the tetrahedral defect: Apart from the dumbbells, there was only one pathway for the tetrahedral defect to migrate which will lead to a ⟨111⟩ dumbbell with an

energy barrier of 0.06 eV.

Pure fcc Ni

Lattice parameter: The lattice constant was found here to be 3.52 Å which was expected as this value was used in the construction of the potential.

Defect formation energies: The formation energies for point defects in pure fcc Ni are shown in table (3.22). The potential underestimates the formation energies of the ⟨111⟩ dumbbell and tetrahedral interstitial defects and the results also show that ⟨100⟩ dumbbell is the most stable interstitial defect.

Configuration	Tucker2008[41] (eV)	Mishin 2004 (eV)
Vacancy	1.43*	1.57
⟨100⟩ dumbbell	4.07	3.95
Octahedral	4.25	4.31
⟨111⟩ dumbbell	4.69	4.22
Tetrahedral	4.69	4.43

Table 3.22: The formation energies of point defects in pure Ni using the Mishin potential, (* The experimental values range from 1.45 to 1.8 eV).

Defect migration energies:

Migration of vacancy: The vacancy migration barrier was found to be 1.19 eV compared to 1.08 eV from the DFT results.

Migration of [100] dumbbell: Similar to Fe, [100] dumbbell was found to form [001] dumbbell or [010] dumbbell by translation and rotation with an energy barrier of 0.21 eV. Rotation to [001] dumbbell or [010] dumbbell required crossing an energy barrier of 0.34 eV. The possible pathways with migration barriers of [100] dumbbell are summarised in table (3.23).

Initial Configuration	Final Configuration	Energy Barriers (eV)(ZA)	Energy Barriers (eV)(Tucker[41])
[100] dumbbell	[001] or [010] dumbbell	0.34	x
[100] dumbbell	Shifted [001] or [010] dumbbell	0.21	0.14

Table 3.23: The table shows the migration barriers of the ⟨100⟩ dumbbell in fcc Ni using the Mishin potential.

Migration of the ⟨111⟩ dumbbell: Rotation of the ⟨111⟩ dumbbell into the ⟨100⟩ dumbbell required only 0.02 eV. No other pathways were found for the ⟨111⟩ dumbbell.

Migration of the tetrahedral interstitial: The tetrahedral interstitial was found to move to the ⟨100⟩ dumbbell when the system is relaxed.

Pure fcc Cr

Lattice constant: Olsson 2005 [70] potential was used within molecular dynamics to calculate the lattice constant of fcc Cr and it was found equal 3.76 Å .

Defects formation energies: Formation energies of vacancy and self interstitial defects were calculated in pure fcc Cr. The results found are shown in table (3.24). There are no ab-initio results, which makes any comparison impossible.

Configuration	Olsson05 (eV)
Vacancy	2.85
⟨100⟩ dumbbell	4.11
Octahedral	5.46
⟨111⟩ dumbbell	4.54
⟨110⟩ dumbbell	5.00
Tetrahedral	4.65

Table 3.24: The table shows the formation energies of point defects in pure Cr using the Olsson potential.

Defects migration energies:

Migration of vacancy: The vacancy migration energy of Cr was found to equal 1.85 eV.

Migration of the [100] dumbbell: There were no results to compare the migration barriers, however, the potential implies higher barriers for Cr and lower for Ni. The [100] dumbbell in fcc Cr was found to shift and rotate into a [010] or [001] dumbbell with an energy barrier of 0.56 eV. Also the [100] dumbbell was found to form a [010] or [001] dumbbell by shifting and rotating to the ⟨111⟩ dumbbell first by an energy barrier of 0.58 eV and then the resulted ⟨111⟩ dumbbell rotates into the new dumbbell by an energy barrier of 0.17 eV. Rotation of the [100] dumbbell to a [010] or [001] dumbbell was found to have an energy

barrier of 0.90 eV. In addition the [100] dumbbell was found to move into an unidentified metastable interstitial defect, which was very close to tetrahedral.

The possible pathways with migration barriers of [100] dumbbell are summarised in table (3.25).

Initial Configuration	Final Configuration	Energy Barriers(eV)
[100] dumbbell	[010] or [001] dumbbell	0.90
[100] dumbbell	Shifted [010] or [001] dumbbell	0.56
[100] dumbbell	Shifted [010] or [001] dumbbell through $\langle 111 \rangle$ dumbbell	0.58
[100] dumbbell	Unidentified metastable defect	0.60

Table 3.25: The table shows the migration barriers of [100] dumbbell in fcc Cr using the Olsson potential.

Migration of the $\langle 111 \rangle$ dumbbell: The rotation of the $\langle 111 \rangle$ dumbbell into a [010] dumbbell or a [001] dumbbell barrier was 0.17 eV. Translation of $\langle 111 \rangle$ dumbbell required an energy barrier of 0.43 eV. However, the rotation of $\langle 111 \rangle$ dumbbell to a new $\langle 111 \rangle$ dumbbell was of 0.057 eV energy barrier.

Initial Configuration	Final Configuration	Energy Barriers(eV)
$\langle 111 \rangle$ dumbbell	$\langle 100 \rangle$ dumbbell	0.17
$\langle 111 \rangle$ dumbbell	Shifted $\langle 111 \rangle$ dumbbell	0.43
$\langle 111 \rangle$ dumbbell	Rotated $\langle 111 \rangle$ dumbbell	0.057

Table 3.26: The table shows the migration barriers of $\langle 111 \rangle$ dumbbell in fcc Cr using Olsson potential.

Migration of the tetrahedral defect: Tetrahedral interstitial defect in fcc Cr was found to drop into $\langle 111 \rangle$ dumbbell with negligible energy barrier ≈ 0.03 eV.

Binding and migration energies in the alloy system

The potential used to calculate some binding energies and vacancy migration energies. There were some noticeable differences between the results obtained and the results provided by Bonny as shown in the following tables.

fcc Ni matrix	1nn(Bonny)	1 nn(ZA)	1nn(JB)	2nn (Bonny)	2nn(ZA)	2nn(JB)
Vac-Vac	0.17	0.17	0.17	0.02	0.02	0.02
Fe-Vac	−0.06	−0.06	−0.06	0.03	0.00	0.00
Cr-Vac	0.09	0.09	0.08	−0.03	−0.03	−0.03
Fe-Fe	−0.07	−0.07	−0.07	−0.03	−0.03	−0.03
Cr-Cr	0.10	0.10	0.1	0.02	0.02	0.02
Fe-Cr	0.14	0.14	0.14	0.07	0.07	0.07
fcc Fe matrix	1nn(Bonny)	1 nn(ZA)	1nn(JB)	2nn (Bonny)	2nn(ZA)	2nn(JB)
Vac-Vac	0.29	0.29	0.29	−0.04	−0.0349	−0.04
Ni-Vac	0.15	0.15	0.15	−0.10	−0.10	−0.10
Cr-Vac	−0.15	−0.15	−0.15	−0.03	−0.03	−0.02
Ni-Ni	0.09	0.09	0.09	−0.07	−0.07	−0.07
Cr-Cr	−0.15	−0.15	−0.15	0.03	0.03	0.03
Ni-Cr	−0.00	−0.00	−0.00	0.01	0.01	0.01
fcc Cr matrix	1nn(Bonny)	1 nn(ZA)	1nn(JB)	2nn (Bonny)	2nn(ZA)	2nn(JB)
Vac-Vac	0.47	0.47	0.47	0.01	0.01	0.01
Fe-Vac	−0.06	−0.06	−0.06	0.01	0.01	0.01
Ni-Vac	0.07	0.06	0.06	−0.06	−0.06	−0.06
Fe-Fe	−0.11	−0.08	−0.08	0.00	0.00	0.00
Ni-Ni	−0.08	−0.08	−0.08	−0.07	−0.07	−0.07
Fe-Ni	−0.01	0.00	0.00	0.00	0.01	0.01

Table 3.27: The table shows comparison of solute-solute and vacancy-solute binding energies (eV) calculated by Bonny [8], JB [5] and ZA (this work) using the first potential (P-100819).

fcc Fe matrix	Bonny	ZA
Vac-Fe	1.45	1.4662
Vac-Ni	1.13	1.1120
Vac-Cr	1.05	1.4001
fcc Ni matrix	Bonny	ZA
Vac-Fe	1.04	1.0628
Vac-Ni	1.19	1.1912
Vac-Cr	1.00	1.0021
fcc Cr matrix	Bonny	ZA
Vac-Fe	1.65	1.8917
Vac-Ni	1.84	1.7017
Vac-Cr	1.84	1.8537

Table 3.28: Comparison of migration energies (eV) of vacancies and point defects calculated by Bonny [8] and ZA (this work) using the first potential (P-100819).

Monte Carlo simulations

To establish stable configurations for the alloys, the required compositions were distributed randomly in a lattice of 2048 atoms. This was followed by running Monte Carlo simulations [64] to get lower energy configurations. All simulations run at 0 K as well relaxing the system and the Monte Carlo simulation temperature used is 600 K.

Ternary system: The total energy versus the number of MC simulations is shown in figure (3.5a). The results from the Monte Carlo simulation for the ternary system showed a small amount of segregation in the system, such as that the Ni and Cr segregate to different regions of the Fe matrix as shown in figure (3.5b).

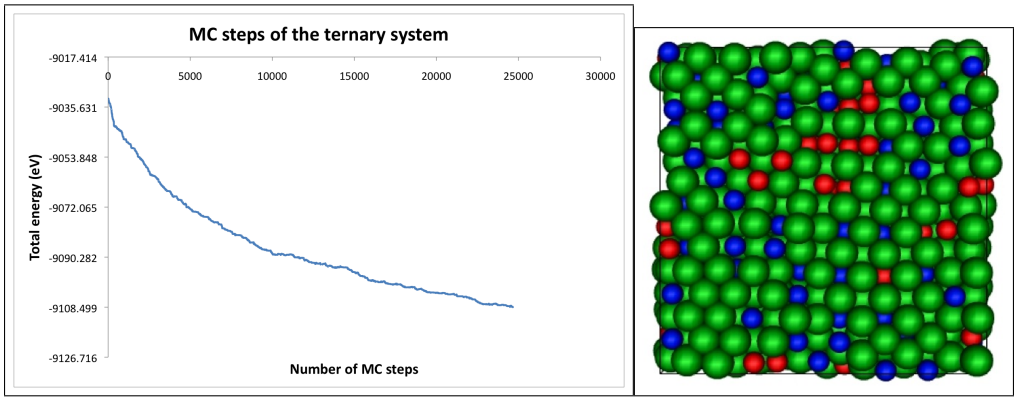

(a) (b)

Figure 3.5: MC in ternary system using the first potential, (a) shows the total energy versus the number of MC steps and (b) shows the system that resulted from the MC simulation. In the figure the green spheres are Fe atoms, the red spheres are Ni atoms and the blue spheres are Cr atoms.

Binary system: The total energy versus the number of MC simulations is shown in figure (3.6a). Picture of the system after MC simulation is shown in figure (3.6b).

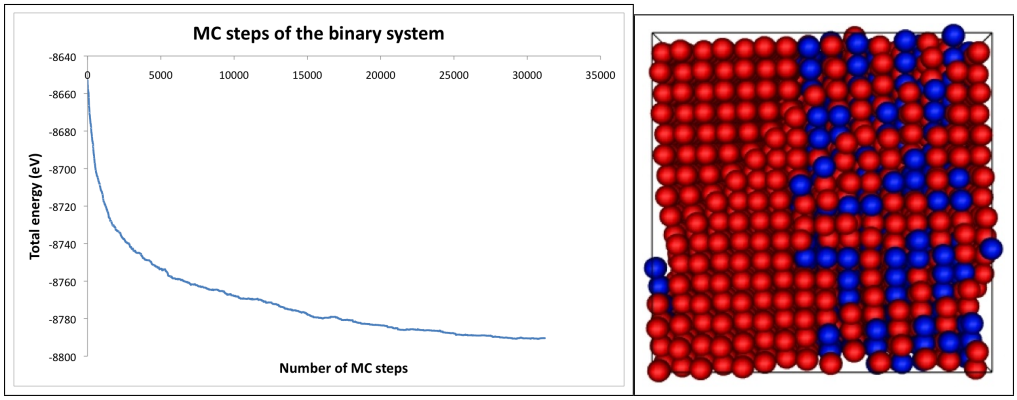

(a) (b)

Figure 3.6: MC in binary system using the first potential, (a) shows the total energy versus the number of MC steps and (b) shows system resulted from MC simulation. In the figure the red spheres are Ni atoms and the blue spheres are Cr atoms.

The binary system was found to segregate into two regions: pure Ni region and Ni-Cr region. The ratio of Ni to Cr in the Ni-Cr region was approximated to 2 which revealed production of Ni_2Cr. Although there were no results of Ni-Cr segregation reported at the same temperature for the binary system, the experimental phase diagram shows possibility of producing Ni_2Cr at the same temperature as shown in figure (3.7).

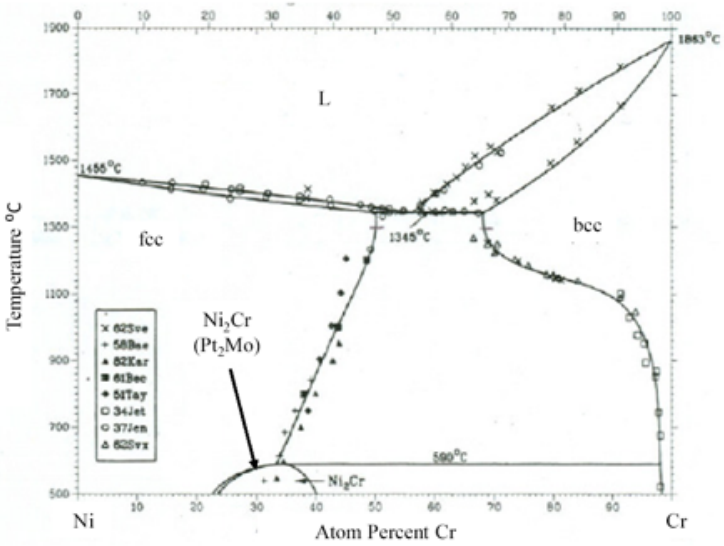

Figure 3.7: : Experimental Ni-Cr phase diagram, this picture is taken from [9].

We looked into the structure on Ni_2Cr to verify that what we are seeing is really Ni_2Cr. The picture of the Ni_2Cr and the sample of our system where we could see the same structure are shown in figure (3.8).

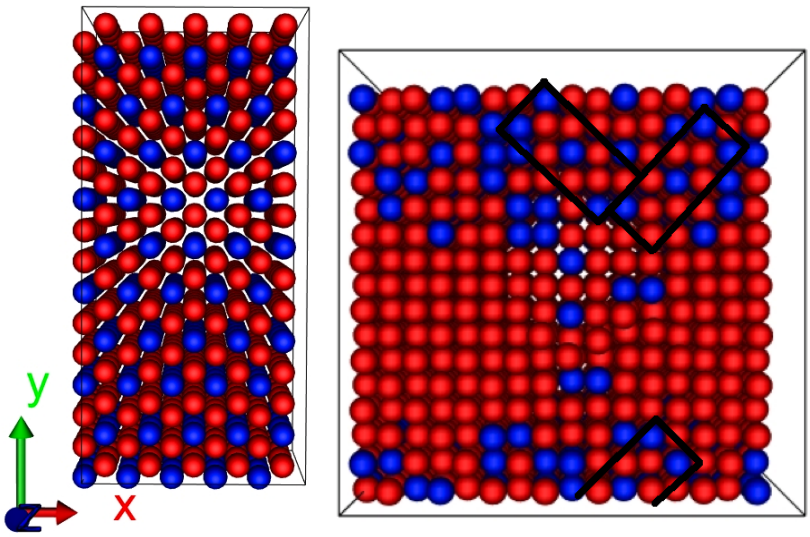

(a) (b)

Figure 3.8: Investigation of the the segregation of the binary system using the first potential, (a) shows the structure of Ni_2Cr and (b) shows part of the binary system where we could see the same structure.

High temperature Molecular Dynamics

Both systems, the ternary and the binary were generated with the required percentages of species randomly and fed to MD simulation at high temperatures. Different temperatures were tried to set up initial systems. The results found are given in this section.

Binary system: Thermalising the initial system to 1200 K was tried. The total potential energy was plotted versus time. Since there was no change in the potential energy, the initial system was thermalised to 1400 K as shown in figure (3.9). The figure shows that the potential energy gradually decreases which gives more stable configuration.

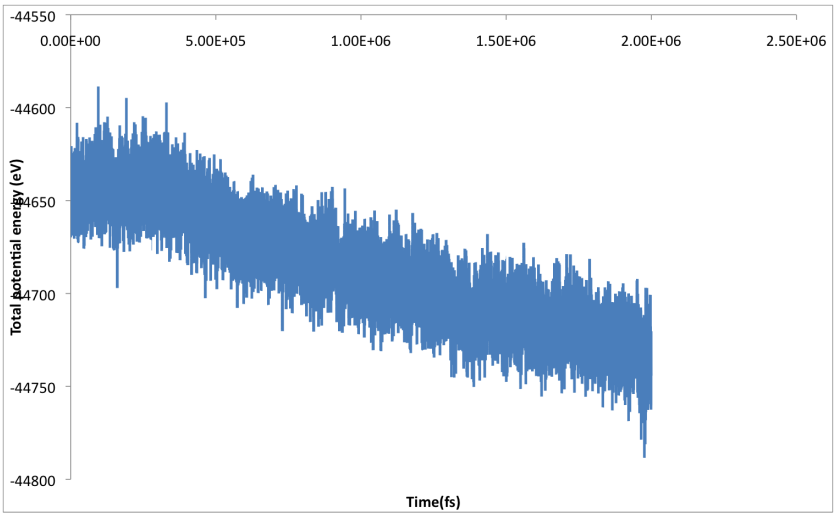

Figure 3.9: High Temperature MD for the binary system at 1400 K using the first potential. The plot shows the total potential energy gradually decreases with time.

Ternary system: Different temperatures were tried with the ternary, but there was no change in the potential energy.

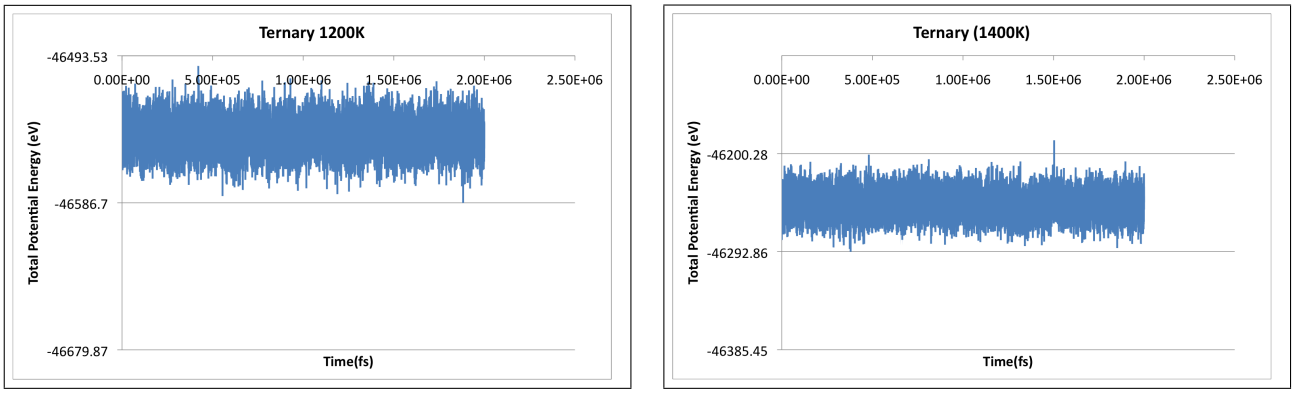

Figure 3.10: Ternary system at high temperature MD simulations using the first potential. The plots shows the total potential energies versus time.

Barrier Distribution in Model Alloy

Migration barriers in the model alloy vary mainly with the local environment and the type of atom migrating. To study the migration barriers in the model alloy, a system of 2048 atoms (70 at.% Fe 20 at.% Cr 10 at.% Ni) was randomly created using a lattice parameter of 3.75 Å. Migration barriers for the vacancy and ⟨100⟩ dumbbell were calculated and statistics were drawn from the results obtained.

Vacancy migration barrier: 400 calculations were performed and 24 migration barriers were calculated at each step. A total of 9,600 migration barriers were found and were distinguished according to the type of atom moving into a vacancy. The distribution of the barriers are shown in figure (3.11).

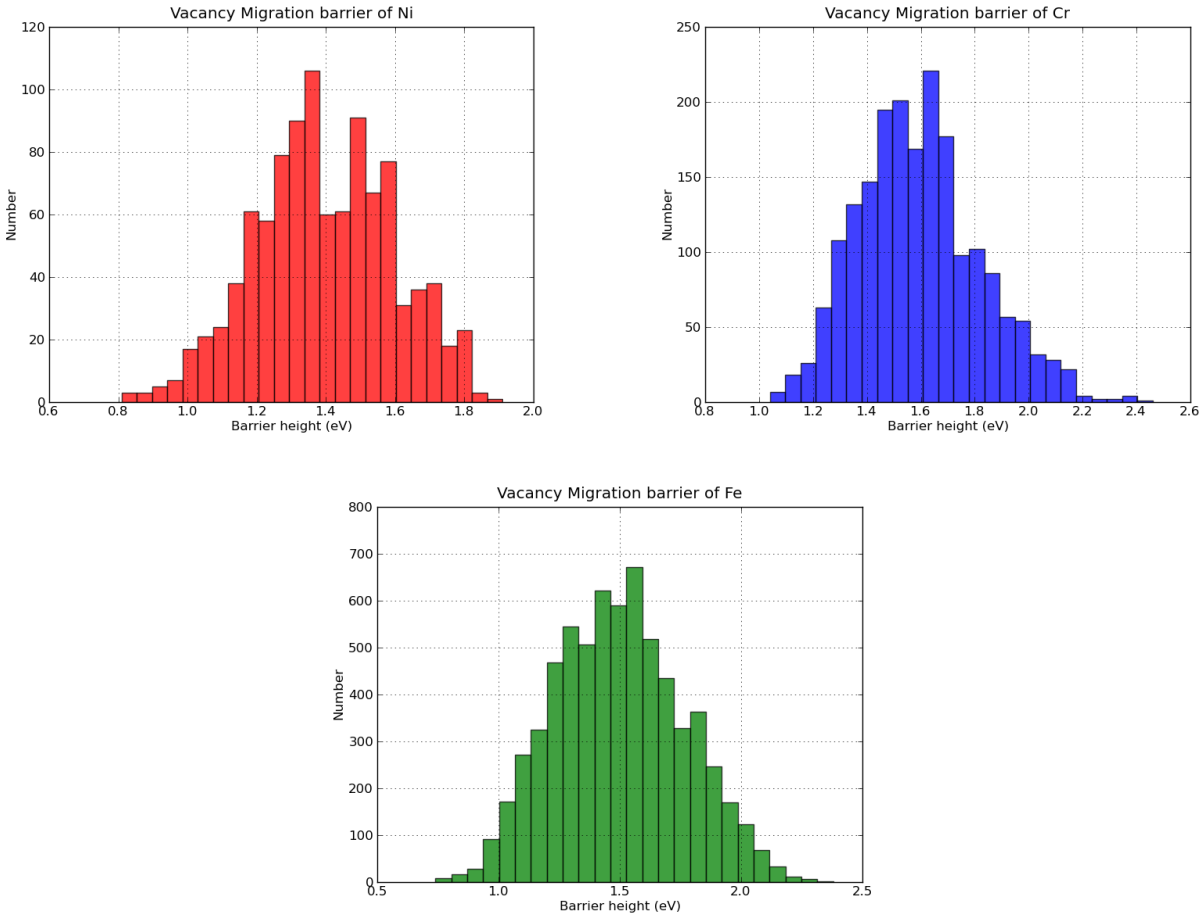

Figure 3.11: Vacancy migration barriers in the ternary alloy using the first potential. The figures show the energy required for an atom to jump into a first nearest neighbour vacancy and these are distinguished according to the type of the jumping atom. The results obtained are shown in histograms, red for Ni, blue for Cr and green for Fe.

⟨100⟩ **Dumbbell:** A similar technique was used to study the rotation, translation and translation and rotation of ⟨100⟩ dumbbell. For a ⟨100⟩ to either rotate or translate, it could pass through more stable defect like tetrahedral defect. Examples are shown in figure (3.12).

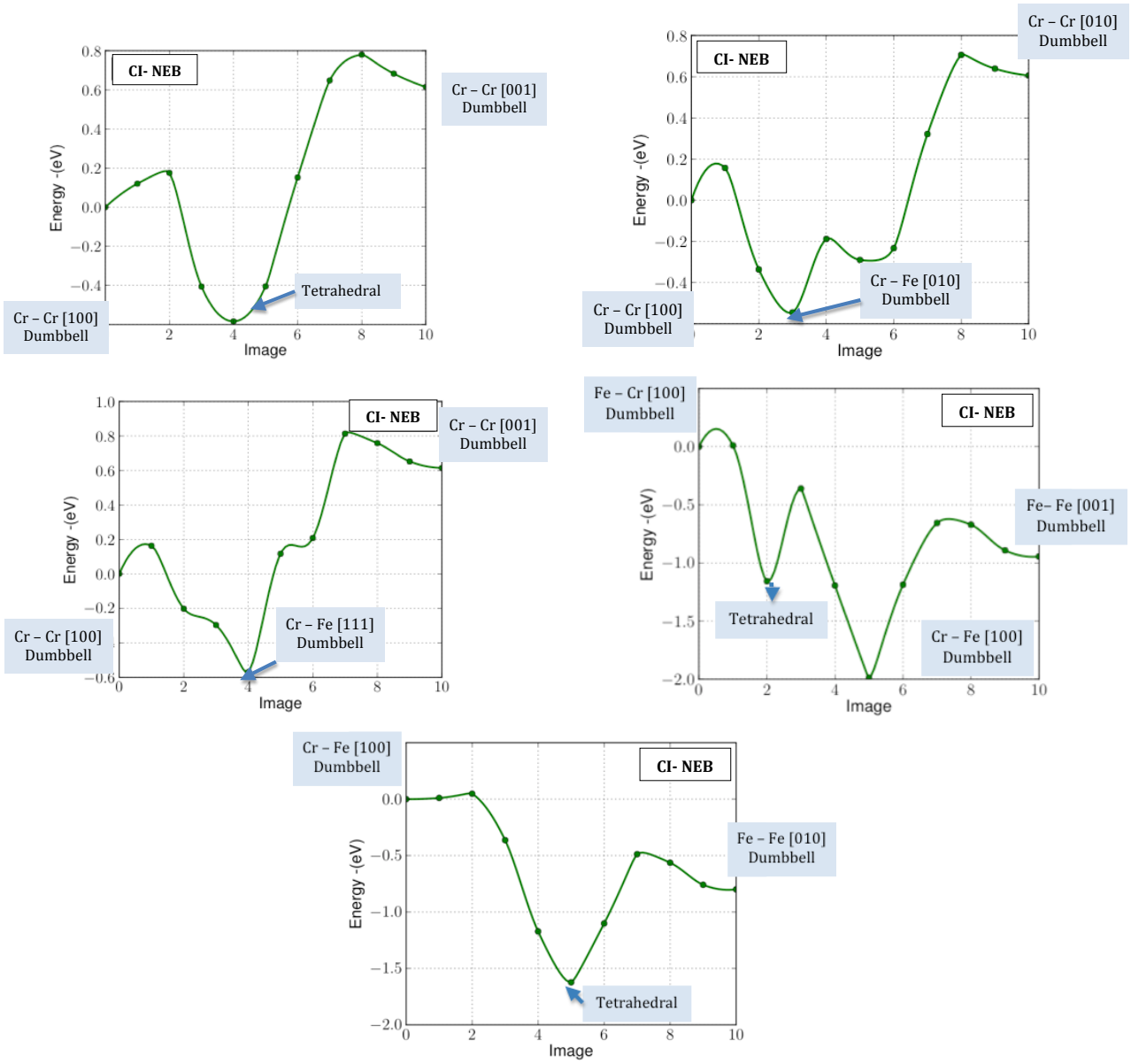

Figure 3.12: ⟨100⟩ Dumbbell migration barriers in the ternary alloy using the first potential. The figures show that ⟨100⟩ dumbbell could pass through more stable defect before rotating or translating.

3.3.5 Difficulties

There are some issues found with this potential; for example, the potential was found to have a negative thermal expansion. However, the main issue found with this potential was that the fcc structure is not stable for the ternary system at the concentration of interest.

Negative thermal expansion

The potential was found to have a negative thermal expansion as shown in figure (3.13). The figure shows the lattice parameter in a ternary alloy ($Fe_{70}Ni_{30-x}Cr_x$) as a function of the Cr percentage at three different temperatures (0, 300 and 600 K). It can be seen from the figure that the lattice parameter decreases as temperature increases, which means that the potential has negative thermal expansion.

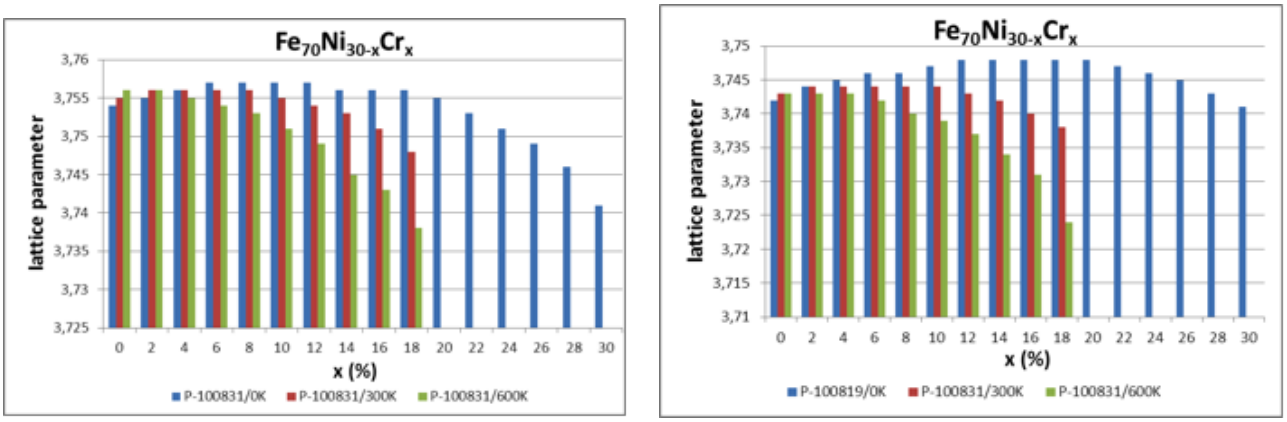

Figure 3.13: Negative thermal expansion of the first potential (Done by J.Baptiste [5]), the figure shows that the lattice parameter decreases as the temperature increases.

Stability

The stability of the ternary system was tested by creating two ternary systems with different concentrations (70 at.% Fe 18 at.% Cr 12 at.% Ni) and (70 at.% Fe 20 at.% Cr 10 at.% Ni). Two values for the lattice parameter (3.643 and 3.75 Å) were used to create each system. These two values have been chosen because the energy of the system used was found to be minimum at these two lattice parameters. At first the systems were thermalised and then collision cascades were implemented using 1 and 5 KeV. The results from these simulations showed that a small change in the lattice parameter affects the stability of the fcc structure. The pictures for the system (70 at.% Fe 20 at.% Cr 10 at.% Ni) after thermalising and after collision cascades are shown in figures (3.14 & 3.15). In those cases using Q4 filter revealed transformation to bcc structure as shown in figure (3.16).

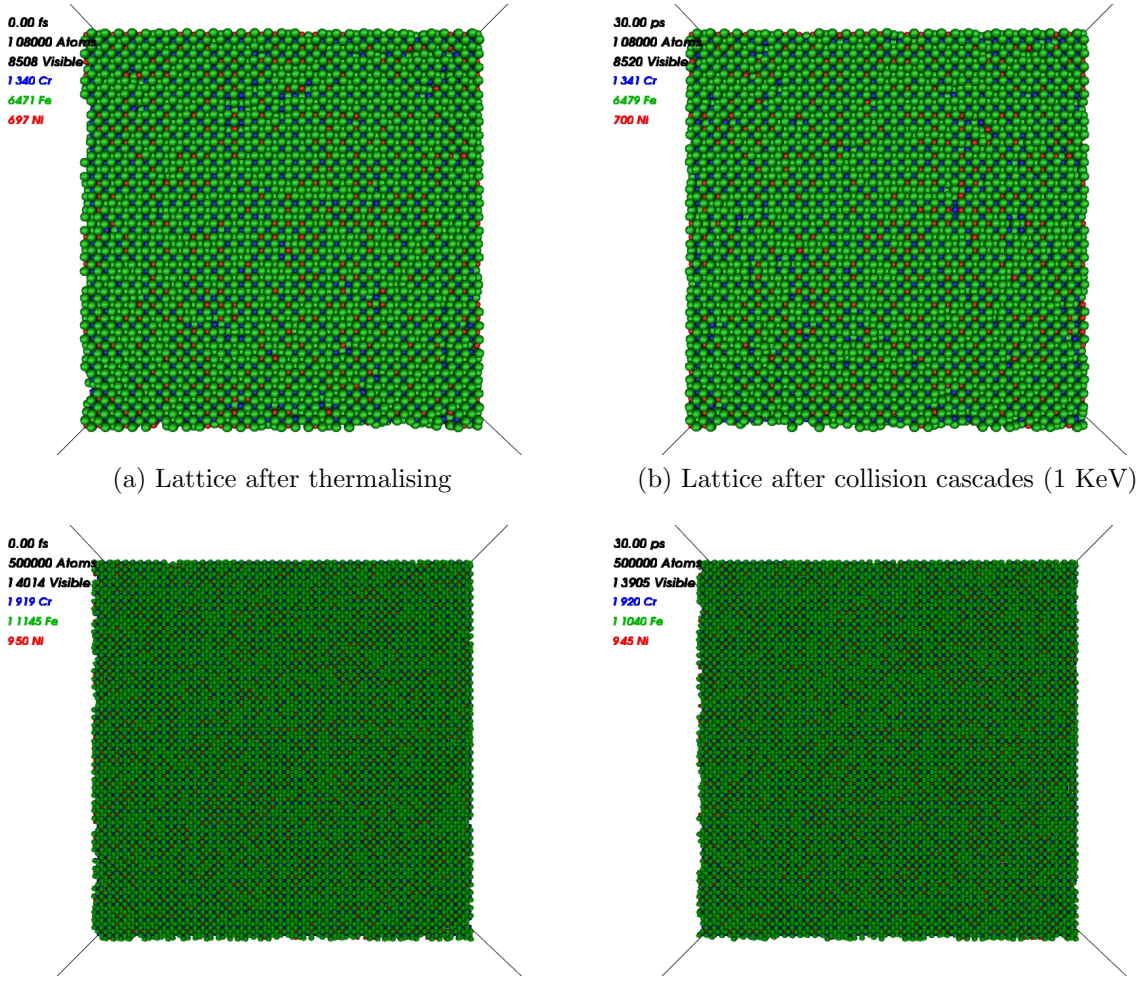

(a) Lattice after thermalising

(b) Lattice after collision cascades (1 KeV)

(c) Lattice after thermalising

(d) Lattice after collision cascades (5 KeV)

Figure 3.14: Illustration of the stability issue found using the first potential (systems using lattice parameter = 3.75 Å).

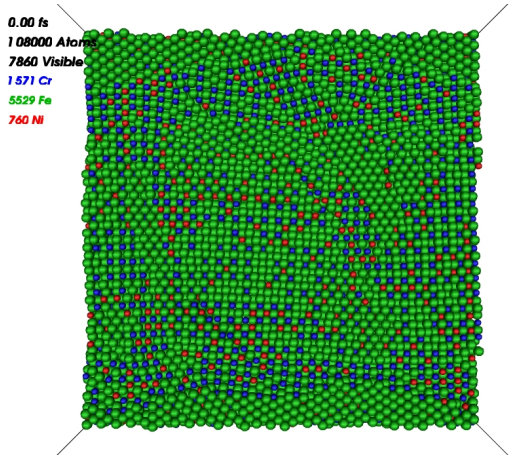

(a) Lattice after thermalising

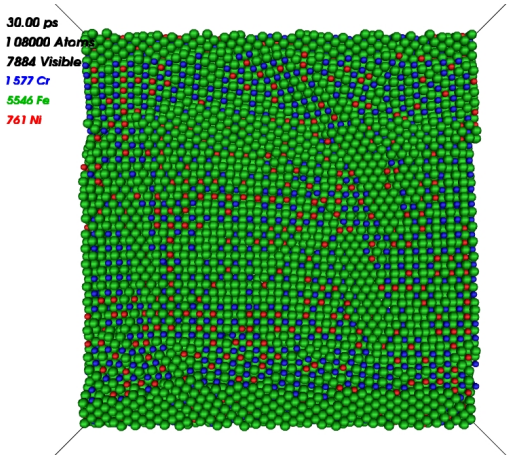

(b) Lattice after collision cascades (1 KeV)

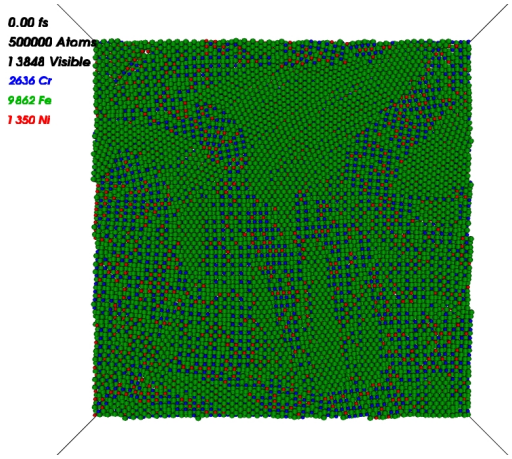

(c) Lattice after thermalising

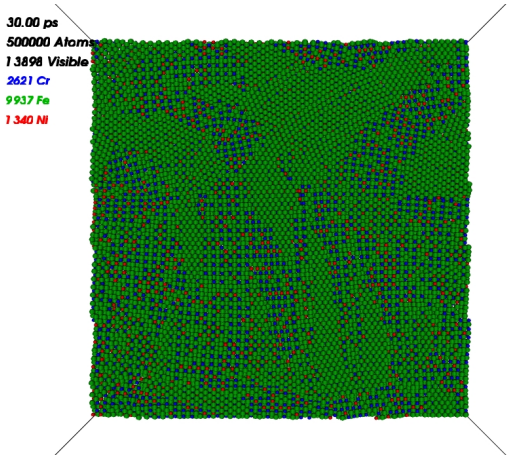

(d) Lattice after collision cascades (5 KeV)

Figure 3.15: Illustration of the stability issue found using the first potential (systems using lattice parameter = 3.643 Å).

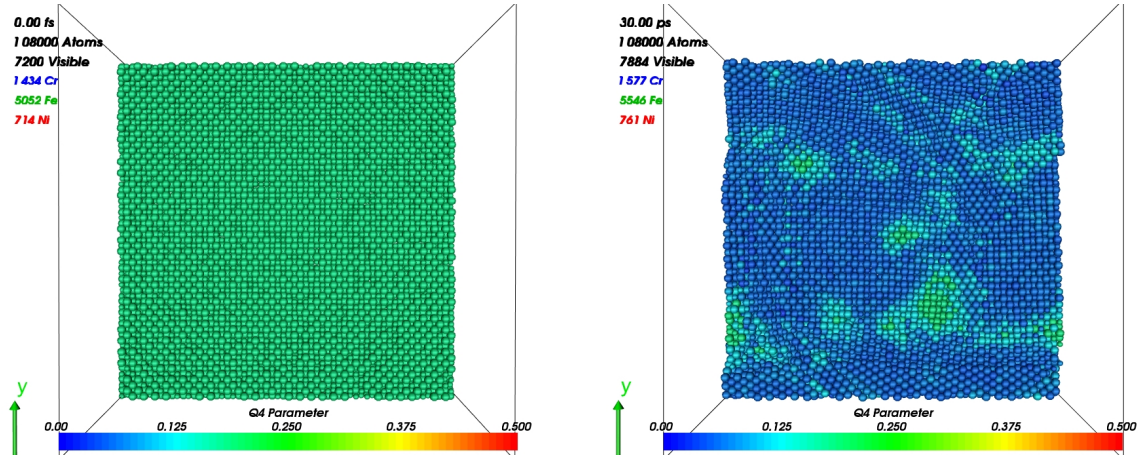

(a) Initial system (b) Final system

Figure 3.16: Illustration of the transformation of fcc structure to bcc structure for the ternary system using the first potential, (a) shows the initial system coloured using Q4 filter which represent that we have an fcc structure at the beginning of our simulation and (b) shows that the Q4 parameters changed to the value associated with bcc structure, which indicates that the initial fcc structure transformed to bcc structure.

3.4 Second Potential

To overcome the stability issue found in the first potential, a second potential was developed by G.Bonny [10] to describe the interactions between Fe, Ni and Cr. The potential was fitted to model plasticity in 316 stainless steel. The potential gave good $\langle 112 \rangle$ gamma cut values as shown in figure (3.17). This potential was implemented within molecular dynamics and the ZBL potential was added to describe the potential for the short distances. The main aim from this section is to investigate this potential and to explain things implemented along with it. The energy formalism of the potential will be discussed first followed by the potential of the pure fcc elements. In each case, we show the embedding term, pair term and how it was fitted to the ZBL potential. The cross potential is discussed after that and difficulties accompanied this potential are shown at the end.

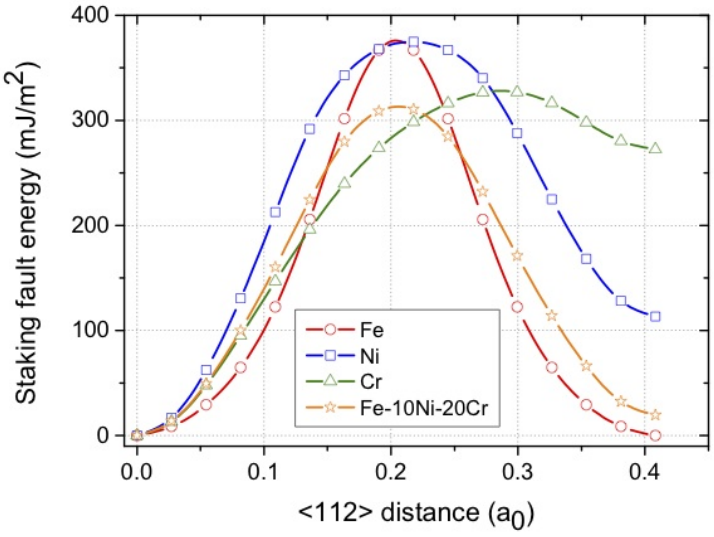

Figure 3.17: ⟨112⟩ gamma cut calculated for the pure elements and Fe-10Ni-20Cr using the second potential. This picture is taken from [10].

3.4.1 Energy Formalism

The atomic interactions were described using embedded atomic method (EAM). The total potential was written in the following form:

$$U = \frac{1}{2}\sum_{i\neq j=1}^{N} V_{ij}(R_{ij}) + \sum_{i=1}^{N}\left(\sum_{j=1}^{N}\phi_{ij}(R_{ij})\right)^{\frac{1}{2}}, \tag{3.21}$$

where the first term represents the pair potential and the second term is the embedding term.

The electron density ϕ was as follows:

$$\phi_{ij}(R_{ij}) = S\frac{\exp(-\beta R_{ij})}{R_{ij}}\frac{x^4}{1+x^4}, \tag{3.22}$$

where S is a normalisation factor, $x = (R_{ij} - r_{cut})/h$, with β and h are fitting parameters and r_{cut} the cut-off distance.

The pair potential was expressed by cubic spline as follows:

$$V(R_{ij}) = \sum_{k=1}^{m}[a_k(r_k - R_{ij})^3 H(r_k - R_{ij})] - K\phi(R_{ij}), \tag{3.23}$$

where a_k, r_k are constants, K is fitting parameter and H is the Heaviside function.
Finally the embedding function F is given by:

$$F(\rho) = A\sqrt{\rho} + B\rho + C\rho^2 + D\rho^4. \tag{3.24}$$

3.4.2 Pure potentials

Potential parameters: The parameters used to describe the pure elements interaction are shown in tables (3.29, 3.30 & 3.31).

k	r_k (Å)	a_k (eV/Å^3)		
1	2.5	2.660526	A = −8.66624513	r_{cut} = 4.0
2	2.8	3.56676207	B = 9.41375492	β = 2.0
3	3.1	−1.2729965	C = −3.23721354	h = 0.25
4	3.4	2.10027686	D = 0.348448677	S = 27.8689586
5	3.7	−0.901005963		K = 18.8275098
6	4.0	0.393902864		
7	2.4	12.0		
8	2.0	100.0		

Table 3.29: Parameters used to calculate the second potential in pure fcc Fe (The energy and distance units are eV and Å, respectively.)

k	r_k (Å)	a_k (eV/Å^3)		
1	2.5	−1.81393425	A = −7.86565625	r_{cut} = 5.6
2	2.84444444	4.30328923	B = 5.95107774	β = 2.0
3	3.18888889	−0.42569056	C = −1.11014159	h = 0.25
4	3.53333333	0.156449935	D = 0.050508392	S = 27.8750306
5	3.87777778	0.035027069		K = 11.9021555
6	4.22222222	0.14936637		
7	4.56666667	0.01083229		
8	4.91111111	−0.01969711		
9	5.25555556	−0.137669014		
10	5.6	0.085392233		
11	2.4	4.5		
12	2.0	100.0		

Table 3.30: Parameters used to calculate the second potential in fcc Ni (The energy and distance units are eV and Å, respectively).

k	r_k (Å)	a_k (eV/Å^3)		
1	2.5	1.73170402	A = −3.62580868	r_{cut} = 5.6
2	2.94285714	1.84143406	B = 2.26636149	β = 2.0
3	3.38571429	0.755016121	C = −0.265780601	h = 0.25
4	3.82857143	−0.468318806	D = 0.019526015	S = 31.2613817
5	4.27142857	−0.047416719		K = 4.53272297
6	4.71428571	0.461509957		
7	5.15714286	−0.410733637		
8	5.6	0.113373503		
9	2.0	100.0		

Table 3.31: Parameters used to calculate the second potential in fcc Cr (The energy and distance units are eV and Å, respectively).

Spline and ZBL Potential: The potential was fitted to a spline function and connected to ZBL potential to make sure it well represent the small atomic interactions. The cutoff distances used are 0.8 and 1.9 Å for all three potentials. Constants used for the spline functions are shown in table (3.32).

Constant	Fe-Fe	Ni-Ni	Cr-Cr
f_1	2.865484	6.413976	3.8586722
f_2	27.754621	12.240552	23.415331
f_3	−61.881241	−35.327644	−56.281745
f_4	55.292298	34.116415	53.126972
f_5	−22.743406	−15.046467	−23.253934
f_6	3.514520	2.482542	3.818025

Table 3.32: Parameters used to fit the spline for pure pair potentials given by the second potential. The f_k's are in units Å^{-k}.

3.4.3 Cross Potentials

The parameters used for the cross potentials are shown in table (3.33).

Interaction	Fe-Cr		Fe-Ni		Ni-Cr	
k	r_k(Å)	a_k(eV/Å^3)	r_k(Å)	a_k(eV/Å^3)	r_k(Å)	a_k(eV/Å^3)
1	2.0	62.3932019	2.0	62.4180774	2.0	71.465182
2	2.34285714	4.64949119	2.35714286	4.44273575	2.47857143	0.686470816
3	2.68571429	2.41093347	2.71428571	2.40263493	2.95714286	1.79996578
4	3.02857143	0.101143751	3.07142857	0.627280711	3.43571429	0.044759399
5	3.37142857	0.439673171	3.42857143	−1.15396215	3.91428571	−0.470971247
6	3.71428571	−0.239918132	3.78571429	1.31839561	4.39285714	0.585425288
7	4.05714286	0.218918034	4.14285714	−0.7078573	4.87142857	−0.41747426
8	4.4	−0.153852387	4.5	0.099942305	5.35	0.1020253

Table 3.33: Parameters used for cross pair potentials given by the second potential.

The cross potentials were connected to ZBL potential for the small ranges. Constants used for the spline function are shown in table (3.34).

Constant	Fe-Cr	Fe-Ni	Ni-Cr
f_1	17.039194	28.816586	27.496537
f_2	−42.138930	−100.632673	−94.124760
f_3	71.845339	186.740407	173.502155
f_4	−68.986269	−179.134983	−165.948002
f_5	33.407157	84.820325	78.450239
f_6	−6.461676	−15.829026	−14.647665

Table 3.34: Parameters used to fit the spline for cross pair potentials given by the second potential. The f_k's are in units Å^{-k}.

3.4.4 Results obtained using the second potential

Pure fcc Fe

The lattice parameter was found to be 3.5 Å . The formation energies for point defects in pure fcc Fe are shown in table (3.35).

Configuration	DFT (Klaver10) [15]	Second potential
Vacancy	1.95	1.94
⟨100⟩ dumbbell	3.63	3.60
Octahedral	4.353	3.86
⟨111⟩ dumbbell	4.559	4.61
Tetrahedral	4.322	4.58

Table 3.35: The formation energies (eV) in pure Fe using the second potential. The results show that the potential underestimates the formation energy of the octahedral point defect and overestimates the one of the tetrahedral point defect.

Similar to the first potential, the results showed that ⟨100⟩ dumbbell is the most stable interstitial defect. Furthermore, the results showed that the empirical potential underestimates the formation energy of octahedral and overestimates the one for the tetrahedral defect when compared to the ab-initio results.

The migration energies of a vacancy and ⟨100⟩ dumbbell in fcc Fe were calculated as shown in table (3.36). From these results, the potential was found to underestimate the migration energy of the vacancy. Furthermore, when the migration energies for ⟨100⟩ dumbbell were compared with the values obtained using the first potential, the second potential was found to produce lower values.

Transition	DFT(Olsson10) [65]	Second potential
Vacancy translation	1.05	0.63
Rotation of ⟨100⟩ dumbbell	x	0.32
Translation of ⟨100⟩ dumbbell	x	0.34
Translation & Rotation of ⟨100⟩ dumbbell	x	0.23

Table 3.36: The migration energies (eV) of vacancy and ⟨100⟩ dumbbell in pure Fe using the second potential.

Pure fcc Ni

Similar to the first potential, the lattice parameter was found to be 3.52 Å. The formation energies for point defects in pure fcc Ni are shown in table (3.37).

Configuration	Tucker2008 [14]	Second potential
Vacancy	1.43*	1.48
⟨100⟩ dumbbell	4.07	4.09
Octahedral	4.25	4.89
⟨111⟩ dumbbell	4.69	4.77
Tetrahedral	4.69	4.99

Table 3.37: The formation energies (eV) in pure Ni using the second potential (* The experimental values range from 1.45 to 1.8 eV).

The results obtained showed that the empirical potential overestimates the formation energy of octahedral and tetrahedral defect when compared to the ab-initio results.

The migration energies of a vacancy and ⟨100⟩ dumbbell in fcc Ni were calculated as shown in table (3.38).

Transition	DFT(Olsson10) [65]	Tucker 2008 [14]	Second potential
Vacancy translation	1.08	x	1.17
Rotation of ⟨100⟩ dumbbell	x	x	0.63
Translation of ⟨100⟩ dumbbell	x	x	0.81
Translation & Rotation of ⟨100⟩ dumbbell	x	0.14	0.33

Table 3.38: The migration energies (eV) of the vacancy and ⟨100⟩ dumbbell in pure Ni using the second potential.

Pure fcc Cr

The lattice parameter was found to be 3.584 Å. The formation energies for point defects in pure fcc Cr were calculated and compared to the values obtained using the first potential as shown in table (3.39).

Configuration	First potential	Second potential
Vacancy	2.85	2.06
⟨100⟩ dumbbell	4.11	5.11
Octahedral	5.46	5.72
⟨111⟩ dumbbell	4.54	5.41
Tetrahedral	4.65	5.57

Table 3.39: The formation energies (eV) of the vacancy and the point defects in pure Cr using the second potential.

The migration energies of a vacancy and ⟨100⟩ dumbbell in fcc Cr were calculated as shown in figure (3.40).

Transition	Second potential
Vacancy translation	1.43
Rotation of ⟨100⟩ dumbbell	0.51
Translation of ⟨100⟩ dumbbell	0.60
Translation & Rotation of ⟨100⟩ dumbbell	0.28

Table 3.40: The migration energies (eV) of the vacancy and ⟨100⟩ dumbbell in pure Cr using the second potential.

Monte Carlo Simulations

Two systems, ternary and binary were created randomly in a lattice of 2048 atoms. The two systems were evolved using Monte Carlo Simulations at 600 K. A total of 500,000 MC steps have been performed.
Slight segregation was observed in the binary system as shown in figure (3.18).

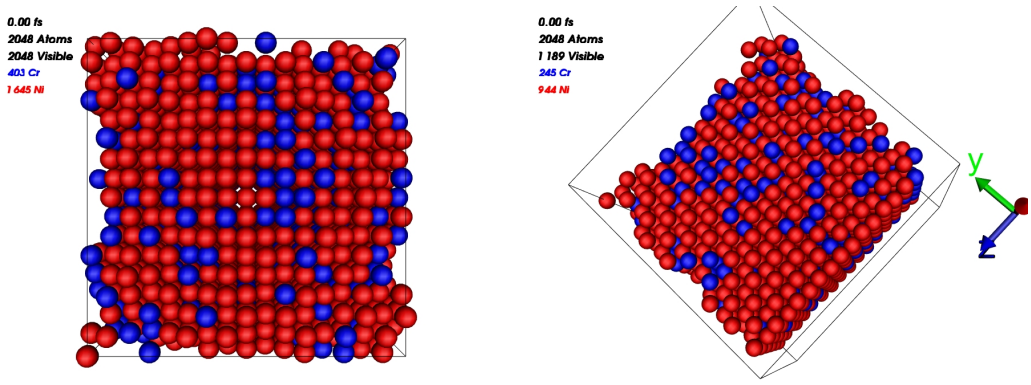

Figure 3.18: The segregation obtained in the binary system using the second potential.

The ternary system: The Ni and Cr atoms were found to segregate into planes in the Fe matrix as shown in figure (3.19).

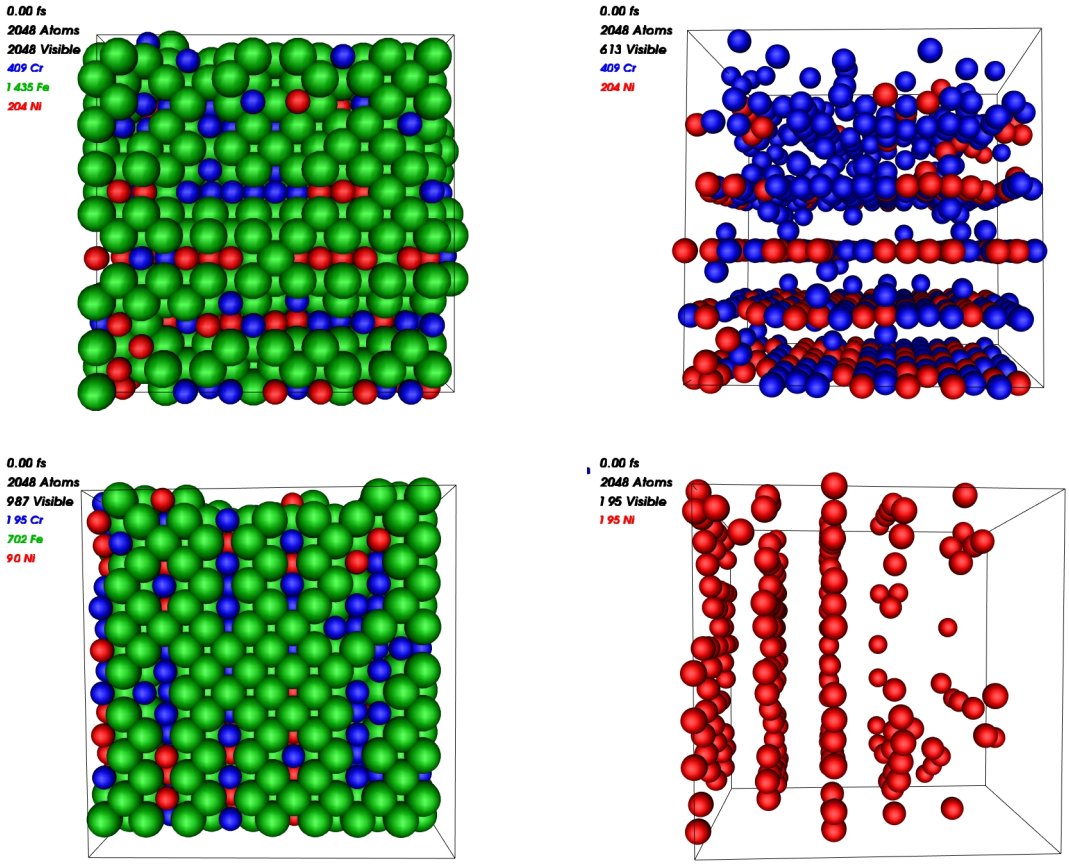

Figure 3.19: The segregation obtained in the ternary system using the second potential. The figure shows that Ni and Cr atoms segregate into planes in the Fe matrix.

An investigation was undertaken to see the forces behind the segregation of Ni and Cr atoms into planes after MC simulation using the second potential. At first, we needed to see which material is mainly responsible for this kind of segregation. Therefore, different systems were created with different concentrations and were fed to MC simulation at 500 K to see if we will get the same kind of segregation. The following are the percentages of the systems chosen: 90 %Fe 10%Ni, 70%Fe 30%Ni, 90%Fe 10%Cr, 70%Fe 30%Cr, 70%Fe 10%Ni 20%Cr and 70%Fe 20%Ni 10%Cr. Pictures of the Ni and Cr atoms in the systems after MC simulation are shown in figure (3.20).

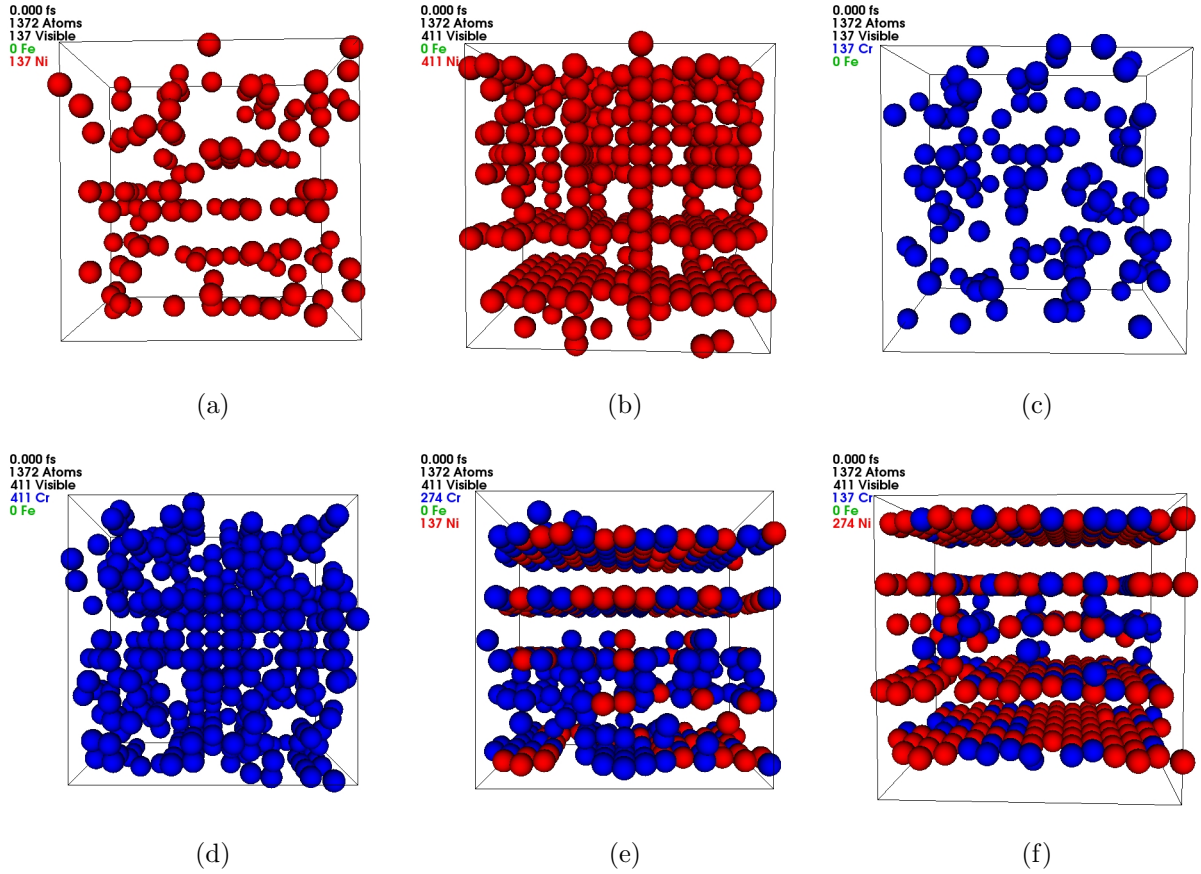

Figure 3.20: Investigation of the planes formed after the MC simulation using the second potential, (a) shows system of 90%Fe 10%Ni, (b) shows a system of 70%Fe 30%Ni, (c) shows a system of 90%Fe 10%Cr, (d) shows a system of 70%Fe 30%Cr, (e) shows a system of 70%Fe 20%Cr 10%Ni and (e) shows a system of 70%Fe 10%Cr 20%Ni.

From pictures above we could see that presence of Ni is a necessity for formation of the planes after MC simulation using the second potential. Another attempt to understand this was to try to see whether this is going to really happen. This was done by taking three systems and creating a simple defect in them and feeding them to long time scale dynamics.

Three systems were created for the KMC run, 90%Fe 10%Ni, 70%Fe 30%Ni and 70%Fe 20%Cr 10%Ni. Small number of vacancies were created in each system to initialise the simulations and allowing atoms to move. It was not clear that the systems segregate into planes. Pictures of the systems after KMC are shown in figure (3.21).

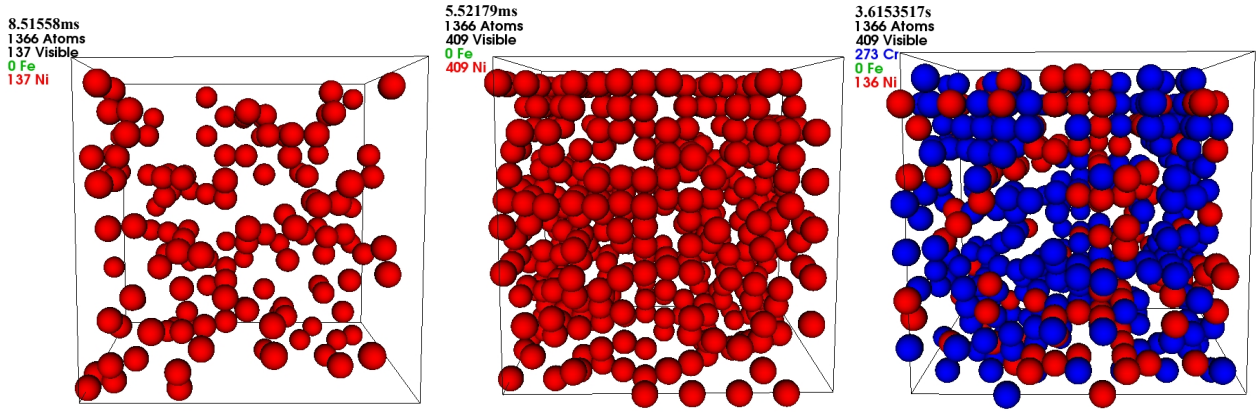

(a) (b) (c)

Figure 3.21: Investigation on the atom arrangements formed after MC simulation using the second potential, the figures show the final systems obtained from otf-KMC simulation after initialisation of the simulation by creating few vacancies in the system, (a) shows system of 90%Fe 10%Ni, (b) shows a system of 70%Fe 30%Ni and (c) shows a system of 70%Fe 20%Cr 10%Ni. From the results obtained, it was not clear that planes were formed in the systems.

High Temperature Molecular Dynamics

Two systems were studied, the binary and the ternary system. Both systems were fed to MD simulation at high temperatures. Different temperatures were tried, however, no change was observed for both systems at any temperature. Pictures for both systems at 1400 K are shown in figure (3.22).

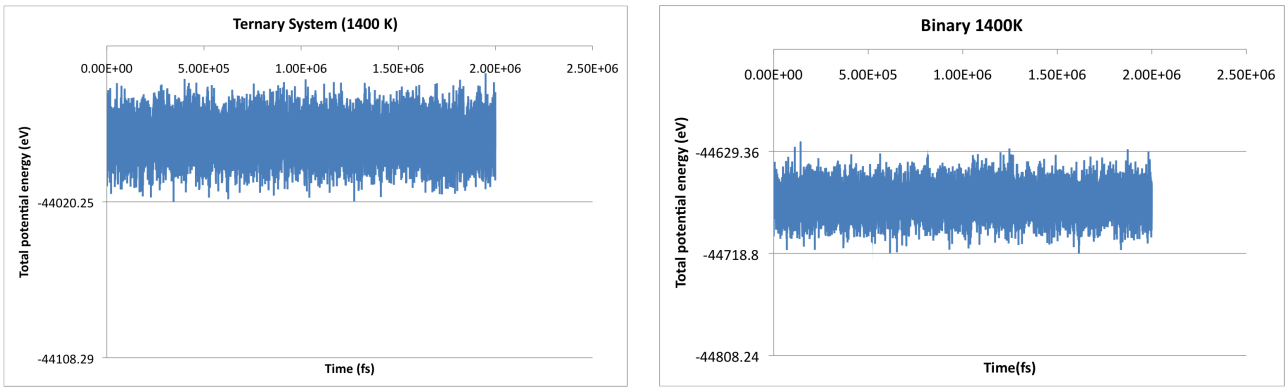

Figure 3.22: High temperature MD in the ternary and the binary systems using the second potential.

3.4.5 Difficulties

The main aim from the project was to use this potential to study the migration barriers. One main difficulty with the second potential was that it did not reproduce the target migration energies very well. The potential was found to underestimate the diffusion barrier for a vacancy in fcc Fe. It was also found to underestimate the formation energies for octahedral in fcc Fe and overestimate tetrahedral and octahedral formation energies in fcc Ni.
When Monte Carlo simulation were performed on the Fe-Ni-Cr ternary alloy, the Ni and Cr were found to segregate into planes in the Fe matrix.

3.5 Third potential

A third potential was written by G. Bonny on February 2012 [73]. The potential was implemented and tested. Here we discuss the energy formalism and some of the results obtained using the potential.

3.5.1 Energy model

G. Bonny used EAM [45] to describe atomic interaction for this potential, so the total potential was represented as follows:

$$U = \frac{1}{2} \sum_{i \neq j=1}^{N} V_{ij}(R_{ij}) + \sum_{i=1}^{N} F_i(\rho_i), \tag{3.25}$$

where V is the pair potential, F is the embedding energy, ρ is the local electron density, N is the total number of atoms in the system, R_{ij} is the distance between atoms i and j. The electron density was represented as follows:

$$\rho_i = \sum_{j=1}^{N} \phi_{ij}(R_{ij}), \tag{3.26}$$

where ϕ is the electron density.
For this potential both the pair potential and the electron density function were constructed depending on three parts:

1. Equilibrium part dominated by electron bonding.
2. Short-range part dominated by electron repulsion.
3. An intermediate part connecting the first two parts (up to the second derivative).

The pair potential

The pair potential was expressed as follows using the same notation as previously used:

$$\begin{aligned} V(R_{ij}) &= H(R_{ij}-R_o)V_{eq}(R_{ij}) \\ &\quad +H(R_o-R_{ij})H(R_{ij}-R_i)\left\{V_{eq}(R_{ij})+\zeta\left(\frac{R_o+R_i-2R_{ij}}{R_o-R_i}\right)[V_{nucl}(R_{ij})-V_{eq}(R_{ij})]\right\} \\ &\quad +H(R_i-R_{ij})V_{nucl}(R_{ij}), \end{aligned} \tag{3.27}$$

$$V_{eq}(R_{ij}) = \sum_{k=1}^{N}[a_k(r_k-R_i)^3H(r_k-R_i)], \tag{3.28}$$

$$V_{nucl}(R_{ij}) = \frac{Z_1Z_2}{R_{ij}}\xi(R_{ij}/r_s), \tag{3.29}$$

where a_k, r_k, R_o and R_i are constants, H is the Heaviside function, Z_1 and Z_2 are the nuclear charges and,

$$r_s = \frac{0.4683766}{Z_1^{2/3}+Z_2^{2/3}}, \tag{3.30}$$

$$\zeta(x) = \frac{3}{16}x^5 - \frac{5}{8}x^3 + \frac{15}{16}x + \frac{1}{2}, \tag{3.31}$$

$$\begin{aligned} \xi(x) &= 0.1818\exp(-3.2x) + 0.5099\exp(-0.9423x) \\ &\quad +0.2802\exp(-0.4029) + 0.02817\exp(-0.2016). \end{aligned} \tag{3.32}$$

The density function

The density function was expressed as follows:

$$\begin{aligned}\phi_{ij}(R_{ij}) &= H(R_{ij}-R_o)\phi_{eq}(R_{ij}) \\ &+H(R_o-R_{ij})H(R_{ij}-R_i)\left\{\phi_{eq}(R_{ij})+\zeta\left(\frac{R_o+R_i-2R_{ij}}{R_o-R_i}\right)[\phi_o-\phi_{eq}(R_{ij})]\right\} \\ &+H(R_i-R_{ij})\phi_0, \end{aligned} \tag{3.33}$$

$$\phi_{eq}(R_{ij}) = C_0(R_0-R_{ij})^3H(R_0-R_{ij}), \tag{3.34}$$

where R_0 is the cut-off knot and C_0 is a fitting parameter.

The embedding function

The embedding function F was represented as follows:

$$F(\rho) = A\sqrt{\rho}+B\rho+C\rho^2+D\rho^4, \tag{3.35}$$

with A, B, C and D are constants.

3.5.2 Pure potentials

Pure fcc Fe

The parameters used to describe the pure elements interactions are shown in tables (3.41, 3.42 & 3.43).

k	r_k (Å)	a_k (eV/Å^3)		
1	2.50000000	15.7082332	A = −4.910388708	$R_i = 1.1$
2	2.76666667	−3.3559449	B = 2.573114483	$R_o = 2.1$
3	3.03333333	5.44180488	C = −0.05896006463	$\phi_0 = 0.558068279$
4	3.30000000	−3.82205447	D = 0.000000000	$C_0 = 0.0206691955$
5	3.56666667	0.52537765		$R_0 = 4.1$
6	3.83333333	1.56978695		
7	4.10000000	−0.840429709		

Table 3.41: Parameters used to calculate the third potential in fcc Fe.

k	r_k (Å)	a_k (eV/Å^3)		
1	2.50000000	8.68106199	A = −6.065576796	$R_i = 1.1$
2	2.94666667	1.10624906	B =3.032788397	$R_o = 2.1$
3	3.39333333	0.00871069308	C = 0.000000000	$\phi_0 = 0.245737969$
4	3.84000000	−0.18038451	D = 0.000000000	$C_0 = 0.00361819338$
5	4.28666667	0.017361504		$R_0 = 5.18$
6	4.73333333	0.127531375		
7	5.18000000	−0.0684284037		

Table 3.42: Parameters used to calculate the third potential in fcc Ni.

k	r_k (Å)	a_k (eV/Å^3)		
1	0.80000000	20000	A = −5.902094585	$R_i = 0.3$
2	2.20000000	−1030	B =5.621095277	$R_o = 0.8$
3	2.25000000	1000	C = −1.89096779	$\phi_0 = 0.450968351$
4	2.50000000	3.12852453	D = 0.277971903	$C_0 = 0.00407776648$
5	2.93333333	0.427388187		$R_0 = 5.10$
6	3.36666667	0.0895592353		
7	3.80000000	0.544690445		
8	4.23333333	−0.571035515		
9	4.66666667	0.307710921		
10	5.10000000	−0.0972495128		

Table 3.43: Parameters used to calculate the third potential in fcc Cr.

3.5.3 Cross Potentials

The parameters used for the cross potential are shown in table (3.44).

Interaction	Fe-Cr		Fe-Ni		Ni-Cr	
k	r_k(Å)	a_k(eV/Å^3)	r_k(Å)	a_k(eV/Å^3)	r_k(Å)	a_k(eV/Å^3)
1	2.30000000	−50.0000000	2.00000000	40.000000	1.80000000	180.00000
2	2.50000000	30.0000000	2.15000000	−200.00000	2.10000000	−180.00000
3	2.61428571	8.23435097	2.24285714	154.808471	2.28000000	142.394996
4	2.98571429	−0.280740148	2.50000000	−5.3000000	2.40000000	−38.000000
5	3.35714286	−0.995297604	2.61428571	6.88117151	2.50000000	11.000000
6	3.72857143	1.30667939	2.98571429	1.1413194	2.54000000	1.20715276
7	4.10000000	−0.485688767	3.35714286	−1.79052163	2.80000000	−1.7907013
8			3.72857143	1.55690129	3.06000000	2.23129554
9			4.10000000	−0.524193207	3.32000000	0.3375609
10					3.58000000	−2.55371442
11					3.84000000	2.73113015
12					4.10000000	−0.987225106

Table 3.44: Parameters used for cross pair potentials given by the third potential (The energy and distance units are eV and Å, respectively).

3.5.4 Results obtained using the third potential

Lattice constants, formation and binding energies

Lattice constants for the pure elements were calculated using the third potential for both fcc and bcc structures and compared versus the target values as shown in table (3.45). The formation energies of point defects were also calculated and compared against the target values as shown in table (3.45). From the results obtained, the potential was found to reproduce well the vacancy formation energies, however, it was found to overestimate the formation energies of the other point defects in both fcc Fe and Ni.

Property	Iron		Nickel		Chromium	
	Target	Potential	Target	Potential	Target	Potential
E_{coh} (fcc) (eV/at.)	-	4.40	4.45	4.45	-	4.2
E_{coh} (bcc) (eV/at.)	4.28	4.28	4.35	4.35	4.10	4.10
a (fcc) (Å)	3.450 - 3.562	3.562	3.519	3.522	3.520 - 3.610	3.534
a (bcc) (Å)	2.832 - 2.860	2.860	2.801	2.800	2.878 - 2.885	2.882
E_f(Vac) (eV)	1.82 - 1.95	1.87	1.37 - 1.45	1.39	2.14	2.19
E_f($\langle 100 \rangle$ SIA)(eV)	3.20 - 3.62	5.23	4.07 - 4.11	5.86	-	4.86
E_f($\langle 111 \rangle$ SIA)(eV)	4.56	6.54	4.69 - 4.72	7.04	-	5.46
E_f(Octa SIA)(eV)	4.35	5.64	4.25 - 4.32	6.18	-	5.01
E_f(Tetra SIA)(eV)	3.66 - 4.32	7.04	4.69 - 4.71	7.19	-	5.40

Table 3.45: Properties of the pure elements using the third potential.

The solute-solute and vacancy-solute binding energies were calculated using the third potential. The results obtained were compared to the available DFT values as shown in table (3.46). Similarly, the solute-interstitial binding energies were calculated and compared to DFT as shown in table (3.47). Most of these values were found to be in very good agreement with the DFT values. However the potential was found to overestimate some of these values such as Fe-Ni and Ni-Ni $\langle 100 \rangle$ dumbbells in Fe matrix and underestimate some of them such as 2nn Vac-Vac binding energy in Ni matrix.

Configuration	Binding energy (eV)			
	DFT		Potential	
	1nn	2nn	1nn	2nn
fcc Ni matrix				
Vac-Vac	0.02	0.12	0.12	0.04
Fe-Vac	−0.02	−0.01	−0.11	0.00
Cr-Vac	−0.05	0.01	−0.05	0.01
Fe-Fe	−0.11	0.02	−0.09	0.02
Cr-Cr	0.04 - 0.11	0.11	0.10	0.01
Fe-Cr	−0.16	0.01	−0.07	−0.03
fcc Fe matrix				
Vac-Vac	0.04 - 0.18	−0.06 - 0.07	0.25	0.04
Ni-Vac	0.02 - 0.09	−0.01 - 0.01	0.02	0.01
Cr-Vac	−0.09 - 0.00	−0.08 - 0.00	0.06	0.01
Ni-Ni	−0.01 - 0.11	−0.01 - 0.07	−0.08	0.04
Cr-Cr	−0.10 - (−0.01)	−0.01 - 0.02	0.13	0.06
Ni-Cr	−0.01 - 0.05	−0.03 - (−0.01)	−0.01	0.02

Table 3.46: Comparison of solute-solute and vacancy-solute binding energies (eV) between DFT and the third potential.

⟨100⟩ Dumbbell	Binding energy (eV)	
	DFT	Potential
fcc Ni matrix		
Ni-Fe	−0.05 - (−0.06)	−0.06
Ni-Cr	0.45 - 0.53	0.52
Fe-Fe	−0.48	−0.51
Cr-Cr	0.93	0.89
Cr-Fe	NA	−0.34
fcc Fe matrix		
Fe-Ni	−0.41 - 0.07	0.54
Fe-Cr	−0.01 - 0.28	−0.05
Ni-Ni	−0.76 - (−0.08)	0.62
Cr-Cr	−0.31 - 0.20	−0.74
Ni-Cr	−0.19 - 0.39	0.55

Table 3.47: Comparison of solute-interstitial binding energies (eV) between DFT and the third potential.

Migration Barriers (pure materials)

Vacancy migration energies: The vacancy migration barriers for the pure materials were calculated. Comparison for the values obtained versus DFT values are shown in table (3.48).

Migration barrier	DFT	Potential
fcc Ni matrix		
Vac → Fe	0.97	1.03
Vac → Ni	1.09	1.09
Vac → Cr	0.83	0.76
fcc Fe matrix		
Vac → Fe	0.62	0.64
Vac → Ni	0.89	0.79
Vac → Cr	0.65	0.68
fcc Cr matrix		
Vac → Fe		
Vac → Ni		
Vac → Cr		0.84

Table 3.48: Comparison of the vacancy migration energy between DFT and the third potential, all values in eV.

⟨100⟩ **Dumbbell migration energies:** The migration barriers for ⟨100⟩ dumbbell were calculated, three main transitions were found for the ⟨100⟩ dumbbell, rotation, translation and both rotation and translation. The values obtained are shown in table (3.49).

Transition	Rotation	Translation	Rotation and translation
fcc Fe matrix	0.85	0.42	0.26
fcc Ni matrix	0.60	0.32	0.176
fcc Cr matrix	0.56	0.11	0.05

Table 3.49: ⟨100⟩ Dumbbell migration energies using the third potential, all values in eV.

Migration barriers (ternary and binary alloy)

Vacancy migration energy: The ternary and the binary system were created randomly and used to calculate the vacancy migration barriers. Figure (3.23) shows the vacancy migration barriers in the ternary alloy and figure (3.24) shows the vacancy migration energies in the binary alloy.

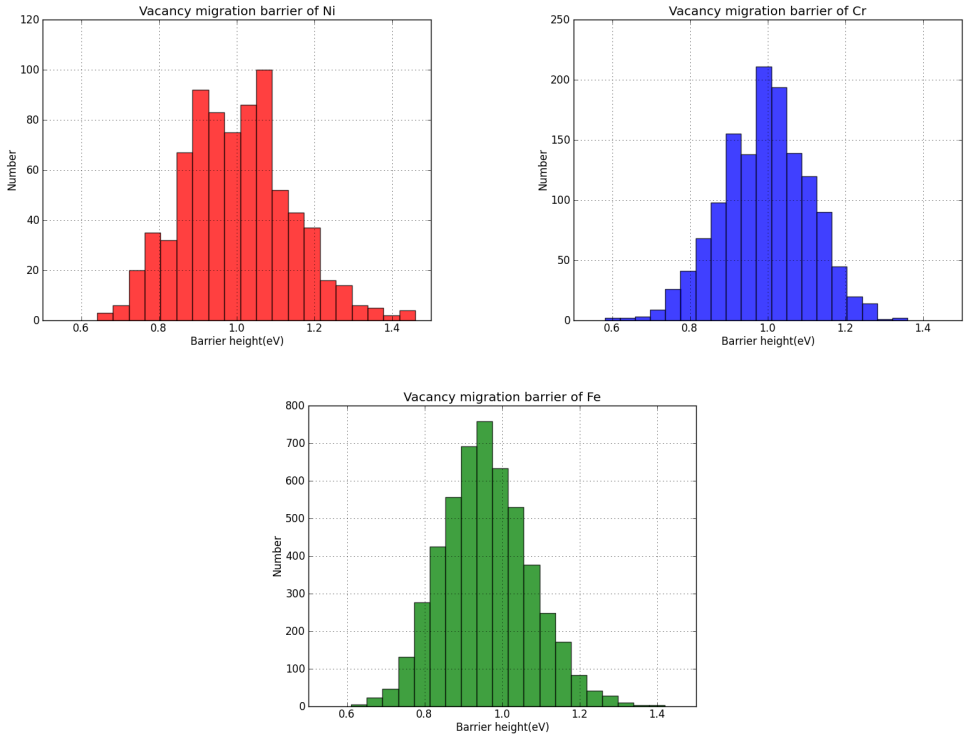

Figure 3.23: Vacancy migration barriers in the ternary alloy using the third potential. Each histogram represent the energy barriers of one type of atoms, red for Ni, green for Fe and blue for Cr.

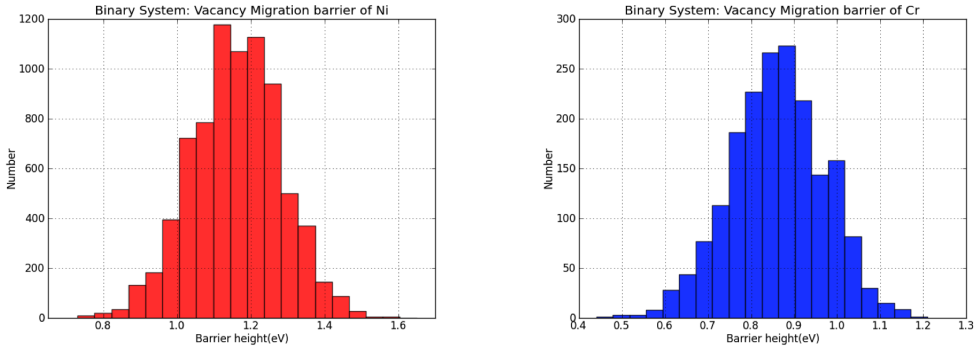

Figure 3.24: Vacancy migration barriers in the binary system using the third potential.

Monte Carlo Simulation

From the MC simulation, the Cr was found to segregate from the Fe matrix in the ternary and from the Ni matrix in the binary system. Pictures of the ternary and the binary systems after MC simulation are shown in figure (3.25).

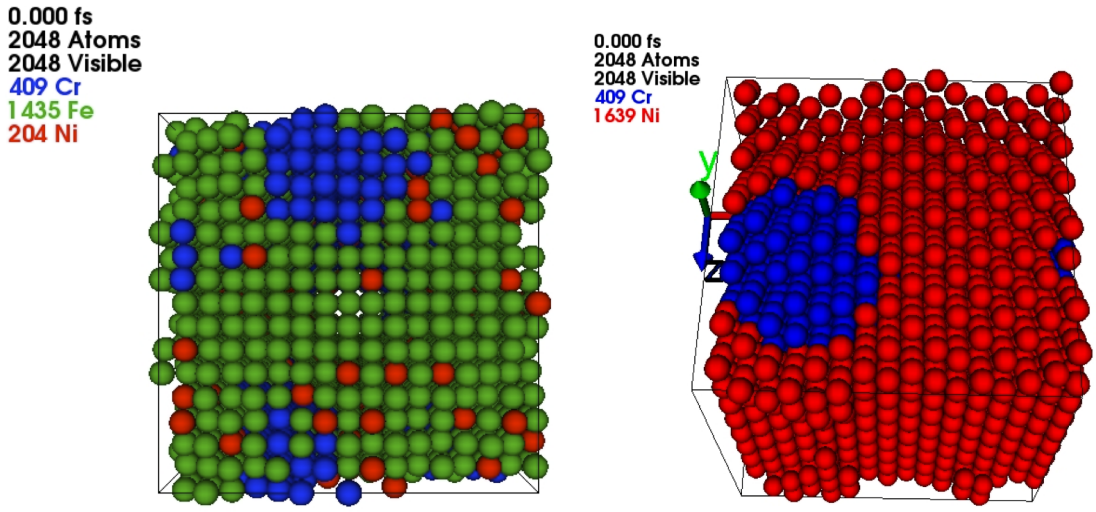

(a) The ternary system (b) The binary system

Figure 3.25: Systems after MC simulation using the third potential, (a) shows the segregation in the ternary alloy which shows Cr segregating from the Fe matrix and (b) shows the segregation in the binary alloy where Cr segregates from the Ni matrix.

Fitting formation and migration energies of Fe vacancy and Fe-Fe ⟨100⟩ dumbbell in Ternary alloy as a function of local environment

Following the work done by Piochaud [5] on fitting the Fe vacancy and ⟨100⟩ dumbbell formation energies in ternary system (70 at.% Fe, 10 at.% Ni and 20 at.% Cr) as a function of Ni and Cr neighbouring atoms using formation energies from DFT calculations, we tried to fit the formation energies calculated using the third potential [73] as a function of the local environment.

For the Fe vacancy formation energies, a good correlation was obtained as a function of the first nearest neighbours. However, poor correlation obtained for the Fe-Fe ⟨100⟩ dumbbell formation energies even with including the second nearest neighbours.

Furthermore, fitting the migration energies of the Fe vacancy in the ternary system has been tried. Climbing Image Nudged Elastic Band (CI-NEB)[61] has been used to calculate the migration energy barriers using 11 images. At first, fitting the migration energies to the local environment has been tried considering the local environment at the initial and the final states. This, however, did not give very good correlation. Therefore, an attempt of including the local environment at the saddle point has been taken which gave better correlation.

The main aim from this part is to discuss the results obtained from fitting the formation

and migration energies to the local environment in the ternary alloy and to compare them with the available data from DFT. This part will discuss the following points:

- Fe vacancy formation energies.
- ⟨100⟩ dumbbell formation energies.
- Fe vacancy migration energies.

Fe vacancy formation energies: Giovanni's potential [73] has been used to calculate the formation energies of Fe vacancies in the ternary system. To directly compare to the values available from the DFT calculations, the same configurations used by Piochaud [5] have been used here. The reference system used contains 256 atoms with 70 at.% Fe, 10 at.% Ni and 20 at.% Cr. An Fe atom has been removed to create the defective system with a total of 60 defective systems used in the fitting. Periodic boundary conditions have been implemented in all directions and the conjugate gradient method used for relaxation. The formation energies have been calculated using the following equation:

$$E_{\text{formation}}^{(\text{Fe})\text{vacancy}} = E_{\text{defective}} - (E_{\text{perfect}} - E_{1\text{Fe}}) \tag{3.36}$$

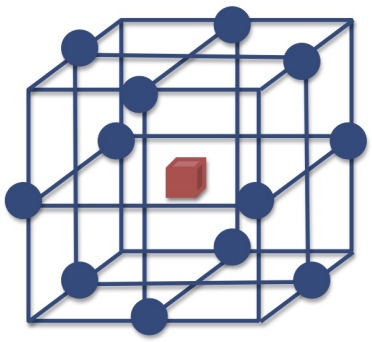

The Fe vacancy formation energies were calculated and compared to the values obtained from DFT results as shown in figure (3.26). From the figure it can be seen that there was no correlation between the formation energies obtained using the potential and the corresponding DFT values. Also, the potential was found to underestimate the Fe vacancy formation energies in the ternary alloy when compared to the value obtained using DFT.

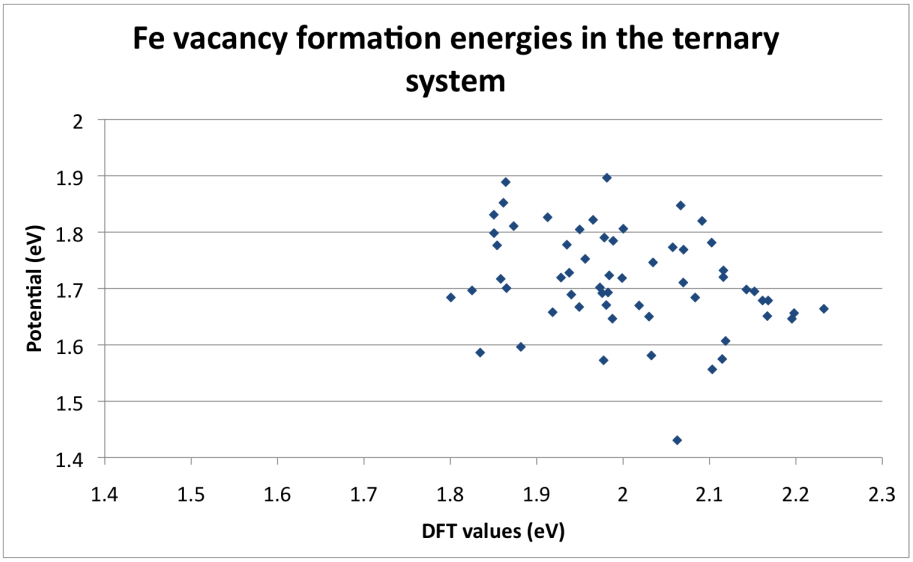

Figure 3.26: Comparison between the values of Fe vacancy formation energies obtained using the third potential and the associated values from DFT.

The formation energies for Fe vacancies in the ternary system obtained from the potential have been used to study the effect of local environment on changing the formation energies. Figures (3.27 & 3.28) show the effect of increasing the number of Cr and Ni atoms on changing the formation energies.

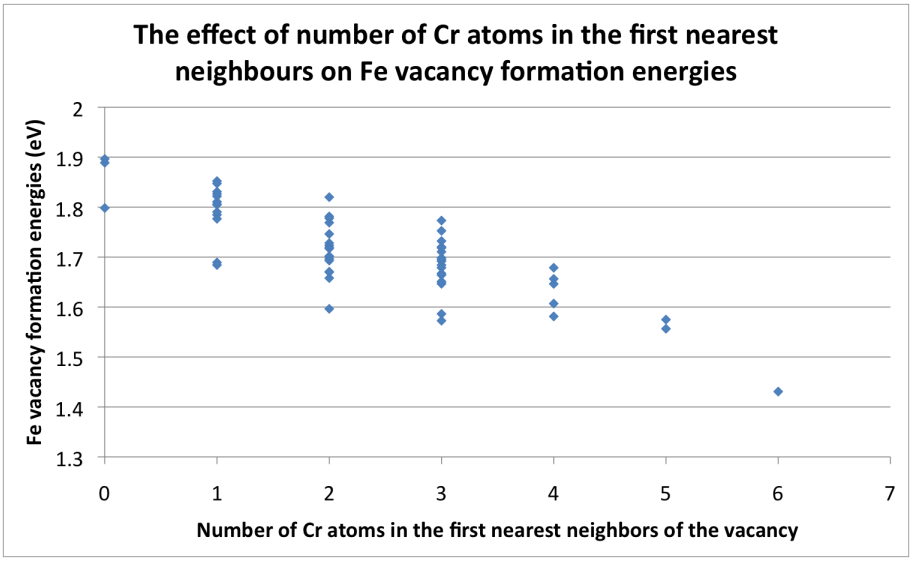

Figure 3.27: Effect of increasing the number of Cr atoms in the first nearest neighbours on the values of Fe vacancy formation energies.

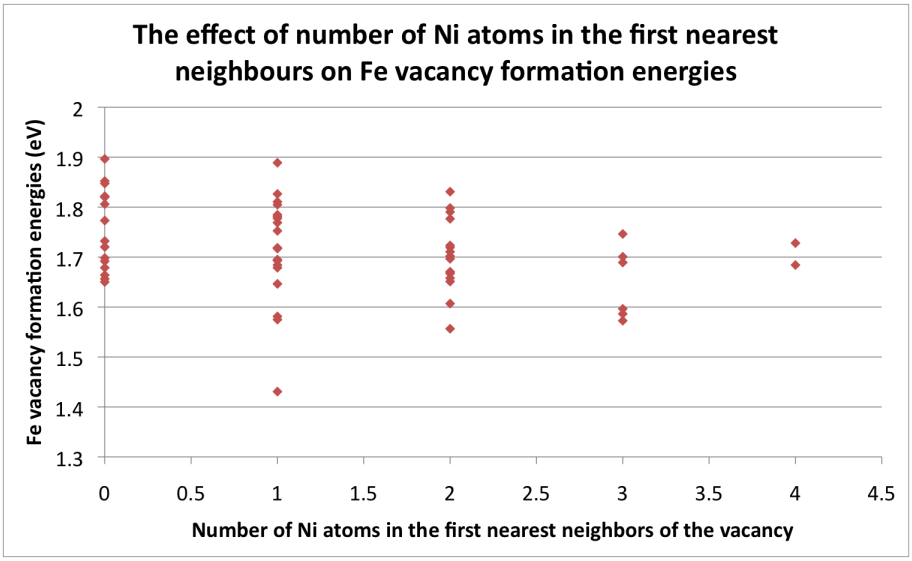

Figure 3.28: Effect of increasing the number of Ni atoms in the first nearest neighbours on the values of Fe vacancy formation energies.

A very good correlation (R) of 0.91 obtained from considering the numbers of first nearest neighbours Ni and Cr atoms. The equation obtained was as follows:

$$E_{\text{formation}}^{(\text{Fe})\text{vacancy}} = -0.06 \times Cr_{1nn} - 0.03 \times Ni_{1nn} + 1.90 \tag{3.37}$$

The formation energies obtained using the equation versus the values calculated using the potential are shown in figure (3.29).

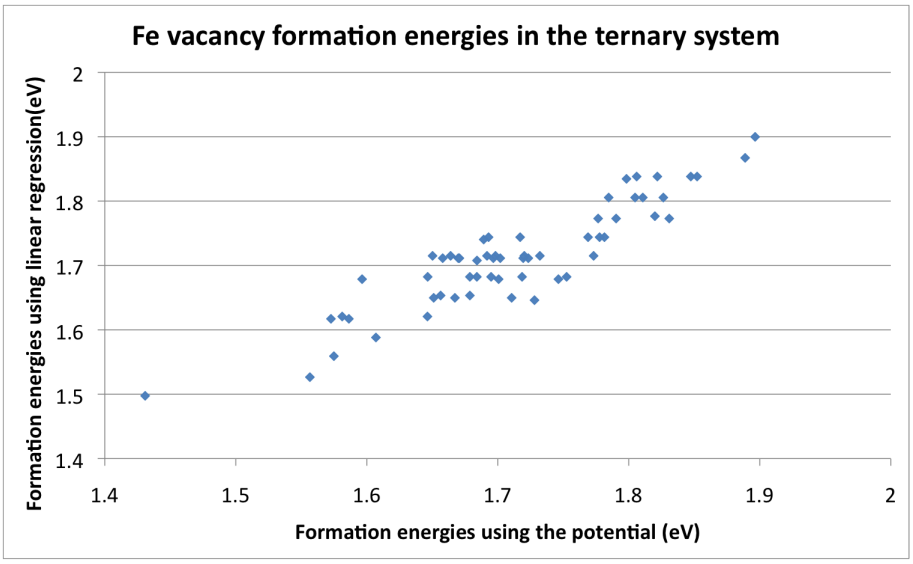

Figure 3.29: The Fe vacancy formation energies calculated using the equation versus the values obtained from the potential.

The Fe vacancy formation energies were fitted for larger number of configurations (216). The equation obtained is found to be similar to the one obtained using the 60 systems with the same correlation. The equation obtained was :

$$E_{\text{formation}}^{(\text{Fe})\text{vacancy}} = -0.06 \times Cr_{1nn} - 0.03 \times Ni_{1nn} + 1.89 \tag{3.38}$$

The values obtained using the above equation versus the values from the potential are shown in figure (3.30).

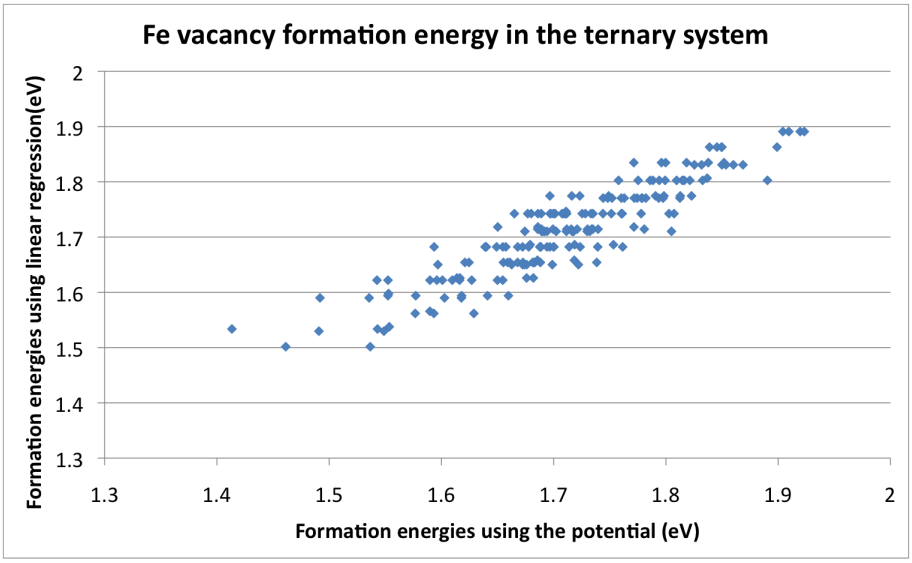

Figure 3.30: The Fe vacancy formation energies calculated using the equation versus the values obtained using the third potential.

The model obtained for Fe vacancy formation energy using DFT [5] was as follows:

$$E_{\text{formation}}^{(\text{Fe})\text{vacancy}} = 0.05 \times Cr_{1nn} - 0.04 \times Ni_{1nn} + 2.0 \tag{3.39}$$

Comparing the two models we can see that increasing the number of Cr atoms in the first nearest neighbours to the vacancy will increase its formation energy using the DFT model and will decrease it using the potential model. Similar effect is found when increasing Ni atoms in the first nearest neighbours for both models with it slightly less in the potential model.

Fe-Fe $\langle 100 \rangle$ dumbbell formation energies: Similar to the vacancy formation energies, Giovanni's potential [73] has been used to calculate the formation energies of $\langle 100 \rangle$ dumbbell using the configurations used by Piochaud [5]. The reference system used is the same as the one used for the vacancies and the defective system is created by adding an Fe atom. The configurations used are a total of 100 with 60 of them [100] dumbbells and 40 [010] dumbbells. The equation used to calculate the formation energy is:

$$E_{\text{formation}}^{(\text{Fe-Fe})\langle 100 \rangle \text{dumbbell}} = E_{\text{defective}} - (E_{\text{perfect}} + E_{1\text{Fe}}) \tag{3.40}$$

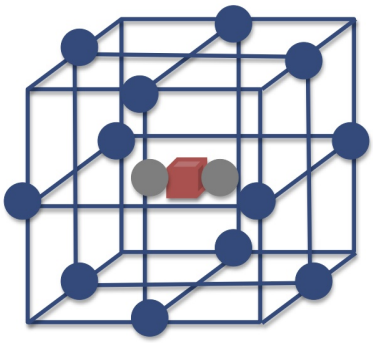

The Fe-Fe ⟨100⟩ dumbbell formation energies were calculated using the potential and compared to the DFT values. The formation energies from the empirical potential are found to be considerably higher than the DFT values as shown in figure (3.31). Also, it can be seen from the figure that there is no correlation between the formation energies obtained with the potential and the corresponding DFT values.

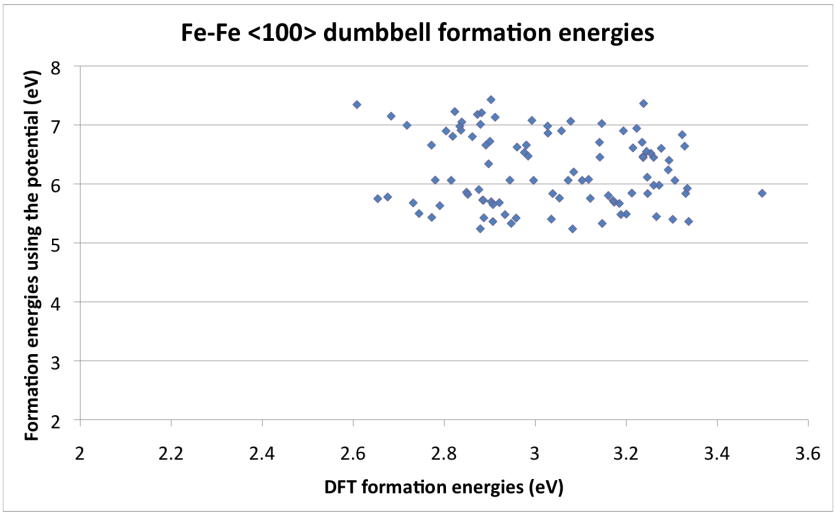

Figure 3.31: Comparison between the values of ⟨100⟩ dumbbell formation energies obtained using the potential and the associated values from DFT.

Similar to Piochaud [5], the first nearest neighbours are divided to two types, the compressive atoms which considered to be under compression and the tensile atoms which are under tension. There will be always 4 tensile atoms and 8 compressive atoms in the first nearest neighbours as shown in the following picture.

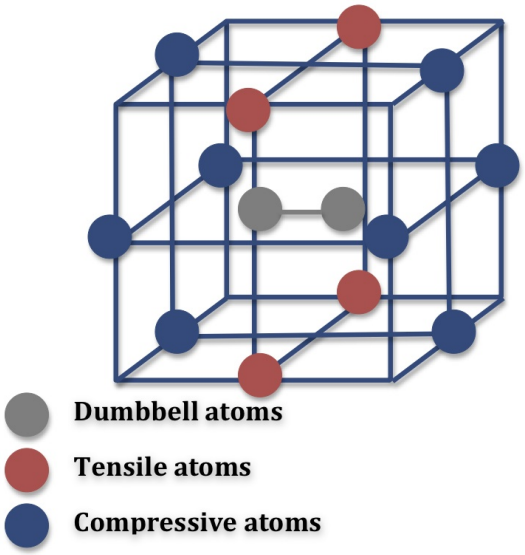

Figure 3.32: Illustration of the atoms at first nearest neighbour separation to a dumbbell defect. The blue atoms represent the compressive atoms, red atoms are tensile atoms and grey atoms are the dumbbell atoms.

The formation energies for Fe-Fe dumbbells in the ternary system obtained from the potential have been used to study the effect of local environment on changing the formation energies. Figures (3.33 & 3.34) show the effect of increasing the number of Cr and Ni atoms on changing the formation energies.

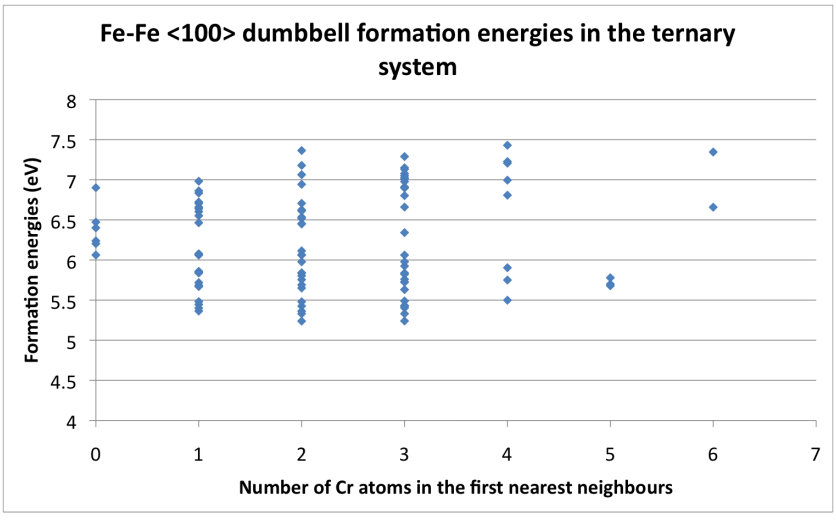

Figure 3.33: Effect of increasing the number of Cr atoms in the first nearest neighbours on the values of Fe-Fe dumbbell formation energies.

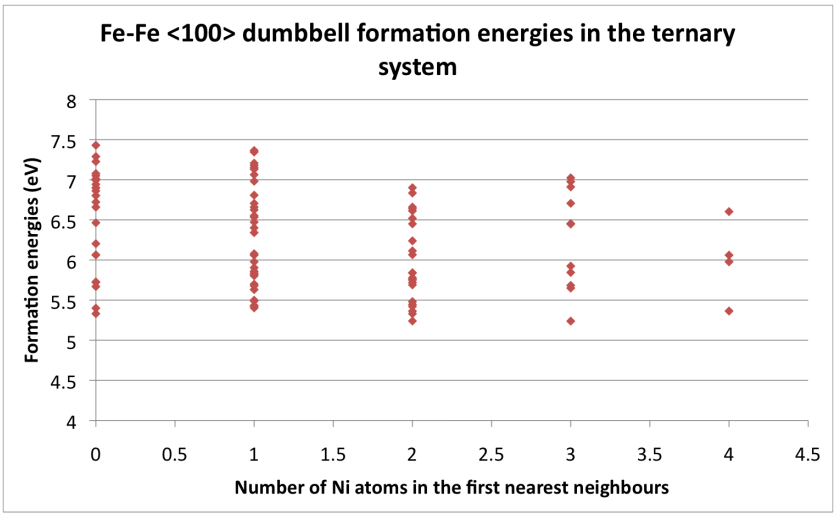

Figure 3.34: Effect of increasing the number of Ni atoms in the first nearest neighbours on the values of Fe-Fe dumbbell formation energies.

Different variables were tried to fit the dumbbell's formation energies as shown in figures (3.35, 3.36 & 3.37), however, none of them gave good correlation.

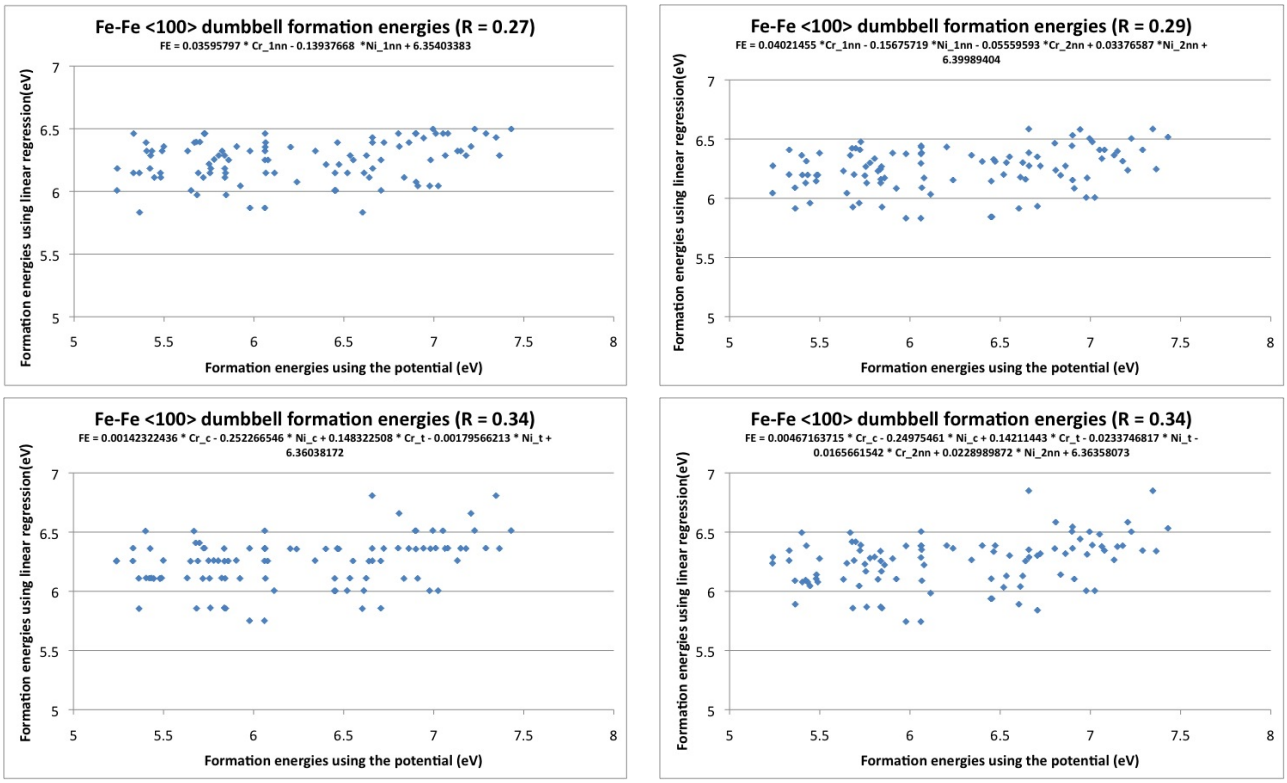

Figure 3.35: Illustration of the attempts to fit the ⟨100⟩ dumbbell formation energies. The top left figure shows the correlation obtained when trying to fit the ⟨100⟩ dumbbell formation energies to the number of Cr and Ni atoms in the first nearest neighbour, where R was found equal to 0.27. In the bottom left figure, the formation energies were fitted to the first nearest neighbours also, however, those were distinguished as tensile and compressive atoms. The top right figure shows that a correlation of 0.29 obtained when including the number of Ni and Cr atoms in the first and second nearest neighbours in the calculations. The bottom right figure shows the correlation obtained when including tensile and compressive atoms in the first nearest neighbours and also the atoms in the second nearest neighbours.

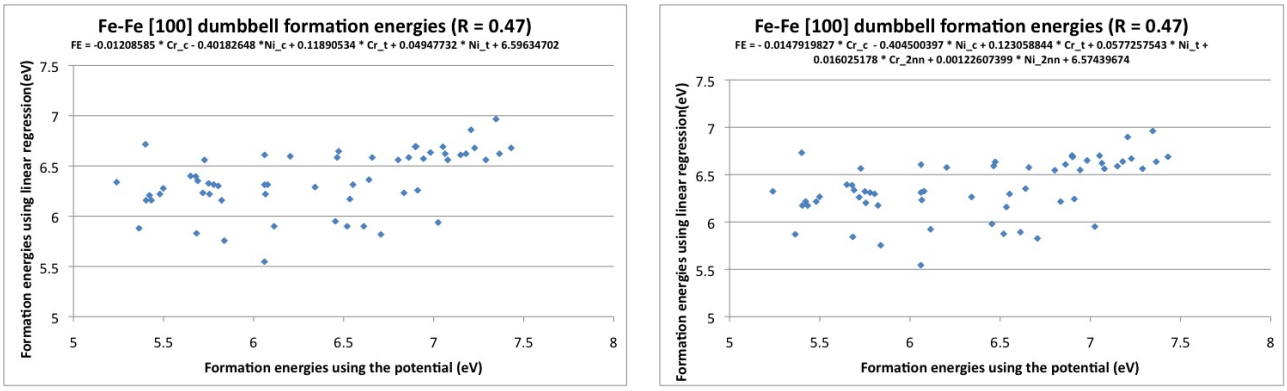

Figure 3.36: Illustration of the attempts to fit the [100] dumbbell formation energies. The left figure shows the correlation obtained when trying to fit the [100] dumbbell formation energies to the number of compressive and tensile Cr and Ni atoms in the first nearest neighbours. The right figure shows the correlation obtained when including the number of Cr and Ni atoms in the second nearest neighbours in the calculations.

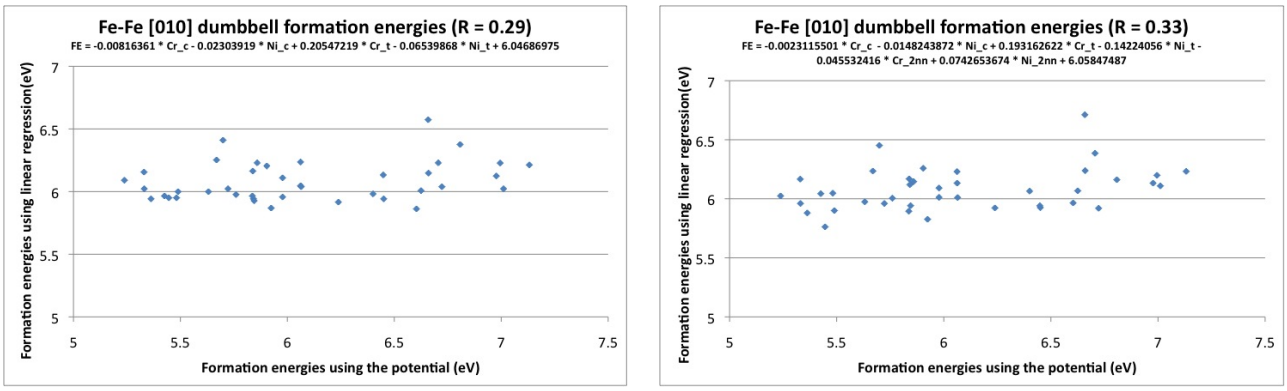

Figure 3.37: Illustration of the attempts to fit the [010] dumbbell formation energies. The left figure shows the correlation obtained when trying to fit the [010] dumbbell formation energies to the number of compressive and tensile Cr and Ni atoms in the first nearest neighbours. The right figure shows the correlation obtained when including the number of Cr and Ni atoms in the second nearest neighbours in the calculations.

Fitting the formation energies has been tried for larger number of configurations (300) as shown in figure (3.38). From the figure it can be seen that different equation for the formation energies obtained when having larger number of data, however, the goodness of the fit was the same.

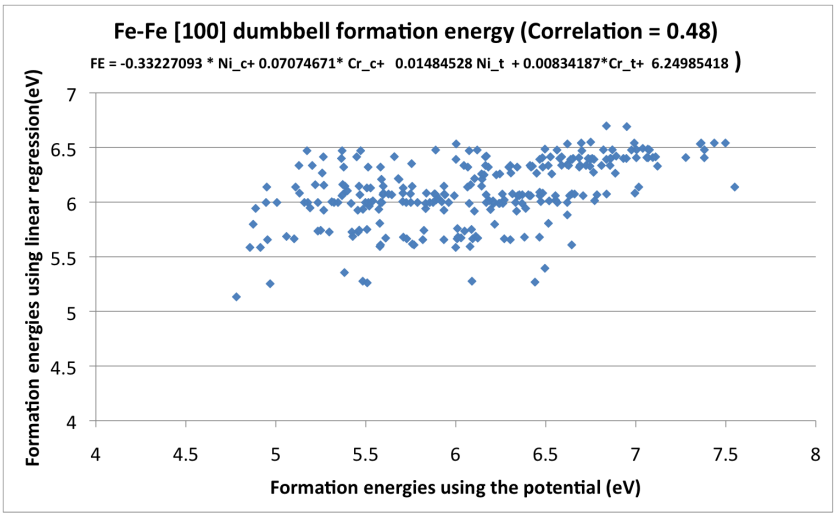

Figure 3.38: Illustration of the correlation obtained to fit the formation energies of [100] dumbbell to the number of compressive and tensile Ni and Cr atoms in the first nearest neighbours. A total of 300 values used in these calculations.

Fe vacancy migration barrier: 60 systems were used for fitting the formation energies have been used as the initial configurations for fitting the Fe vacancy migration energies. The final configurations were obtained by moving the vacancy to a 1nn Fe atom. The migration barriers were calculated using CI-NEB [61] and using 11 images. Both forward and reverse barriers were included in the fitting which gave a total of 988 migration barriers.

The local environment at the saddle has been studied. The number of neighbours to a saddle point and the distance from it are shown in table (3.50). A picture illustrating the nearest neighbours to a saddle are shown in figure (3.39).

Ordering	Number of atoms	Distance from saddle
1nn	4	$\frac{\sqrt{3}}{2\sqrt{2}}a$
2nn	4	$\frac{\sqrt{5}}{2\sqrt{2}}a$
3nn	8	$\frac{\sqrt{5+2\sqrt{2}}}{2\sqrt{2}}a$
4nn	6	$\frac{3}{2\sqrt{2}}a$

Table 3.50: Neighbours to a saddle point considered for fitting

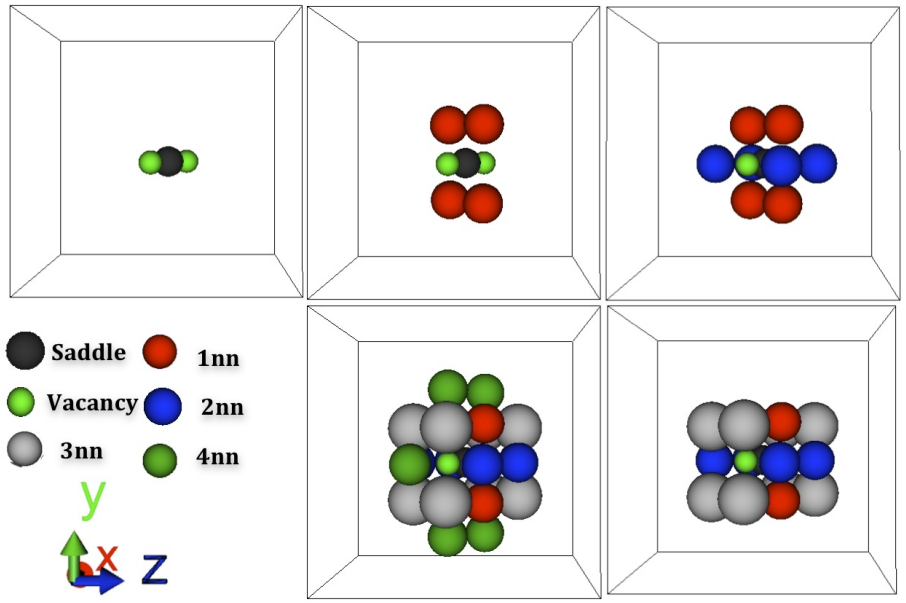

Figure 3.39: Local environment of a saddle point considered in the fitting.

Different attempts were tried to fit the migration energies for Fe vacancies in the ternary alloy with respect to the neighbours. Since a good correlation was obtained for the vacancy formation energies, a good way to fit the migration barriers is to use the equation obtained for the formation energies to calculate the formation energies at the initial and final states. Then, try to fit a fixed value E_b so,

$$E_{\mathrm{m}}^{\mathrm{forward}} = E_{\mathrm{b}} + \frac{E_{\mathrm{final}}^{\mathrm{formation}} - E_{\mathrm{initial}}^{\mathrm{formation}}}{2} \tag{3.41}$$

$$E_{\mathrm{m}}^{\mathrm{reverse}} = E_{\mathrm{b}} - \frac{E_{\mathrm{final}}^{\mathrm{formation}} - E_{\mathrm{initial}}^{\mathrm{formation}}}{2} \tag{3.42}$$

Illustration of this is shown in figure (3.40).

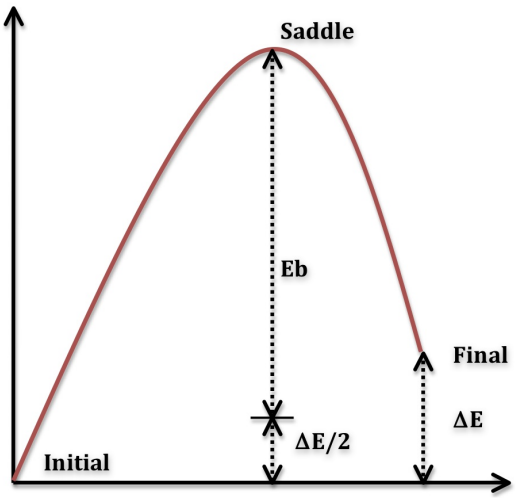

Figure 3.40: Illustration of attempt to fit the vacancy migration barriers in the ternary alloy to the local environment at the initial and final states, the figure illustrates the need to calculate the fixed value E_b.

Finding a fixed value of E_b has been tried, however this result in a very poor correlation as shown in figure (3.41).

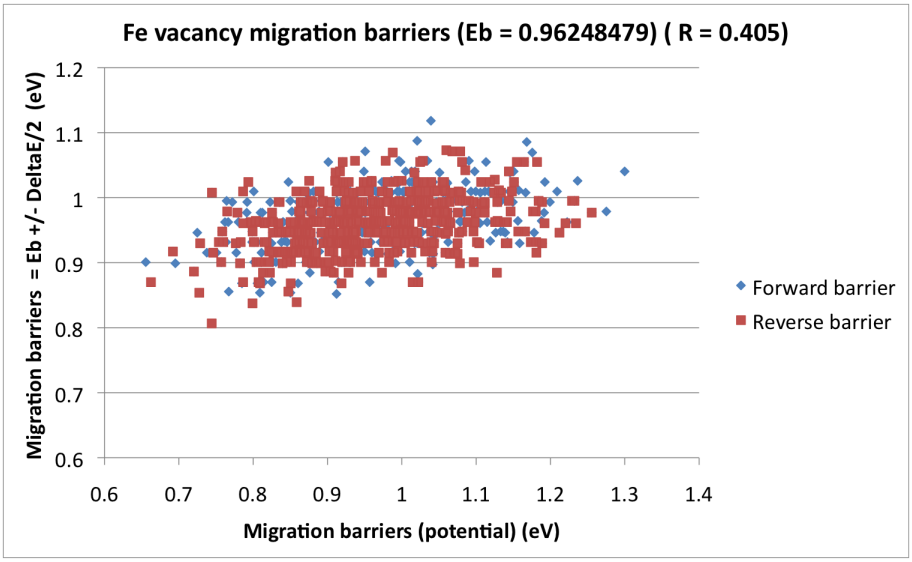

Figure 3.41: An attempt to fit E_b to calculate Fe vacancy migration barrier.

Another attempts were to try to fit the value of E_b to the local environment at the saddle point as shown in figure (3.42). These attempts included trying to fit the value of E_b to number of Cr and Ni atoms at the saddle point. A good correlation of 0.70 was obtained when including up to the fourth nearest neighbours in the calculations.

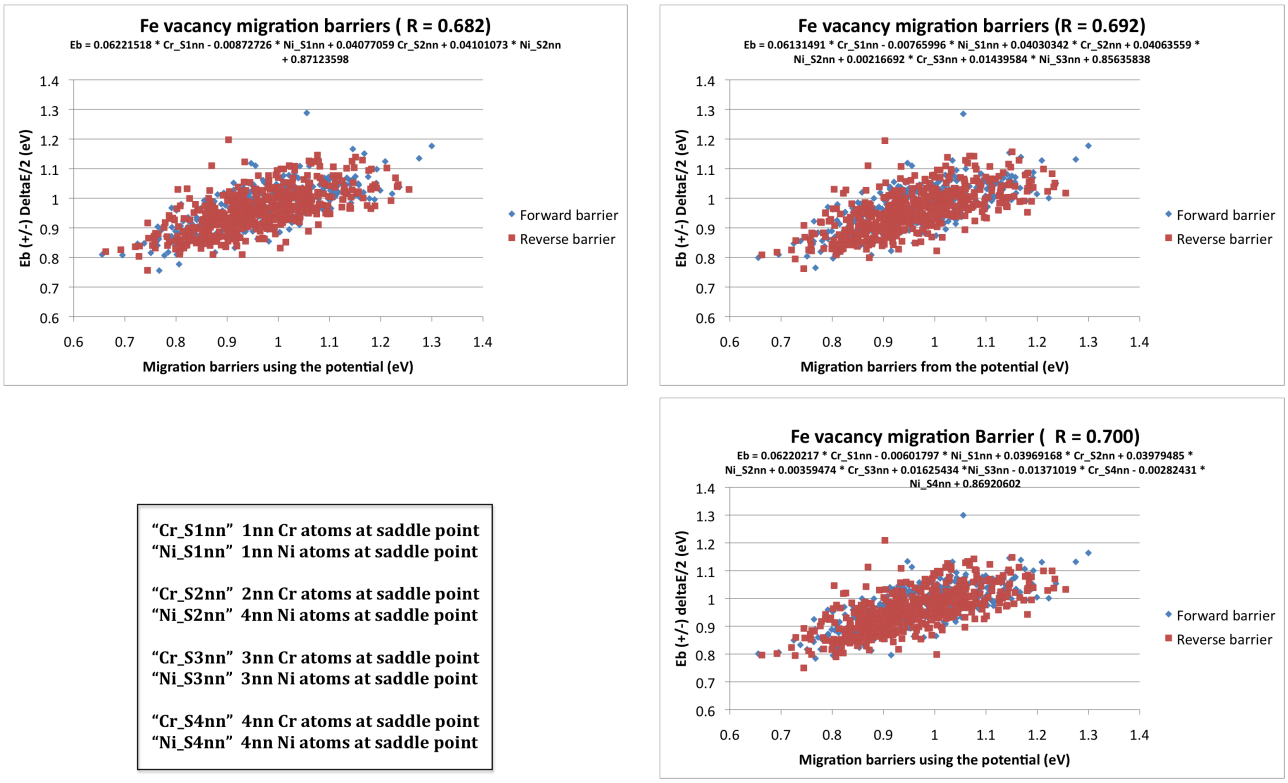

Figure 3.42: Illustration of the attempts to fit E_b to calculate Fe vacancy migration barrier. The top left figure shows the correlation obtained when including the number of Cr and Ni atoms in the first and second nearest neighbours at the saddle. The top right figure shows the result obtained when including the third nearest neighbours at the saddle in the calculations. The bottom right figure shows that a correlation of 0.70 was obtained when including up to the fourth nearest neighbours at the saddle point in the calculations.

Another way to fit the migration barriers is to fit them directly to the local environment at the initial, final and the saddle points as shown in figure (3.43). The highest correlation obtained was equal 0.68 when including the number of Ni and Cr atoms in the nearest neighbours at the initial, saddle and final configurations.

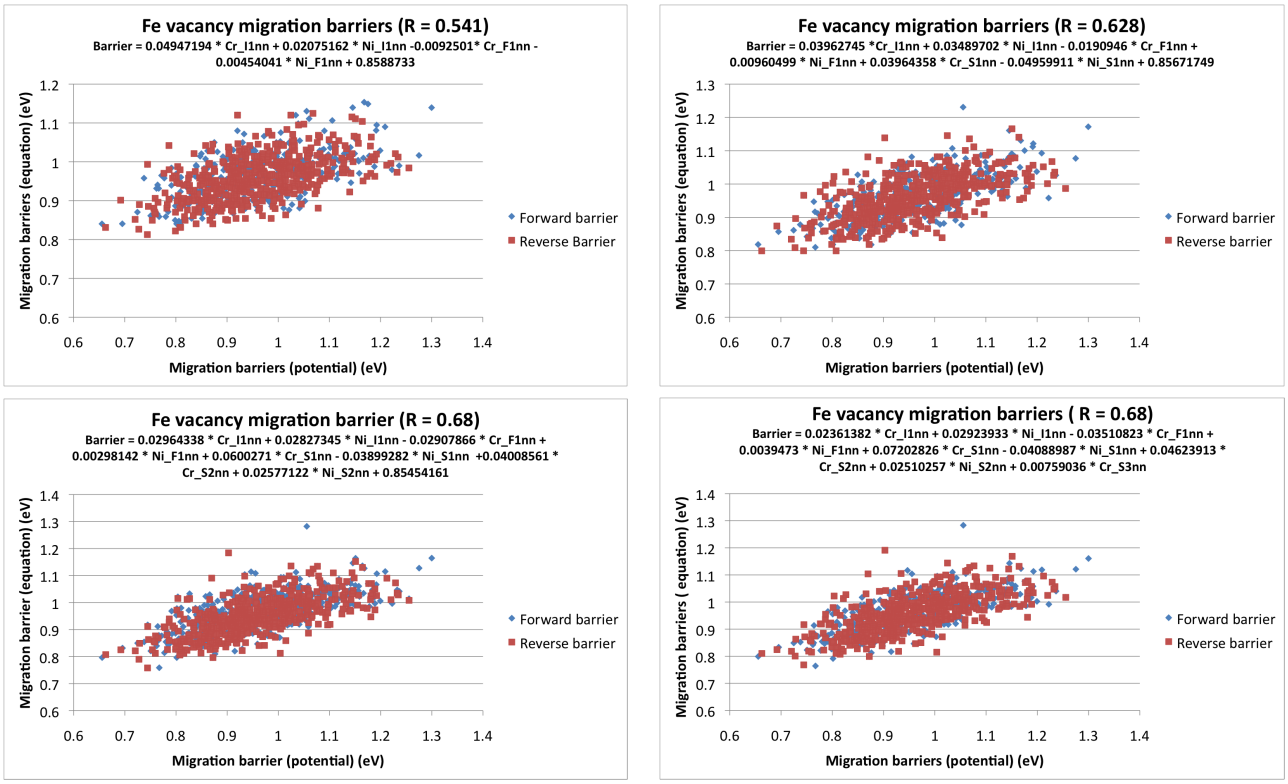

Figure 3.43: Illustration of the attempts to fit Fe vacancy migration barrier to the local environment. The top left figure shows the correlation obtained when including the first nearest neighbours at the initial and final configurations. The top right figure shows the correlation obtained when including the first nearest neighbours at the initial, saddle and final configurations. The bottom left figure shows including the local environment at the saddle up to the second nearest neighbours and the bottom right figure shows the correlation obtained when including up to the third nearest neighbours at the saddle point.

Since the best correlation (0.70) has been obtained when fitting the value of E_b to the local environment at the saddle point up to the fourth nearest neighbours, the equation was used to reproduce the migration barriers for another set of migration barriers (450 values) and this gave a correlation of 0.66 to the associated values from the potential.

3.6 Discussion and Conclusion

Three potentials were provided by Bonny to describe the interatomic separation in the ternary alloy. Various tests and calculations have been done using these three potentials to decide whether a potential is good enough to represent the ternary alloy. The main aim from this chapter was to show what is required from the potential and whether one of these potentials can be a good candidate to represent the ternary alloy interactions and therefore

one would could rely on the results produced by the particular potential.

The first stage in investigating the potential is to determine what is the potential will be used for in order to determine the main properties that the potential should reproduce. As the main aim from the potential is to calculate the formation and migration energies, the values for the latter ones which obtained from ab-initio or DFT data have been set to be the main targets for the potential.

To judge whether the potential is a reliable potential, various calculations have been done. For example, the vacancy and point defects formation, migration and binding energies have been calculated and compared with the available data. Also segregation has been tested using Monte Carlo Simulation for both ternary and binary systems. Furthermore, high temperature MD simulations have been investigated for both systems.

Bonny [8] chose potentials from the literature for the pure potentials in his first potential. He used Ackland 1997 [68] for Fe, Mishin 2004 [69] for Ni and Olsson 2005 [70] for Cr. The potential was found to overestimate the vacancy migration energy for Fe and overall the migration of the self interstitial defects were found to be quite low and it is very important to understand how realistic they are. From Monte Carlo simulations, the Cr and Ni were found to segregate to different regions in the Fe matrix in the ternary alloy. For the binary alloy, the system segregated into two regions, a pure Ni and a Ni-Cr region. Studying the Ni-Cr region revealed the possibility of producing Ni_2Cr, which agrees well with the experimental phase diagram. However, the potential was found to have a negative thermal expansion and the fcc structure was not stable in most cases as changing the lattice parameter slightly causes a transformation to bcc structure.

To overcome the stability issue seen in the first potential, Bonny developed another potential for the purpose of the project. The second potential [10] was made for the plasticity purposes originally so did not reproduce formation and migration energies very well. From MC simulation the Ni and Cr atoms were found to segregate into planes in the Fe matrix in the ternary potential. We tried to study the forces behind the formation of these planes, we found that Ni was the responsible element for these planes although we could not see the same kind of segregation using otf-KMC simulation.

A third potential was written by Giovanni [73] that was able to overcome the stability issues found in the first potential. However, the third potential overestimates the formation

energies for the self interstitial defects. From the MC simulation, it has been found that Cr segregates away from the Fe matrix in both ternary and binary system.

Attempts were undertaken to fit the Fe vacancy and ⟨100⟩ dumbbell formation energies in the ternary system (70 at.% Fe, 10 at.% Ni and 20 at.% Cr) as a function of Ni and Cr neighbouring atoms using formation energies calculated using Giovanni's potential [73]. The reason behind doing these calculations was to investigate the role of local environment on these formation energies and whether the simple knowledge of the local environment can help in finding the formation energies without the need to any computational effort. Also, the obtained models could be used to build models to study the RIS in the ternary alloy. From comparing the formation energies obtained using the empirical potential and the DFT formation energies, poor correlation was obtained where the potential was found to underestimate the formation energies of the Fe vacancy in the ternary alloy and overestimate the formation energies of the ⟨100⟩ dumbbell. A very good correlation (0.91) was obtained for the Fe vacancy formation energies as a function of the first nearest neighbours. However, poor correlation obtained for the Fe-Fe ⟨100⟩ dumbbell formation energies even when including the second nearest neighbours. The best correlation obtained for calculating the Fe vacancy migration barriers was 0.7 and this by fitting the E_b to the local environment at the saddle point up to the fourth nearest neighbours.

Chapter 4

Modelling radiation damage at grain boundaries in fcc Nickel and Ni-based alloy using Long Time Scale Dynamics Techniques

4.1 Introduction

The long timescale evolution of radiation damage near grain boundaries (GB) in fcc Ni and a Ni-Cr alloy has been investigated. Molecular dynamics (MD) combined with the on-the-fly kinetic Monte Carlo (otf-KMC) has been used to study the evolution of defects in bulk, $\Sigma 5$ and $\Sigma 3$ GB systems resulting from 1 keV collision cascades.

In the first section of this chapter the methodology employed is discussed. This includes an explanation of how the GBs have been constructed along with the simulation technique used. The findings for the pure Ni are discussed followed by the results for the Ni-Cr. In each part the collision cascades in the bulk system are discussed first. This is followed by discussion of the results obtained from LTSD for 1 keV collision cascades for the $\Sigma 5$ and $\Sigma 3$ GBs.

4.2 Methodology

Fcc Ni and a Ni-Cr binary alloy (80 at.% Ni 20 at.% Cr) have been studied in this work. The bulk, symmetrical tilt $\Sigma 5$ and $\Sigma 3$ GB have been studied for both materials.

4.2.1 Choosing the potential

Three versions of a Ni-Cr potential produced by G.Bonny [8] are available along with a further potential aimed at describing plasticity [10]. Since in all of these potentials, Mishin 2004 [69] is used to describe the interactions for the pure Ni, the main aim was to choose the potential that will describe the Ni-Cr part in the best way. Therefore, the Vac-Cr migration energy in the Ni matrix has been calculated using the four potentials and compared to the available data from DFT calculations as shown in table (4.1).

Method	Vac-Ni (eV)	Vac-Cr (eV)
DFT[41]	1.08	0.82
P-100819	1.19	1.00
P-100826	1.19	0.96
P-100831	1.19	0.95
Plasticity	1.17	1.04

Table 4.1: The table shows a comparison between Ni and Cr vacancy migration barriers in the Ni matrix using different potentials with the associated values from DFT.

In addition, 1NN MEAM potential has been implemented for pure Ni to see whether we can get better potential to represent our system. This potential gave good estimates of the cohesive energy and vacancy formation energy, however, it overestimates the vacancy migration energy as shown in table (4.2).

.

Property	Tucker [41]	MEAM
E_c (eV)	-4.45	-4.45
$\mathrm{Vac}_{\mathrm{formation}}$ (eV)	1.43	1.50
$\mathrm{Vac}_{\mathrm{migration}}$ (eV)	1.08	1.66

Table 4.2: The table shows a comparison between the values of cohesive energy, formation and migration energies of a vacancy in pure Ni obtained using MEAM potential and associated values obtained from DFT.

Since P-100831 is the best potential in describing the Vacancy-Cr migration energy in Ni matrix as it gave the closer value to the DFT value, it has been chosen to represent interactions in Ni-Cr system. This potential has been connected to ZBL potentials to describe small interatomic separations. The cutoff distances used here are 0.6 and 1.2 Å for pure Ni and 0.8, 1.95 Å for Ni-Cr and 0.5 and 1.2 Å for pure Cr. The constants used for the spline function are shown in table (4.3).

Constant	Ni-Ni	Ni-Cr	Cr-Cr
f_1	112.14736	7.89648	22.23683
f_2	-663.14010	4.98182	-94.25723
f_3	1642.09119	-22.90594	244.57324
f_4	-1977.42337	24.27168	-323.38485
f_5	1143.53095	-11.44775	203.00507
f_6	-254.71295	1.97130	-48.32878

Table 4.3: Parameters used to fit the spline for pair potentials (P-100831). The f_k's are in units Å^{-k}.

A binary system has been created by randomly distributing the required percentage of the Cr in the Ni matrix. The system has been used to investigate segregation using the MC [64] method. The results obtained show similar segregation obtained earlier with the potential (P-100819) as was shown in chapter 3 where the system segregates into two different regions, pure Ni region and a Ni-Cr region which shows possibility of getting Ni_2Cr as was predicted by the experimental phase diagram [9]. A picture of the system after MC is shown in figure (4.1).

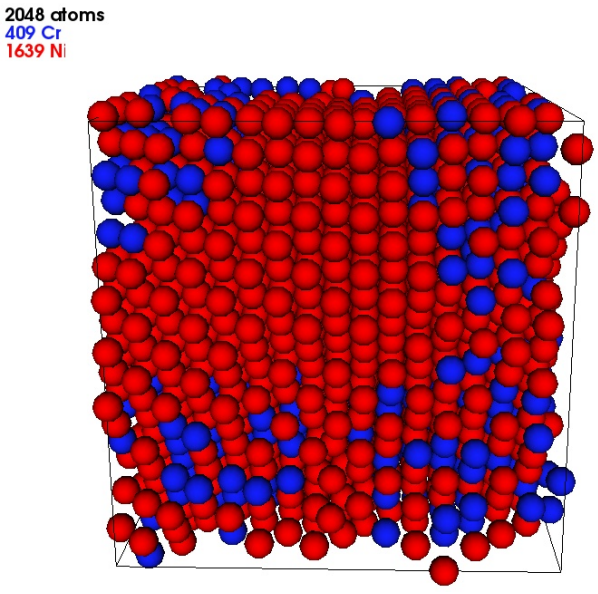

Figure 4.1: The binary system after MC simulation using P-100831 potential which shows that the system segregates into two regions, pure Ni region and a Ni-Cr region.

4.2.2 Choosing the search method

The Relaxation and Translation technique (RAT) [56] has been employed to find all possible unique transitions in the otf-KMC simulation for the NiCr binary system. However, this method was not able to find all expected transitions. For example, the method will find all transitions associated with Ni atoms hopping into a vacancy but it will fail to find the transitions associated with a Cr atom hopping into the vacancy. A system with one vacancy has been used to investigate the problem. The vacancy in the system has ten Ni atoms and two Cr atoms in the first nearest neighbours. The RAT [56] method finds the ten transitions of the Ni atoms into the vacancy but not the Cr atoms. The barriers of the twelve expected transitions have been checked using CI-NEB [11] as shown in figure (4.2).

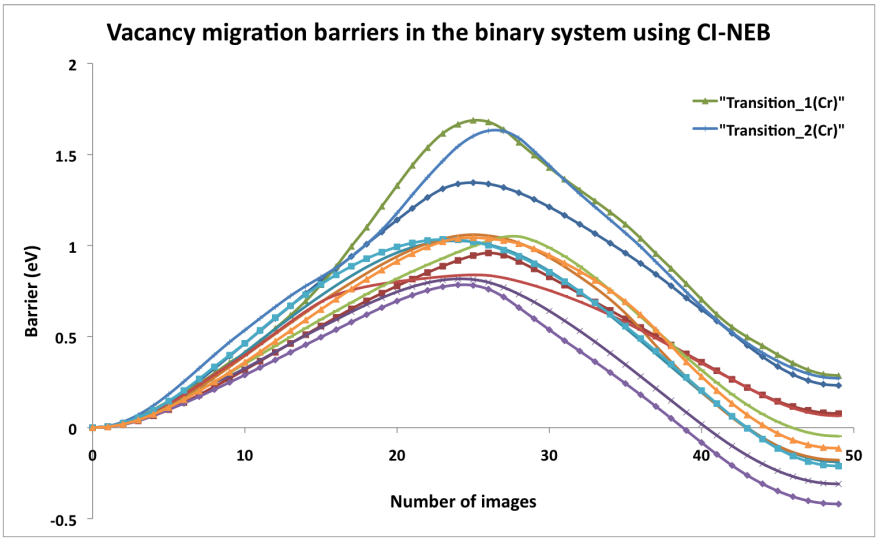

Figure 4.2: Energy pathways for possible transitions of a vacancy in the binary system using CI-NEB [11]. The vacancy has ten Ni atoms and two Cr atoms in the first nearest neighbours. The figure shows that the energies required for the Cr atoms to hop into the vacancy are higher than the one needed for Ni atoms.

From figure (4.2), it can be seen that the barriers for the Cr atoms to move into the vacancy are higher than for the Ni atoms. However, those transitions are still valid and we expect that the search method should find them. Therefore, trials have been undertaken to force the RAT [56] technique to find the transitions associated with Cr atoms. For example, the atoms that can move during the search have been restricted to be only the 12 nearest neighbours. Also, RAT was forced to initially choose the Cr atom when searching for transitions. However, all of these trials failed to find the Cr transitions. Therefore, we looked into other searching methods such as Activation and Translation method (ART) [58] which succeeded in finding all expected transitions for the same particular system. Furthermore, the ART technique is

found to find more unique transitions when compared with the RAT technique. For example, figure (4.3) shows a comparison between the transitions found using the two methods for a bulk system with several defects. The number of transitions have been normalised to allow comparison of the range of barriers found. As a result, the ART technique has been used in the otf-KMC technique in all simulations explained in this chapter.

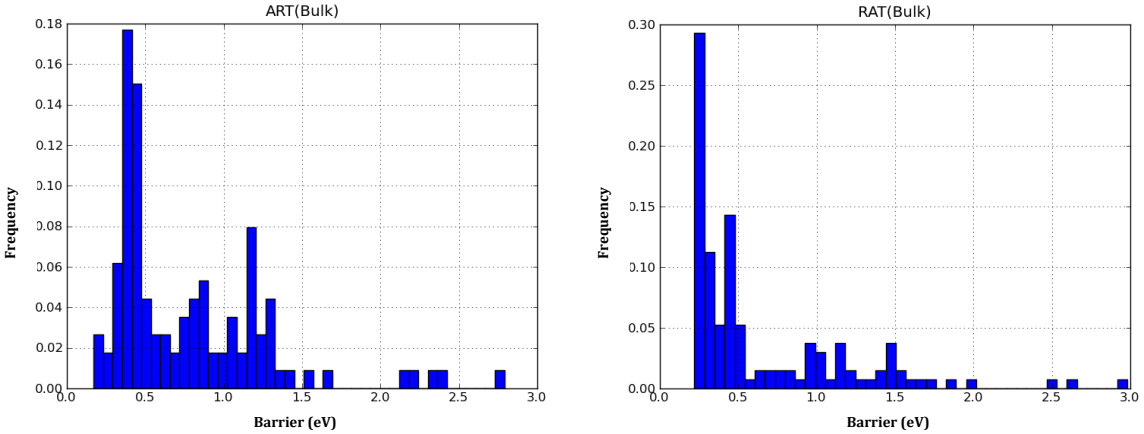

(a) ART method (b) RAT method

Figure 4.3: Comparison between the transitions found for a bulk system with several defects, (a) shows results using RAT method and (b) using ART technique.

The next step is to decide the number of searches required for each KMC step to ensure that all possible unique transitions have been found with the lowest computational cost. The ART method has been used to find the transitions for a defective system with 200, 400 and 600 searches. The transitions found at those number of searches are shown in figure (4.4).

As one is interested in the low barriers more than the high barriers as there are bigger chance that they will be chosen in the otf-KMC simulation, 400 searches give reasonable number of transitions with reasonable computational cost. Therefore, the otf-KMC simulation has been set to do 400 searches at each step in all simulation in this chapter.

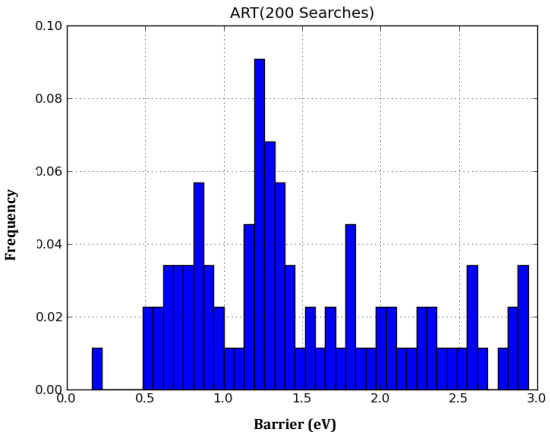

(a) 200 Searches

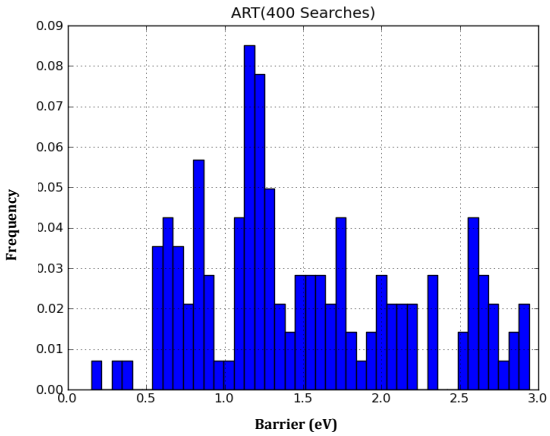

(b) 400 Searches

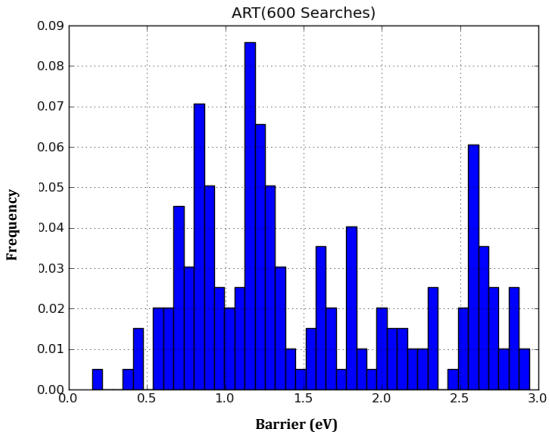

(c) 600 Searches

Figure 4.4: Comparison between the transitions found for a defective system using a different number of searches in the ART method, (a) shows the transitions found using 200 searches, (b) shows the results from 400 searches and (c) shows the transitions found by doing 600 searches.

4.2.3 Grain Boundary Construction

Due to the free volume at its interface, the GB region is considered to be more likely subject to deterioration than other regions of the material. GBs are usually classified according to the mis-orientation angle between the grains. There are two well known types of the GBs. The first type is called tilt GBs, in which the rotation axis is parallel to GB plane. The second type of GB is the twist GBs where the rotation axis is perpendicular to the GB plane. Pictures of the two types of GBs can be seen in figure (4.5).

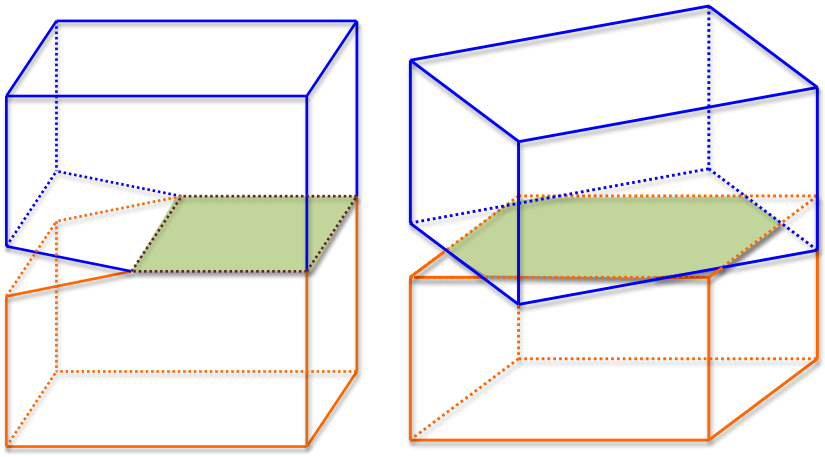

(a) Tilt GB (b) Twist GB

Figure 4.5: Types of the Grain Boundaries, (a) shows the tilt GBs where the rotation axis is parallel to GB plane and (b) shows the twist GBs where the rotation axis is perpendicular to the GB plane.

The GB is usually distinguished using Σ factor, which can be calculated as follows:

$$\Sigma = \frac{\text{Number of lattice sites}}{\text{Number of Coincident Sites Lattice (CSL)}}, \tag{4.1}$$

where CSL refers to when the units that form the GB is repeated. An example of how to calculate Σ is shown in figure (4.6).

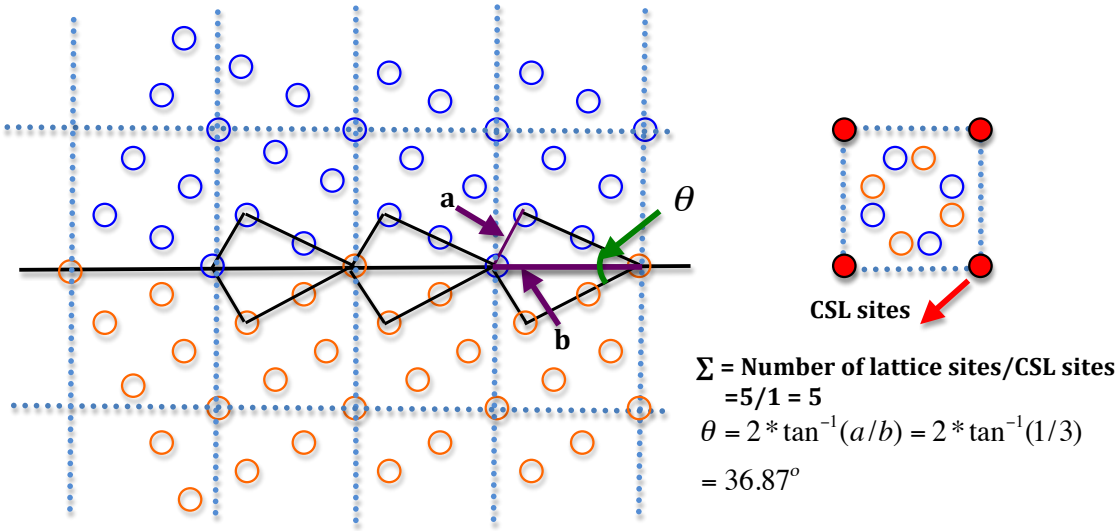

Figure 4.6: Example of the GB highlights the CSL sites and shows how to calculate Σ and the angle between the grains. Adapted from [6].

In this research, symmetrical tilt $\Sigma 5$ and $\Sigma 3$ (twin) grain boundaries have been studied. In

the following we explain the construction process.

$\Sigma 5$ **Grain Boundary**

The symmetrical tilt $\Sigma 5$ GB has been created taking the tilt axis in the [001] direction with an angle of 36.87° between the two grains. The following are the main steps involved in construction of GB:

1. The first step is to generate an fcc structure with (001) orientation.

2. Next is to look for an atom site lattice in the middle of the cell in both x and y direction to rotate the crystal in the z direction.

3. Once the middle is identified, two crystals are generated from the original one by rotating in the z direction once with $\theta/2$ and another with $-\theta/2$. The rotation of the lattice site vectors of the original crystal, $\vec{r} = (r_1, r_2, r_3)$ to new lattice site vectors $\vec{r'} = (r'_1, r'_2, r'_3)$ has been performed using the rotation formula [74] which can be represented for the rotation of r to r' about the rotation axis $\vec{\rho}$ by angle θ as follows:

$$r'_i = \sum_{j=1}^{3} R_{ij} r_j, \tag{4.2}$$

   where

$$R_{ij} = (\cos\theta)\delta_{ij} + \rho_i\rho_j(1 - \cos\theta) - \sum_{k=1}^{3} \varepsilon_{ijk}\rho_k \sin\theta, \tag{4.3}$$

   where δ_{ij} is Kronecker delta and ε_{ijk} is the permutation tensor.

4. For the grain boundary system, periodic boundary conditions are implemented in both x and z directions. For that reason a layer is removed from both directions so we have a match.

For the GB system, in addition to the periodic boundary conditions in the x and z directions, a few layers are fixed in the y direction as was explained in chapter 2.

After generating the GB system, it is time to look for the minimum energy GB, this has been done by shifting the GB first in y direction, and then in x and z direction to find the optimal values of the shift in the y direction (Δy), the shift in the x direction (Δx) and the shift in the z direction (Δz). Figure (4.7) shows the values used for the GB's separation in all directions.

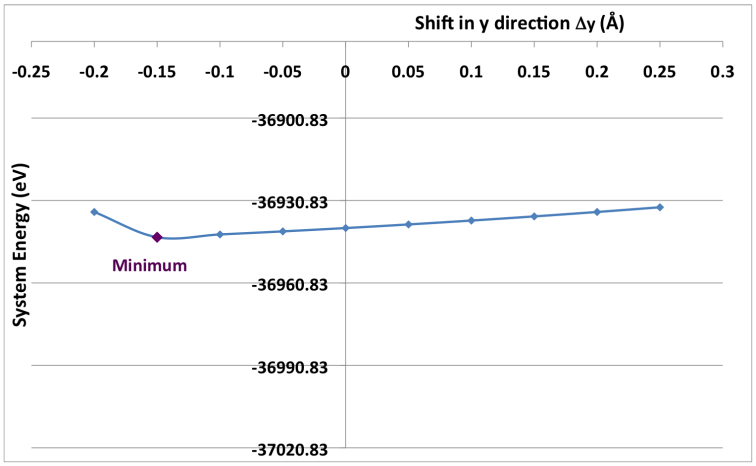

(a)

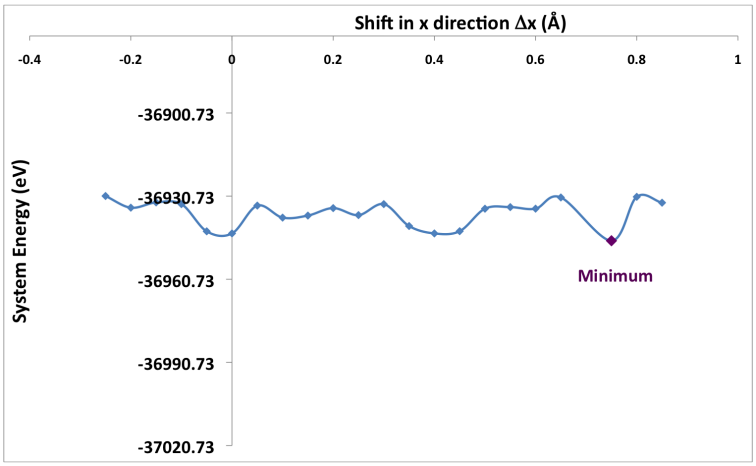

(b)

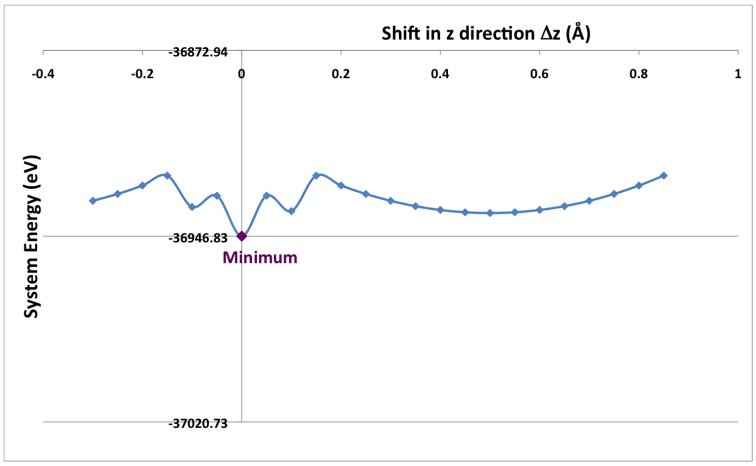

(c)

Figure 4.7: Finding the minimum GB energy, (a) shows the shift in the y direction with the minimum energy when $\Delta y = -0.15$ Å, (b) shows the shift in the x direction with the minimum energy when $\Delta x = 0.75$ Å, (c) shows the shift in the z direction with the minimum energy when $\Delta z = 0$ Å.

Systems with different sizes have been used in this research. First a system of 8470 atoms has been used to model the vacancy segregation at different sites from the GB and the evolution of a single vacancy to the GB. The same system is used to model the evolution of defects after single and multiple 1 keV collision cascades. A larger system of approximately 55k atoms has been also used to model the evolution of defects after 1 keV collision cascades. A picture of the system is shown in figure (4.8).

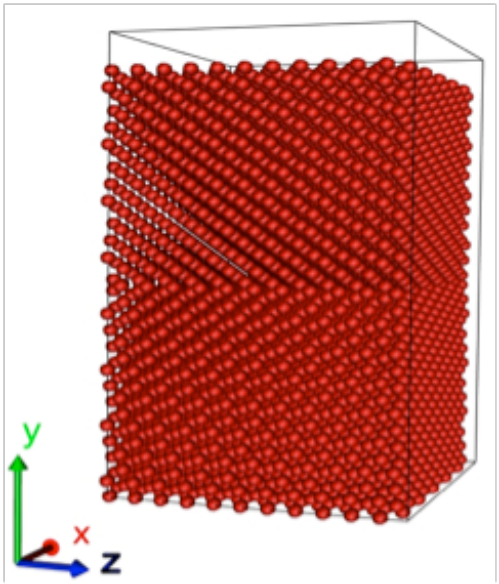

Figure 4.8: Symmetrical tilt Σ5 grain boundary.

Σ3 Grain Boundary (Twin GB)

For the twin GB, the first crystal of the system is constructed by generating a (111) fcc structure and the second crystal is by rotating the original fcc structure and placing it in top of the first crystal. One layer of the twin GB is shown in figure (4.9).

A twin GB system of approximately 55k atoms has been used to model the evolution of defects generated in the system after 1 keV collision cascades using the same boundary conditions used in Σ5 GB.

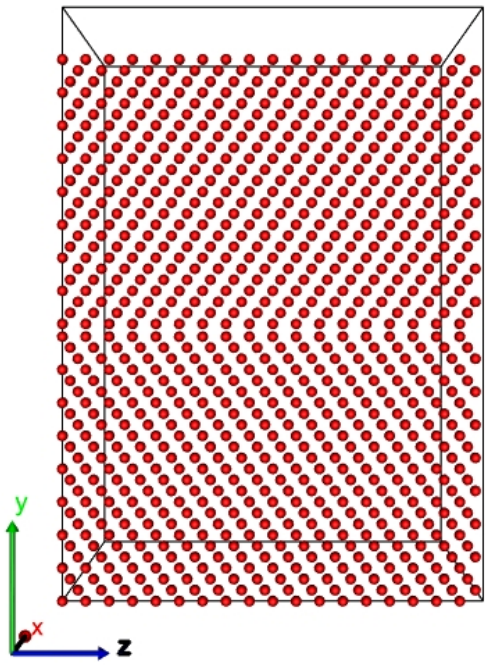

Figure 4.9: One layer of the twin grain boundary.

4.2.4 Simulation Methodology

The modelling carried out can be divided to two main stages. The first stage was modelling collision cascades in the system and the second stage was modelling the evolution of the defects that resulted from the cascades. Systems modelled contained approximately 55k atoms with periodic boundary conditions in three dimensions for the bulk system and in the plane of GB with the top few layers fixed on the edges parallel to the GB for the GB systems.

An energy of 1 keV was used to perform the collision cascades. The PKA has been chosen randomly and in case of the GB the direction of the collision cascades has been directed towards the GB. The initial collision cascade phase is modelled using MD, with the velocity Verlet [50] algorithm used to evolve the system. The collisions runs for 20 ps with a variable time step depending on the kinetic energy and potential energy within the system. All collision cascades in this work were carried out at 0 K so no thermostat has been applied during the MD simulations.

Otf-KMC [19, 21, 20] has been used to model the evolution of defects after the collision cascades. The temperature for the evolution of the system was taken to be 500 K as this is representative of what would be found in a next generation reactor.

4.3 Results and Discussion (Pure fcc Ni)

4.3.1 Bulk System

Displacement Threshold energy

The displacement threshold energies were calculated for fcc Ni. This has been done by using a system of 2048 atoms for 66 PKA trajectories. Simulations were resumed by setting 0 and 100 eV to be the minimum and maximum energy respectively. The initial collision is set at PKA energy of the maximum energy for 10 ps. The defects in the resulted system is checked against the perfect system. If defects were found in the system, the collision cascades were run at the mid of the maximum energy and lower energy. The energy that will result in defects in the system is set to be the maximum energy. If the energy did not produce any defects in the system then it will be set as the minimum energy and the process will be continued until the difference between them is less than 0.1 eV. The results obtained were represented by showing the PKA trajectories as shown in figure (4.10a) and by plotting a histogram as shown in figure (4.10b).

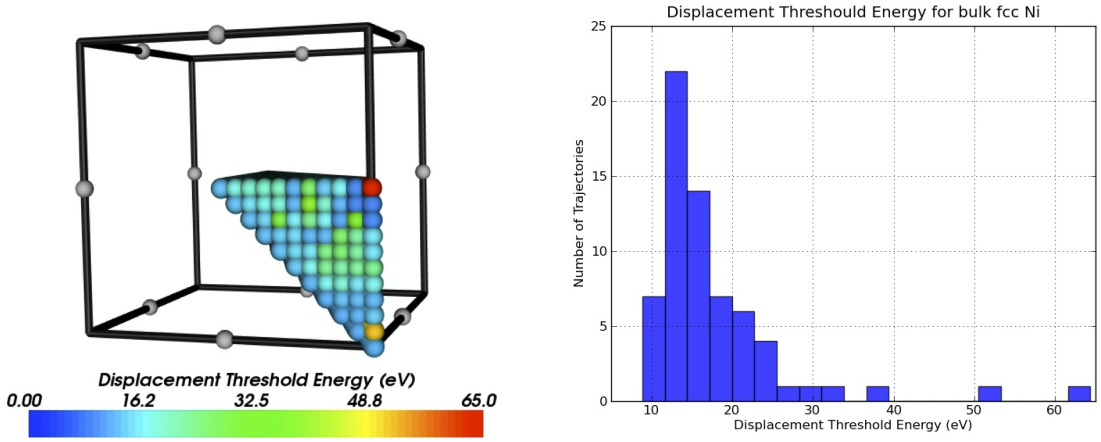

(a) (b)

Figure 4.10: Displacement Threshold Energies for fcc Ni for 66 PKA trajectories, (a) shows the results calculated for the set of 66 directions and (b) shows the distribution of the DTEs found. The PKA is taken to be the atom in the middle of the system.

The maximum DTE was found in the direction $\langle 1\ 1\ 0 \rangle$ with value of 64.4 eV and the minimum DTE was found to be 8.89 eV in the direction $\langle 1\ 0.9\ 0 \rangle$. The average DTE was found to be 17.8 eV.

Collision Cascades (1 keV)

A system containing 55,296 atoms has been used to study the damage after 1 keV collision cascades. The system was first thermalised to room temperature for 8 ps with thermal layers of 3 Å. The resulted system has been used to run 66 collision cascades with different PKA trajectories. The results obtained from collision cascades were analysed by looking at the displacement of atoms after collision cascades as shown in figure (4.11a) and to the defects as shown in figure (4.11b).

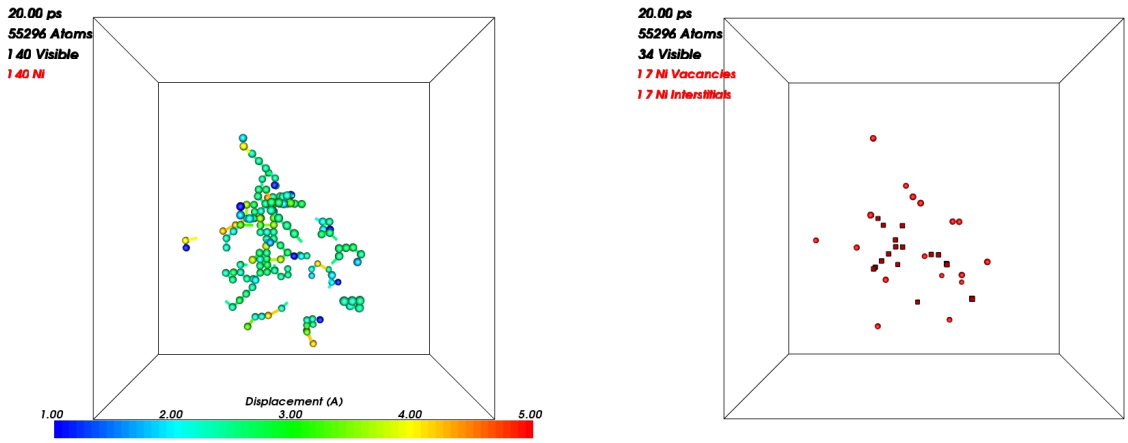

(a) (b)

Figure 4.11: Damage after 1 keV collision cascades, (a) shows the displacement of atoms, (b) shows the defects in the system after collision cascades. (In all figures sphere is an interstitial and cube is a vacancy).

Investigating the damage produced after 1 keV collision cascades shows a variation in the number of defects produced between 20 and 42 after 20 ps as shown in figure (4.12a). An illustration of the number of defects against the PKA trajectories is shown in figure (4.12b) and pictures of the maximum and the minimum defects present in the system after collision cascades are shown in figure (4.13).

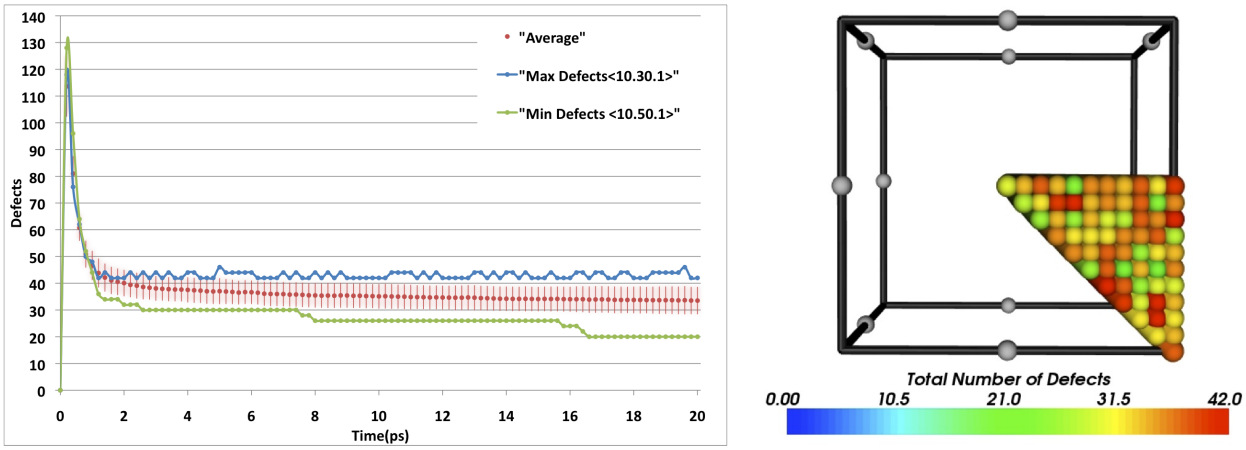

(a) (b)

Figure 4.12: a)1 keV bulk Ni cascade defect evolutions as a function of time. Blue and green lines represent the PKA trajectories that will give maximum and minimum number of defects after 20 ps, b)The number of defects in all trajectories. The PKA is taken to be the atom in the middle of the system.

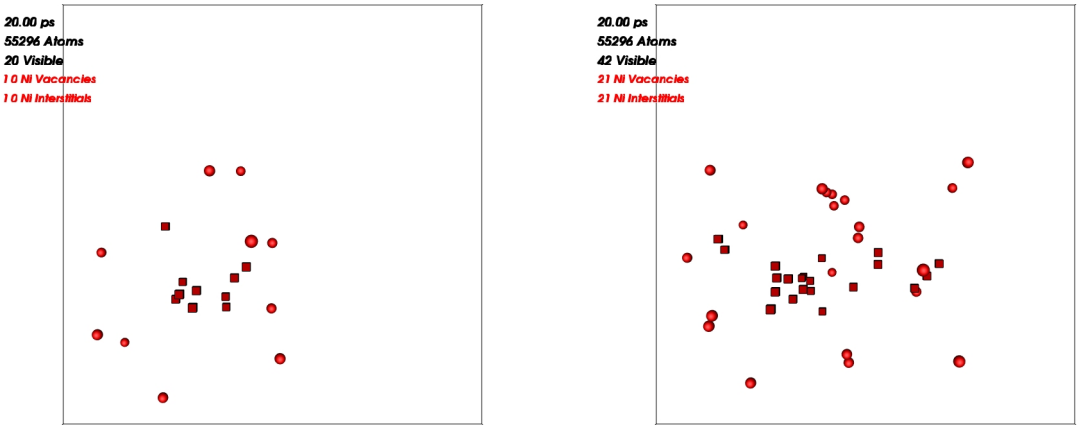

(a) (b)

Figure 4.13: Damage after 1 keV collision cascades, (a) shows the minimum number of defects produced with trajectory ⟨1 0.5 0.1⟩, (b) maximum defects obtained with ⟨1 0.3 0.1⟩ direction. (In all figures sphere is an interstitial and cube is a vacancy).

Long Time Scale Dynamics

Results from KMC for the bulk system are discussed here. For the system chosen, a vacancy cluster formed in the system during the MD phase. During the otf-KMC, there was little change in the number or location of the defects. This was due to the movement within the vacancy cluster with very low barriers, which prevented other transitions happening in the

system. We studied the transitions that happened over that time and we found that these movements within the cluster had barriers of less than 0.2 eV and atoms moved less than 1.5 Å (These small barriers will be discussed in more details in the next section). Furthermore, we studied the other transitions that could have happened to make sure that none of the other transitions satisfied these criteria. We blocked these transitions after which we could see that interstitials are more mobile than vacancies and lots of recombination between vacancies and interstitials happened. Figure (4.14) shows the system after the collision cascade containing 42 defects and the system after the otf-KMC with only 26 defects after 12.53 ns.

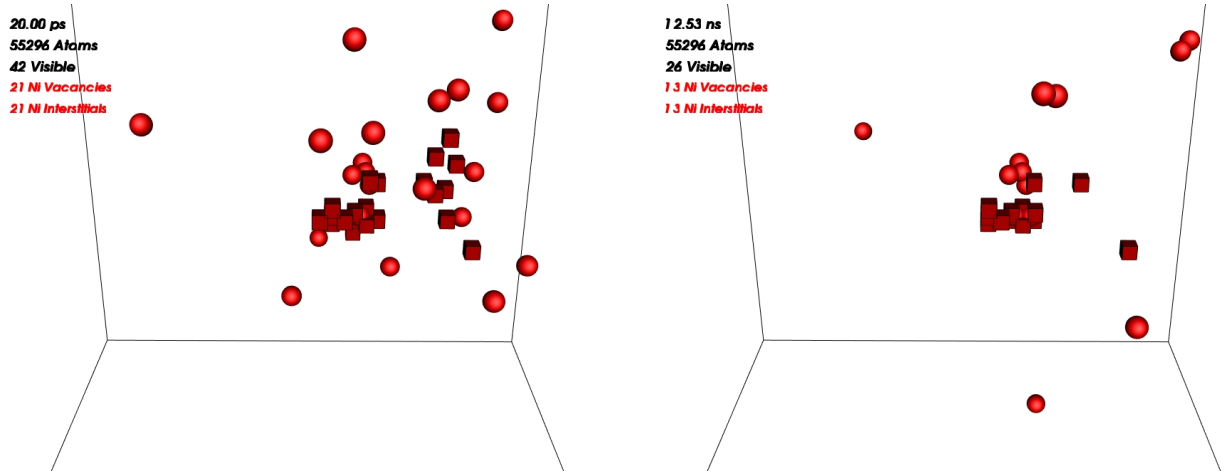

Figure 4.14: Evolution of radiation damage in the fcc Ni bulk system, (a) shows the system after the MD simulation, (b) after otf-KMC. (In all figures sphere is an interstitial and cube is a vacancy).

Small barriers investigation

Very small barriers were found during the otf-KMC simulation. These small barriers were studied to understand if they really have any influence on the system. The chosen barrier at each step in the KMC simulation is shown in figure (4.15). From this figure we can see that most of the chosen transitions have energy barriers less than 0.2 eV. Examples of these transitions are shown in figure (4.16).

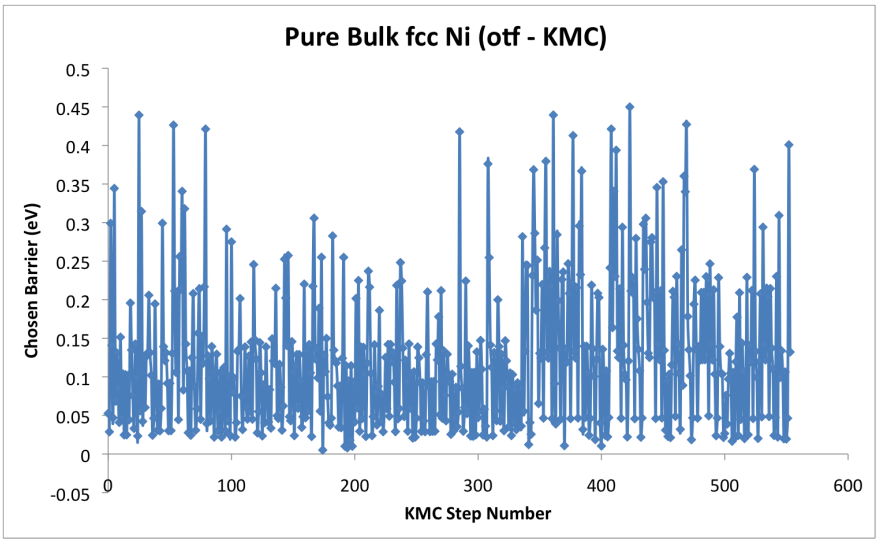

Figure 4.15: Energy barriers of the chosen transitions for pure bulk fcc Ni during the KMC simulation.

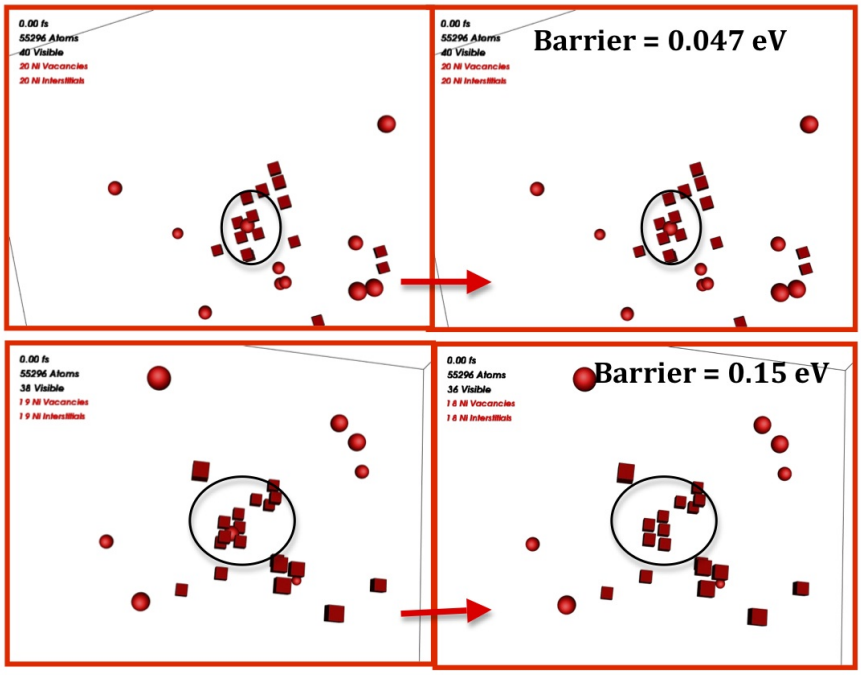

Figure 4.16: Examples of the transitions with small barriers seen during KMC simulation in bulk fcc Ni.

A small test was performed by taking the initial system and running MD for the time reached using the KMC to see if we could see the same diffusion happened during MD simulations. The system after collision cascades has been thermalised to 500 K first before running MD

for 400 ps. We could see the same movement within the cluster seen in the KMC simulation. A picture of the defects in the system after 400 ps using both KMC and MD simulation are shown in figure (4.17).
From figure (4.17) we can see similar diffusion mechanism to the one obtained using otf-KMC with more recombinations happened using MD simulation which shows that the barriers found during the KMC simulation were very small and causing delay in the process. One reason for this delay could be due to using fixed value for the prefactor which is not true in practise. Therefore those transitions have been blocked to explore the diffusion of the defects in the system.

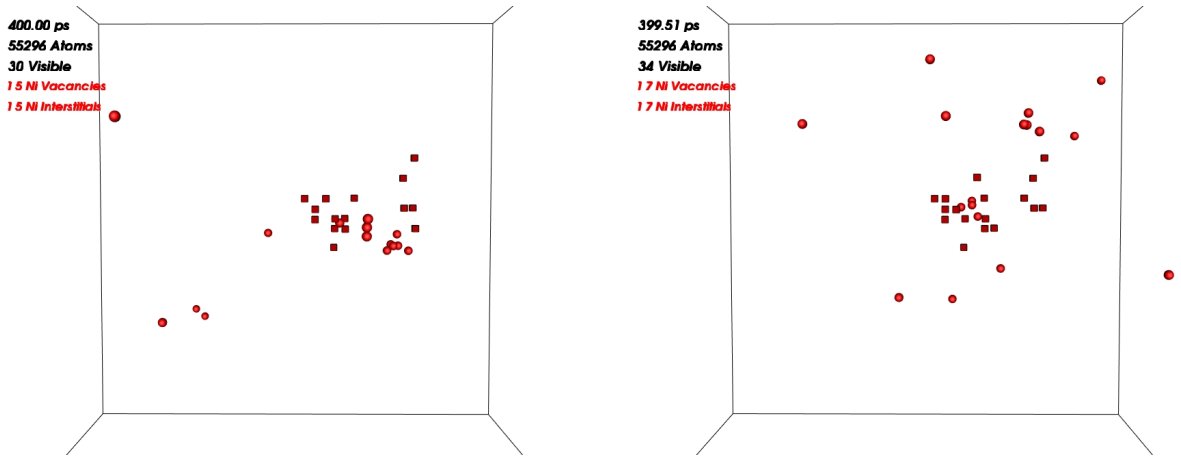

(a) (b)

Figure 4.17: Comparison between the MD and KMC simulations for the bulk fcc Ni, (a) System after MD simulation, (b) System after oth-fly KMC Simulation. (In all figures sphere is an interstitial and cube is a vacancy).

Recombination between vacancy and interstitial

Many recombinations between vacancies and interstitials occurred during the KMC simulation. Examples of the mechanisms observed are shown in figure (4.18). From these figures we can see that most of recombinations happened by introducing a chain of interstitials between the vacancy and the original interstitial defect. This technique has been seen for defects that are even 5th nearest neighbours, with a lower barrier than the one associated with the vacancy or interstitial diffusing.

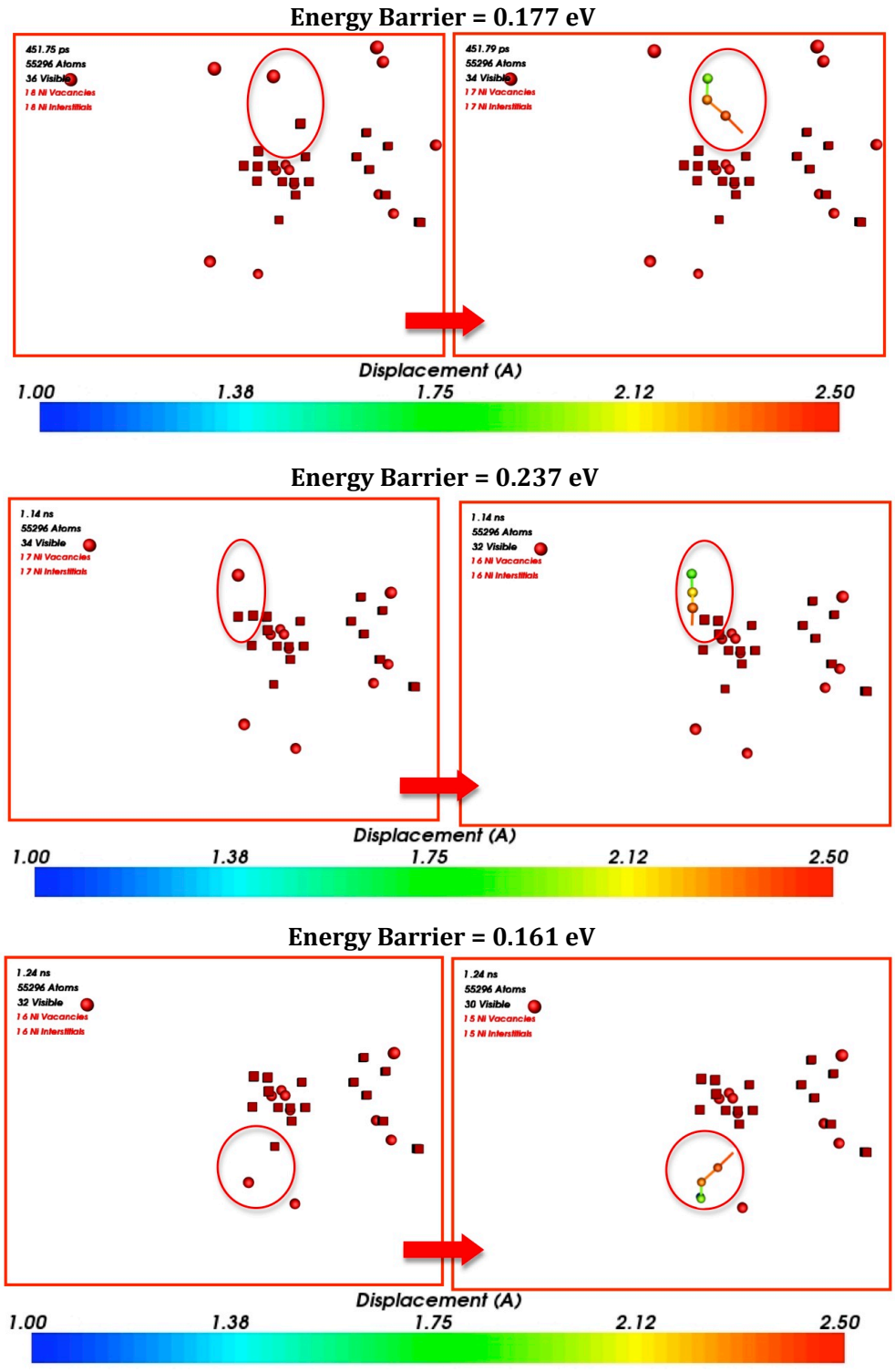

Figure 4.18: Examples of recombination between vacancy and interstitial in pure bulk fcc Ni during the KMC simulations. A vacancy and an interstitial are found to recombine from large distances by introducing a chain of interstitial between them. (In all figures sphere is an interstitial and cube is a vacancy).

4.3.2 GB System

Width of the grain boundary

The width of the Σ5 GB has been checked by slicing the system into layers parallel to the GB plane and checking the average potential energy for each layer. It has been found that the width of the grain boundary is 8 Å as shown in figure (4.19).

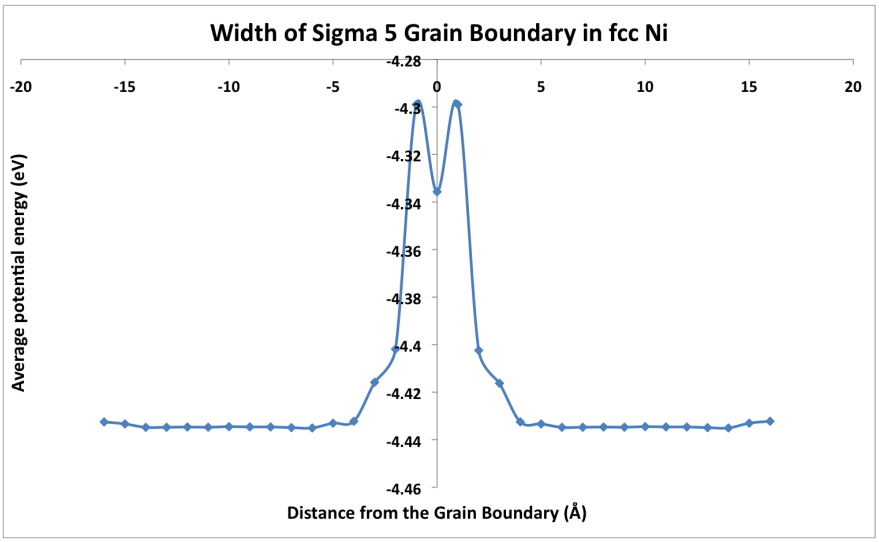

Figure 4.19: The width of Σ5 GB in fcc Ni.

Vacancy segregation at different sites from the grain boundary

The formation energy of a vacancy in the lattice has been computed at different sites near the grain boundaries in order to understand the driving forces for the segregation of vacancies to the GB. The values obtained were compared to the vacancy formation energy in the bulk site,

$$E_s = E^V_{GB} - E^V_{bulk}, \tag{4.4}$$

where E^V_{GB} is the formation energy of the vacancy near the GB and E^V_{bulk} is the formation energy of the vacancy in the bulk. The results obtained shows that there are some sites near the GB that prefer to have a vacancy as shown in figure (4.20).

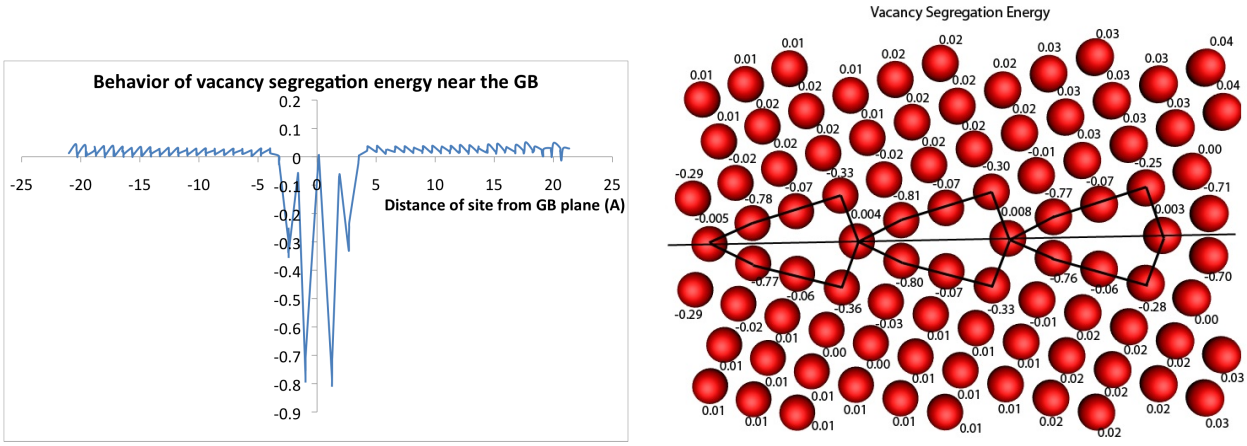

(a) (b)

Figure 4.20: Vacancy segregation energy (eV) (a) as a function of the distance from the GB and (b) at the different sites near the GB. The figure illustrates that there are some regions near the GB that prefer to host a vacancy.

Vacancy migration toward the grain boundary

Although the vacancy segregation energies in figure (4.20) illustrate a preference for vacancies to sit near the GB they do not show if the vacancies will diffuse toward the GB. The diffusion of a vacancy towards the GB has been investigated. This is done by creating a single vacancy at different sites near the GB and simulating the diffusion using otf-KMC. It has been found that the vacancy moves toward the GB in most cases as shown in Figure (4.21). The typical diffusion barrier for the vacancy is 0.9 eV. For instance, a vacancy created at distance equal to 20 Å from the GB took 0.846 ms to reach the GB as shown in Figure (4.21b) and 2.23 μs from distance of 5 Å as shown in Figure (4.21a). In the cases where the vacancy does not diffuse to the GB, it diffused to the fixed boundaries and got trapped. This is an artefact of our simulation boundary conditions.

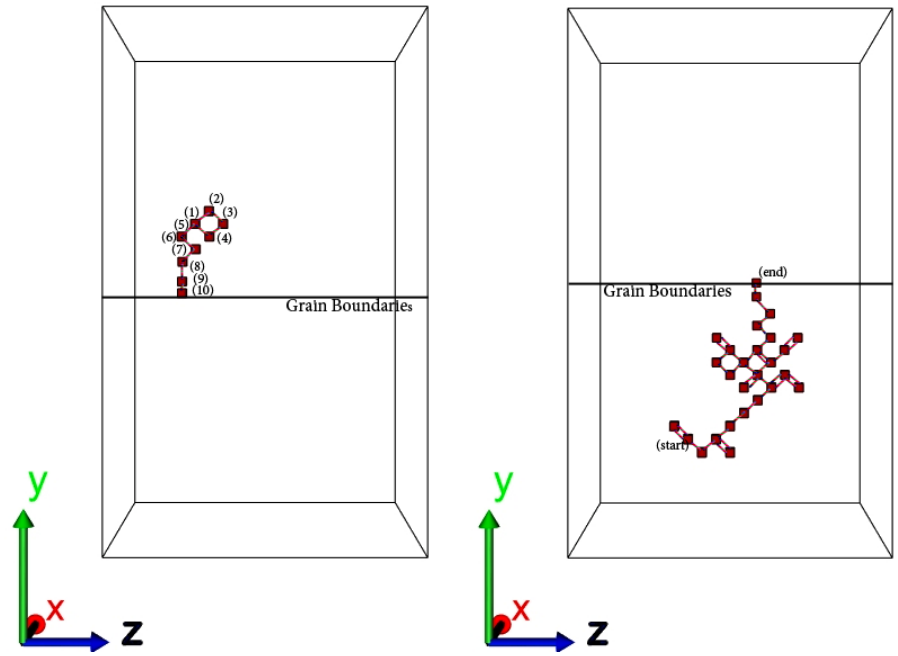

(a) (b)

Figure 4.21: Vacancy diffusion pathways at different sites toward the GB. These figures illustrate how vacancies are attracted towards the GB (a) shows the diffusion of a vacancy created at distance of 5Å from the GB towards the GB in 2.23 μs, (b) shows the diffusion of a vacancy created at distance of 20 Å in 0.846 ms towards the GB.

Evolution of defects after 1 keV cascades

Results for 1 keV collision cascades have been investigated in a pure Ni GB system with 8470 atoms. It has been found that after simulating a collision cascade for 20 ps using MD most defects accumulated on the GB as shown in figure (4.22a). Otf-KMC was then used to simulate the evolution of defects in the resulting system at a temperature of 500 K. Most of the interstitials either annihilated or recombined with vacancies and the vacancies were found to form clusters or combine with interstitials as shown in figure (4.22b). Although we could see some vacancy diffusion to the GB, the vacancies diffuse over much longer timescales and are more likely forming clusters than the interstitials.

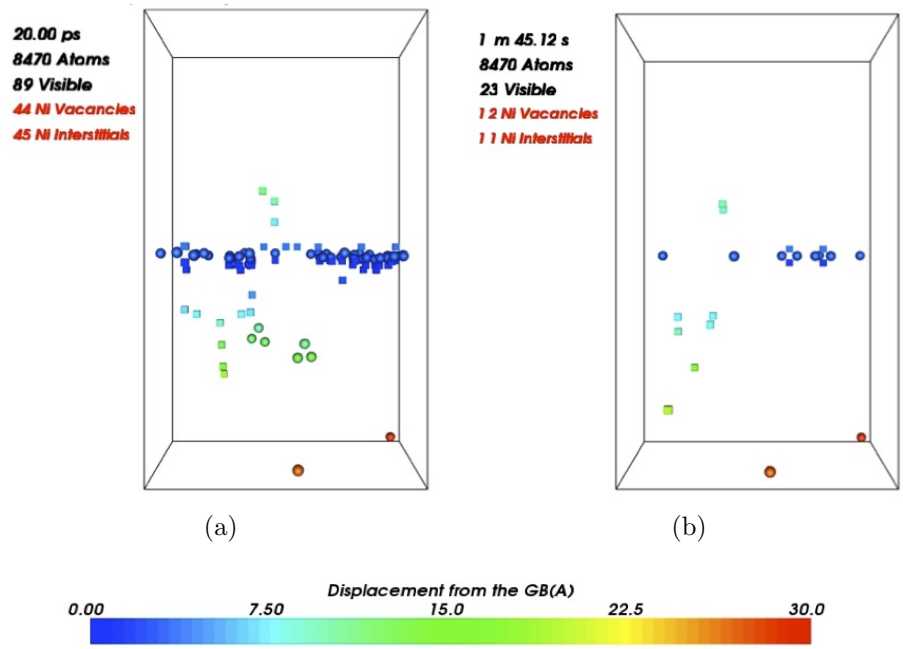

Figure 4.22: The figure shows the result obtained from simulating the defects resulted from 1 keV collision cascades with the defects coloured according to their distance from the GB, (a) The pure Σ5 GB system after a 1 keV collision cascades. (b) The system after otf-KMC. In all figures sphere is an interstitial and cube is a vacancy.

The evolution of defects in the Σ5 GB system after 1 keV collision cascades has been also studied using bigger system (approximately 55k atoms). Similar diffusion mechanisms have been observed as the defects initially accumulated at the GB during the collision cascades, as shown in figure (4.23a). During the otf-KMC the mobility of interstitials was observed to be much higher than that of the vacancies. A number of defects annihilated due to recombinations between vacancies and interstitials. The vacancies were found to be attracted to the GB if they were near the GB. After an otf-KMC time of 4.93 μs, 16 recombinations had occurred between vacancies and interstitials as shown in figure (4.23b).

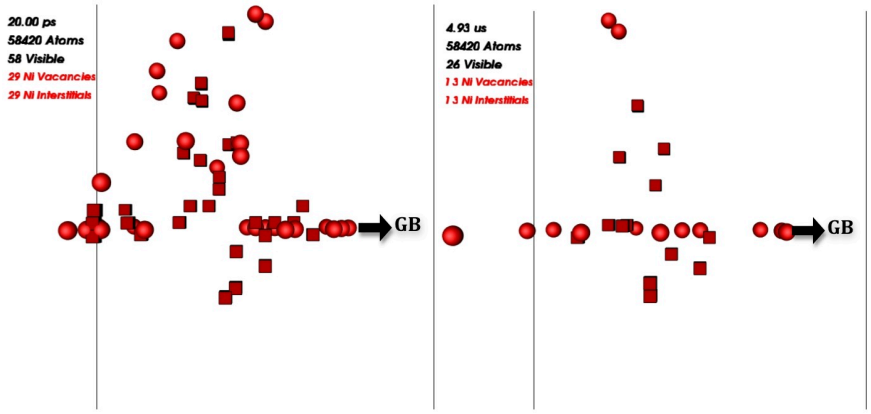

(a) (b)

Figure 4.23: Evolution of radiation damage in the fcc Ni Σ5 system, (a) shows the damage after the MD simulation, (b) after the otf-KMC. In all figures sphere is an interstitial and cube is a vacancy.

A number of interesting transitions were observed during the otf-KMC simulations, which illustrate the power of these methods for the evolution of radiation damage. In agreement with the work of Bai *et al.* [75] we observed a number of cases where interstitials were emitted from the GB to recombine with a vacancy sitting near GB. An example of such an event is shown in figure (4.24).

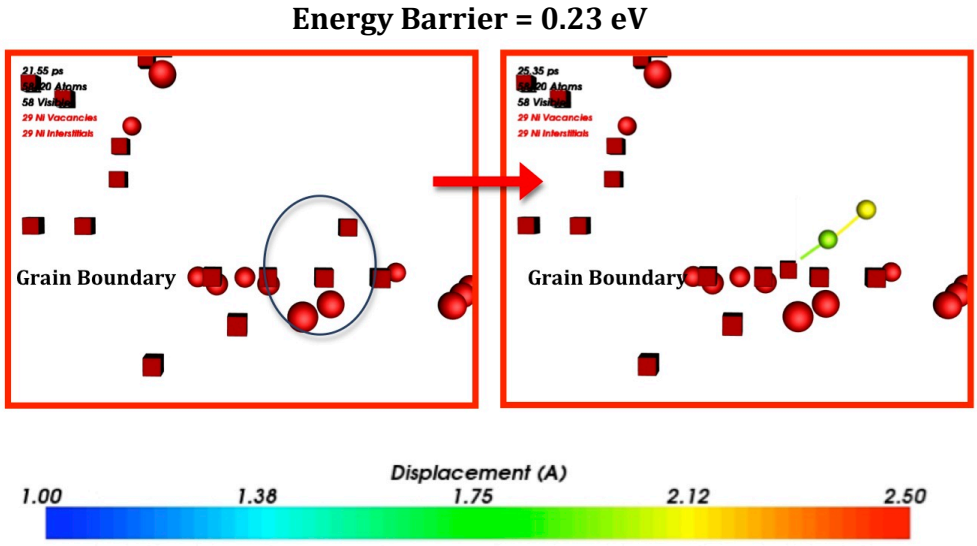

Figure 4.24: The emission of an interstitial from the GB to combine with vacancy sitting near the GB. In all figures sphere is an interstitial and cube is a vacancy.

Similar to the bulk system, a number of transitions involving concerted motions of interstitials were observed in the simulation. These include recombinations with vacancies in the

bulk, where the vacancy and interstitial are separated by few Angstroms; for example see figures (4.25a & 4.25b). Also, the diffusion of an interstitial towards a GB is shown in figure (4.25c).

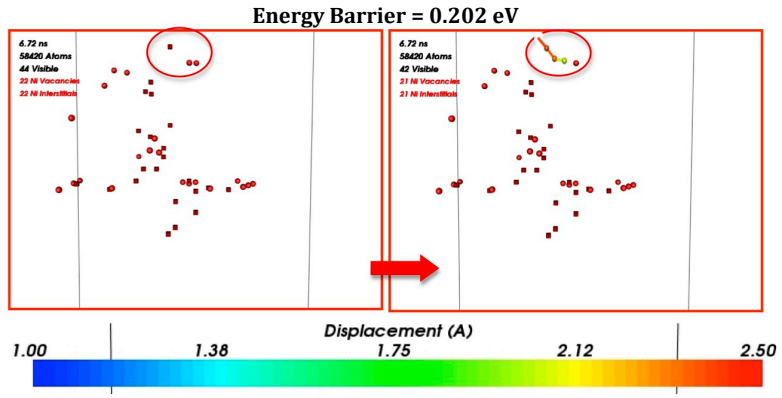

(a)

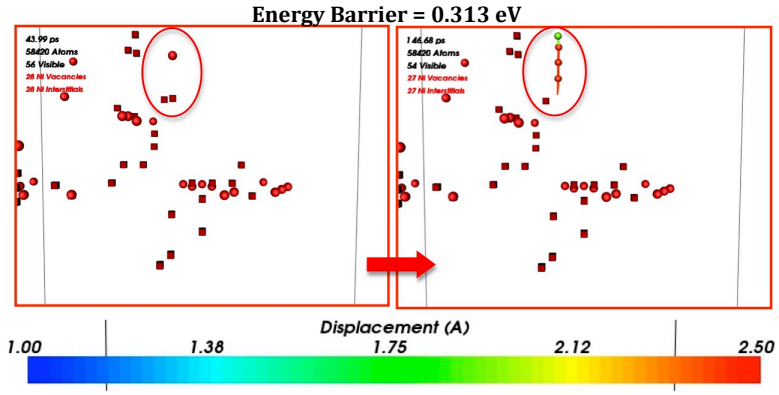

(b)

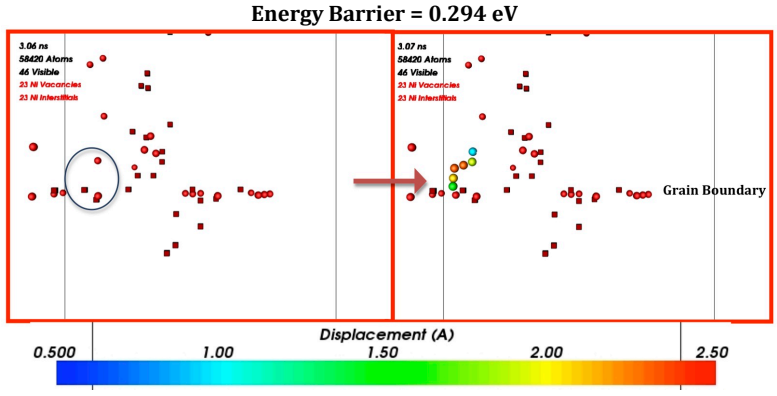

(c)

Figure 4.25: Examples of concerted movements of interstitials during the otf-KMC phase of the simulation. (a) and (b) shows a long range recombination of a vacancy and an interstitial, (c) shows the migration of an interstitial to a GB in a single hop. In all figures sphere is an interstitial and cube is a vacancy.

The twin GB, as expected, did not have a big influence on how defects were distributed in the system or their migration. The defects were scattered in the system after the collision cascade. During the otf-KMC simulation a number of vacancy-interstitial recombinations happened in the system, before a vacancy cluster formed which resulted in the simulation being dominated by vacancy hops in the cluster. After we blocked these very low barriers, with the previous method explained for the bulk system, more recombinations occurred to leave a system of only 8 defects after 15.2 μs. Originally there were 36 defects after the collision cascade. The defects in the twin GB system after the collision cascade and after the otf-KMC are shown in figure (4.26).

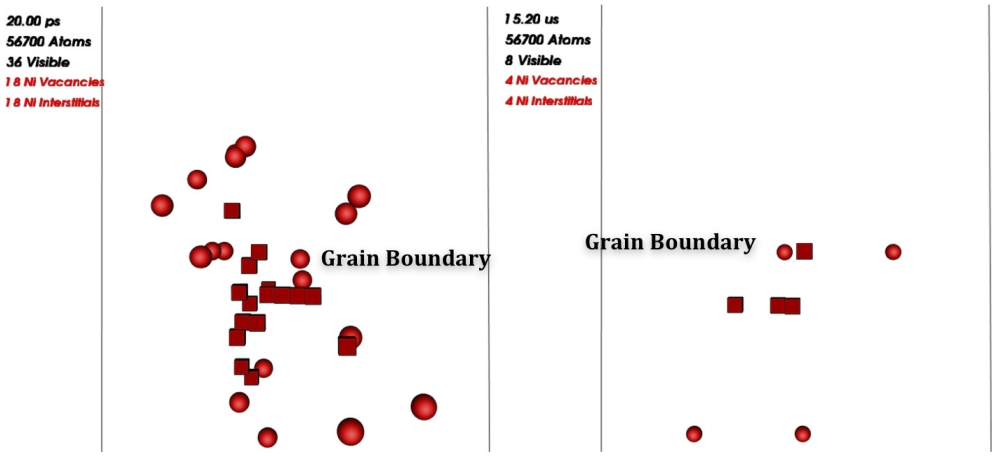

(a) (b)

Figure 4.26: Evolution of radiation damage in the fcc Ni $\Sigma 3$ system, (a) shows the damage after the MD simulation, (b) after the otf-KMC. In all figures sphere is an interstitial and cube is a vacancy.

Similar mechanisms of recombination between vacancy and interstitial have been observed in the simulation of the twin grain boundary as shown in figure (4.27).

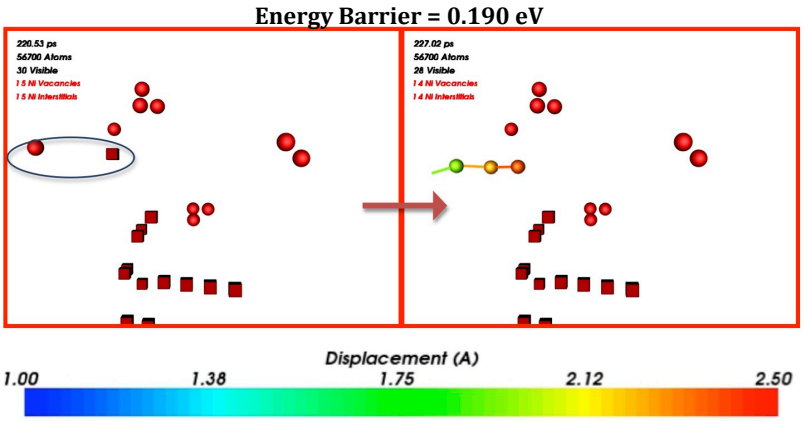

Figure 4.27: Recombination between an interstitial and a vacancy in twin GB system fcc Ni. In all figures sphere is an interstitial and cube is a vacancy.

Multiple collision cascades

The system with the 8470 atoms has been used to model multiple collision cascades using the same simulation conditions. Each cascade modelled for 20 ps using MD with the cascade initiated in a random direction with the PKA atom randomly chosen. After the collision cascade stopped, the system was simulated with the otf-KMC for approximately 0.2 seconds after which a further collision cascade was simulated in the system. The time between cascades has been calculated as follows:

1. We have an Ion flux of : 9.5×10^{15} ions/(cm^{2}s).
2. We assume a penetration depth of 2 μm.
3. We multiply the flux by the volume of our simulation box:

   Number of events $= \frac{9.5\times10^{15}\ \text{ions}}{2\times10^{-10}\ \text{m}^3\text{s}} \times (41.11 \times 65.669 \times 38.72 \times 10^{-30}\text{m}^3) = 4.96$ events/s, which means that we will have $\approx 0.2\ s$ between events.

Figure (4.28) shows the system at the end of three consecutive collision cascades; part (a) figures are at the end of MD steps and the part (b) figures their subsequent otf-KMC steps, the clock has been restarted after each collision cascade.

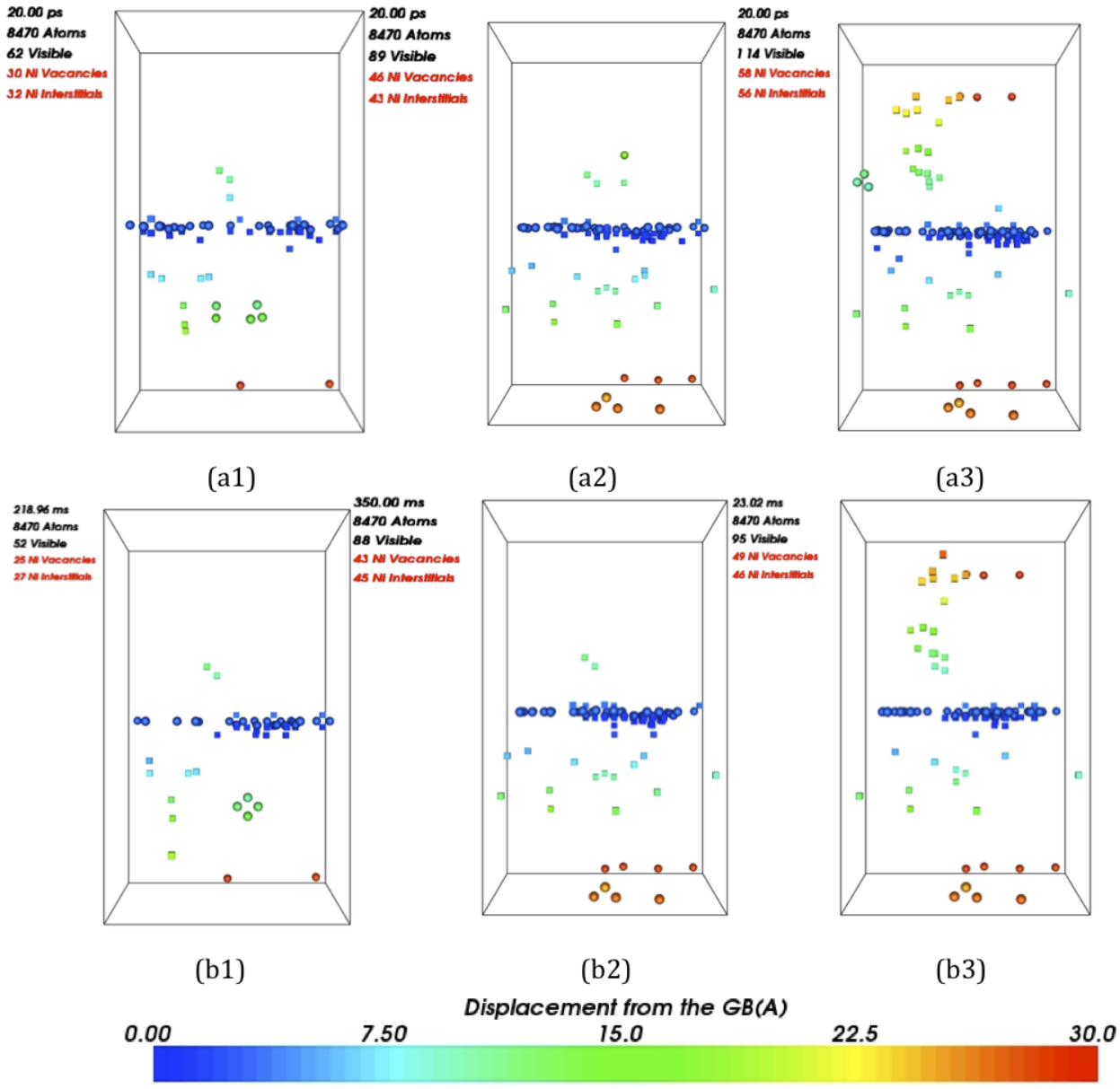

(a)

Figure 4.28: Simulation of Σ5 GB pure Ni with multiple 1 keV collision cascades. The PKA is chosen randomly and the collision cascades is directed towards the GB. Three steps are shown in the figure. (a1, a2 & a3) show the system after collision cascades at each step. (b1, b2 &b3) show the system after otf-KMC at each step.

The results obtained show that most defects will accumulate near the GB. After the otf-KMC steps it can be noticed that it is mainly vacancies that are left in the bulk, with almost all interstitials present in the bulk being accumulating at the fixed boundary conditions. Vacancies show a tendency to form clusters and overall there is only small growth in total defects numbers after the three collision cascades.

4.4 Results and Discussion (Ni-Cr Binary Alloy)

4.4.1 Bulk System

Displacement Threshold energy

The DTEs in the binary system depend on the local environment of the PKA where we start the collision cascade. We calculated a sample of the energies required to create defects to have an insight of the effects of Cr atoms on changing the DTEs. We picked the PKA randomly and calculated the DTEs for 66 trajectories starting from that atom. The same steps used in the pure Ni have been used here where the DTE has been calculated with max error of +/- 0.1 eV. The results obtained were represented by showing the PKA trajectories as shown in figure (4.29a) and by plotting a histogram as shown in figure (4.29b).

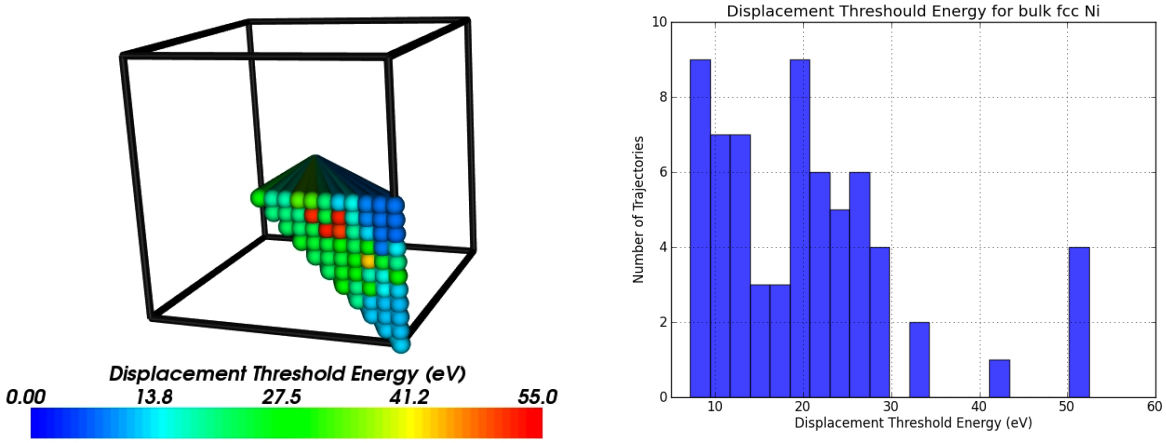

(a) (b)

Figure 4.29: Displacement Threshold Energies for the binary system for 66 PKA trajectories, (a) shows the results calculated for the set of 66 directions and (b) shows the distribution of the DTEs found. The PKA is chosen to be the atom in the middle of the system.

The maximum DTE was found at direction ⟨1 0.8 0.5⟩ with value of 52.44 eV and the minimum DTE was found to be 7.13 eV at direction ⟨1 0.8 0⟩. The average DTE was found to be 20.35 eV. Therefore, we can see that the presence of Cr atoms decreased the overall DTE, which we expect due to the difference of orientations of Ni and Cr atoms.

Collision Cascades (1 keV)

A system containing 55,296 atoms has been used to study the damage after 1 keV collision cascades. The system was first thermalised to room temperature for 8 ps with thermal layers

of 3 Å. The resulted system has been used to run 66 collision cascades with different PKA trajectories.

Investigating the damage produced after 1 keV collision cascades shows variation in the number of defects produced between 18 and 54 after 20 ps as shown in figure (4.30a). An illustration of the number of defects against the PKA trajectories is shown in figure (4.30b). Figure (4.31) shows pictures of the maximum and minimum number of defects produced after 1 keV in NiCr binary system.

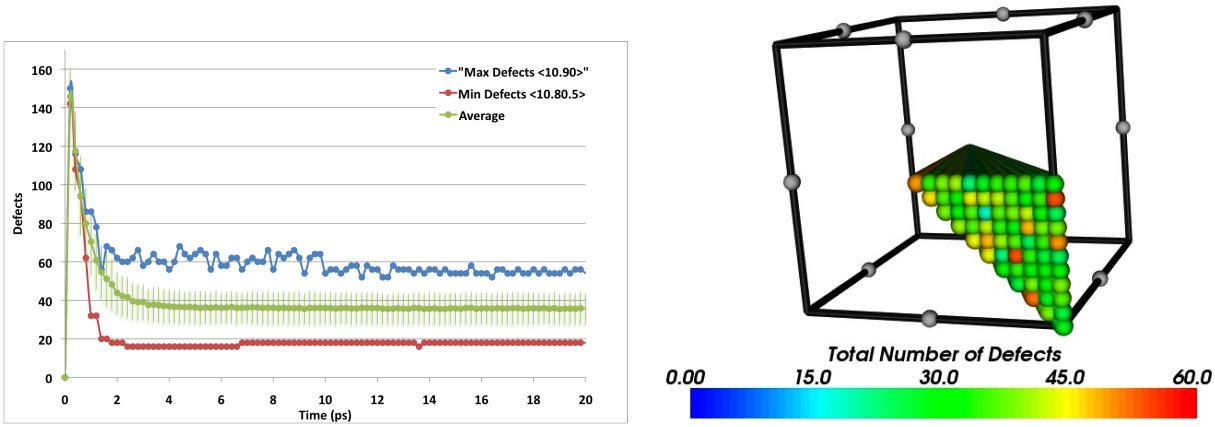

(a) (b)

Figure 4.30: a)1 keV Ni-Cr cascade defect evolution as a function of time. Blue and red lines represent the PKA trajectories that will give maximum and minimum number of defects after 20 ps, b)The number of defects in all trajectories.

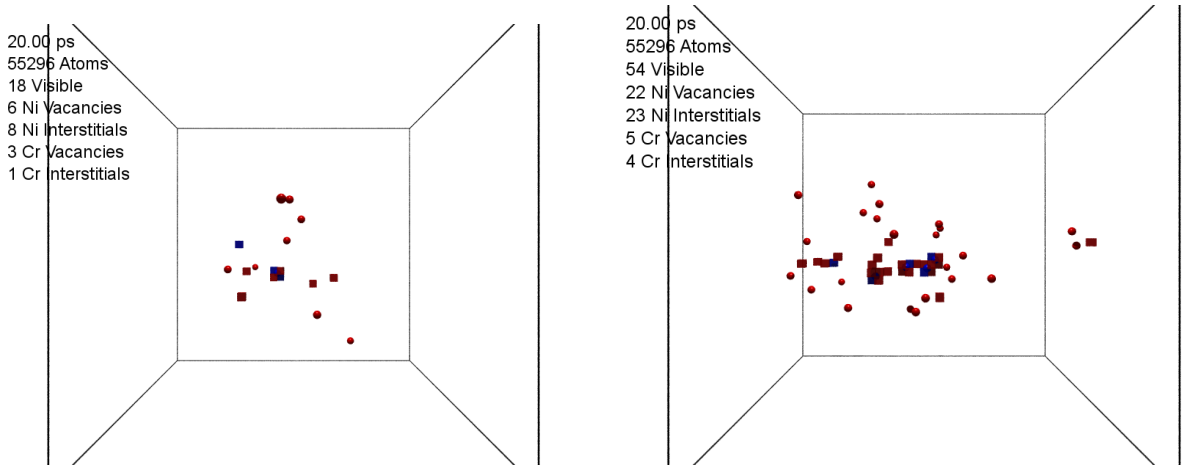

(a) (b)

Figure 4.31: Damage after 1 keV collision cascades in Ni-Cr binary system. (a) shows the minimum number of defects produced with trajectory ⟨1 0.8 0.5⟩, (b) maximum defects ⟨1 0.9 0⟩.

Collision cascades (Lower Energies)

A system containing 32,000 atoms was used in this simulation, the system was thermalised to 298 K. Collision cascades carried at energy of 100, 200, 300, 400, 500 and 600 eV. At each energy 66 directions were performed. Pictures shows the number of defects remained in the systems after collision cascades are shown in figures (4.32, 4.33).

From these figures, the number of defects increase with the increase of the energy as was expected. Also the average of the increment of the number of defects is approximately linear with the increase of the collision energy as can be seen in figure (4.33).

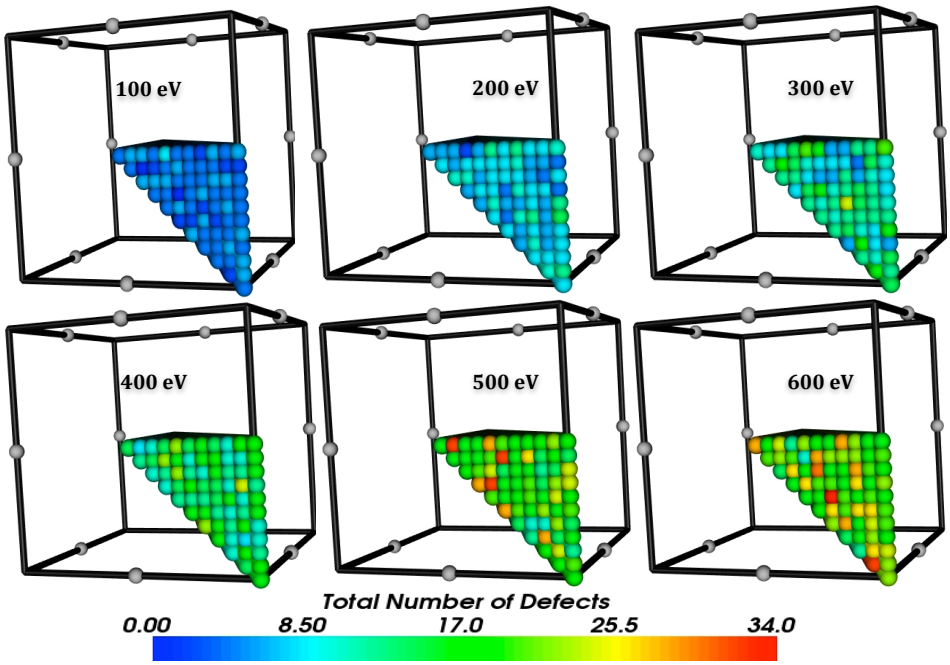

Figure 4.32: Damage in Ni-Cr binary alloy after 20 ps collision cascades. The figure shows the results calculated for the set of 66 directions with 100, 200, 300, 400, 500 and 600eV.

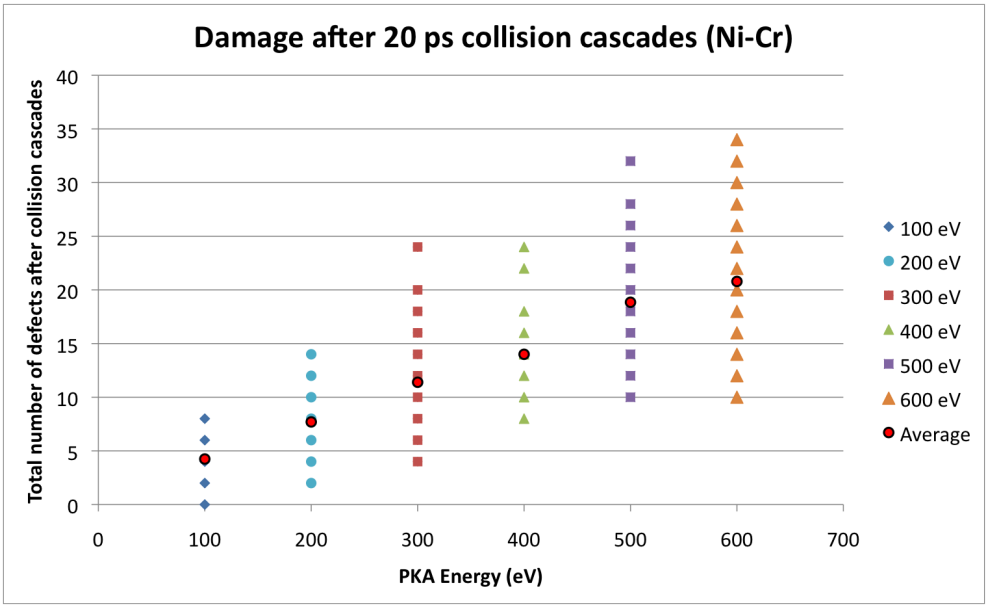

Figure 4.33: Damage in Ni-Cr binary alloy after 20 ps collision cascades.The figure shows the damage left in the binary system after 100, 200, 300, 400, 500 and 600 eV collision cascades in 66 directions and highlights the average of the defects at each energy.

Long Time Scale Dynamics

Similar to the pure fcc Ni, the bulk alloy system contains approximately 55k atoms and has been modelled with periodic boundary conditions in 3 dimensions using an energy of 1 keV to perform the collision cascades. For the bulk alloy system the observed transitions had higher barriers than those for the pure Ni system. A vacancy cluster resulted from the collision cascades as was seen for the pure fcc Ni case. The cluster and a few dumbbells are still present after running for 11 ms in the otf-KMC, with the results similar to the pure Ni case. Pictures of the system after collision cascades and after otf-KMC are shown in figure (4.34).

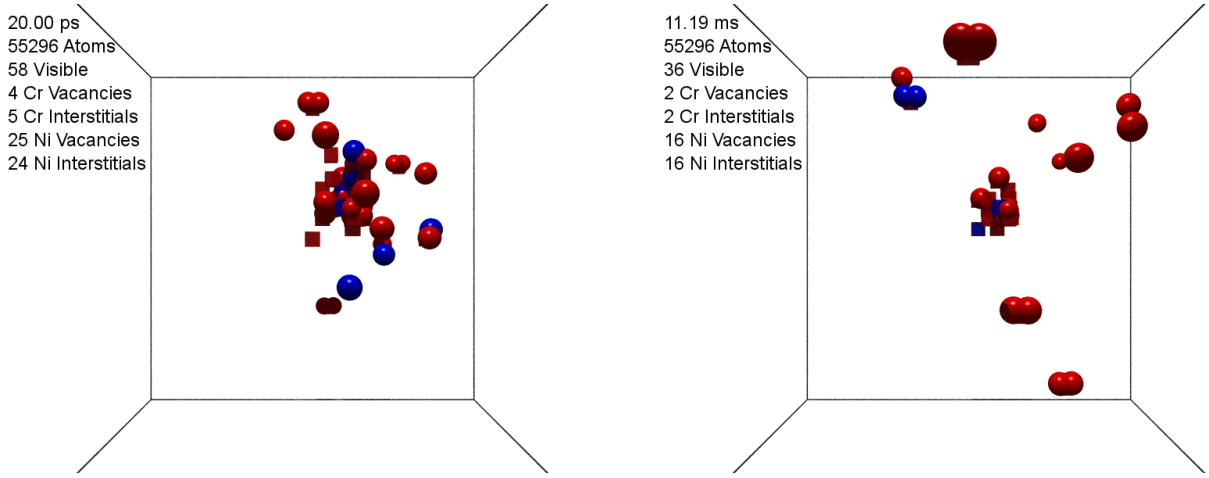

Figure 4.34: Evolution of radiation damage in the Ni-Cr bulk system, (a) shows system after MD simulation, (b) after otf-KMC. In all figures sphere is an interstitial and cube is a vacancy.

From figure (4.34), the number of defects decreased from 58 to 36 during the KMC simulation. In other words, 11 recombinations between vacancies and interstitials in 11.19 ms. There are a range of interesting transitions noticed in the KMC simulation similar to the pure Ni case. Examples of these transitions are shown in figure (4.35).

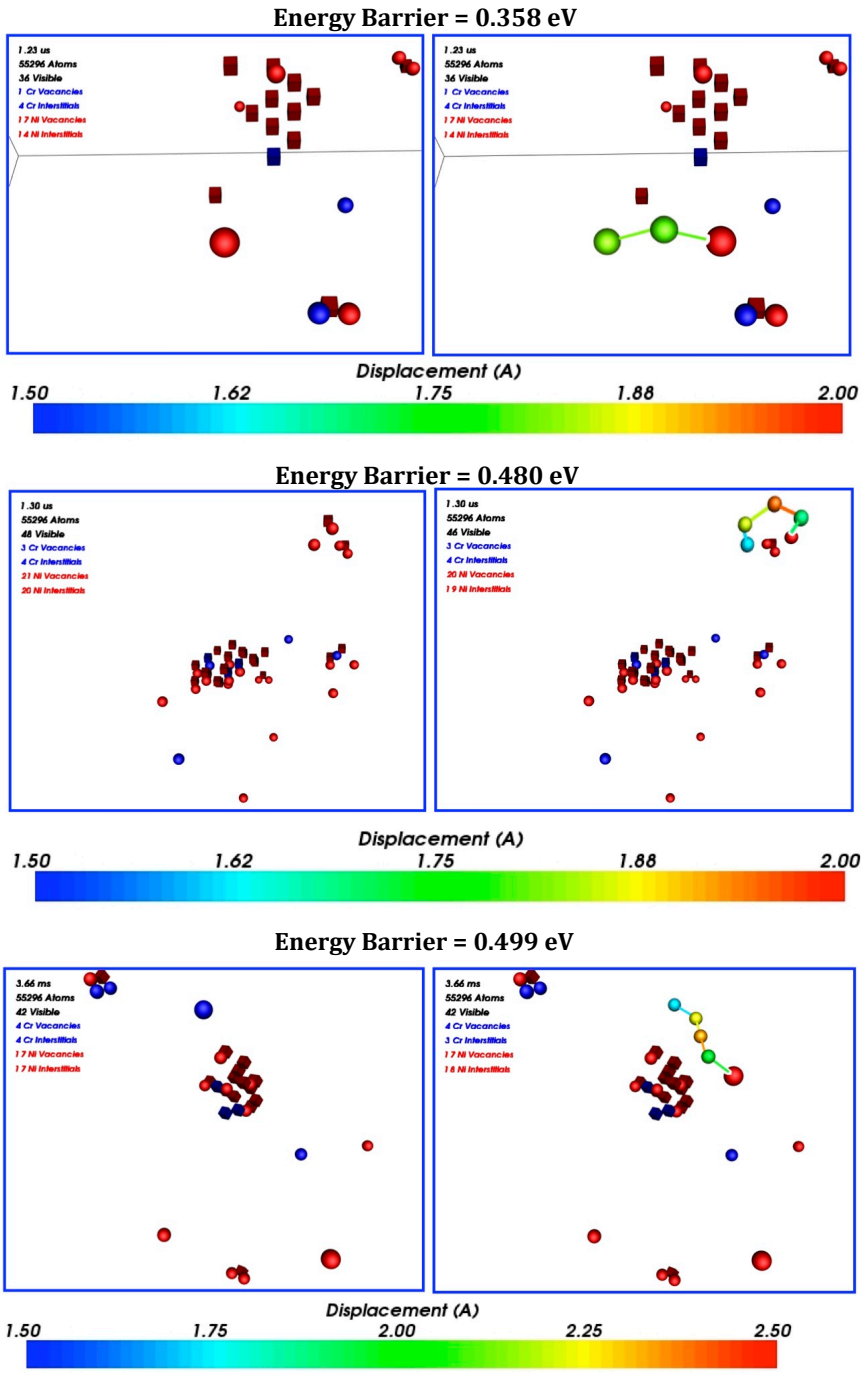

Figure 4.35: The pictures show examples of concerted movements of interstitials seen during the otf-KMC simulation for the Ni-Cr bulk system. The pictures illustrate the mechanism of the long movements for the interstitials through an intermediate chain of interstitials up to few Angstroms. In all figures sphere is an interstitial and cube is a vacancy.

4.4.2 Grain Boundaries

Cr segregation at different sites from the Grain Boundaries

The Cr segregation to the GB boundary has been checked by placing a Cr atom in the pure Σ5 GB system at different sites from the GBs and comparing the energy with the energy of depositing the Cr atom in the bulk system. From the results obtained, the Cr atom is found to prefer to sit at some sites near the GB as shown in figure (4.36).

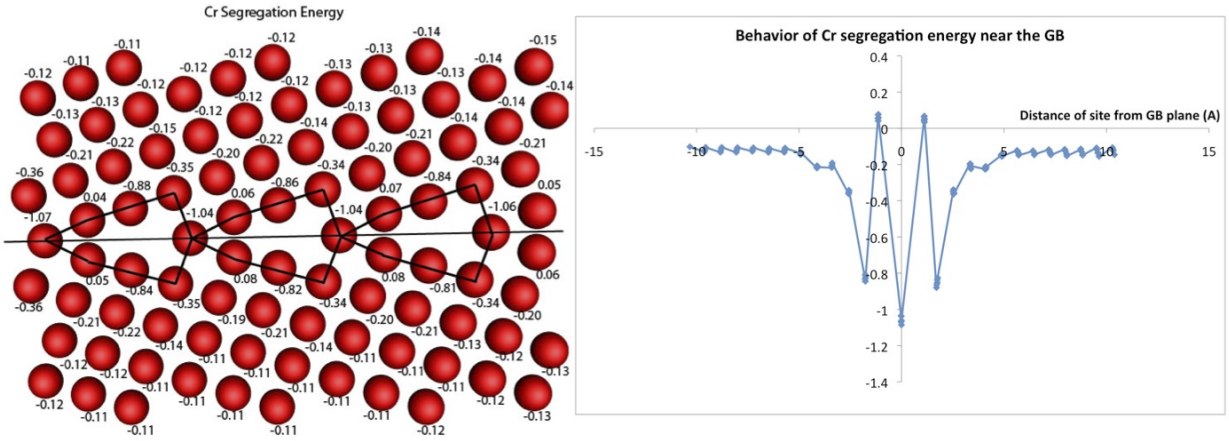

Figure 4.36: Behaviour of Cr segregation energy near the GB.

Long Time Scale Dynamics

The Cr atoms were distributed randomly in the system with the required percentage. Similar to the pure GBs, periodic boundary conditions are implemented in X and Z directions and a few layers are fixed in edges parallel to the GB. Both Σ5 and Σ3 GBs have been fully relaxed and a 1 keV collision cascades with the PKA chosen randomly and directed towards the GB was modelled.

Twin Grain Boundary

The twin boundary in the Σ3 alloy system was found to have more influence on defects than for the pure Ni system. Figure (4.37) shows a snapshot of the system immediately after the collision cascades and after the otf-KMC. Very little recombination is seen to occur in the 242 μs simulated and there is a far greater accumulation of defects at the GB.

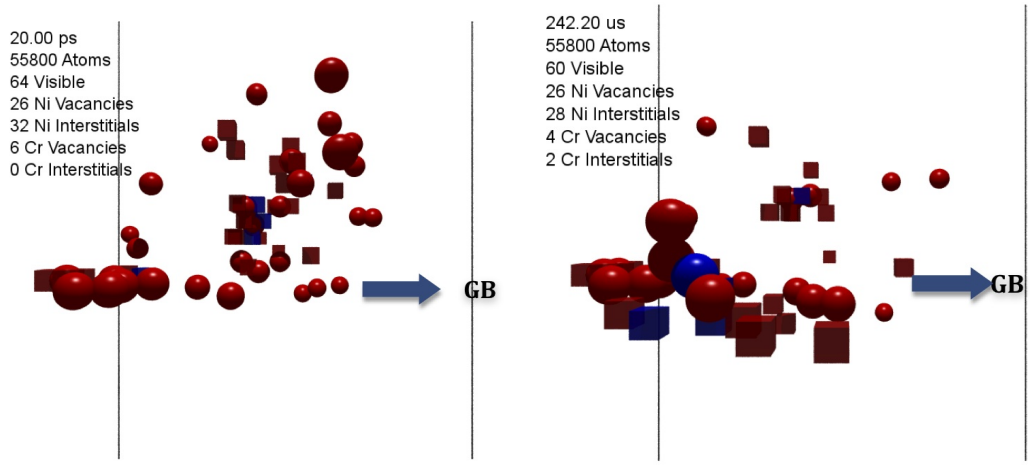

Figure 4.37: Evolution of radiation damage in the Ni-Cr twin GB system, (a) shows the system after the MD simulation, (b) after otf-KMC. In all figures sphere is an interstitial and cube is a vacancy.

Similar transitions have been seen in the otf-KMC simulation. Figure (4.38) shows a mechanism of vacancy and interstitial recombination and concerted movement of an interstitial.

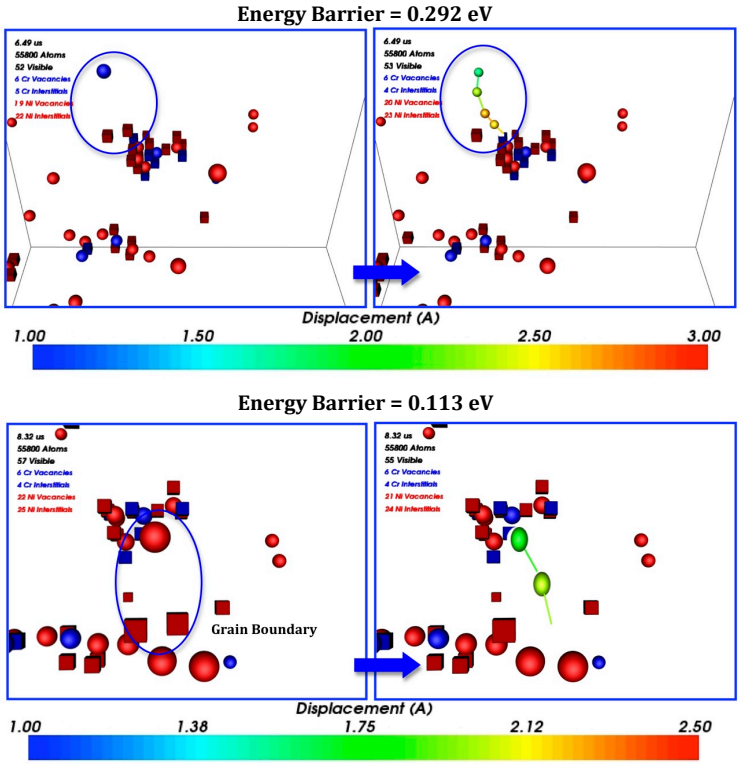

Figure 4.38: Examples of transitions in the Ni-Cr twin GB system during the KMC simulation. The figures illustrate the mechanism of recombination between a vacancy and an interstitial that are a few Angstroms apart from each other by introducing a chain of interstitials between both defects. The top figure shows recombination seen in the bulk and the bottom figure shows the recombination of a vacancy on the GB and an interstitial sitting near the GB.

$\Sigma 5$ **Grain Boundary**

In the $\Sigma 5$ GB alloy system most of the defects accumulated at the GB. During the otf-KMC simulation vacancies were observed to migrate quickly to the GB, if they were near the GB. Most defects further away either annihilated by recombination between vacancies and interstitials or migrated towards the GB. Figure (4.39) shows snapshots of the system immediately after the collisions cascade and after the otf-KMC.

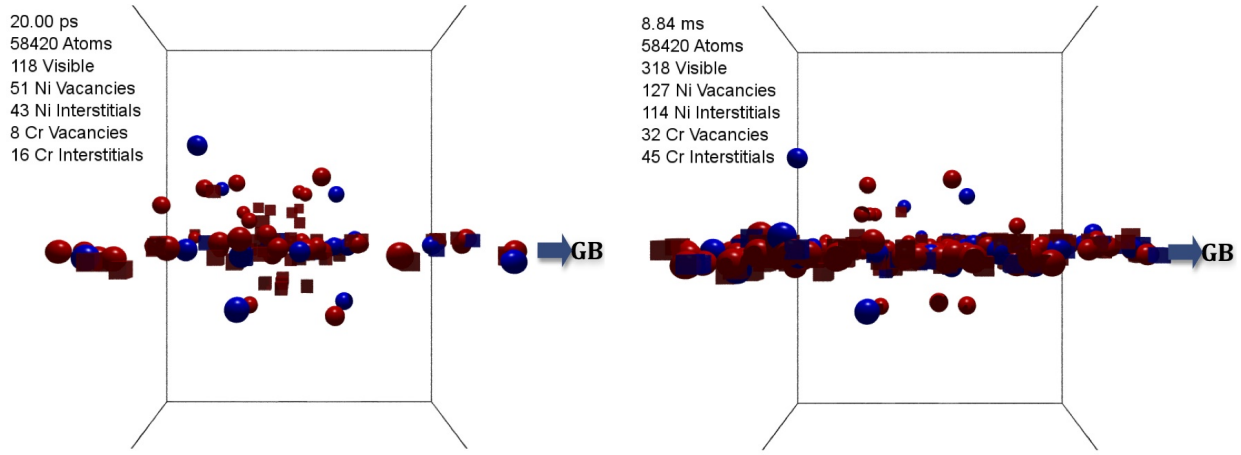

Figure 4.39: Evolution of radiation damage in the Ni-Cr Σ5 GB system, (a) shows system after MD simulation, (b) after otf-KMC. In all figures sphere is an interstitial and cube is a vacancy.

Similar transitions were observed during the otf-KMC simulations, which illustrate the power of these methods for the evolution of radiation damage. Examples of these transitions seen in the simulation of the Σ5 GB system are shown in figure (4.40). In addition, a vacancy is found to be attracted to the GB. Figure (4.41) illustrates the steps of vacancy migration to the GB.

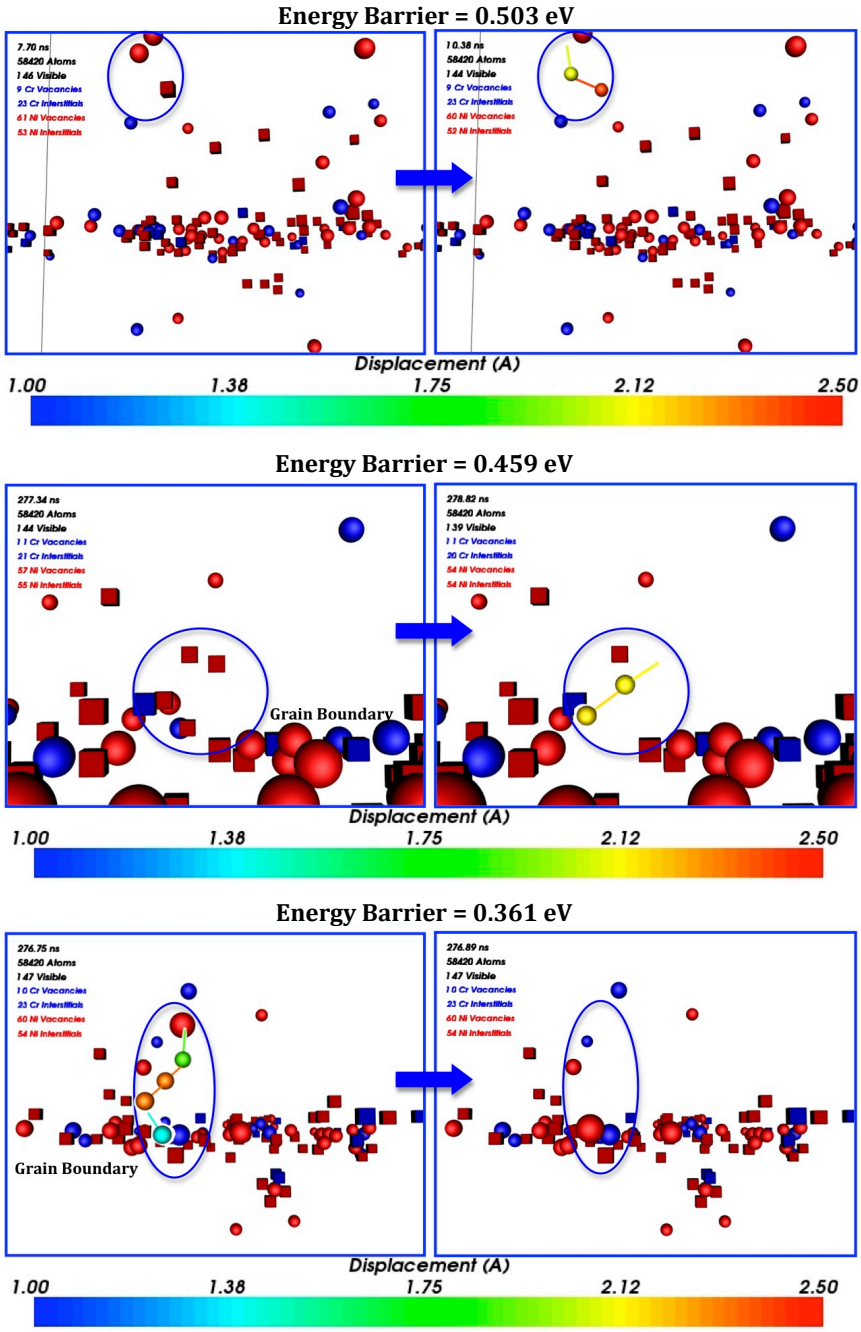

Figure 4.40: Examples of transitions seen in the Ni-Cr Σ5 GB system during otf-KMC simulation. The figures illustrate the mechanism of recombinations between a vacancy and an interstitial that are few Angstroms apart from each other by introducing a chain of interstitials between both defects. The top figure shows recombination seen in the bulk and for interstitials on the GB and vacancies sitting near the GB. The bottom figure shows a concerted movement of an interstitial to the GB. In all figures sphere is an interstitial and cube is a vacancy.

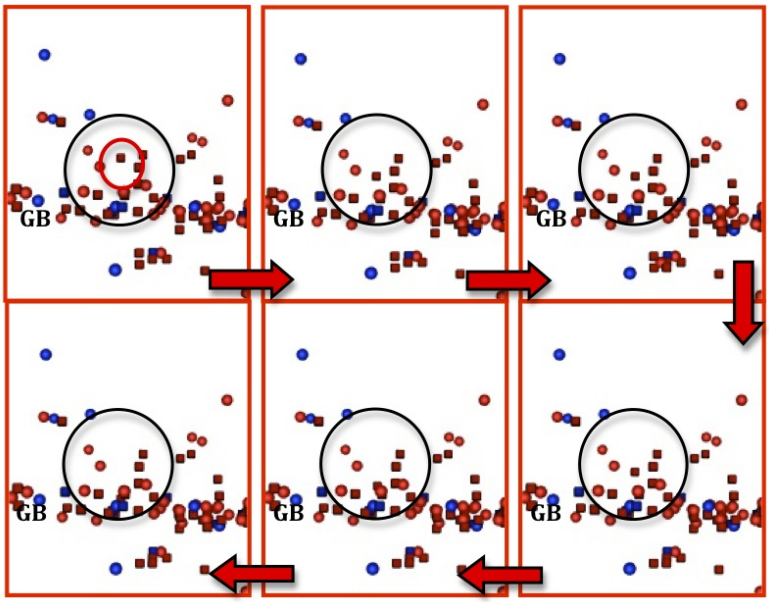

Figure 4.41: Pictures show the migration of vacancy towards the Σ5 GB during the otf-KMC simulation.

4.5 Roughening of the GB

For the case of the Σ5 GB in the alloy system, we found that the number of defects increased during the otf-KMC simulation. The GB at the start of the simulation is clearly defined by a plane. Due to the displacement and migration of atoms sites during the simulation, sites that were part of the top GB become part of the bottom GB. Thus the GB can no longer be defined by a plane. We tried to look if there is any roughening happened in the Σ5 GB for both pure Ni and the Ni-Cr systems. We extended the coincident site lattices of the top and bottom grains and looked whether atoms have changed grains. Figure (4.42) shows the process of extending both grains and figure (4.44b) shows an example of the roughening obtained in the GB for the Σ5 alloy system.

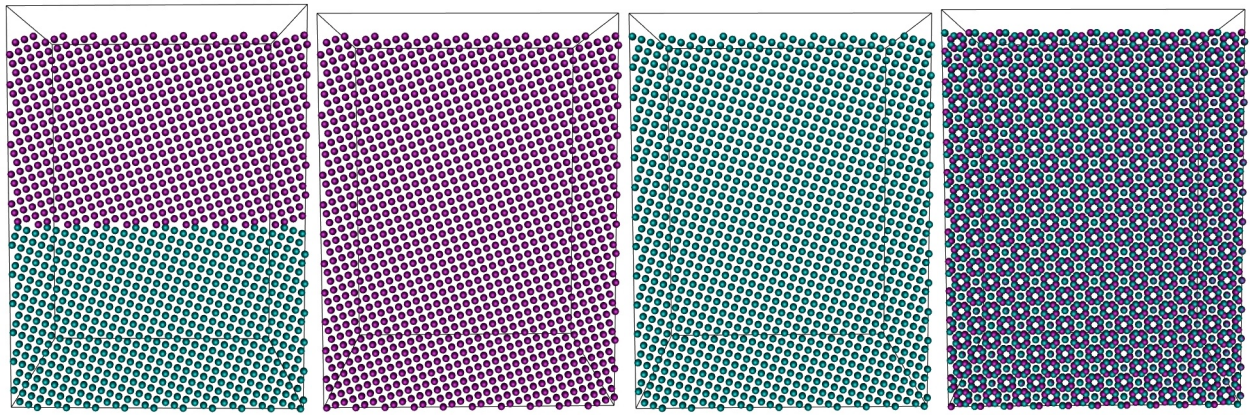

(a) (b) (c) (d)

Figure 4.42: Grain boundary roughening; (a) shows the two grains, (b) shows the top grain after extending the coincident site lattices, (c) shows the bottom grain after extending the coincident site lattices and (d) shows both extended grains.

After extending the original grains, the system checked to see whether atoms have changed grains. Those atoms were considered to be defects. A slight roughening has been noticed for the pure Σ5 GB as shown in figure (4.43).

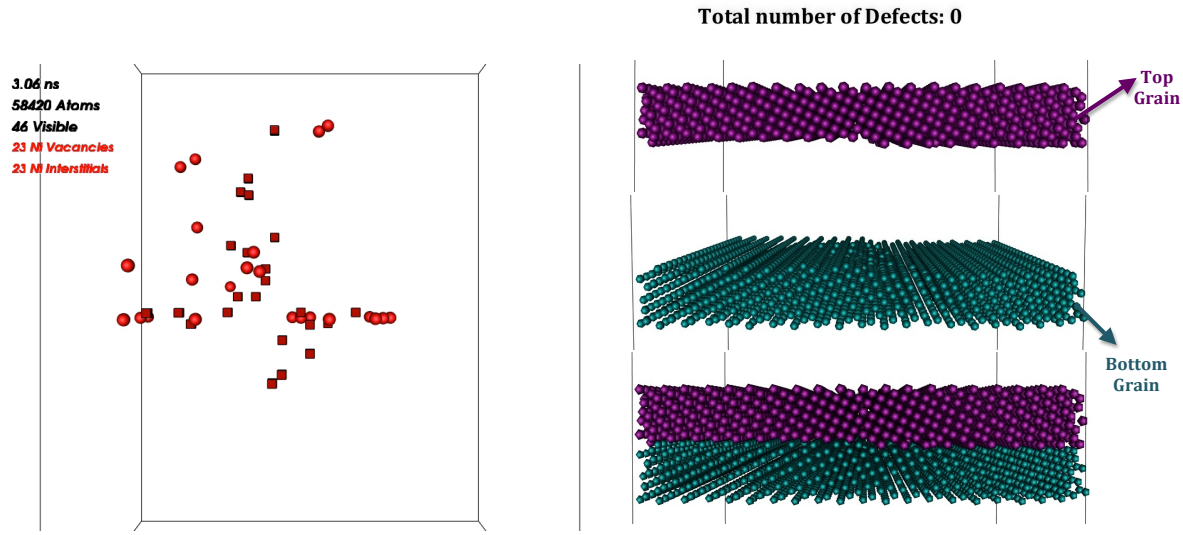

(a) (b)

Figure 4.43: GB roughening in Σ5 GB in pure Ni; (a) shows the damage after the otf-KMC by comparing the system to the reference system, (b) shows the two grains after otf-KMC where slight GB roughening can be seen.

For the case of the Σ5 GB in the alloy system, we observed that there was a large amount of roughening at the GB for this system and the number of real defects decreased from 306

defects to only 55 defects, as shown in figure (4.44).

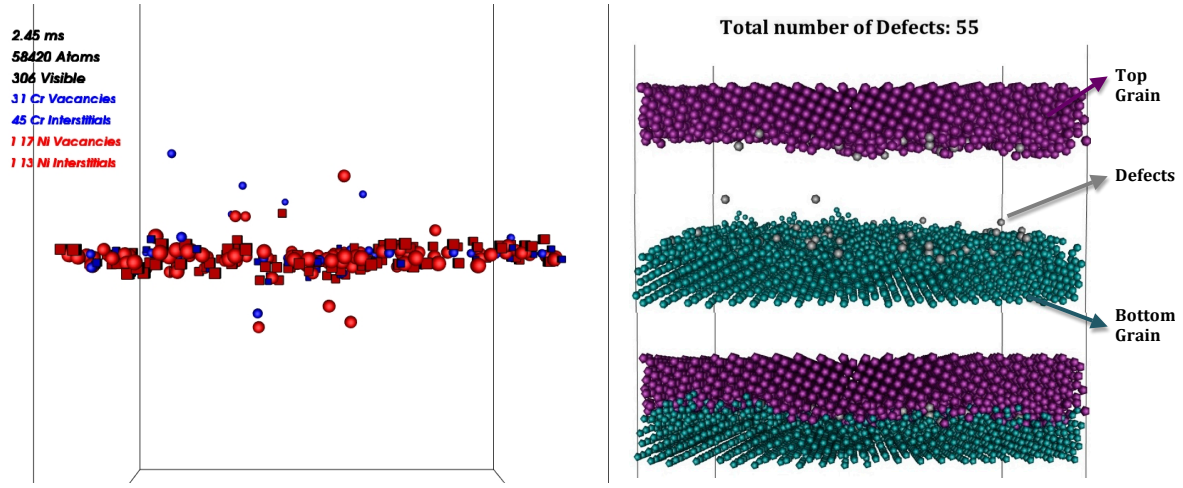

(a) (b)

Figure 4.44: The roughening of the GB for the Σ5 alloy system observed after long timescale evolution of the radiation damage; (a) shows the damage after the otf-KMC by comparing the system to the reference system; (b) shows the two grains after otf-KMC where slight GB roughening can be seen.

4.6 Discussion and conclusions

MD along with otf-KMC has been used to model radiation damage near a GB in pure Ni. Two types of GBs have been studied, symmetrical tilt Σ5 and Σ3 GBs. A small system of Σ5 GB (8470 atoms) has been used to study the vacancy segregation at different sites from the GB. It has been found that some sites near the grain boundaries are more favourable to host a vacancy. The same system has been used to study the vacancy diffusion towards the GB and it has been found that a vacancy in the bulk site will be attractive to the grain boundary and will diffuse towards it in most cases. In the cases that a vacancy does not diffuse to the GB, it got trapped at the fixed layers.

Two Σ5 systems have been used to model the evolution of defects after 1 keV collision cascades, a system with 8470 atoms and a system with 55k atoms. For both systems, the defects resulting from collision cascades are found to accumulate on the GB and most of the interstitials annihilate or recombine with vacancies. The mobility of interstitials is found to be much higher than the vacancies which were found to form clusters in the bulk.

The 8470 atoms system has been used also to model the evolution of defects after multiple

1 keV collision cascades. The first cascades has been modelled for 20 ps after the resulting defects were simulated using otf-KMC for 0.2 s before another collision cascades is modelled to the system. The process has been repeated for collision cascades with 3 consecutive KMC modelling. From the results obtained, the defects were found to accumulate on the GB and the same diffusion mechanism has been seen from single collision cascades for the interstitial and vacancies diffusion as has been seen in the multiple collision cascades. Overall, the growth of the total number of defects is found to be small when the system is subjected to multiple collision cascades. For example, the number of the vacancies increases from 25 to 49 after 3 collision cascades.

The twin GB system has been used to model the evolution of defects after 1 keV collision cascades. The twin GB has been found to have no effect on the distribution of the defects after collision cascades and they were scattered in the system. This was expected as the twin GB has orientation similar the bulk with a slight difference at the GB.

During the simulation, interesting diffusion mechanisms have been seen. For example, an interstitial was found to be emitted from the GB to combine with a vacancy sitting near the GB. This transition occurred with a lower barrier than the one associated with the migration of the vacancy itself. Also, an interstitial is found to migrate to GB in a single hop from a few Angstroms. Lots of recombinations between vacancies and interstitials have been seen during the simulation. These recombinations happened between vacancies and interstitials which are few Angstroms apart from each other. A chain of interstitials between both defects occurs for these kind of recombinations.

The Cr segregation to the GB has been investigated by comparing the energies of placing a Cr atom in both bulk sites and GB sites in the Ni matrix. From the results obtained, it has been found that there are some regions near the GBs that prefer to host a Cr atom.

Radiation damage has been studied for the Ni-Cr binary system under similar conditions. Overall, similar diffusion has been seen in the pure system, as has been seen for the alloy system. For example, otf-KMC simulations of the diffusion of vacancies to GBs show that in most cases a vacancy is found to be attracted to the GB. Also, the presence of large vacancy clusters in the simulations causes the simulation to go slower because of the small movement within the cluster in the bulk system. Furthermore, during the otf-KMC simulations numerous concerted motion transitions occurred. Examples of these include the recombination of an interstitial and vacancy and the concerted motion of the interstitial over a few Angstroms

with low barriers. The twin GB in case of the alloy has been found to have more influence on the diffusion of the system.

There has been an increase in the number of defects on Σ5 GB alloy system. Therefore, an investigation has been undertaken to study roughening at the GB. Large roughening has been noticed in the case of Σ5 GB alloy system when compared with the pure system compared to a slight roughening in Σ5 pure system post the simulation. This has been observed by extending the grains and checking whether atoms belong to which grain.

Chapter 5

Modelling Radiation Damage in fcc Ni with relation to the Experimental Results

5.1 Introduction

In experimental work on the project, radiation damage in pure Ni has been studied [12]. In these experiments pure Ni was irradiated with He_4 at 1 MeV with an ion flux in the range 1×10^{13} – 5×10^{16} ion/(cm^2 s) at room temperature. Furthermore, experiments were performed to study the radiation damage in the binary alloy NiCr, where two types of irradiation conditions have been investigated: NiCr with 1.5 MeV He_4 with ion flux in the range 1×10^{14} – 1×10^{16} ion/(cm^2 s) at room temperature and NiCr with 5 MeV Ni ions at 200°C and 450°C. The main results obtained from the experiment on pure Ni is that defects are dispersed in the system and no vacancy clusters have been seen at room temperature. In addition, the positron lifetime changes when the samples are annealed at 200°C, which indicates that the type of defects in the system has changed.

Results were obtained from SRIM calculations [12] in case of pure Ni irradiated with He_4 at 1 MeV while fixing the displacement threshold energy to 28 eV. From these results, the energies of the collision cascades were dominated by low energies. For instance, 50% of the energies of the collision cascades are found to be equal to 64 eV or less, 11% of the PKA have an energy in range 100 - 150 eV and 3.4% of the PKAs have an energy included in the range between 400 and 600 eV. Furthermore, it has been found that the number of PKAs with energy higher than 2 keV is very low (1.23%).

In this work, these experiments were modelled to provide insight into the experimental observations. The long timescale evolution of radiation damage in fcc Ni has been investigated. Molecular Dynamics (MD) combined with the on-the-fly Kinetic Monte Carlo (otf-KMC) method to study the evolution of defects in bulk Ni after collision cascades at room temperature. The energies of the collision cascades have been chosen according to the probability of them occurring in the experiments. Also the damage resulted in a system after multiple collision cascades has been studied. Furthermore, the interstitial-vacancy annihilation events seen during the simulation have been investigated to understand their mechanisms and the timescales required for them to occur. The diffusivity of the vacancy and interstitial clusters resulting from the simulation has been also studied at 200°C.

In this chapter, the methodology used is explained first and explanations of the results obtained are shown in the second section. Conclusions are presented at the end of this chapter.

5.2 Methodology

The systems used contains 55,296 atoms for the system used to model the 1 keV cascade and 32,000 atoms for the other energies. The Mishin 2004 [69] potential has been used to describe Ni-Ni interactions. The potential has been splined to the ZBL potential [49] to correctly describe interactions at small atomic separations. The cutoff distances used to connect the pair potential to the spline function and the spline function to the ZBL potential are 0.6 Å and 1.2 Å.

The simulation process can be divided into two main stages:

1. MD stage: The system used is thermalised to the required temperature before a collision cascades is run on the system at the same temperature.

2. Otf-KMC stage: The defective system resulting from collision cascades is used as input to otf-KMC to model the evolution of these defects over long time scale at the same temperature.

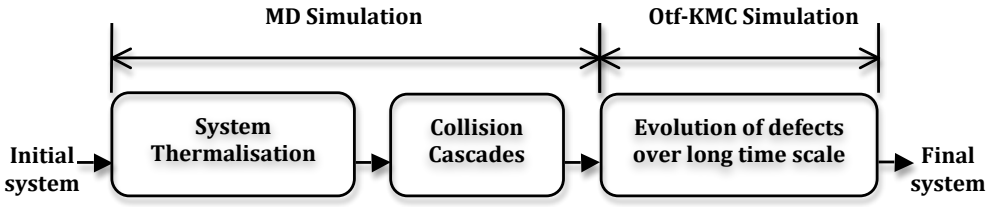

Figure 5.1: The simulation process used can be divided into two stages, the thermalisation and collision cascades are carried out using MD and the long time evolution of defects using otf-KMC.

5.2.1 Molecular Dynamics (MD)

Periodic boundary conditions in all directions have been implemented for all simulation boxes in this work. The system is first thermalised to room temperature, as this is representative of the temperature used in experiment. A Berendsen thermostat [51] has been used as a heat bath to bring the system to the required temperature. Once the system is thermalised, a collision cascade is initiated in the system. The range of collision cascades energies has been chosen according to the probability of them being seen in experiment [12]. From these experiments, 98.77% of the energies of the PKA were found to fall between 0 and 2000 eV as can be seen in figure (5.2). In our simulation, we found that no lasting damage or defects immediately recombine for energies below 100 eV, therefore, we ignored all energies below 100 eV in this work. Furthermore, since the probabilities for the energies greater than 1 keV were found very low (less than 2%), we ignored these in our model. As a result, the PKA energies used in our simulations starts from 100 eV and goes up to 1 keV.

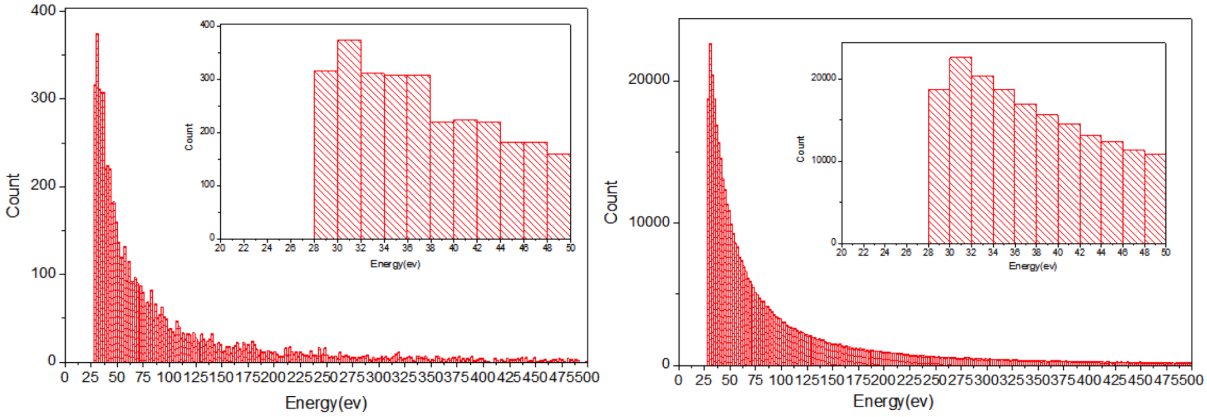

(a) Distribution (200 nm) (b) Distribution (2000 nm)

Figure 5.2: Results of SRIM calculations [12] in the case of pure Ni irradiated with He_4 at 1 MeV. The figures show the distribution of PKA energies found in experiment for bulk Ni. It has been found that 98.77% of energies fall between 0 and 2000 eV. The distribution across the surface is the same at penetration depths of 200 and 2000 nm, therefore, we could ignore the effect surface in our model.

The evolution of defects has been investigated in 10 systems that resulted from 100 eV collision cascades performed in different directions. Similarly 10 systems resulted from 200 eV, 8 systems from 300 eV and 4 systems from 1 keV have been investigated.

Furthermore, multiple collision cascades have been carried out to look into the evolution of defects in a system after exposing it to more than one collision cascades. A total of four systems have been used to study multiple collision cascades. For these collision cascades, the direction of the collision and the location of the PKA have been chosen randomly. The energy of each cascade has been chosen in a range from 100 to 1000 eV with probability considered as shown in figure (5.3). The number of events per second is calculated by multiplying the flux by the volume of our simulation box. The flux is calculated by dividing the ion flux ($5 * 10^{16}$ ions/cm^2/s) over the penetration depth ($2\ \mu m$), where these values obtained from experimental results. Therefore, the number of events was calculated as follows:

$$\text{Number of events} = \frac{5 \times 10^{16}\ \text{ions}}{2 \times 10^{-10}\ \text{m}^3\text{s}} \times (70.4^3 \times 10^{-30}\text{m}^3) = 87.22\ \text{events/s}. \tag{5.1}$$

Since we consider the energies which are greater than 100 eV and less than 1 keV and the probability for this range is only 0.344, then:

$$\text{Number of events} = 0.344 \times 87.22 = 30\ \text{events/s}, \tag{5.2}$$

which means that we will have ≈ 0.033 s between events.

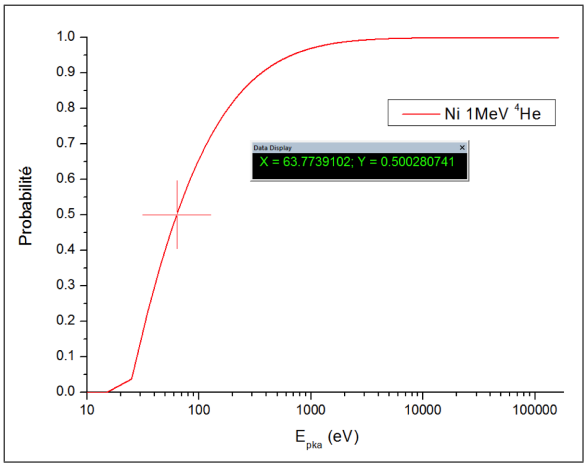

(a)

PKA energy range (eV)	Probability (curve)	Probability (rescaled)
100 - 200	0.176	0.55
200 - 300	0.056	0.175
300 - 400	0.032	0.10
400 - 500	0.016	0.05
500 - 600	0.016	0.05
600 - 700	0.008	0.025
700 - 800	0.008	0.025
800 - 900	0.004	0.0125
900 - 1000	0.004	0.0125

(b)

Figure 5.3: Probabilities of the collision cascade energies; (a) shows probabilities seen in experiment [12] and (b) shows probabilities of the collision cascade energies used for the multiple collision cascades in bulk fcc Ni.

5.2.2 On-the-fly Kinetic Monte Carlo

The otf-KMC technique ([19], [21] & [76]) has been used to model the diffusion of defects resulting from collision cascades. The main steps for the otf-KMC technique used as explained in chapter 2 start with identifying defects by comparing the system after the collision cascade with the reference system. Defect volumes are constructed around defects so only atoms that surround the defect within a certain distance are included in the search for possible transitions. Each defect volume is given a private label which is used to identify if we have the same defect later on during the simulation. For the defect volumes that intersect where more than one defect volumes share atoms, combined volumes are constructed to include both defect volumes. This makes sure that possible transitions between both volumes will be also found. Once all sub volumes and combined volumes are constructed, we try to find all possible transitions for each defect volume and for the combined ones. For the sub volumes, the hash key for each defect volume is compared to the stored hash keys for the defect volumes that have been seen previously in the simulation. If the hash key is on the list, then a transformation matrix is used to reuse the transitions found previously.

For other defect volumes and also for the combined volumes, large number of searches are initialised using Dimer method [59] combined with Lanczos algorithm to find all possible unique transitions. The search starts with Dimer method and switches to Lanczos algorithm

[57] when negative curvature reached which indicates that we are very close to a saddle. The Lanczos algorithm is used to convert the Hessian matrix into a tridiagonal matrix where minimisation along the eigenvector corresponding to the lowest eigenvalue should bring us to the saddle. The activation barrier is the energy difference between the initial system and the saddle. If the success rate is more than the specified value, then the transitions found for the defect volume are stored for use in next steps.

5.3 Results and Discussions

In most of the systems simulated, we found the defects annihilate by recombination between vacancies and interstitials. The recombination between vacancies and interstitials were found to happen from quite large distances with low barriers. For example, when collision cascades were initiated with 64 eV energy for up to 20 ps in a 2048 atoms system, a total of 4 defects remained in the system after the collision cascades. Otf-KMC has been used to model the evolution of those defects. The system took 6.76×10^{-9} seconds before all the defects recombined. The recombinations happened during the simulation between vacancies and interstitials which are separated by a few Å through a chain of interstitials between the two defects [76]. Pictures of the recombinations seen are shown in figure (5.4). In general, most of recombinations seen in all the simulations we performed happened by the same mechanism.

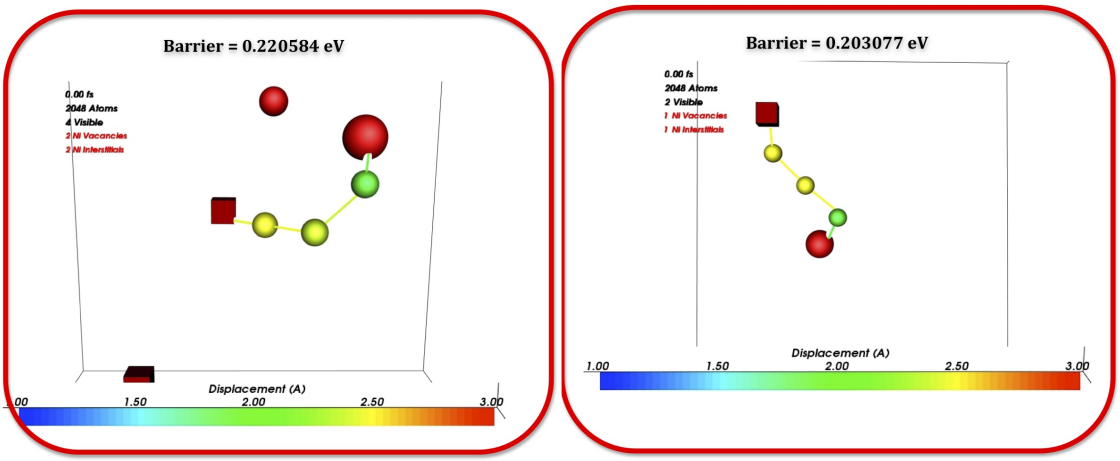

(a) (b)

Figure 5.4: Recombinations between vacancy and interstitial occurred during the KMC simulation.

For the systems that still have defects at the end of the simulation time we found the

interstitials form clusters, that diffuse very slowly in those system. Also, we observed that the more interstitials in a cluster the lower the diffusivity of the cluster.

5.3.1 Collision cascades

We implemented collision cascades at energies of 100, 200, 300, 400, 500 and 600 eV. We initially thermalised the system to room temperature before performing collision cascades in 66 directions for each energy. Pictures show the number of defects resulted in the system after collision cascades are shown in figure (5.5).

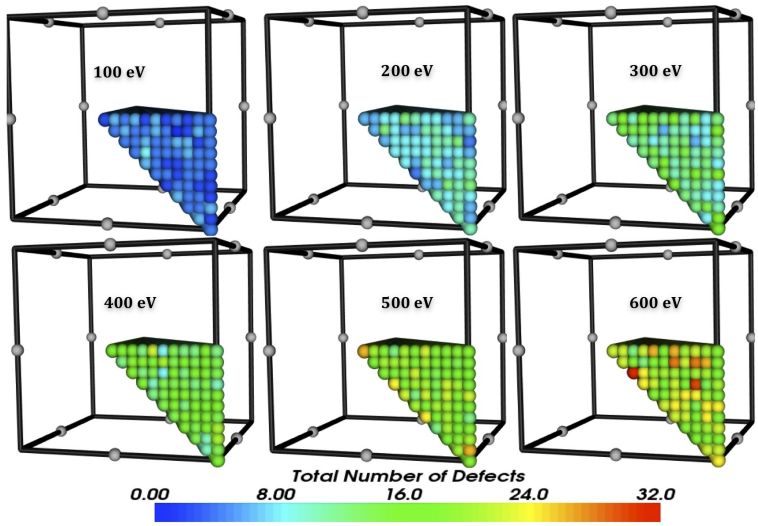

(a)

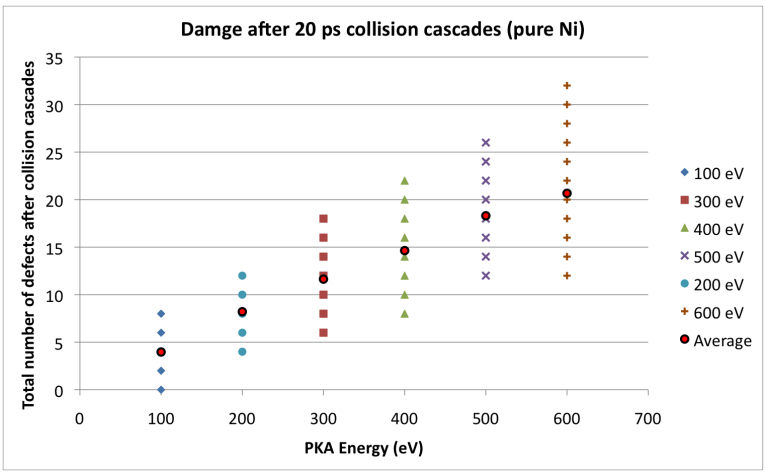

(b)

Figure 5.5: Damage left in a system after implementing collision cascades at energies of 100, 200, 300, 400, 500 and 600 eV; (a) shows the total number of defects for each energy using 66 directions and (b) shows the total number of defects at these 66 directions and also highlights the average of defects at each energy.

From figure (5.5), it can be seen that the number of defects in a system increases with increasing the PKA energy and overall the number of defects remained in the system after collision cascades is relatively small at these low energies.

5.3.2 Recombination between vacancies and interstitials

A large number of recombinations have been observed during simulation of our systems. We tried to study these recombinations in term of the distance between the interstitial and the vacancy and also the energy barrier required for such an event to occur. Therefore, we distinguished the recombinations seen in simulation according to the distance between both defects in term of nearest neighbours. Figure (5.6b) shows the recombinations seen in simulation versus the distance between the vacancy and the interstitial in terms of nearest neighbours. We tried to see if there is a relation between the number of recombinations seen at specific distances and the number of atoms at the same distance according to the fcc structure. Figure (5.6a) shows number of nearest neighbours in fcc structure.

From figure (5.6) we can see that the probability of a recombination to occur is more when we have more atoms at that distance. For example, the highest recombinations were found when the interstitial and the vacancy are seventh or ninth nearest neighbours where the fcc structure has more atoms at these distances.

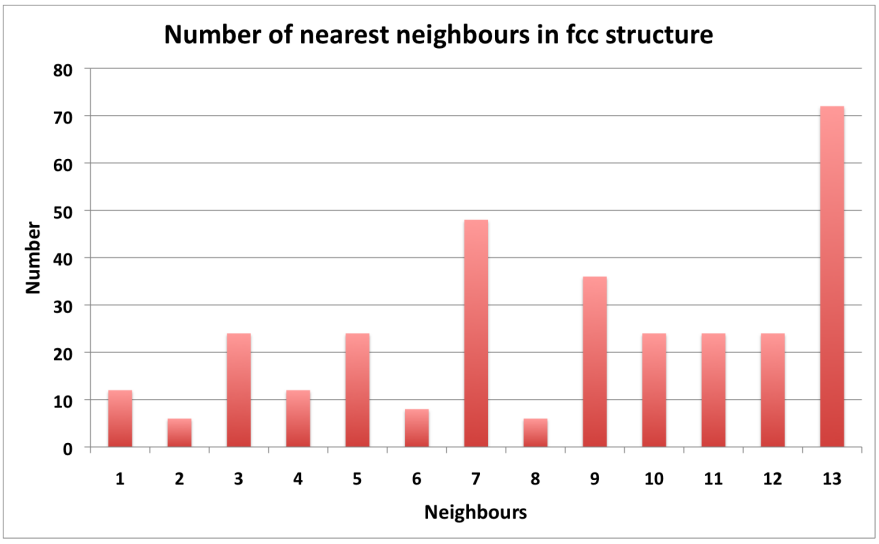

(a)

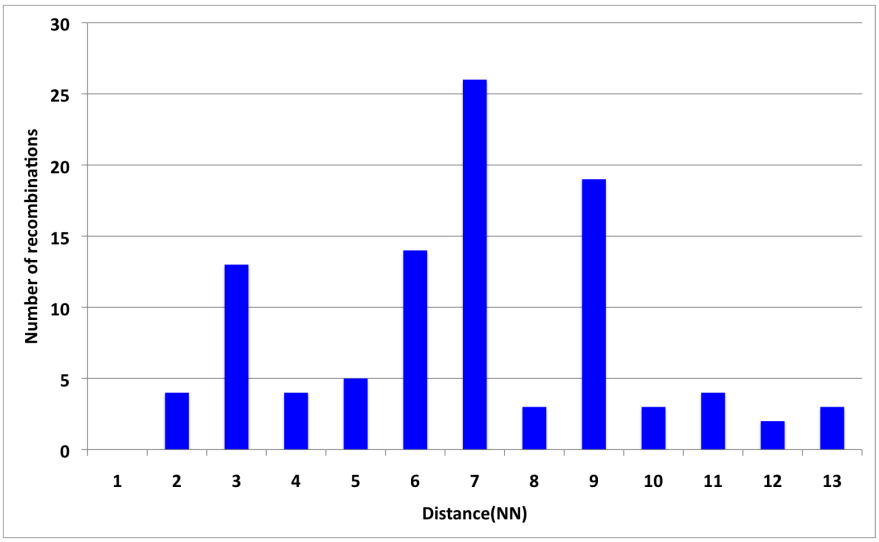

(b)

Figure 5.6: Investigation of the recombination between vacancies and interstitials seen during the simulation; (a) shows the number of first nearest neighbours in the fcc structure and (b) shows recombinations seen during the simulation versus the distance between both defects in term of nearest neighbours.

Geometries of the nearest neighbours and their effect on the recombination of vacancy and interstitial

Furthermore, we tried to examine if the geometries of the atoms in nearest neighbours have an effect on the recombination. Geometries along with the distances of the nearest neighbours in the fcc structure are shown in table (5.1) using a lattice parameter of 3.52 Å for Ni.

NN	Distance (Å)	Geometry	NN	Distance (Å)	Geometry
1	2.489	[0.5,0.5,0]	8	7.040	[2,0,0]
2	3.520	[1,0,0]	9	7.467	[1.5,1.5,0]
3	4.311	[1,0.5,0.5]	10	7.871	[1,0,2]
4	4.978	[1,1,0]	11	8.255	[1,1.5,1.5]
5	5.566	[1.5,0.5,0]	12	8.622	[2,1,1]
6	6.097	[1,1,1]	13	8.974	[1.5,0.5,2]
7	6.585	[1.5,0.5,1]	14	9.640	[1,0.5,2.5]

Table 5.1: Geometries and distances of first nearest neighbours in fcc structure.

We investigated the recombination that occurs between a vacancy and an interstitial when they are located in each of the possible geometries. We found that there are specific geometries at specific distances where the recombination between a vacancy and a dumbbell interstitial does not require any energy to occur. For example, for a vacancy and an interstitial at first nearest neighbours, we found that recombination occurs only by minimising the system in eight positions out of the twelve. Similarly, we found that two positions at 2 NN, sixteen positions at 3 NN and eight positions at 4 NN would also allow recombination of a vacancy and an interstitial with only relaxing the system. Figure (5.7) gives explanations of these special positions. Furthermore, figures (5.8, 5.9 & 5.10) show examples of the recombination steps involved at these special geometries.

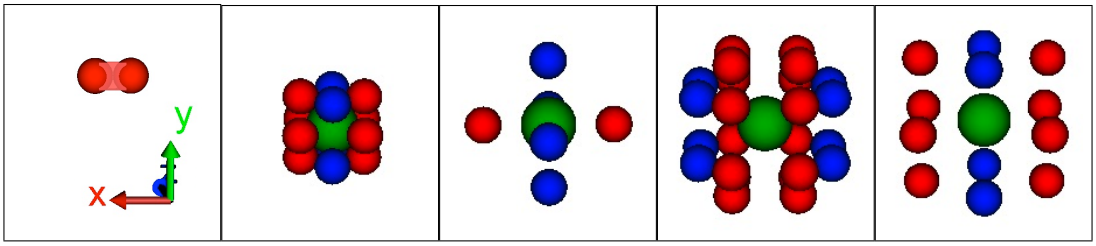

(a) [100] Dumbbell (b) 1 NN (c) 2 NN (d) 3 NN (e) 4 NN

Figure 5.7: Recombination of the [100] dumbbell located at certain distances from a vacancy, (a) shows [100] dumbbell, (b), (c), (d) and (e) show the different available geometries at 1, 2, 3, 4 NN where the green sphere represents the vacancy, red spheres represent the positions of the interstitials that recombine spontaneously and blue spheres represent the positions where both defects require to traverse a larger energy barrier to recombine.

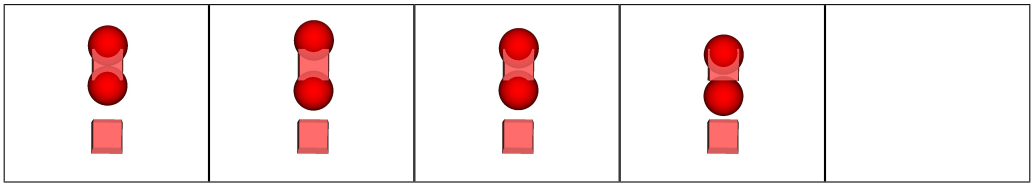

Figure 5.8: Recombination stages for the dumbbell and the vacancy by relaxation from second nearest neighbour distances.

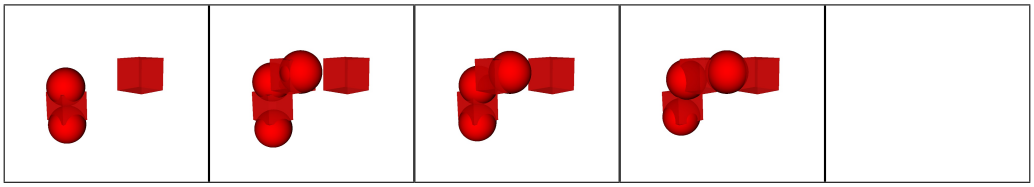

Figure 5.9: Recombination stages for the dumbbell and the vacancy at 3 NN by relaxation.

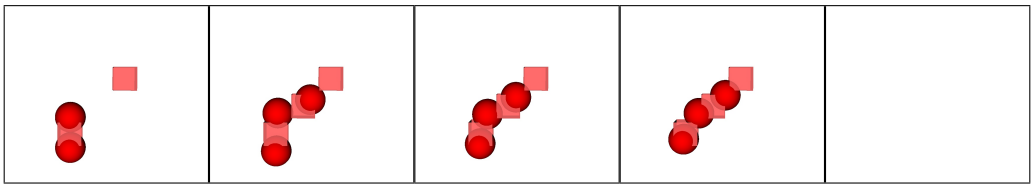

Figure 5.10: Recombination stages for the dumbbell and the vacancy at 4 NN by relaxation.

For other positions where a vacancy and an interstitial did not recombine by relaxation above, we found a larger energy barrier is required for the recombination to occur. We used the Climbing Image Nudged Elastic Band (CI-NEB) [11] to calculate the energies required for the recombination to occur and we found that the barriers obtained are relatively low. For example, we found that it requires 0.0005 eV, 0.06 eV, 0.084 eV and 0.18 eV for the recombination of a vacancy and an interstitial that are 1 NN, 2 NN, 3 NN and 4 NN respectively and do not spontaneously recombine. Figures (5.11, 5.12 & 5.13) illustrates the recombination barriers and mechanism for a vacancy and an interstitial that are second, third and fourth nearest neighbours.

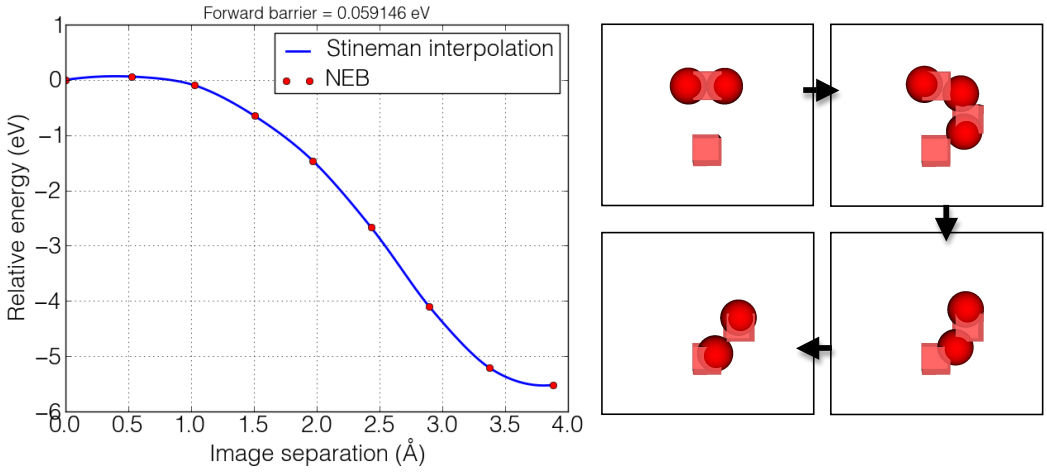

Figure 5.11: Recombination for an interstitial and a vacancy at 2 NN using CI-NEB, the left figure shows the minimum energy pathway obtained and right pictures show snapshots of the recombination stages.

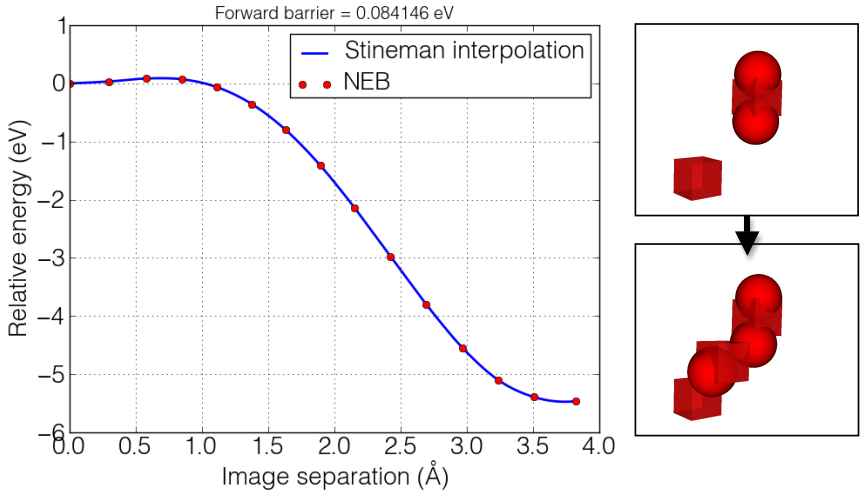

Figure 5.12: Recombination for an interstitial and a vacancy at 3 NN using CI-NEB, the left figure shows the minimum energy pathway obtained and right pictures show snapshots of the recombination stages.

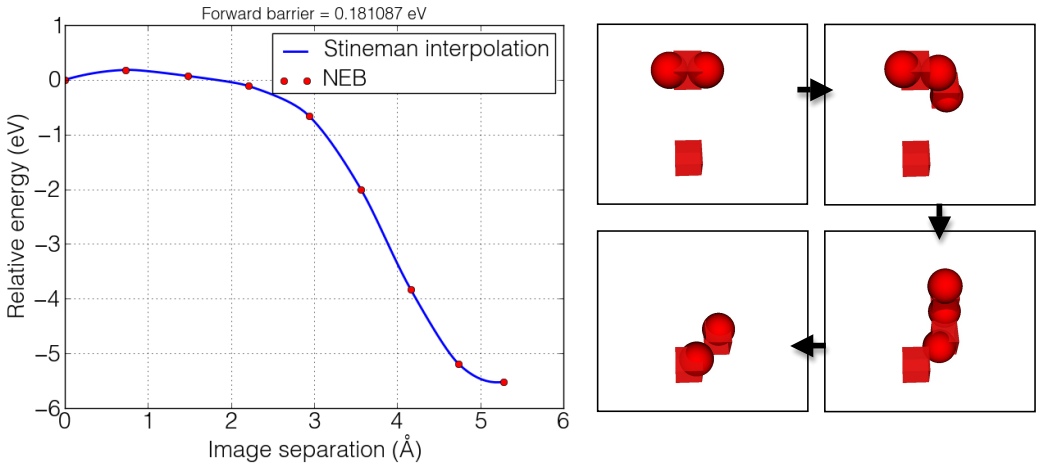

Figure 5.13: Recombination for an interstitial and a vacancy at 4 NN using CI-NEB, the left figure shows the minimum energy pathway obtained and right pictures show snapshots of the recombination stages.

We studied the recombinations that occurred when the interstitial and the vacancy are separated by more than 4 NN. We found that the recombinations from these distances occur by single jumps to one of the positions that do not require energy for recombination as was discussed previously. For instance, we found that a dumbbell rotates and translates from fifth or seventh nearest neighbours to the fourth nearest neighbours with an energy barrier of 0.19 eV and recombines with the vacancy straightaway from there as shown in figure (5.14 & 5.15). This is because that the seventh and the fifth nearest neighbours to a vacancy are also the first nearest neighbour to its fourth nearest neighbour so it is easy for the dumbbell to rotate and translate to one of the special positions at the fourth nearest neighbours and recombine from there. A similar mechanism exists for an interstitial and a vacancy recombination that are sixth nearest neighbours, which have also been seen to use the dumbbell translate and rotate mechanism to one of the special geometries at the third nearest neighbour position with an energy barrier of 0.2 eV before total recombination occurs from there as shown in figure (5.16). Furthermore, we found that a dumbbell from the ninth nearest neighbour position can recombine with the vacancy by a single hop with an energy barrier of 0.12 eV as shown in figure (5.17). We found the mechanism by which this recombination occurs is similar to the one from seventh nearest neighbours as the dumbbell moves to the fourth nearest neighbour first, however, the energy required for this move is lower here.

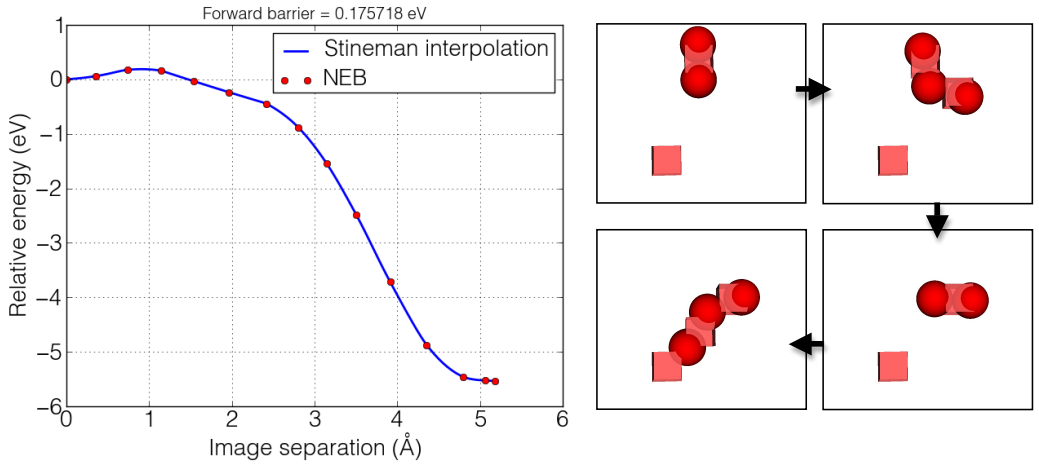

Figure 5.14: Recombination of a dumbbell and a vacancy at 5 NN using CI-NEB. The dumbbell in this case rotates and translates to one of the special positions at the fourth nearest neighbours and recombines straightaway from there. The left picture shows the minimum energy pathway and the right pictures show snapshots of the recombination stages.

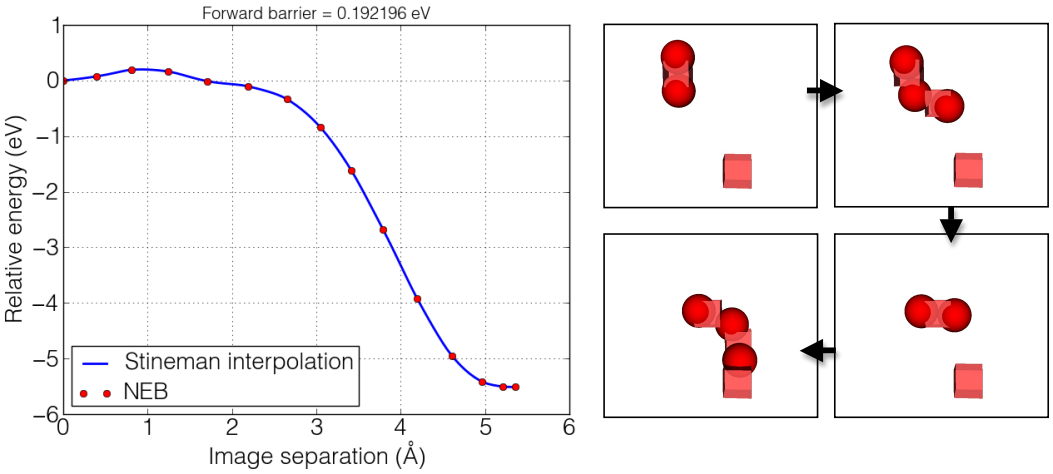

Figure 5.15: Recombination of a dumbbell and a vacancy at 7 NN using CI-NEB. The dumbbell in this case rotates and translates to one of the special positions at the fourth nearest neighbours and recombines straightaway from there. The left picture shows the minimum energy pathway and the right pictures show snapshots of the recombination stages.

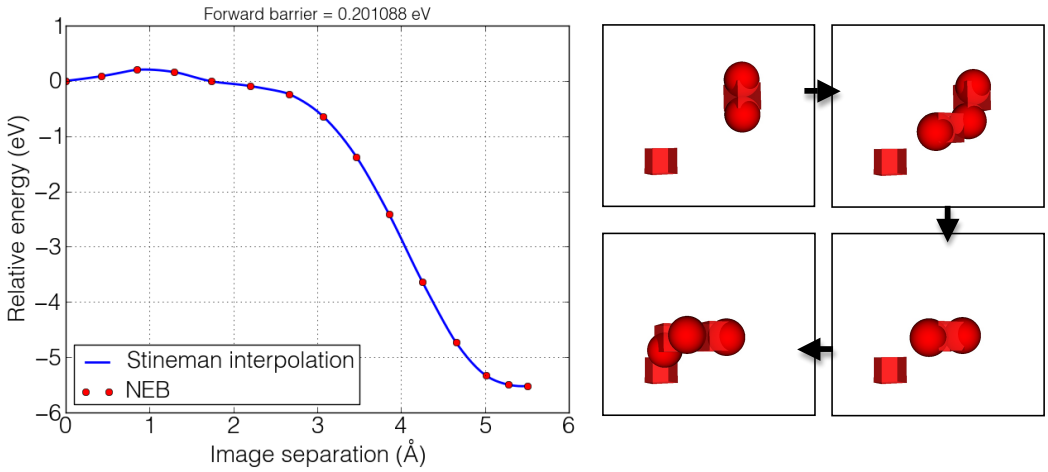

Figure 5.16: Recombination of a dumbbell and a vacancy at 6 NN using CI-NEB. The dumbbell in this case rotates and translates to one of the special positions at the third nearest neighbours and recombines straightaway from there. The left picture shows the minimum energy pathway and the right pictures show snapshots of the recombination stages.

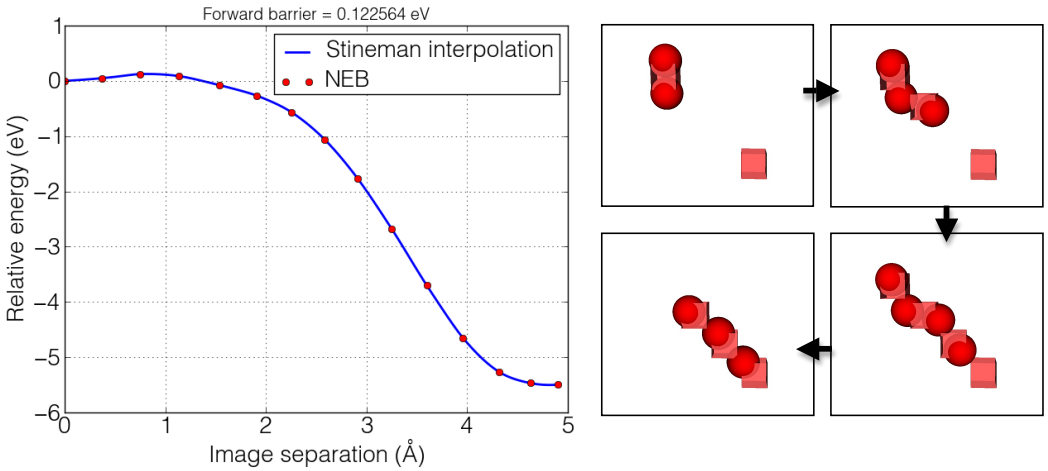

Figure 5.17: Recombination for a dumbbell and a vacancy at 9 NN using CI-NEB. The recombination involves movement of the dumbbell from the ninth nearest neighbours to the fourth nearest neighbours with energy of 0.12 eV where it recombines from there with the vacancy. The left picture shows the minimum energy pathway and the right pictures show snapshots from the recombination stages.

5.3.3 Defect annihilation time

For most of the systems studied, we found that defects resulting from low energy cascades (100 - 300) eV recombined completely during the simulation. Also, we found that the simulations were dominated by the diffusion of interstitials, with an average barrier of 0.2 eV and these tend to recombine with the vacancies. Furthermore, we found the time needed for

whole recombination of defects in the system studied did not exceed the range of a few micro seconds. Table (5.2) shows the maximum and the minimum healing time for those systems.

PKA energy (eV)	Minimum healing time (s)	Maximum healing time (s)
100	1.11E-09	2.52E-07
200	1.01E-08	9.20E-06
300	4.69E-09	1.86E-06

Table 5.2: The maximum and the minimum time needed for annihilation of all defects produced after low energies collision cascades (100 - 300 eV).

5.3.4 Interstitial clustering observed in simulation

For the remaining systems where the defects did not recombine completely, we found that the interstitials tend to form clusters, which are less mobile than the single interstitial. In fact we investigated the diffusivity of those clusters and found it to be less as the cluster contain more interstitials. In addition, we observed that the big clusters diffuse very slowly during the simulation with most of the transitions at that stage resulting in rearrangement in the clusters rather than diffusing them in the system. Examples of the cluster formed during simulation are shown in figures (5.18 & 5.19).

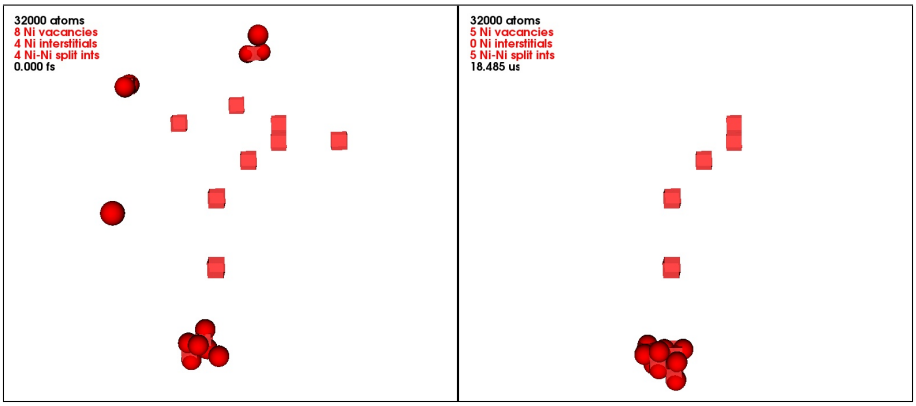

(a) After Collision cascades. (b) After otf-KMC simulation.

Figure 5.18: Example of interstitial clustering seen during the simulation, (a) shows the system after collision cascades and (b) shows the system after otf-KMC which ended with a five interstitials cluster and five vacancies.

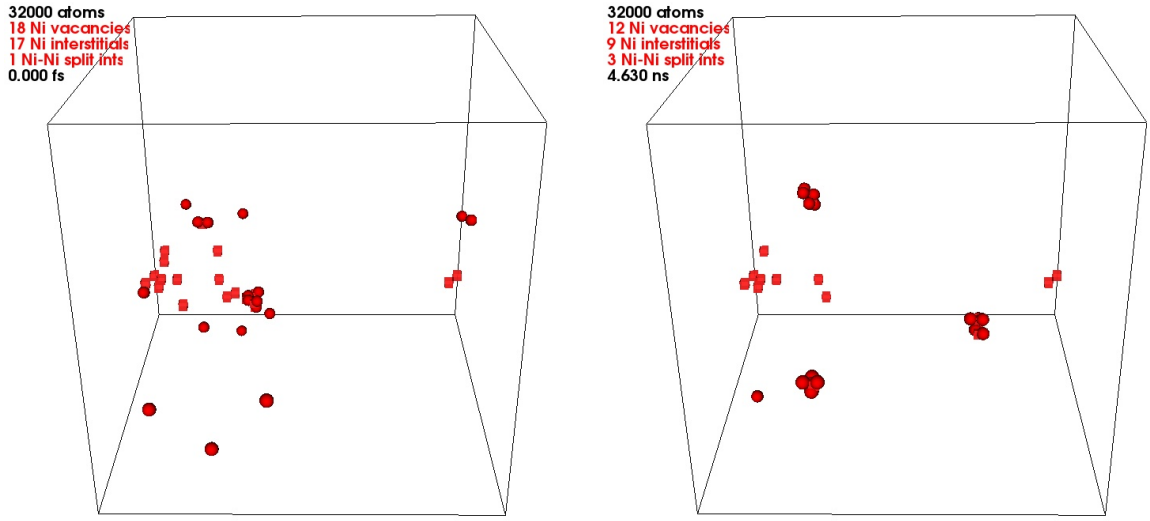

(a) After Collision cascades.

(b) After otf-KMC simulation.

Figure 5.19: Example of interstitial clustering seen during the simulation, (a) shows the system after collision cascades and (b) shows the system after otf-KMC that has collections of three interstitial clusters.

5.3.5 Vacancy clustering seen in simulation

As the large interstitial clusters seen in the simulation tend to be approximately immobile, we tried to model the evolution of the vacancies remained in a system to look whether these vacancies tend to form clusters as well. Therefore, we removed the interstitial clusters from our systems and used otf-KMC to model the evolution of the vacancies. The typical vacancy diffusion barrier was found to equal 1.2 eV and we found that for most cases vacancies form Stacking Fault Tetrahedral (SFT) or something similar as shown in figures (5.20 & 5.21). The timescale where the SFT was found to form varies from about 300 ms to 1.99 seconds of the real time.

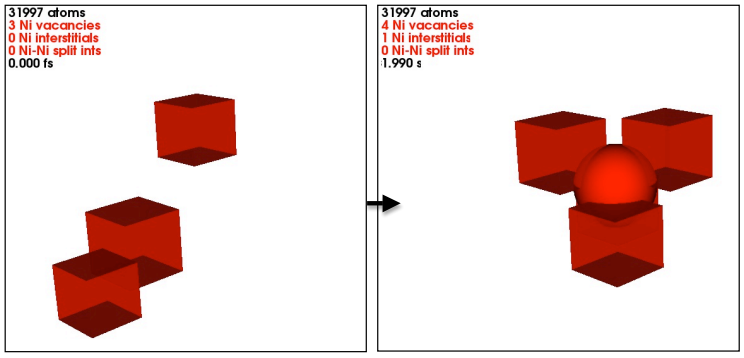

Figure 5.20: Modelling the diffusion of 3 vacancies using otf-KMC at room temperature. This figure shows transformation of 3 vacancies into 3 vac SFT in 1.99 seconds (real time).

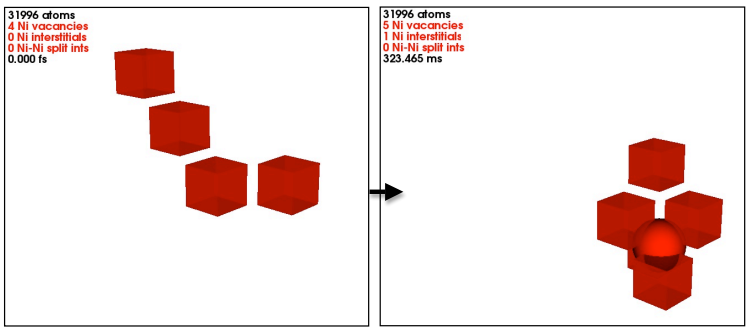

Figure 5.21: Modelling the diffusion of 4 vacancies using otf-KMC at room temperature, this figure shows transformation of 4 vacancies into vacancies cluster similar to SFT in 323.465 ms (real time).

The next step was trying to see if bigger vacancy clusters can be produced in the simulation. Therefore, we investigated the diffusion of 6 vacancies to study the possibility of producing a 6 vacancy SFT. From the results obtained, we found that the 3 vacancy SFT formed during the simulation in 787 ms of the real time. After that, the vacancy cluster became larger by including the fourth vacancy in a long timescale of approximately 2 days of the real time and we did not see a larger vacancy cluster for the time simulated. Pictures of the vacancy clusters produced are shown in figure (5.22).

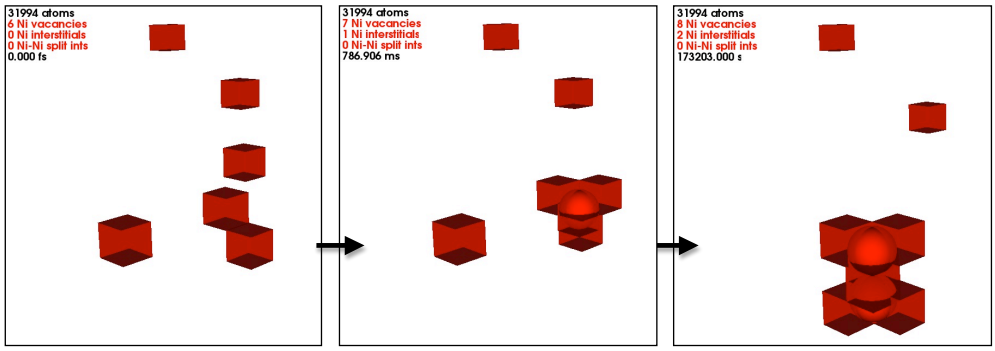

Figure 5.22: Modelling the diffusion of 6 vacancies using otf-KMC at room temperature. 3 Vacancies SFT was found to be formed in 787 ms and a lager vacancy cluster of 4 vacancies in approximately 2 days of the real time.

There are no reports from experiment that SFT can form at room temperature, however, the SFT would appear as very similar to isolated vacancies or not be observed due to their low free volume. The positron lifetime for the vacancy and SFT with 3, 6, 10 and 15 vacancies are very close [12]. For instance, in the case of Ni irradiated with He ions, two types of defects are detected depending on the fluence of He ions. The first type of defects can be either single vacancy or other vacancy defects such as SFT and the second type is a dislocation.

5.3.6 Energy barriers associated with transformation from isolated vacancies to SFT

We studied the energy barriers associated with the transformation of isolated vacancies to SFT at room temperature. The typical barrier for an isolated vacancy in pure Ni is 1.2 eV, however, if the vacancies get closer, we found them to diffuse with around 0.5 to 0.75 eV. Also, an energy of 0.16 eV was required for the rearrangement of defects to form the SFT. Overall, we found the energy barriers required for transformation from vacancies to SFT to fall in range of 0.16 eV to 0.75 eV. Snapshots of the transformation of vacancies into 3 vacancies SFT are shown in figure (5.23).

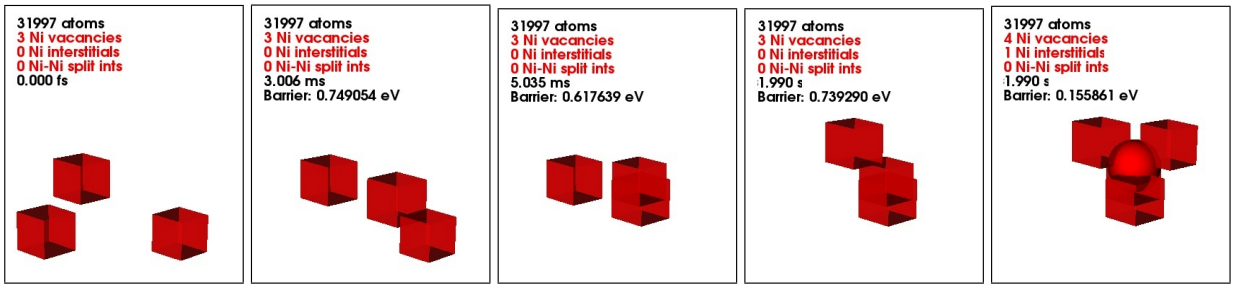

Figure 5.23: Snapshots of the steps involved in transformation of 3 vacancies into 3 vacancies SFT, associated energy barriers are shown at each snapshot.

Multiple collision cascades

In this work, we investigated the damage remaining in a system after exposure to multiple collision cascades in four systems. From the results obtained, we found all defects produced after collision cascades to recombine in a system before another collision cascades is planned to be implemented to the system. This was the case if the energy of PKA is chosen in range from 100 to 300 eV which will be almost the case because of their high probabilities. If higher energies were chosen for the PKA, then we found this resulted in interstitial clusters which diffuse slowly. Example of such results can be seen in figure (5.24).

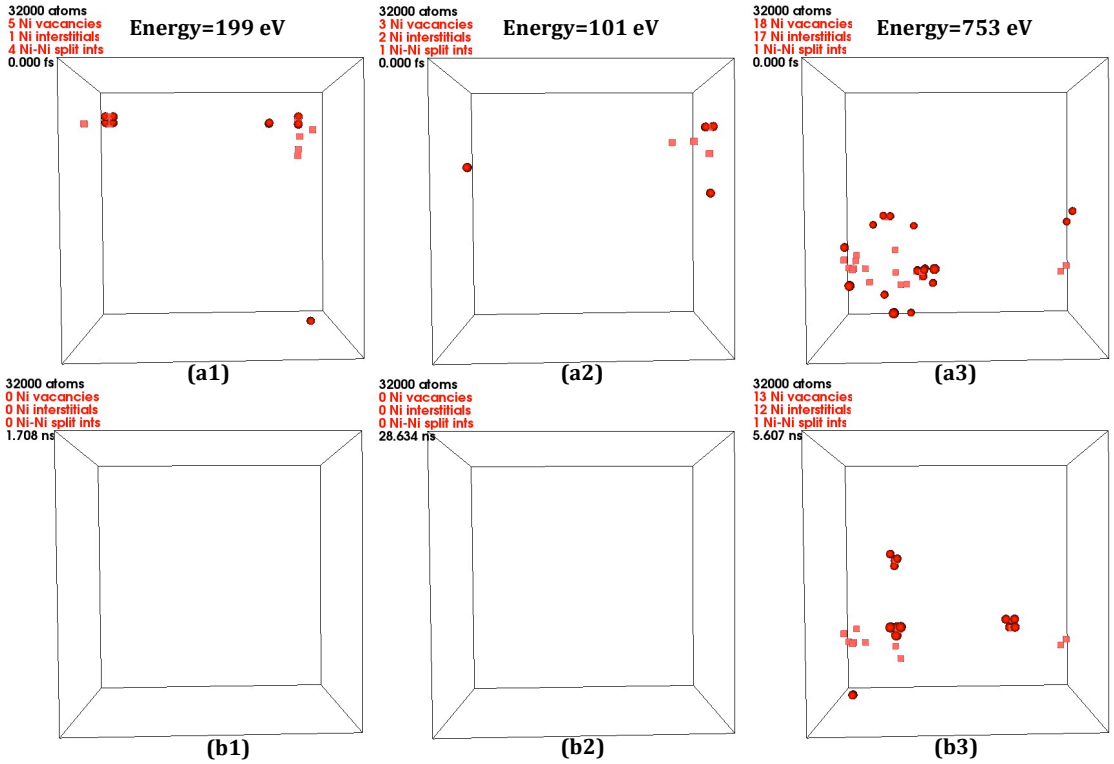

Figure 5.24: Simulation of bulk Ni with multiple collision cascades. Three steps are shown in the figure. (a1, a2 & a3) show the system after collision cascades at each step. (b1, b2 & b3) show the system after otf-KMC at each step. The figure shows that all defects created in the system after the first and the second collision cascades recombine and interstitial clusters form from the third collision which diffuse slowly in the system.

From figure (5.24), one can see that the damage in a system exposed to low energies collision cascades is very small. Although the formation energies of the interstitials are high (3.95 eV) in pure Ni when compared to the vacancy (1.57 eV), the interstitials were found to move very quickly with an average barrier of 0.2 eV and the vacancies were found to be static because of their high migration energies (1.2 eV). Once the interstitial gets close to the vacancy, this results in vacancy-interstitial annihilation. Furthermore, the damage produced with these low energies heals very fast leaving the systems with no defects when it is time for the second collision cascade. Therefore, there will be no damage or a very small amount in the system due to the exposure to multiple low energy collision cascades. This is very important as it reflects the ability of Ni to absorb damage. The same figure also shows that interstitial clusters form when higher energy collision cascades implemented in the system.

5.3.7 Results at 200°C

SFT Dissociation

From experiments the positron lifetime changes at 200°C, which indicates a change in the size of the defects [12], therefore, we performed some calculations at 200°C. For instance, we investigated the diffusion of the SFT produced in previous simulation using otf-KMC at 200°C. From the results obtained, we found that the SFT dissociate at 200°C in approximately 64.469 ms. Snapshots of the initial SFT used for this simulation and the final system are shown in figure (5.25).

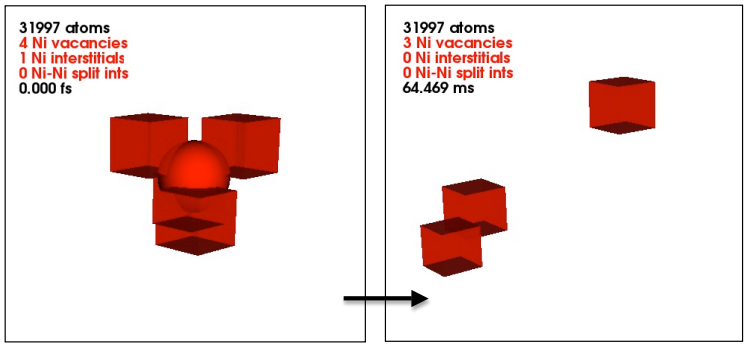

Figure 5.25: Results from studying the possibility of SFT dissociation at 200°C. This figure shows the initial SFT which dissociate into single vacancy and a di-vacancies in approximately 64.469 ms.

Since the SFT was found to dissociate at 200°C, which can explain the different signal obtained with positron in experiment when irradiation of Ni at the same temperature.

Interstitial clusters diffusivity at 200°C

Furthermore, we studied the diffusivity of the interstitial clusters formed in previous simulation at 200°C using MD. The first observation from these simulation was that the diffusivity of these clusters is higher at 200°C than it is at room temperature with the smaller clusters diffusing far faster than larger clusters at 200°C. For example, we tried to calculate the diffusion coefficients for 2 interstitials and 3 interstitials clusters by plotting the Mean Square Displacement (MSD) versus time using the data we obtained from MD simulation as shown in figure (5.26).

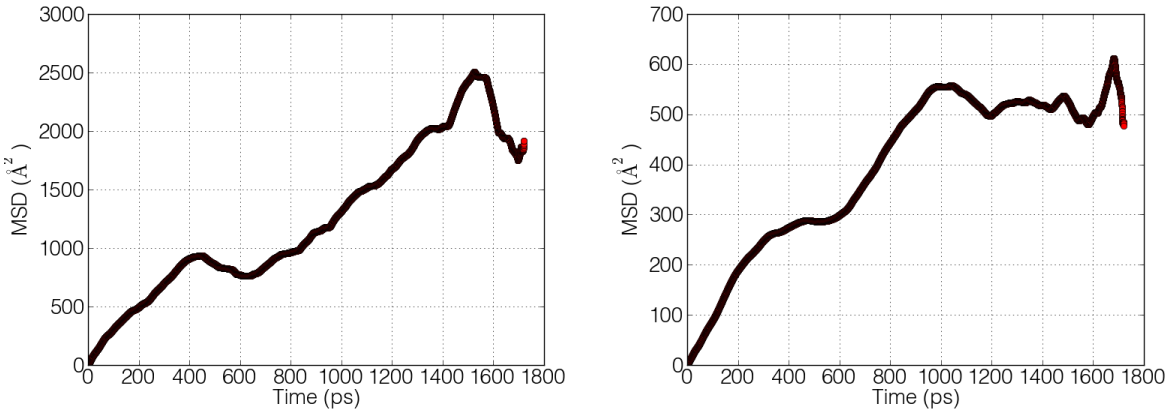

(a) 2 interstitials Cluster.

(b) 3 interstitials Cluster.

Figure 5.26: Investigating the diffusivity of interstitial clusters at 200°C, (a) shows the MSD versus time for the 2 interstitials cluster and (b) shows the MSD versus the time for the 3 interstitials cluster. The figure shows that the diffusivity of the 2 interstitials cluster is higher than the diffusivity of the 3 interstitials cluster.

From figure (5.26), we can see that we did not have enough statistics that enabled us to calculate the diffusion coefficients, however, from this figure we can conclude that the diffusivity of a 2 interstitials cluster is more than the diffusivity of 3 interstitials cluster. Pictures of the system before and after MD simulation are shown in figure (5.27). In some cases, we found a tendency of the interstitial clusters to combine and form bigger interstitial clusters. An example can be seen in figure (5.28).

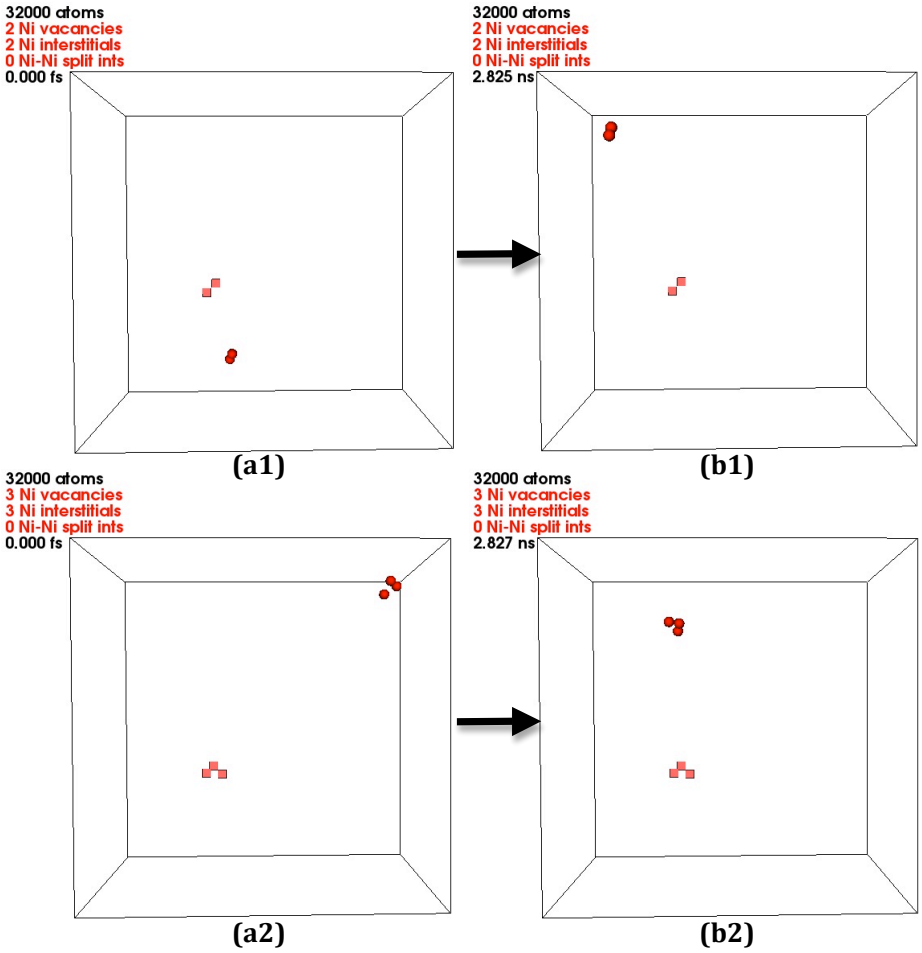

Figure 5.27: Investigating the diffusivity of interstitial clusters using MD simulation at 200°C; (a1) & (b1) show a system of 2 interstitials clusters before and after the simulation; (a2) & (b2) show the system with 3 interstitial clusters before and after the simulation. The clusters did not dissociate at higher temperature in the time reached in the simulation and the diffusivity of the smaller cluster is found far more than the bigger one.

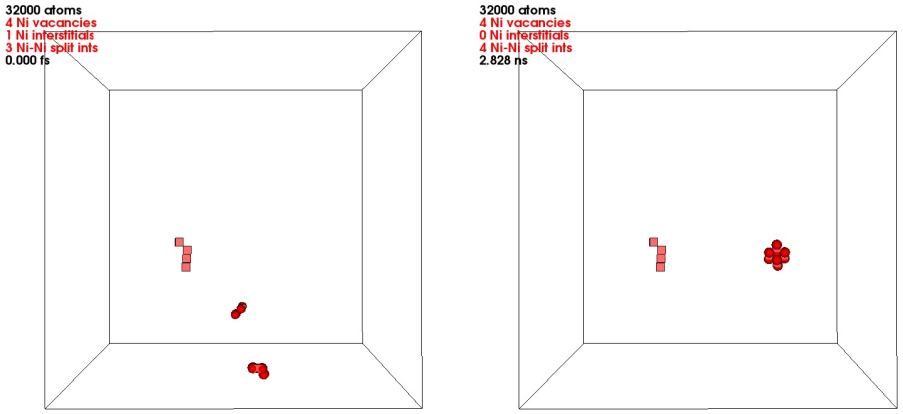

(a) Initial system. (b) Final system.

Figure 5.28: Modelling the diffusion of interstitial clusters at 200°C; (a) shows the initial system which contains two (2 interstitials) clusters and (b) shows the system after simulation where the two clusters combine to form a four interstitials cluster that is found to diffuse slowly.

The diffusivity of bigger interstitial clusters has been also investigated. We found a 4 interstitials cluster diffuses very fast, however, the diffusion mechanism was one dimensional only as can be seen in figure (5.29). On the other hand, 5 interstitials cluster was found to be very stable and hardly moved from its position during the simulation as shown in figure (5.30).

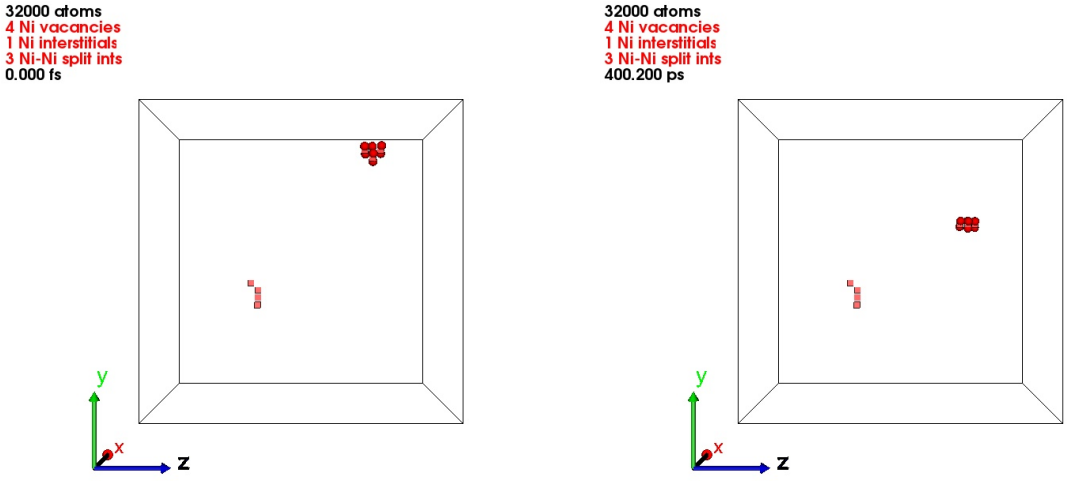

(a) Initial system. (b) Final system.

Figure 5.29: Modelling the diffusion of interstitial clusters at 200°C; the figure shows a 4 interstitial cluster which diffuses in a one dimension only.

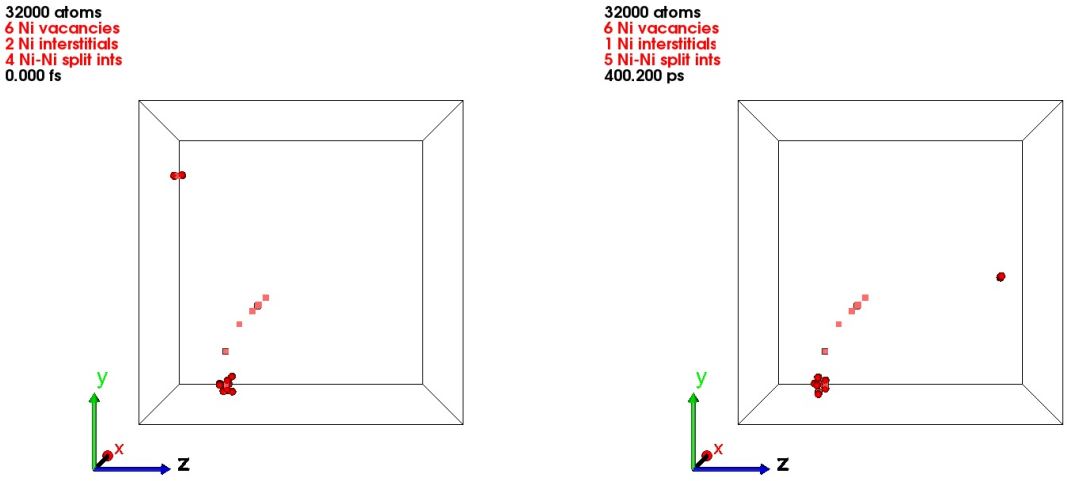

(a) Initial system.

(b) Final system.

Figure 5.30: Modelling the diffusion of interstitial clusters at 200°C; the figure shows the diffusion of a five interstitial cluster which is found to diffuse slowly during the simulation.

5.4 Discussions and Conclusions

The main aim from this work was to provide insight into the results obtained from experiments on pure Ni irradiated with He_4 at 1 MeV at room temperature. MD simulation along with otf-KMC has been used to model the radiation damage in pure fcc Ni in relation with these experiments. The energies for the collision cascades have been chosen according to their probability being observed in experiments.

The main results obtained from modelling these systems are that in most of the systems studied, defects totally recombined or interstitials are found to form clusters that diffuse slowly in the system. Total recombination was the case especially at low energies 100 - 300 eV. For instance, the defects produced after collision cascades in 10 out of 10 from 100 eV, 9 out of 10 from 200 eV and 6 out of 8 from 300 eV were found to totally recombined during the simulation.

The recombination seen during the simulation has been studied and it has been shown that there are specific geometries where the vacancy and the interstitial could recombine from certain distances with low barriers. This has been observed happening up to the fourth nearest neighbour distance. The energies required for different geometries and also longer distances have been calculated. It has been found that recombination from longer distances happened

by only one hop to the one of the specific geometry that allow direct recombination. For example, a vacancy and an interstitial is found to recombine from the ninth nearest neighbour distance with only 0.12 eV by hopping through the fourth nearest neighbour to the vacancy. Also, comparing the number of recombinations seen from specific distance and the number of nearest neighbours in the fcc structure, shows that there is a positive relation between the number of recombinations and the number of the nearest neighbours at the associated distance. For example, the largest recombinations were found to occur when the vacancy and the interstitial are seventh nearest neighbours where there are 48 seventh nearest neighbours in an fcc structure.

The diffusion of the vacancies left in the system with the interstitial clusters have been investigated at room temperature using otf-KMC. The vacancies are found to form SFT or something similar depending on how many vacancies are there. Formation of vacancies clusters have been observed to include 4 vacancies but we could not see a 6 vacancies SFT formation in the simulation time studied. The energy required for the formation of the SFT were found in range of 0.15 - 0.75 eV. There has been no SFT observed in experiments at room temperature, owing to the positron signal for those SFT and single vacancy being very close.

The dissociation of the 3 vacancies SFT has been investigated using otf-KMC at 200°C. It has been found that the SFT could dissociate in approximately 64 ms. This explains the change in the signal seen in experiments at 200°C.

The diffusion of the interstitial clusters has been investigated at 200°C and it has been found that these clusters diffuse faster than they do at room temperature with the smaller cluster diffusing faster than the bigger clusters at 200°C. For example, the diffusivity of 2 interstitials cluster is found to be far more than the diffusivity of 3 interstitials clusters. In some cases, the interstitials clusters are found to combine to form bigger clusters which will result in slower diffusion. Furthermore, the diffusivity of larger clusters has been also investigated at 200°C. For example, a 4 interstitials cluster was found to diffuse quickly in the system, however, the mechanism by which it diffuses was found to be only one dimension diffusion. A five interstitials cluster, however, was found to be very stable and the simulation was dominated by rearrangement of the cluster rather than diffusing it.

Chapter 6

Conclusions and Future Work

6.1 Conclusions

The need for better knowledge of the effect of radiation damage on the properties of materials has grown recently, because nuclear energy is seen a promising source of electricity at competitive prices. The PERFORM60 project works by combining the experimental and the modelling studies to obtain better knowledge of radiation damage. Our main role in this project was to obtain point defect migration energies in austenitic stainless steel. The work focussed on the stainless steel and Ni-based alloys because these materials represent an interesting class of materials for the next generation of nuclear power plants. This is due to their high temperature properties and their ability to survive the corrosive environment in the nuclear power plant.

There has been a large amount of work aimed at understanding radiation damage in stainless steel and Ni-based alloys. The main goal for most of the experimental studies was to study RIS in these materials. This being due to the very important effects this form of radiation damage has on degradation of a material's properties through causing embrittlement to the material especially at the GBs. The experiments obtained succeeded to explore the general trend of the Ni and Cr in the stainless steel at the GBs. The general trend obtained for the segregation was the Ni enrichment and Cr depletion at the GBs.

There has been lack of models developed for studying the RIS in stainless steel. This is due lack of good potentials that are capable of describing the interactions of the the three elements Fe, Ni and Cr correctly. A few models that aimed to study RIS in stainless steel were developed based on the DFT data. However, due to the large computational effort accompanied with DFT, these models were restricted to very small system sizes and for short time.

In modelling, choosing the right potential to describe the atomic interactions in the system is crucial in getting results that would occur in reality. A total of six potentials were developed by G. Bonny to study the radiation damage in the ternary alloy during the time allocated for this project. Our first work based on implementing these potentials and testing them to make sure that we can rely on the results would obtained using them. Since it was difficult to obtain a potential that will work for all cases, G. Bonny tried to develop a potential that will be capable of reproducing the DFT migration and formation energies for point defects.

We used different techniques to study the available potentials, for instance, we performed lots of calculations to calculate the formation, migration and binding energies for point defects and compared them to the available DFT values. Also, we performed high temperature MD simulation in the binary and the ternary alloy. Furthermore, we studied the segregation in these alloys using Monte Carlo simulation. In general from the results obtained, none of these potentials was capable of producing all the target DFT data correctly. For example, two main issues exist with the first potential (three versions): the stability of the fcc structure which found to easily convert to bcc structure during the simulation and the negative thermal expansion. The second potential did not reproduce the DFT values well owing to the fact it was developed to study the plasticity in the stainless steel and not the point defects. The third potential (two versions) was found to maintain the fcc structure of the ternary alloy, however, it overestimated the formation energies of the point defects in the pure materials which could effect the simulation. This is in addition to that the Cr was found to segregate from the Fe matrix in the ternary alloy and from the Ni matrix in the binary alloy.

The potential developed did not meet the expectation for the ternary alloy, however, the first potential was found to represent the Ni-Cr binary alloy quite well. For example, the segregation obtained using the potential on the binary alloy matches what has been seen in experiment. Therefore, this potential has been used to study the radiation damage near a GB in fcc Ni and a Ni-Cr binary alloy. The main findings from this study are that we found that a vacancy prefers to sit in certain sites near the GB and from the studying the segregation of Cr at the GB we also found that a Cr atom prefers to sit near the GB. From investigating the vacancies diffusion to the GB we found vacancies to be attracted to the GB and diffuse towards it. A general conclusion from modelling the damage produced from 1 keV collision cascades is that interstitials were found to be more mobile than the vacancies and

they diffuse quickly to the GB. Vacancies were found to diffuse to the GB if they are near the GB or form clusters in the bulk if they are far from the GB. An interesting mechanism was found for the vacancy diffusing towards the GB where an interstitial is emitted to recombine with a vacancy sitting near the GB leaving a vacancy in its place. Other interesting results obtained from studying the GB is the large roughening obtained in the GB in which atoms were found to change grains during the simulation. Overall the effect of the symmetrical tilt $\Sigma 5$ GB on controlling the defects locations or diffusion after the collision cascades and during the otf-KMC simulation were found to be more than the twin GB. Also the growth of defects on the GB after multiple collision cascades was found relatively low.

In relation to the results obtained from experiments, we modelled the radiation damage in bulk fcc Ni. We used both MD and otf-KMC to study the evolution of defects resulted from collision cascades. The energies for the collision cascades were chosen according to them being seen in experiment which implies low collision cascades in the range from 100 to 1000 eV. From these results we found that the damage produced at low energies (100 - 300 eV) is relatively low and the defects produced after the collision cascades completely recombined in order of micro seconds. For other systems that the defects were not found to recombine completely. Interstitial clusters were found to form during the simulation which were found to diffuse slowly.

The recombination between the vacancies and interstitials seen during the simulation were found to occur when both defects a few Å far from each other with relatively low barriers. We distinguished the recombinations seen during the simulation according to the distance between the vacancy and the interstitial when the recombination occurred in term of nearest neighbours and compared them to the number of the nearest neighbours in fcc structure. We found that more recombinations occurred at distances where fcc structures has more neighbours. For instance, more recombinations seen when the vacancy and the interstitial are seventh or ninth nearest neighbours. The mechanism by which these recombinations happened were by introducing a chain of interstitials between the defects.

Investigating these recombinations showed that there are special geometries at specific distances that allow direct recombination between the vacancy and the interstitial without any energy. This has been seen for vacancies and interstitials that are up to fourth nearest neighbours. For longer distances, the dumbbell was found to rotate and translate to one of the special geometries and recombine with the vacancy from there. For example, a dumbbell at the ninth nearest neighbour to a vacancy was found to rotate and translate to one of the

special geometries at the fourth nearest neighbours where it can recombine with the vacancy straightaway from there. The ability of the otf-KMC to capture such events was very important and this provides insight into moves that need to be included in atomic KMC and object KMC approaches.

Investigating the vacancies diffusion that remained in the systems with interstitial clusters show the possibility to produce SFT defects at room temperature. These SFT can dissociate at 200°C. Furthermore, the diffusivity of interstitial clusters at 200°C was found to be higher for 2 interstitials cluster than for 3 interstitials cluster. A 5 interstitials cluster was found to be very stable and 4 interstitials cluster was found to diffuse quickly in one dimension only.

Using MD simulation along with the otf-KMC allows us to explore interesting results and provide a good understanding on the effect of radiation damage in Ni and Ni-based alloys at the bulk and at the GBs. These methods were modified by a material modelling group at Loughborough University during the time allocated for this research. This includes implementing the reuse and modifying the parallelisation which boost our simulation. This is in addition to modifying how the search methods work by following the minimum mode algorithm to climb up to the saddle rather than using NEB which saves lots of time. The results obtained during this research were realistic and in good agreement with the experimental results which illustrates the power of the methods used. These results have significant implications for the models used in industry for predicting the lifetime of materials. They also aid the understanding of whether ion implantation can be used to replicate the conditions in a nuclear power plant.

6.2 Future Work

Modelling radiation damage in materials requires continued improvement of the algorithms used to optimise the simulation. One modification to the otf-KMC technique used will be trying to deal with the low barriers that cause delay in the simulation and does not have any influence on the simulations. Examples of these transitions are the small movement seen at the GBs and the rearrangement seen in the clusters formed in the simulation. Currently, the modelling group at Loughborough University are working on implementing different algorithms to deal with low barriers events. Furthermore, the reuse helped boosting the simulation, however, it did not help in the case of the defects that are part of combined volumes. A modification will be to try to store these transitions and also to reuse the transitions for combined volumes.

The work points out the need to a ternary potential that will describe the interaction between the Fe, Ni and Cr correctly and hence can be used to model the radiation damage in the ternary alloy. A possible perspective will be studying the RIS in the ternary alloy using this potential. Furthermore, studying the radiation damage at different GBs in the ternary alloy that would result from multiple collision cascades. Another expansion will be looking effect of incorporating He in the stainless steel and its effect on swelling and RIS.

We studied the radiation damage in Ni and Ni-Cr binary alloy at $\Sigma 5$ and $\Sigma 3$ symmetrical tilt GBs. We found that the GBs work as sinks for the interstitials and vacancies. An extension will be to try to study more types of GBs such as the twist GBs and measure the effect of these GBs on scattering these defects and to study the Cr segregation at the GB.

We modelled the radiation damage in fcc Ni in relation with the experiments. An expansion will be to model the same experiments which performed in Ni-Cr binary alloy. It will be interesting to compare the damage result in the system with the pure case and to look through the recombinations between the point defects.

Bibliography

[1] *Nuclear Power Plant*, http://chemistry.tutorvista.com/nuclear-chemistry/nuclear-power-plant.html.

[2] G. V. Raynor and V. G. Rivlin. Cr-Fe-Ni, Phase Equilibria in Iron Ternary Alloys. *Institute of Metals*, pages 316–332, 1988.

[3] A. K. Majumdar and P. v. Blanckenhagen. Magnetic phase diagram of $Fe_{80-x}Ni_xCr_{20}$ ($10 \leq x \leq 30$) alloys. *Phys. Rev. B*, 29(7):4079–4085, Apr 1984.

[4] P. Nash. In binary alloy phase diagrams. *ASM International, Materials Park*, 2(1289–1302), 1990.

[5] J. B. Piochaud. *Modelling of radiation induced segregation in austenitic fe alloys at the atomistic level*. PhD thesis, University of Lille, 2013.

[6] H. Hurchand. *Modelling intergranular Segregation in Nuclear Pressure Vessel Ferritic Steels*. PhD thesis, Loughborough University, 2005.

[7] C. Scott. 3D Visualiser. Loughborough University, 2012.

[8] G. Bonny. FeCrNi potential and its properties. Perform 60, private communication, September 2010.

[9] P. Nash. *Phase diagrams of binary nickel alloys*. ASM International, Materials Park, OH, 1991.

[10] G. Bonny, R. C. Pasianot, D. Terentyev, S. Poncé, and A. Bakaev. Interatomic potential to study plasticity in stainless steels: the FeNiCr model alloy. *Modelling and Simulation in Materials Science and Engineering*, pages 085008–14, 3 November 2011.

[11] G. Henkelman, B. P. Uberuaga, and H. Jónsson. A climbing image nudged elastic band method for finding saddle points and minimum energy paths. *The Journal of Chemical Physics*, 113(22):9901–9904, 2000.

[12] M F. Barthe. *Experimental results in pure Ni.* PERFORM60, Personal communication.

[13] H. Matter, J. Winter, and W. Triftshäuser. Phase Transformations and Vacancy Formation Energies of Transition Metals by Positron Annihilation. *Appl. Phys*, 20:135–140, 1979.

[14] J.D. Tucker. *Ab initio based modeling of radiation effects in the Ni-Fe-Cr system.* PhD thesis, University of Wisconsin-Madison, 2008.

[15] P. Klaver. *Fe-Cr Workshop.* Zürich , Switserland, 2010.

[16] R. Smith, D. E. Harrison, and B. J. Garrison. kev particle bombardment of semiconductors: A molecular-dynamics simulation. *Phys. Rev. B*, 40(1):93–101, Jul 1989.

[17] D. Mulliah, S. D. Kenny, and R. Smith. Modeling of stick-slip phenomena using molecular dynamics. *Phys. Rev. B*, 69(20):205407, May 2004.

[18] A. F. Voter, F. Montalenti, and T.C. Germann. Extending the time scale in atomistic simulation of materials. *Annu. Rev. Mater. Res.*, 32:321–346, 2002.

[19] G. Henkelman and H. Jonsson. Long time scale kinetic monte carlo simulations without lattice approximation and predefined event table. *The Journal of Chemical Physics*, 115, 21(9657), 2001.

[20] S. Blackwell and R. Smith and S. D. Kenny and J. M. Walls. *Modeling the Sputter Deposition of Thin Film Photovoltaics using Long Time Scale Dynamics Techniques*, 2011.

[21] C. Scott, S. Blackwell, L. Vernon, S. Kenny, M. Walls, and R. Smith. Atomistic surface erosion and thin film growth modelled over realistic time scales. *J. Chem. Phys.*, 135(174706), 3 November 2011.

[22] R. E. Hanneman and T. R. Anthony. Effects of non-equilibrium segregation on near-surface diffusion. *Acta Metallurgica*, 17(9):1133–1140, 1969.

[23] A. J. Jacobs, R. E. Clausing, L. Heatherly, and R. M. Kruger. Effects of Radiation on Materials 14th International Symposium. *ASTM*, I, 1989.

[24] T. R. Allen, J. I. Cole, J. Gan, G. S. Was, R. Dropek, and E. A. Kenik. Swelling and radiation-induced segregation in austentic alloys. *Journal of Nuclear Materials*, 342:90 – 100, 2005.

[25] B.H. Sencer, G.S. Was, M. Sagisaka, Y. Isobe, G.M. Bond, and F.A. Garner. Proton irradiation emulation of pwr neutron damage microstructures in solution annealed 304 and cold-worked 316 stainless steels. *Journal of Nuclear Materials*, 323(1):18–28, 2003.

[26] J. Gan and G. S. Was. Microstructure evolution in austenitic Fe-Cr-Ni alloys irradiated with rotons: Comparison with neutron-irradiated microstructures. *Journal of Nuclear Materials*, 297:161–175, August 2001.

[27] Z. Jiao and G. S. Was. The role of irradiated microstructure in the localized deformation of austenitic stainless steels. *Journal of Nuclear Materials*, 407(1):34–43, December 2010.

[28] Z. Jiao, J.T. Busby, and G.S. Was. Deformation microstructure of proton-irradiated stainless steels. *Journal of Nuclear Materials*, 361(2–3):218 – 227, 2007.

[29] T. R. Allen, J. I. Cole, E. A. Kenik, and G. S. Was. Analyzing the effect of displacement rate on radiation-induced segregation in 304 and 316 stainless steels by examining irradiated ebr-ii components and samples irradiated with protons. *Journal of Nuclear Materials*, 376(2):169–173, May 2008.

[30] M. J. Hackett, J. T. Busby, M. K. Miller, and G. S. Was. Effects of oversized solutes on radiation-induced segregation in austentic stainless steels. *Journal of Nuclear Materials*, 389:265–278, 2009.

[31] J. T. Busby, G. S. Was, and E. A. Kenik. Isolating the effect of radiation-induced segregation in irradiation-assisted stress corrosion cracking of austeinic stainless steels. *Journal of Nuclear Materials*, 302:20–40, 2002.

[32] T. R. Allen, L. Tan, G. S. Was, and E. A. Kenik. Thermal and radiation-induced segregation in model Ni-base alloys. *Journal of Nuclear Materials*, 361:174–183, 2007.

[33] M. Nastar. Segregation at grain boundaries: from equilibrium to irradiation induced steady states. *Philosophical Magazine*, 85(4–7):641–647, 2005.

[34] C. Dimitrov and O. Dimitrov. Influence of nickel concentration on point defect migration in high-nickel Fe-Cr-Ni alloys. *Journal of Nuclear Materials*, 152:21–29, 1988.

[35] C. Dimitrov and O. Dimitrov. Defect recovery in irradiated high-purity austenitic Fe-Cr-Ni alloys: activation energies and dependence on initial defect concentration. *Journal of Nuclear Materials*, 105:39–47, 1982.

[36] D.A. Terentyev, G. Bonny, and L. Malerba. Strengthening due to coherent Cr precipitates in Fe-Cr alloys: Atomistic simulations and theoretical models. *Acta Materialia*, 56(13):3229–3235, August 2008.

[37] G. Bonny, D. Terentyev, and L. Malerba. Identification and characterization of Cr-rich precipitates in FeCr alloys: An atomistic study. *Computational Materials Science*, 42(1):107–112, March 2008.

[38] G. Bonny, D. Terentyev, and L. Malerba. The hardening of iron-chromium alloys under thermal ageing: An atomistic study. *Journal of Nuclear Materials*, 385(2):278–283, March 2009.

[39] D. Terentyev, G. Bonny, and L. Malerba. Mobility of dislocations in thermal aged and irradiated Fe-Cr alloys. *Journal of Nuclear Materials*, 386–388:257–260, April 2009.

[40] R. W. Smith and G.S. Was. Application of molecular dynamics to the study of hydrogyn embrittlement in Ni-Cr-Fe alloys. *Physical Review B*, 40(15), 1989.

[41] J. D. Tucker. *Ab initio based modeling of radiation effects in the FeCrNi system.* PhD thesis, University of Wisconsin-Madison, 2008.

[42] B. J. Alder and T. E. Wainwright. Phase Transition for a Hard Sphere System. *J. Chem. Phys.*, 27(5):1208, 1957.

[43] R. Smith, editor. *Atomic and ion collisions in solids and at surfaces: theory, simulation and applications.* Cambridge University Press, 1997.

[44] M. W. Finnis and J. E. Sinclair. A simple empirical n-body potential for transition metals. *Philosophical Magazine A*, 50(1):45–55, 1984.

[45] S. D. Murray, M. F. Stephen, and I. B. Michael. The embedded-atom method: a review of theory and applications. *Materials Science Reports*, 9:251 – 310, 1993.

[46] M. S. Daw and M. I. Baskes. Embedded-atom method: Derivation and application to impurities, surfaces, and other defects in metals. *Phys. Rev. B*, 29:6443–6453, Jun 1984.

[47] M. I. Baskes. Modified embedded-atom potentials for cubic materials and impurities. *Phys. Rev. B*, 46:2727–2742, Aug 1992.

[48] M.I. Baskes. Modified embedded atom method calculations of interfaces. Number SAND–96-8484C; CONF-9603153–1, 1996.

[49] J. F. Ziegler, J. P. Biersack, and U. Littmark. *The Stopping and ranges of ions in matter*. New York : Pergamon, 1985.

[50] W. C. Swope. A computer simulation method for the calculation of equilibrium constants for the formation of physical clusters of molecules: Application to small water clusters. *The Journal of Chemical Physics*, 76(1):637, 1982.

[51] H. J. C. Berendsen, J. P. M. Postma, W. F. van Gunsteren, A. DiNola, and J. R. Haak. Molecular-dynamics with coupling to an external bath. *Journal of Chemical Physics*, 81(8):3684, 3690 1984.

[52] S. Nose. A unified formulation of the constant temperature molecular-dynamics methods. *Journal of chemical physics*, 81(1):511–519, 1984.

[53] William G. Hoover. Canonical dynamics: Equilibrium phase-space distributions. *Phys. Rev. A (American Physical Society)*, 31(3):1695–1697, March 1985.

[54] R. H. Magnus and S. Eduard. Methods of conjugate gradients for solving linear systems. *Journal of Research of the National Bureau of Standards*, 49(6):409–436, 1952.

[55] M. Robinson. *Modelling Radiation Damage in Plutonium*. PhD thesis, Loughborough University, 2010.

[56] L. J. Vernon. *Modelling Growth of Rutile TiO_2*. PhD thesis, Loughborough University, April 2010.

[57] A. Pedersen, S. F. Hafstein, and H. Jónssen. Efficient sampling of saddle points with the minimum-mode following method. *Society for Industrial and Applied Mathematics*, 33(2):633–652, 2011.

[58] N. Mousseau and G. T. Barkema. Traveling through potential energy landscapes of disordered materials: The activation-relaxation technique. *Phys. Rev. E*, 57:2419–2424, Feb 1998.

[59] G. Henkelman and H. Jónsson. A dimer method for finding saddle points on high dimensional potential surfaces using only first derivatives. *The Journal of Chemical Physics*, 111(15):7010–7022, 1999.

[60] J. Chen, N. Nakajima, and M. Okamoto. Shift-and-invert Lanczos algorithm for ideal MHD stability analysis. *Computer Physics Communications*, 113:1–9, 1998.

[61] G. Henkelman and H. Jónsson. Improved tangent estimate in the nudged elastic band method for finding minimum energy paths and saddle points. *The Journal of Chemical Physics*, 113(22):9978–9985, 2000.

[62] E. Weinan, R. Weiqing, and E. V. Eijnden. String method for the study of rare events. *Physical Review B*, 66(052301), 2002.

[63] B. Peters, A. Heyden, A. T. Bell, and A. Chakraborty. A growing string method for determining transition states: Comparison to the nudged elastic band and string methods. *The Journal of Chemical Physics*, 120(17):7877–7886, 2004.

[64] N. Metropolis, W. A. Rosenbluth, N. M. Rosenbluth, H. A. Teller, and E. Teller. Equation of State Calculations by Fast Computing Machines. *The Journal of Chemical Physics*, 21(6):1087–1092, 1953.

[65] P. Olsson, T. P. C. Klaver, and C. Domain. Ab initio study of solute transition-metal interactions with point defects in bcc fe. *PHYSICAL REVIEW*, 2010.

[66] P. Ehrhart. Properties and interactions of atomic defects in metals and alloys. *Springer Materials*, 25(chapter 2):88, 1991.

[67] C. Domain and C.L. Becquart. Report F16O-CT-2003-508840. PERFECT IP, 2007.

[68] G. J. Ackland, D. J. Bacon, A. F. Calder, and T. Harry. Computer simulation of point defect properties in dilute Fe–Cu alloy using a many-body interatomic potential. *Philosophical Magazine A*, 75(3):713–732, 1997.

[69] Y. Mishin. Atomistic modeling of the γ and γ' phases of the Ni-Al system. *Acta Materialia*, 52(6):1451–1467, 2004.

[70] Pär Olsson, Janne Wallenius, C. Domain, K. Nordlund, and L. Malerba. Two-band modeling of alpha-prime phase formation in fe-cr. *Physical Review B. Condensed Matter and Materials Physics*, 72(21):1–6, 2005. QC 20100525.

[71] Y. Mishin. Atomistic modeling of the γ and γ' phases of the Ni-Al system. 2004. [Tabulated data for Ni-Ni potential: http://www.ctcms.nist.gov/~cbecker/Al-Ni.html].

[72] M. I. Mendelev, S. Han, D. J. Srolovitz, G. J. Ackland, D. Y. Sun, and M. Asta. Development of new interatomic potentials appropriate for crystalline and liquid iron. *Philosophical Magazine*, 83(35):3977–3994, 2003.

[73] G. Bonny. FeNiCr potential and its properties. Perform 60, February 2012.

[74] A. P. Sutton and R. W. Balluffi. *Interfaces in Crystalline Materials*. Oxford Science Publications, 1996.

[75] X-M. Bai, A. F. Voter, R. G. Hoagland, M. Nastasi, and B. P. Uberuaga. Efficient annealing of radiation damage near grain boundaries via interstitial emission. *Science*, 327:1631–1634, 2010.

[76] Z. Al Tooq and S.D. Kenny. Modelling radiation damage at grain boundaries in fcc nickel and Ni-based alloy using long time scale dynamics techniques. *Nuclear Instruments and Methods in Physics Research*, Nuclear Instruments and Methods in Physics Research, 2012.